# Study of the time-dependent CP asymmetry in D° decays in the Belle II experiment

Robert Daniel Maria

# UNIVERSITÉ DE STRASBOURG

*ÉCOLE DOCTORALE DE PHYSIQUE ET CHIMIE-PHYSIQUE*

**Institut Pluridisciplinaire Hubert CURIEN (IPHC), UMR7178**

# THÈSE présentée par :

**Robert Daniel MARIA**

soutenue le : **30 octobre 2015**

pour obtenir le grade de : **Docteur de l'université de Strasbourg**

Discipline/ Spécialité : Physique des particules

# Study of the time-dependent CP asymmetry in $D^0$ decays in the Belle II experiment

**THÈSE dirigée par :**
**Mme. RIPP-BAUDOT Isabelle** — IPHC Strasbourg

**RAPPORTEURS :**
**M. PÖSCHL Roman** — LAL Orsay
**M. CLÉMENT Benoît** — LPSC Grenoble

**AUTRES MEMBRES DU JURY :**
**M. BLOCH Daniel** — IPHC Strasbourg

## Résumé

Nous étudions la sensibilité de Belle II avec 50 $ab^{-1}$ de données sur l'angle $\beta_c$ du triangle d'unitarité, avec une mesure en fonction du temps de l'asymétrie de CP dans les désintégrations des mésons $D^0$. Nous montrons que cette mesure est limitée statistiquement, avec une incertitude totale attendue de l'ordre de 3°. La mesure de $\beta_c$ nécessite la reconstruction de trajectoires de particules de très faible impulsion, impactée par le bruit de fond induit par SuperKEKB.
Deux échelles PLUME vont être utilisées pour étudier ce bruit de fond. Ici, une étude des performances de PLUME est effectuée. Ainsi, la résolution spatiale avec des traces à 0° et 36° est mesurée, de 1,8 $\mu$m et 3,5 $\mu$m respectivement.
Par ailleurs nous proposons d'améliorer la mesure des faibles impulsions en utilisant la charge déposée par la particule dans le trajectomètre interne au silicium. L'estimateur permet d'améliorer par 2 % la résolution sur l'impulsion pour les particules n'atteignant pas le trajectomètre interne.

**Mots clés**: Belle II, SuperKEKB, nouvelle physique, angle $\beta_c$, triangle d'unitarité $c-u$, matrice CKM, mesure en fonction du temps, violation de CP, échelle PLUME, capteurs CMOS, faible impulsion.

## Abstract

We are studying the sensitivity of Belle II with 50 $ab^{-1}$ data to the $\beta_c$ angle of the $c-u$ unitarity triangle, with a time-dependent measurement of the CP asymmetry in the $D^0$ decays. We show that such a measurement is still statistically limited, with a total expected incertitude of 3°.

This measurement relies on the reconstruction of soft momenta, impacted by the SuperKEKB induced background. Two PLUME ladders will be used to study this background, therefore a study on the performances of PLUME was performed. The spatial resolution is of 1.8 $\mu$m and 3.5 $\mu$m for 0° and 36° tilted tracks respectively.

We also propose to improve the estimation of soft momenta using the energy depositions of charged particles in the silicon layers of the inner tracker. Our estimator improves by approximately 2 % the resolution on momentum for particles which do not penetrate the central tracking system.


**Keywords**: Belle II, SuperKEKB, new physics, $\beta_c$ angle, $c-u$ unitarity triangle, CKM matrix, time-dependent measurement, CP violation, PLUME ladder, CMOS sensors, low momentum.

# Acknowledgements

First of all, I would like to express my deepest appreciation for my supervisor, Isabelle Ripp-Baudot. It was a pleasure to work with such a great person. I am thankful for her confidence and guidance. I am thankful for the encouragements she gave me and for sharing her wide knowledge with me. Her commitment to excellence inspired me.

A very special thanks goes to the following people: Jerôme Baudot for his help related to programming and for physics discussions; Alejandro Perez, for sharing his knowledge and for challenging my imagination during lunch breaks; Loïc Cousin for helping even while busy in finishing his own thesis; Mathieu Goffe for providing useful information on PLUME; Auguste Besson, for the suggestions during the defense preparation; Qian-Yuan Liu, for helping me overcoming programming issues; Yannick Patois, for helping me working on the grid. I would like to say thank you to my good friends Alessandro Minotti and Georgian Melinte for accepting to be my guinea pigs during the rehearsals of the thesis defense. I would also like to thank my devoted friends Surdu Nicolae and Mihai Dragoi, the Python and C++ masters.

A special thanks for the jury members, for reading this document and providing useful corrections and suggestions: Cristina Cârloganu, Roman Pöschl, Benoît Clément and Daniel Bloch.

And last but not least, I want to express my gratitude to Aline Fontaine, for her love, encouragements and patience. You lighted up my life during these last years!

# Contents

**Introduction** 11

**1 Theoretical framework** 14
- 1.1 A brief view of the Standard Model of particle physics . . . 14
  - 1.1.1 Bases of the Standard Model . . . 14
  - 1.1.2 Status of the Standard Model and new physics searches . . . 16
- 1.2 The CKM formalism . . . 18
  - 1.2.1 Strange particles . . . 18
  - 1.2.2 The Cabibbo angle . . . 18
  - 1.2.3 The CKM matrix . . . 21
  - 1.2.4 Parametrizations of the CKM matrix . . . 23
  - 1.2.5 The unitarity triangles . . . 27
  - 1.2.6 The $c-u$ unitarity triangle . . . 29
- 1.3 $D^0$ mixing and oscillations . . . 31
  - 1.3.1 Formalism . . . 32
  - 1.3.2 Current knowledge of mixing parameter values . . . 36
  - 1.3.3 Phenomenology of $D^0$ -$\overline{D}^0$ oscillations . . . 37
- 1.4 CP violation . . . 39
  - 1.4.1 Indirect CP violation due to mixing . . . 39
  - 1.4.2 Direct CP violation in decay . . . 40
  - 1.4.3 Indirect CP violation due to interference between mixing and decay . . . 41

**2 Experimental Framework** 42
- 2.1 The KEKB collider . . . 42
- 2.2 The upgrade scheme . . . 43
  - 2.2.1 The $\beta$-function and betatron oscillation . . . 43
  - 2.2.2 The luminosity of a collider . . . 44
- 2.3 The SuperKEKB collider . . . 47
  - 2.3.1 SuperKEKB operation schedule . . . 48

2.3.2 Background particles produced by SuperKEKB . . . . . 51
2.4 The interaction region (IR) . . . . . 55
2.5 The Belle II detector . . . . . 57
2.5.1 Introduction . . . . . 57
2.5.2 The Inner Tracking System . . . . . 60
2.5.3 The CDC detector . . . . . 68
2.5.4 The barrel TOP counter . . . . . 70
2.5.5 The end-cap ARICH detector . . . . . 71
2.5.6 The ECL detector . . . . . 72
2.5.7 The KLM detector . . . . . 73
2.6 Belle II on-line and off-line software tools . . . . . 73
2.6.1 The Belle II analysis framework . . . . . 73
2.6.2 The Belle II High Level Trigger . . . . . 76

**3 Sensitivity of Belle II to the $\beta_c$ angle of the charm unitarity triangle 77**
3.1 Introduction . . . . . 77
3.2 Experimental results on CP violation in $D^0 \to h^+h^-$ decays . . . . . 78
3.2.1 Time-integrated CP asymmetry measurements . . . . . 78
3.2.2 Time-dependent CP asymmetry measurements . . . . . 80
3.3 Principle of the $\beta_c$ measurement . . . . . 82
3.4 Ingredients of the time-dependent CP asymmetry measurement . . . 85
3.4.1 Analysis overview . . . . . 85
3.4.2 Reconstruction of $D^0$ candidates . . . . . 85
3.4.3 Flavour tagging . . . . . 87
3.4.4 $D^0$ flight time estimation . . . . . 91
3.5 Simulation and reconstruction of the CP asymmetry in $D^0$ decays . . 94
3.5.1 Simulation of the CP asymmetry in $D^0$ decays . . . . . 94
3.5.2 Reconstruction of the CP asymmetry in $D^0$ decays . . . . . 95
3.5.3 Estimation of the statistical uncertainty . . . . . 96
3.6 Study of the sensitivity of Belle II to $\beta_{c,eff}$ . . . . . 97
3.6.1 Impact of the main ingredients on the measurement . . . . . 97
3.6.2 Sensitivity of Belle II to $arg(\lambda_f)$ and $\beta_{c,eff}$ . . . . . 98
3.6.3 Discussion on systematic uncertainties . . . . . 100
3.7 Conclusion . . . . . 101

**4 Estimation of low momenta using energy deposition in Belle II silicon detectors 102**
4.1 Low momentum tracks in Belle II . . . . . 102

4.2 Principle of the momentum estimation based on energy loss . . . . . 106
4.2.1 The Bethe-Bloch formula . . . . . 106
4.2.2 Application of this method to Belle II . . . . . 108
4.3 Proposition of a low momentum estimator in Belle II . . . . . 110
4.3.1 Simulation study parameters . . . . . 111
4.3.2 Building a momentum estimator based on energy deposition in the inner tracking system . . . . . 112
4.3.3 Truncated mean . . . . . 113
4.3.4 Conclusions . . . . . 118
4.4 Performances of the proposed low momentum estimator . . . . . 118
4.4.1 The final proposed low momentum estimator . . . . . 118
4.4.2 Performances of the low momentum estimator . . . . . 121
4.5 Conclusions and outlooks . . . . . 126

**5 Performance studies of a PLUME ladder 129**
5.1 Introduction . . . . . 129
5.2 CMOS Pixel Sensors . . . . . 130
5.2.1 General considerations . . . . . 130
5.2.2 Benefits of CMOS Pixel sensors . . . . . 131
5.2.3 Finding the optimal working point . . . . . 132
5.2.4 CMOS sensors working principle . . . . . 133
5.2.5 Basic pixel architectures . . . . . 133
5.2.6 Conclusion . . . . . 135
5.3 MIMOSA-26 Sensors . . . . . 136
5.3.1 Introduction . . . . . 136
5.3.2 Working principle . . . . . 136
5.3.3 Performances . . . . . 138
5.4 The PLUME ladder . . . . . 139
5.5 The PLUME beam test setup and the analysis procedure . . . . . 141
5.5.1 Beam test setup . . . . . 141
5.5.2 Alignment of the telescope . . . . . 143
5.6 Estimation of the gap between two adjacent sensors . . . . . 147
5.7 Tracking performances with tilted tracks . . . . . 149
5.7.1 DUT configurations . . . . . 149
5.7.2 Alignment of the tilted DUT . . . . . 149
5.7.3 Estimation of the sensor deformation dimensions . . . . . 155
5.7.4 Cluster shapes induced by tilted tracks . . . . . 155

5.7.5 Benefit of double-sided pixelated layers . . . . . 158
5.8 Conclusions . . . . . 162

**Conclusion and outlook** **162**

**APPENDICES** **164**

**A Approximation of the path of a charged particle through a silicon layer** **165**

**B Alignment of sensor 11, for $\theta = 0^{o}$** **168**

**C Pixels in matched hits for sensors: 11 and 9** **169**

**Résumé en français** **170**

# List of Figures


1.1 Elementary particles in the standard model. . . . . 16

1.2 The Cabibbo angle and amplitudes of transitions between quarks of two families [26]. . . . . 20

1.3 The Unitarity Triangle representation in the complex plane. . . . . 29

1.4 The $c-u$ unitarity triangle (not to scale). . . . . 30

1.5 The normalized $c-u$ unitarity triangle. Triangle not to scale. . . . . 30

1.6 The unmixed (equivalent to the pure decay rate, represented by a continuous line) and the mixed (dashed line) amplitude as a function of $\Gamma t$ in case of an initially pure $D^0$, $B^0$, $B_s^0$ and $K^0$ state. For each neutral meson it was considered that $q/p = 1$ (i.e. indirect CP violation effects are neglected). The scale used for the $D^0$ system is logarithmic. . . . . 35

1.7 One to five $\sigma$ contours of allowed regions for x and y, taken from [52]. 37

1.8 One to five $\sigma$ contours of the allowed region for $q/p$, taken from [52]. 37

1.9 Box diagrams contributing to $D^0$ oscillations. . . . . 38

1.10 Di-penguin diagram contributing to $D^0$ oscillations. . . . . 38

1.11 The three types of CP violation for $D^0$ mesons (and for other neutral mesons): (A) in decay, (B) in mixing and (C) in interference between mixing and decay. Image taken from [19]. . . . . 39

1.12 Interference between mixing and decay amplitudes. . . . . 41

2.1 Integrated luminosity registered respectively by Belle at KEKB and by BaBar at PEP-II [60]. . . . . 43

2.2 An example of a phase-space plot. The area of the ellipse is always constant, equal to $\pi\epsilon$. The emittance $\epsilon$ cannot be changed by the focusing properties, it remains constant throughout the whole beam transport system. . . . . 44

2.3 Particle trajectories x(s) and the beam envelope E(s), in the upper image for 2 particles in the beam and in the lower image for 18 particles [61]. . . . . 44

2.4 Schematic plan of SuperKEKB summarizing the main upgrades undertaken, taken from [69]. . . . . 48

2.5 Targeted integrated and instantaneous luminosities of SuperKEKB, taken from [70]. A shift of about 1 year has been applied with respect to the plot, to account for the latest calendar. . . . . 49

2.6 Feynman diagram of a 2 photons QED-pair production, with 2 $e^+e^-$ pairs in the final state. . . . . 53

2.7 Example of a radiative Bhabha Feynman diagram with initial state and final state radiations. . . . . 54

2.8 In the left image the continuous injection scheme at SuperKEKB is presented. The right image illustrates the particle rate induced by the collider background. The damping due to the feedback system at KEKB, which is about 1 ms (in the image, the square representing 1 ms contains in fact data every 10 $\mu$s), appears much shorter than the radiation damping (incoherent damping). This prediction is empirically determined, and it represents the damping of the center of gravity of the bunch, but there can still be particles with high oscillations amplitude during about 20-40 ms. Images taken from [73]. 55

2.9 The magnetic field B (T) as a function of z (m) in the IR, between -4 m and +4 m around the collision point [77]. . . . . 57

2.10 A general view of Belle II detector with the main improvements indicated with respect to the Belle detector, taken from [70]. . . . . 58

2.11 Geometry of the PXD detector, with the first layer placed at 14 mm and the second layer at 22 mm from IP [77]. . . . . 61

2.12 Schematic view of a DEPFET cell taken from [77]. . . . . 63

2.13 The layout of a DEPFET half ladder [81]. . . . . 63

2.14 A cross section of the SVD detector, on the top in the Rz plane and on the bottom in the xy plane [84]. . . . . 66

2.15 The two shapes of sensors equipping the SVD sensor: trapezoidal sensors in the slanted part and rectangular sensors for the rest of the detector. With light blue color is represented the active area. [77]. . . 67

2.16 The effect of Lorenz tilt on electron and hole spreading [77]. . . . . 67

2.17 The impact parameter resolution along z axis of the Belle II inner tracking system, estimated from simulation and compared with the Belle measured vertex detector performances [88]. . . . . 69

2.18 Schematic view of a TOP counter showing photons emitted by a charged kaon (red) and a charged pion (green). The photons are emitted at different angles therefore they will be detected at different times [89]. . . . . 71

2.19 A chain of modules with common DataStore access (taken from [100]). 74

3.1 Results from Belle, BaBar, CDF and LHCb on time-dependent CP asymmetries in $D^0$ decays, yielding an average asymmetry $A_\Gamma = (-0.58 \pm 0.04)\%$. From [115]. . . . . 81

3.2 Two body hadronic $D^0$ decays to $\pi^+\pi^-$: (1) tree, (2) penguin and (3) W exchange topologies, together with the CKM matrix elements involved in the transitions. . . . . 84

3.3 Two body hadronic $D^0$ decays to $K^+K^-$: (1) tree, (2) penguin and (3) W exchange topologies, together with the CKM matrix elements involved in the transitions. . . . . 84

3.4 Event display view of a $D^{*\pm}$ originating from the hadronization of $c\bar{c}$ continuum events, decaying to $D^{*\pm} \to D^0\pi^+$ followed by $D^0 \to K^+K^-$. The charged pion is represented in brown, neutral particles but photons in violet, photons in green and charged kaons in red. The upper picture displays the extrapolated tracks inside the vacuum chamber, where the blue dotted line represents the $D^0$ flight distance. The bottom pictures show the soft pion curled track in the CDC, and tracks of the $K^+$ and $K^-$ decay products of the $D^0$ meson. This event was simulated in the Belle II detector with the basf2 framework. . . . 88

3.5 Distribution of the reconstructed mass of $D^0$ mesons (upper image) and $D^{*+}$ (lower image). . . . . 89

3.6 Distribution of the energy released in the $D^{*\pm}$ decay, as $Q = (M_{D^*} - M_{D^0} - M_\pi)c^2$. . . . . 89

3.7 Sketch of the $D^{*\pm}$ production from $c\bar{c}$ continuum (prompt production). The $D^{*\pm}$ can decay to a $D^0$ and a slow pion. The flavour identification relies on the charge of the soft pion: a positive slow pion corresponds to a $D^0$ , while a negative pion to a $\bar{D}^0$. . . . . 90

3.8 Distribution of the flight distance of $D^0$ mesons in the laboratory frame displayed as a function of the flight time in the $D^0$ rest frame (left) and mean values of this distribution (right). . . . . 91

3.9 The Belle II expected resolution on the reconstructed $D^0$ flight distance. 92

3.10 Expected resolutions on the reconstructed $D^0$ production vertex (left column) and decay vertex (right column). . . . . 93

3.11 The proper time distributions of $D^0$ (left) and $\bar{D}^0$ (right) generated with our fast simulation tool, here with $arg(\lambda_f) = 10^o$, $|\lambda_f| = 1$ and a dataset of $5{\times}10^6$ $D^0$ - $\bar{D}^0$. . . . . 94

3.12 Simulated asymmetry with $arg(\lambda_f) = 10^o$, $|\lambda_f| = 1$ and a dataset of $5{\times}10^6$ $D^0$ - $\bar{D}^0$. . . . . 95

3.13 CP asymmetries as a function of time, generated with different values of $|\lambda_f|$ and $arg(\lambda_f)$. Continuous lines correspond to generated asymmetries with different values of $|\lambda_f|$, while dotted lines correspond to generated asymmetries with different values for $arg(\lambda_f)$. On the left plot we see the variation of the asymmetry as a function of time, with the influence of both $|\lambda_f|$ and $arg(\lambda_f)$, while on the right plot only the influence of $|\lambda_f|$ is considered. . . . . 95

3.14 Time-dependent CP simulated asymmetry with $arg(\lambda_f) = 10^o$, $|\lambda_f| = 1$ and a dataset of $5{\times}10^6$ $D^0$ - $\bar{D}^0$ . The fit to the asymmetry is superimposed (red). Here, a measured value of $arg(\lambda_f) = 6.97^o \pm 3.6^o$ is obtained from the fit. . . . . 96

3.15 The statistical dispersion of the measured value of $arg(\lambda_f)$ in 1000 experiments. $5{\times}10^6$ $D^0$ -$\bar{D}^0$ mesons were generated, with $arg(\lambda_f) = 10^o$. . . . . 97

3.16 Estimated statistical uncertainty on the measured value of $arg(\lambda_f)$ as a function of the generated value of $arg(\lambda_f)$, observed for the expected $D^0 \to K^+K^-$ decay statistics (red triangles) and for the expected $D^0 \to \pi^+\pi^-$ decay statistics (blue circles) in Belle II. . . . . 98

3.17 Estimated statistical uncertainty on the measured value of $arg(\lambda_f)$ as a function of the number of reconstructed mesons, here displayed for a generated value $arg(\lambda_f) = 10^o$. . . . . 99

3.18 Estimated statistical uncertainty on measuring $arg(\lambda_f)$ as a function of the flavour mis-identification (here displayed for a generated value $arg(\lambda_f) = 5^o$). The red triangles correspond to the $D^0 \to K^+K^-$ decay channel and the blue circles to the $D^0 \to \pi^+\pi^-$ decay channel. 99

4.1 Illustration of the difficulty to reconstruct low momentum tracks. These two pictures are event displays of the Belle II detector, showing a transversal view of the detector. Two tracks were reconstructed by mistake instead of one curling track. On the upper view, the two reconstructed tracks are represented in blue and in the zoom below, we represent in red how the reconstructed track should have looked like. . . . . 103

4.2 Momentum distribution of final state particles in generic $\Upsilon(4S) \to B\bar{B}$ events. The left figure displays generated momenta and the right one displays reconstructed momenta. Pion spectrum is represented in red, electron with black, kaon with blue, muon with green and proton with violet. . . . . 104

4.3 Momentum distribution of soft pions originating from $\Upsilon(4S) \to B\bar{B}$ events with one $B$ decaying to a $D^{*\pm}X$ followed by $D^{*\pm} \to \pi^{\pm}D^0(\bar{D}^0)$ (on the left), and originating from continuum $c\bar{c}$ events producing $D^{*\pm} \to \pi^{\pm}D^0(\bar{D}^0)$ (on the right). . . . . 105

4.4 Stopping power of pions in silicon. Figure taken from [130]. . . . . 107

4.5 Distributions of energy deposition (ADC counts) measured in silicon layers in Belle II, of pions produced with different soft momenta ranging from 60 MeV to 200 MeV. . . . . 108

4.6 Mean energy deposition $\Delta E/\Delta x$ (ADC counts) for the PXD detector encoded with 5 bits (up) versus the SVD detector, encoded with 10 bits (down). . . . . 110

4.7 Ratio between the charge collected on the p-side strips and on the n-side strips of a same wafer of the SVD detector and for a same crossing particle. . . . . 111

4.8 Energy deposition (ADC counts) of low momentum particles as a function of the momentum (GeV). . . . . 113

4.9 Cluster multiplicity in the SVD vs. the momentum, for protons, kaons and pions produced with a polar angle $\theta \in [17, 150]°$. . . . . 114

4.10 Distribution of truncated mean energy deposition compared to the one of raw mean energy deposition, of 70 MeV generated pions. . . . 115

4.11 Energy deposition distributions in the SVD layers (left), and the corresponding fits (right) for pions generated with momentum of 80 MeV and an incident polar angle of $\theta = 45°$. . . . . 117

4.12 Energy deposition distributions in the SVD layers (left) and the corresponding fits (right) for pions generated with momentum of 80 MeV and an incident polar angle of $\theta = 90°$. . . . . 117
4.13 SVD cluster multiplicities observed for pions generated with different momenta and $\theta$ polar angles. . . . . 119
4.14 Truncated mean energy deposition $\Delta E/\Delta x$ (ADC counts) versus the charged particle momentum. . . . . 120
4.15 Estimation of the "mean value" (see text) of the $\Delta E/\Delta x$ for one momentum bin of the 2D histogram of the mean truncated $\Delta E/\Delta x$ as a function of the momentum. . . . . 121
4.16 Momentum as a function of the mean truncated $\Delta E/\Delta x$ (as the MPV obtained from a Landau fit) with the parametrization 4.7 superimposed. The uncertainty error bars are asymmetric, one for the left and one for the right part of the MPV. . . . . 122
4.17 Helix-estimated momentum resolution for pions generated with an incident polar angle $\theta = 45°$. For 50 MeV pions, the fit was realized with half of a Gaussian, because no tracks with momentum below 50 MeV are reconstructed in Belle II. For reconstructed tracks of pions with momenta between 60 and 140 MeV, a sum of two or three Gaussians is used: each individual Gaussian is represented in blue, green or black and the sum in red. . . . . 123
4.18 Relative momentum resolution observed in different momentum bias, of the estimator considering both PXD and SVD detectors, for pions generated with an incident polar angle $\theta = 45°$. . . . . 125
4.19 Comparison of the momentum resolution observed with a $\Delta E$-based estimator considering the 6 minimum energy deposition in both PXD and SVD detectors and an estimator considering the 4 minimum energy deposition only in the SVD detector. The pions were generated with uniform momentum distribution between 0.05 and 0.14 GeV, uniform azimuthal angle $\theta$ in the acceptance of the detector and an incident polar angle $\theta = 45°$. The error bars are smaller than the black squares for momenta higher than 0.05 GeV. . . . . 126
4.20 Relative momentum resolutions observed with the helix-based estimation (red colour) and with the dE/dx-based estimator (blue colour) for low pions generated with incident polar angle $\theta = 45°$. The error bars are smaller than the black / red squares for momenta higher than 0.05 GeV. . . . . 127

5.1 Illustration of the correlation between all the performances which looks like a problem of squaring the circle. Image taken from [136]. . 132

5.2 Transverse cross section of an active CPS (left) and the electrostatic potential through the sensor substrate (right), taken from [140]. Charges are created along the path of the particle in the epitaxial layer, where the doping is low enough to allow these charges to diffuse thermally towards the sensing element. The depleted region, in brown, represents a small part of the whole sensitive volume. . . . . 134

5.3 Schematic view of the 3T baseline pixel architecture (a) and of the SB baseline architecture (b). . . . . 135

5.4 MIMOSA-26 layout. . . . . 136

5.5 The readout scheme consisting in reading a column at a time. Figure taken from [159] . . . . . 138

5.6 Performances of the MIMOSA-26 sensor with a standard epitaxial layer 14 $\mu$m thick. [160]. . . . . 139

5.7 The layout of the PLUME-1 ladder, composed of 6 MIMOSA-26 sensors thinned down to 50 $\mu m$ placed on each side of a foam. . . . . 140

5.8 The PLUME ladder equipped with 12 sensors, 6 on each side. The 6 sensors of one side of the ladder (dark green) are slightly shifted along the $V$-axis with respect to the sensors from the opposite side of the ladder (light green). The beam spot on the sensors is illustrated in orange. . . . . 141

5.9 Views from the top of the setup used for the runs registered with DUT tilts $\theta$=0°, 36° (top) and 60° (bottom). The distances are measured from the center of the PLUME device to the center of each telescope arm. The numbering scheme used for the telescope sensors increases from the beam side. The telescope planes, DUT and the distances between them are not in scale. . . . . 142

5.10 Distribution of the residues $\Delta x = x_{track} - x_{hit}$ (horizontal axis) after the telescope alignment procedure of the four telescope sensors. . . . 146

5.11 Distribution of the residues $\Delta y = y_{track} - y_{hit}$ (vertical axis) after the telescope alignment procedure of the four telescope sensors. . . . . 146

5.12 Distribution of the residues obtained with the DUT placed perpendicularly to the beam (only sensor 2): (a) $\Delta u$ residue as a function of the local $v$ coordinate, (b) $\Delta u$ residue as a function of the local $u$ coordinate, (c) $\Delta v$ residue as a function of the local $u$ coordinate, (d) $\Delta v$ residue as a function of the local $v$ coordinate, (e) $\Delta u$ residue and (f) $\Delta v$ residue. . . . . 147

5.13 Distribution of the reference hits (extrapolations of the telescope tracks) on the DUT plane in the global (x,y) coordinates system and projection of this distribution on the x-axis (bottom). Each bin corresponds to 5 $\mu$m. . . . . 148

5.14 The mean gap distance measured with two step functions. . . . . 149

5.15 Distributions of the $\Delta u$ residue obtained with $\theta$=36° tilt (here for sensor 2). Residues are displayed as a function of the $u$ coordinate (top) and of the $v$ coordinate (middle), and integrated along $u$ and $v$ (bottom). Left figures correspond to the residue observed after an alignment performed globally for the whole sensor, while right figures display the distributions observed after the alignment of a small region of the sensor (as it can be seen from the $u$ and $v$ coordinates). . . . . 151

5.16 Distributions of the $\Delta u$ residue obtained with $\theta$=36° tilt (here for sensor 11). Residues are displayed as a function of the $u$ coordinate (top) and of the $v$ coordinate (middle), and integrated along $u$ and $v$ (bottom). Left figures correspond to the residue observed after an alignment performed globally for the whole sensor, while right figures display the distributions observed after the alignment of a small region of the sensor (as it can be seen from the $u$ and $v$ coordinates). . . . . 152

5.17 Distributions of the $\Delta u$ residue obtained with $\theta$=60° tilt (here for sensor 4). Residues are displayed as a function of the $u$ coordinate (top) and of the $v$ coordinate (middle), and integrated along $u$ and $v$ (bottom). Left figures correspond to the residue observed after an alignment performed globally for the whole sensor, while right figures display the distributions observed after the alignment of a small region of the sensor (as it can be seen from the $u$ and $v$ coordinates). . . . . 153

5.18 Distributions of the $\Delta u$ residue obtained with $\theta$=60° tilt (here for sensor 9). Residues are displayed as a function of the $u$ coordinate (top) and of the $v$ coordinate (middle), and integrated along $u$ and $v$ (bottom). Left figures correspond to the residue observed after an alignment performed globally for the whole sensor, while right figures display the distributions observed after the alignment of a small region of the sensor (as it can be seen from the $u$ and $v$ coordinates). . . . . 154

5.19 The sensor deformations measured estimated by the geometrical approximation $\Delta z = \frac{\Delta u}{tan(\theta)}$, where $\Delta z$ is the shift along the z-axis of the reconstructed hit and $\theta$ is the angle of the track. . . . . 156

5.20 Distributions of cluster dimensions (total number of pixels used to reconstruct the cluster) observed at tilts $\theta = 0°$ (sensor 2), $\theta$=36° (sensor 2) and $\theta$=60° (sensor 4). . . . . 157

5.21 Distributions of cluster dimensions along the lines ($u$-coordinate, left) and the columns ($v$-coordinate, right) of the pixel matrix. . . . . 157

5.22 With the 2 hits measured in the double-sided DUT layer, a mini-vector is reconstructed (represented by the green line). The black line represents the reference track reconstructed with the telescope. . 159

5.23 2D-distributions ($v$ vs $u$) of the extrapolated positions of the reference tracks (reconstructed with the telescope) on the DUT (red points) and measured hits in the DUT (black points) for two PLUME sensors placed back-to-back on the PLUME ladder. . . . . 160

5.24 Resolution measured along the $v$ direction, for tilts = 0°and 36° (sensor 2). . . . . 161

5.25 The angular resolution obtained with mini-vectors. . . . . 161

A.1 Sketch with the path of a particle through a silicon layer: in the absence of a magnetic field (black), with a magnetic field (purple) and the path estimated by us (red). . . . . 166

A.2 Sketch of the curved path of a charged particle. . . . . 166

B.1 Distribution of the residues obtained with the DUT placed perpendicular to the beam for sensor 11: (a) Residue $\Delta u$ as a function of the $v$ local coordinate, (b) residue $\Delta u$ as a function of the $u$ local coordinate, (c) residue $\Delta v$ as a function of the $u$ local coordinate, (d) residue $\Delta v$ as a function of the $v$ local coordinate, (e) residue $\Delta u$ and (f) residue $\Delta v$. . . . . 168

C.1 Sum of all pixels (for both $u$ and $v$) in matched hits for $\theta = 0^o$ (sensor 2), $\theta$=36$^o$ (sensor 2) and $\theta$=60$^o$ (sensor 4). . . . . 169
5.2 Production de $D^{*\pm}$ à partir du continuum $c\bar{c}$, le $D^{*\pm}$ se désintègre ensuite en un $D^0$ et un pion mou. . . . . 174
5.3 Les distributions de temps propre des désintégrations de $D^0$ (gauche) et de $\bar{D}^0$ (droite) générées avec une simulation rapide, avec $arg(\lambda_f)$ = 10°, $|\lambda_f| = 1$ et 5×10$^6$ mésons $D^0$. . . . . 175
5.4 L'asymétrie simulée avec $arg(\lambda_f) = 10°$, $|\lambda_f| = 1$ et 5×10$^6$ mésons $D^0$. . . . . 175
5.5 Dispersion statistique de 1000 mesures de $arg(\lambda_f)$. 5×10$^6$ mésons neutres $D^0$ ont été générés avec $arg(\lambda_f) = 10°$. . . . . 176
5.6 Distribution de la moyenne tronquée de l'énergie déposée, comparée à la moyenne de l'énergie déposée, pour des pions d'impulsion 70 MeV. 178
5.7 Résolution sur l'impulsion obtenue avec l'estimateur construit à partir des amas d'énergie reconstruits dans le SVD (courbe bleue) et a partir des amas reconstruits dans l'ensemble du trajectromètre interne SVD + PXD ( courbe rouge). . . . . 179
5.8 Les résolutions sur l'impulsion relative obtenues par l'ajustement de la trajectoire par une hélice (noir), et avec notre estimateur utilisant le dE/dx (rouge). . . . . 180
5.9 La distribution des impacts des particules du faisceau sur deux plans adjacents du DUT. Chaque intervalle d'histogramme correspond à une distance de 5 $\mu$m. . . . . 181
5.10 Les distributions du résidu $\Delta u$ observé pour traces inclinées de $\theta$=36° par rapport au DUT. La partie gauche correspond à un alignement globale de tout le capteur et la droite, à un alignement d'une sous-partie du capteur considéré comme plan au niveau micromètrique. . . 183

# List of Tables


1.1 The six unitarity triangles, their corresponding off-diagonal unitarity relations and magnitudes of the sides of the triangles in terms of $\lambda$. . 28

2.1 Beam parameters of KEKB using the crab cavitiy scheme and SuperKEKB based on the nano-beam scheme. Phase 2 corresponds to the commissioning, discussed later in this chapter and phase 3 to the physics run. Values taken from [66, 67]. . . . . 47

2.2 Predicted occupancy rates in the two pixel layers, for different background sources except synchrotron radiation and injection noise [74]. 56

2.3 Description of each silicon layer of the inner tracking system of Belle II [77–79]. . . . . 60

2.4 The main characteristics of the CDC detector of Belle II, compared to those of the former Belle CDC [77]. . . . . 69

3.1 Systematic uncertainties on $arg(\lambda_f)$ due to uncertainties on the mixing parameters $x$ and $y$. . . . . 100

5.1 Average distances measured between two adjacent sensors of the PLUME device. Uncertainty due to the binning is 5 $\mu$m. . . . . 149

5.2 Different configurations considered for the tilted tracks study. . . . . 150

# Introduction

Despite of the immense success of the standard model of particle physics (SM), several experimental observations are still waiting for an explanation. One of them is the observed dominance of matter with respect to antimatter in the Universe. A. Sakharov demonstrated in 1967 that CP violation, combined violation of C (charge conjugation) and P (parity) symmetries, is one of the necessary conditions for this to occur [1].
In the standard model, the CP violation is encoded in a single complex phase in a 3 x 3 quark mixing matrix, the so-called Cabibbo-Kobayashi-Maskawa (CKM) mixing matrix [2, 3]. Experimentally, CP violation has been observed over the past 40 years in both K [4] and B decays [5–8] and all these measurements agree with their SM predictions. Only recently the first hint of CP violation was reported in time integrated rates in $D^0$ decays by the LHCb [9] and then also by CDF [10] and Belle [11] collaborations. More precision is needed in order to clarify whether these measurements are in agreement with the SM expectations or correspond to a manifestation of physics beyond the SM.

This thesis aims at investigating several aspects addressing Belle II inner tracker performances. The physics subject is organized around the study of indirect CP violation effects in $D^0$ decays, which proves to be a particular good benchmark in this context. This study is based on a time dependent analysis, where the reconstruction of the $D^0$ flight distance is disadvantaged by the relatively short lifetime of the $D^0$ with respect to $B$ meson's lifetime, and also by the presence of a soft pion in the final state. The aforementioned soft pion is used to identify the flavor of the neutral $D^0$ meson and to reconstruct its flight time in order to perform the time dependent measurement. Soft momenta are difficult to reconstruct because tracks are significantly impacted by multiple scattering in addition to their curling in the inner tracker, and they may not reach the Central Drift Chamber of Belle II. In this thesis, an alternative method is proposed to improve the momentum estimated from a helix fit of the track. The method makes use of the information on the particle energy loss measured in the Belle II inner tracker detectors.

The Belle II detectors will register collisions delivered by the SuperKEKB collider at the highest ever achieved instantaneous luminosity. To reach such a high intensity, a new collision scheme will be used based on flat beams, with transverse dimension of about 50 nm in one dimension. These very intense beams will produce an overwhelming level of background particles through beam-beam interactions as well as interactions of particles within each beam, with major impact in particular on the inner tracker layers. The safe operation of the inner tracker will be tested during the commissioning phase of the Belle II experiment, called BEAST II, scheduled before the start of the Belle II physics run. One of the devices which will be used to characterize the background induced by SuperKEKB in the inner tracker volume during BEAST II will be based on PLUME ladders equipped with CMOS pixellated sensors. In this thesis, several performances of the PLUME ladder are studied with beam test data in this thesis.

The thesis report is organized as follows:
In Chapter 1, the theoretical context is presented, with a brief overview of the SM and a deeper focus on CP violation in the charm sector. Chapter 2 describes the experimental context of this thesis, consisting in the SuperKEKB collider and the Belle II experiment. The three following chapters are devoted to the studies performed during this thesis. In Chapter 3, the sensitivity of the Belle II experiment to the $\beta_c$ angle of the charm unitarity triangle is studied with simulated data. Chapter 4 reports on the estimation of low momenta using the energy deposition of the charged particles in the inner tracker detectors. Chapter 5 deals with the PLUME detector and several measured performances related to their tracking efficiency. Finally, the conclusion summarizes the work performed in this thesis and discusses its outlook.

# 1. Theoretical framework

In this chapter, Section 1.1 is devoted to a brief introduction to the standard model of particle physics. The CKM formalism is described in Section 1.2. $D^0$ mixing and oscillation formalism are introduced in Section 1.3. Finally, Section 1.4 points out the different ways to violate the CP symmetry.

## 1.1 A brief view of the Standard Model of particle physics

### 1.1.1 Bases of the Standard Model

The standard model of particle physics (SM) is a theory based on special relativity and quantum mechanics, in the framework of the Quantum Field Theory. It describes elementary particles and their interactions. The four fundamental interactions are electromagnetic, weak, strong and gravitational. However, gravitation is not described in the frame of the SM as there is no theory of a quantum gravity yet. Particles at the scales we are considering are not significantly sensitive to gravitation, whose magnitude can be neglected with respect to the three other interactions.

The idea of searching for the elementary building blocks of matter goes back to the ancient times. We call an elementary particle, a particle which cannot be divided into other parts. In ancient times it was believed that the four basic blocks of matter were fire, water, earth and air. Later, due to the eighteenth and nineteenth-century chemists works, atoms replaced these elementary building blocks of matter. The answer to the question "what is matter made of?" continued to be the driving force in physics in the twentieth century.
In 1897 the electron was discovered, and it remains until today an elementary particle, in the limit of our experimental sensitivity. Since then, other elementary particles were found while others were removed from the classification. The atom, for instance, is no more considered as elementary, the proton and neutron neither.

In 1964 M. Gell-Mann and G. Zweig proposed the quark model [12, 13]. Quarks were introduced with three flavours: up, down and strange, of half integer spin and electrical charge +2/3 for up and -1/3 for down and strange. Even though the quarks were never seen singly in any experiment, this model explained the fact that many of the particles experimentally observed and thought as elementary, were in fact bound states of quarks. Since then, three other quarks were theoretically predicted and experimentally found. The present six quarks are: up (u), down (d), charm (c), strange (s), top (t) and bottom (or beauty, b). Today, quarks are considered to be elementary particles.

In the quark model, baryons are composed of three quarks ($qqq$) and mesons are composed of a quark and an antiquark ($q\bar{q}$). Bound states of four and five quarks were also reported [14, 15].

We can consider the quarks as having six degrees of freedom called flavour. Through charged weak interaction, one quark flavour can change into another quark flavour. Another degree of freedom for quarks is the colour charge, which is of three types: R (red), G (green) and B (blue) and their corresponding anticolours. The strong interaction is the interaction between quarks due to the colour charge.

Another kind of elementary particles is represented by leptons: $e^-, \mu^-, \tau^-$ and their corresponding neutrinos $\nu_e, \nu_\mu, \nu_\tau$. Leptons do not participate in strong interactions and have no colour degrees of freedom. Neutrinos participate to weak and gravitational interactions and , while $e^-, \mu^-, \tau^-$ being charged particles, participate also to electromagnetic interactions.

Interactions between particles are mediated by a corresponding boson. Electromagnetic interactions are mediated by photons ($\gamma$), weak interactions by $W^\pm$ and $Z$ gauge bosons, and strong interactions by gluons. Gravitation is supposedly intermediated by gravitons, massless particles whose existences have not been confirmed yet. The Higgs boson (H) completes the theory of particles and fields.

The full SM picture of fundamental particles is represented in Fig. 1.1, where for each particle we have to add the corresponding antiparticle. We can observe a classification in families (corresponding to SU(2) doublets), where the members of families differ only by a succeeding increase of mass between families. Each member of the three families, up-type or down-type, carry identical quantum numbers.

To summarize, the SM is a renormalizable quantum field theory constructed under the principle of local gauge invariance under the $SU(3)_C \times SU(2)_L \times U(1)_Y$ symmetry group. Gauge fields arise from the requirement that the Lagrangian is invariant under these gauge symmetries. The gluons, $W^\pm$, $Z$ and photons are the quanta,

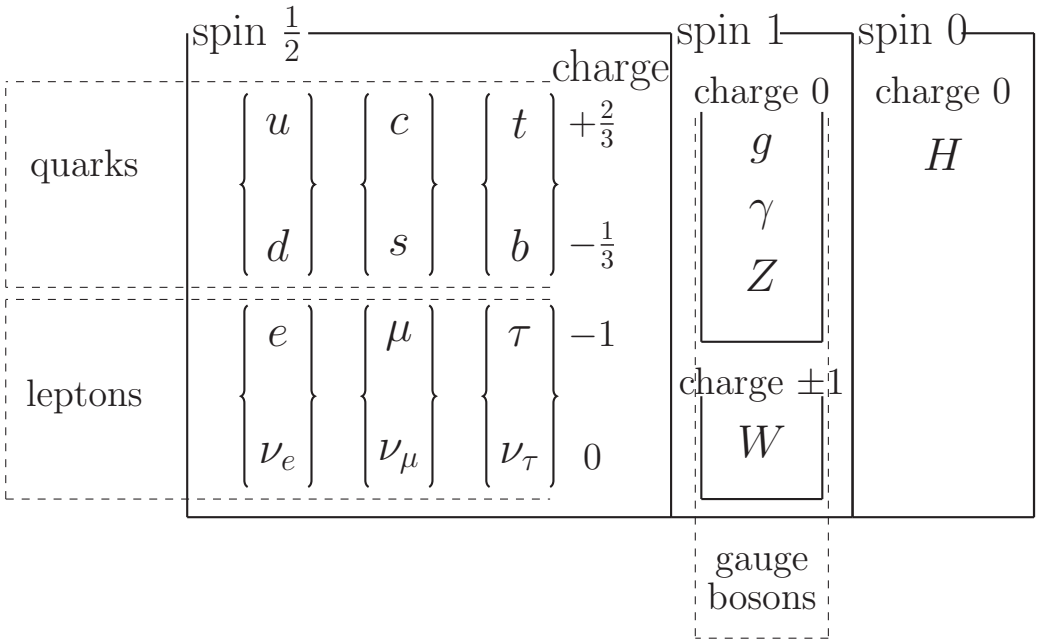


**Figure 1.1:** Elementary particles in the standard model.

called gauge bosons, of these fields. A Higgs field must be added ad hoc to the theory to enable the description of massive gauge bosons with a Lagrangian invariant under $SU(2)_L \times U(1)_Y$. This Higgs field introduces a spontaneous symmetry breaking and creates the Higgs boson as the longitudinal field component.

### 1.1.2 Status of the Standard Model and new physics searches

The SM is currently confirmed, after being successfully tested with a tremendous amount of precise measurements in the gauge boson, quark and lepton sectors, and recently also in the Higgs sector. It describes very well the results of many particle physics experiments. If we compare the SM with a jigsaw puzzle, then, over the last 120 years all the individual puzzle pieces were discovered, culminating with the last piece, the Higgs boson, discovered in 2012 by ATLAS and CMS collaborations [16, 17]. However, there are clues indicating that the SM is not a complete theory, meaning that we do not have the full picture yet. It is generally considered that the SM is an effective theory, that means a low energy representation of a wider theory. At this stage, no clear indication exists to understand at which energy the SM will cease to be valid to describe elementary particles and interactions. Some guides are brought by experimental observations, for instance that lepton flavour is not conserved, that an additional source of CP violation must exist, that some mechanism is responsible for the neutrino masses, that unknown particles should explain part

of the dark matter, and that dark energy exists.
A global effort is made to search for physics beyond the standard model, or the new physics (NP): using two complementary approaches: at the energy and intensity frontiers (this is a simple classification).
The discovery of neutrino oscillations at Super-Kamiokande experiment in 1998 [18] was a first step to overcome the SM and unravel its flavour structure, attacking this mystery from the lepton sector (at the intensity frontier). This may open the door to reveal CP violation in the lepton sector, which might drive baryogenesis in a Big Bang Universe [19]. The MINOS and T2K experiments have already made some progress in this direction. But the next major breakthrough from neutrino physics may only occur at the horizon 2025-2030, in particular thanks to a future Long Baseline experiment.
Many non-collider experiments, based on very intense sources of particles participate to the indirect search for NP, as for neutron electric dipole moment and muon g-2 measurements, and searches for charged lepton flavour violating decays.
At the energy frontier, LHC is already searching for NP at 13 TeV and this high center-of-mass energy may allow to produce heavy, yet undiscovered, particles like supersymmetric partners of quarks, leptons and gauge bosons, or new particles linked to extra dimensions. If these particles are ever seen at LHC, precision measurements at the intensity frontier will be needed in order to study their properties.
Belle II experiment will rely on an intense source of electrons and positrons, and ultra-sensitive detectors in order to detect tiny deviations from the SM predictions. Mechanisms like neutral meson mixing and rare B, D and $\tau$ decays are mediated by loop processes involving virtual particles and are sensitive to possible NP contributions. Belle II physics program is complementary to the direct searches performed at the LHC, and it is likely to be sensitive to much higher masses of the virtual particles than the reach of the LHC collisions.

## 1.2 The CKM formalism

This section presents how the quark mixing was discovered after observation of strange particles, beginning with only three types of quarks and then extended to three families of quarks.

### 1.2.1 Strange particles

In 1947 the K meson was spotted in cosmic rays [20]. It was the first "strange" particle to be discovered, with a mass approximately 1000 times larger than the electron's one. In these early times of particle physics, these particles were called V-particles, because of the typical angular appearance of their decays. All the V-particles are now identified and given a specific name. The name "strange" comes from the fact that they are produced at a time scale of $10^{-23}$ s and decay after $10^{-8}$ - $10^{-10}$ s. Now we know that this difference results from the fact that the production mechanism is governed by the strong interaction while the decay is due to the weak interaction.
In 1955-1956, K. Nishijima [21] and M. Gell-Mann [22] proposed the existence of a property, lately called "strangeness", which is conserved in the strong interaction but not in the weak one. M. Gell-Mann categorized the known particles in 2 types: ordinary particles, like pions and nucleons (and their antiparticles) and strange particles, like kaons and hyperions (V-particles whose decay products always include a proton).
Ordinary particles are assigned a strangeness S = 0, while strange particles carry strangeness S $\neq$ 0. They are always produced in pairs, such that the total strangeness is about 0.

### 1.2.2 The Cabibbo angle

The experimentally observed suppression of $\Delta S = 1$ transitions compared to $\Delta S = 0$ transitions was explained in 1963 by N. Cabibbo [2]. N. Cabibbo wanted to keep the total weak current of hadrons unchanged, assuming that it flows into two branches, one with $\Delta S = 1$ and one with $\Delta S = 0$:

$$J_\mu = a j_\mu^{(0)} + b j_\mu^{(1)} \tag{1.1}$$

Where $j_\mu^{(0)}$ and $j_\mu^{(1)}$ are currents corresponding to $\Delta S = 0$ and $\Delta S = 1$ transitions, respectively. Assuming that the total weak hadronic current remains unchanged, $J_\mu$

is required to be normalized to unity:

$$a^2 + b^2 = 1 \tag{1.2}$$

The weak current 1.1 can finally be written:

$$J_\mu = cos(\theta_c) j_\mu^{(0)} + sin(\theta_c) j_\mu^{(1)} \tag{1.3}$$

Where $\theta_c$ is the Cabibbo angle, experimentally determined to be about 13°. The normalization condition 1.2 is automatically satisfied.
The interpretation of N. Cabibbo's work is that $d$ and $s$ quarks implied in weak interactions are actually a mixture of $d$ and $s$ physics quarks (the mass eigenstates). Quarks participating to weak interactions correspond to the following linear combinations:

$$\begin{aligned} d' &= d\, cos\theta_c + s\, sin\theta_c \\ s' &= -d\, sin\theta_c + s\, cos\theta_c \end{aligned} \tag{1.4}$$

Here $d'$, $s'$ are weak eigenstates and $d$, $s$ are mass eigenstates.

But this model raises another issue, because it allows the change of flavour realized by neutral currents (FCNC), which has never been experimentally observed. All flavour changing processes are realized by the intermediate of $W^+$ or $W^-$. The solution to this issue was brought by S. L. Glashow, J. Iliopoulos and L. Maiani in 1970, by what is now called the GIM mechanism [23]. At the time of the introduction of the Cabibbo angle, only 3 quarks were known. The quark-lepton symmetry was not respected in the weak current, which featured two lepton isospin doublets and only one quark doublet. The GIM mechanism restored the quark-lepton symmetry, by proposing the existence of a fourth quark enabling partial cancellation of FCNC amplitudes. This fourth quark was called the charm quark. Four years later, the $J/\Psi$, a meson containing a charm quark and an anti-charm quark, was discovered [24, 25]. The $J/\Psi$ is the first excited state of charmonium, with an invariant mass of about 3097 MeV.
Therefore, we end up with the two quark families:

$$\begin{pmatrix} u \\ d' \end{pmatrix} = \begin{pmatrix} u \\ d\, cos\theta_c + s\, sin\theta_c \end{pmatrix} \tag{1.5}$$

$$\begin{pmatrix} c \\ s' \end{pmatrix} = \begin{pmatrix} c \\ s\, cos\theta_c - d\, sin\theta_c \end{pmatrix} \tag{1.6}$$

The two weak eigenstates can be written in terms of the mass eigenstates:

$$\begin{pmatrix} d' \\ s' \end{pmatrix} = V \begin{pmatrix} d \\ s \end{pmatrix} \tag{1.7}$$

where V is the Cabibbo matrix:

$$V = \begin{pmatrix} cos\theta_c & sin\theta_c \\ -sin\theta_c & cos\theta_c \end{pmatrix} \tag{1.8}$$

Now, having two quark families, we can show a graphical representation of the Cabibbo angle, as shown in Fig. 1.2, where $A$ is the transition amplitude and $A^2$ is the transition probability.

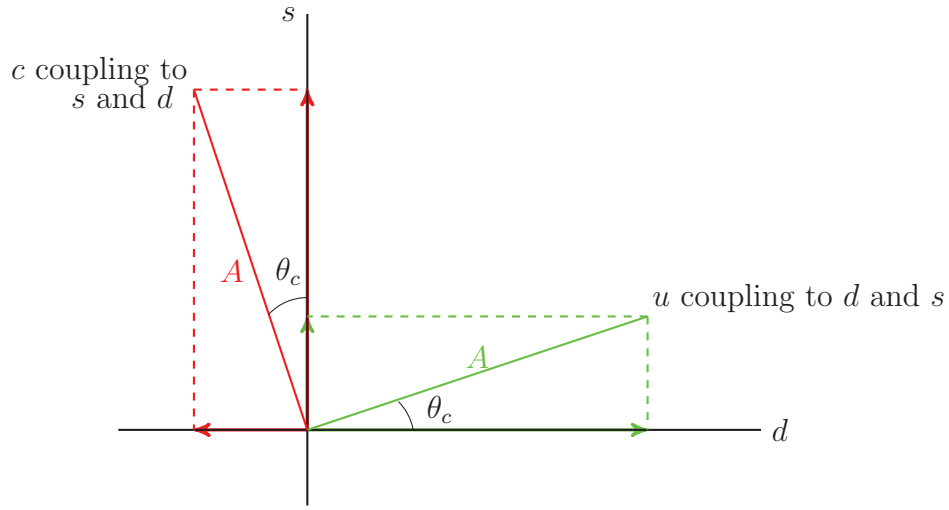


**Figure 1.2:** The Cabibbo angle and amplitudes of transitions between quarks of two families [26].

The suppression of $\Delta S = 1$ transitions are therefore explained by the small value of $\theta_c$, those events being proportional to $sin^2\theta_c$, while the transitions with $\Delta S$ =0 are favored, being proportional to $cos^2\theta_c$, i.e. close to 1.
We introduce three terms used later in this thesis: Cabibbo Favored (CF), Cabibbo Suppressed (CS) and Doubly Cabibbo Suppressed (DCS):

- Cabibbo favored: decay rates involving transitions as $c \to s$ or $u \to d$, proportional to $cos^2\theta_c$.

- Cabibbo suppressed: decay rates involving $s \to u$ or $c \to d$, proportional to $sin^2\theta_c$.

- doubly Cabibbo suppressed: decay rates involving both $c \to d$ and $s \to u$, proportional to $sin^4\theta_c$.

With a model of four quarks and four leptons, grouped into two families of isospin doublets, the CP asymmetry cannot be explained yet. By diagonalizing the quark mass matrices, which are in general complex, we end up with real matrices for the case of four quarks, which cannot account for CP violation in weak interactions.
S.L. Glashow, J. Iliopoulos and L. Maiani did not go further in predicting another quark family, because they were already worried about the implications of predicting the charm quark [27]. M. Kobayashi and T. Maskawa are the ones who proposed in 1973 a third doublet of quarks in order to explain the CP violation through the weak interaction [3], as detailed in the next section.

### 1.2.3 The CKM matrix

The electroweak standard model is based on the $SU(2)_L \times U(1)_Y$ gauge group. The gauge bosons corresponding to $SU(2)_L$ and $U(1)_Y$ are respectively $W^i_\mu$ and $B_\mu$ ($i =$ 1,2,3) and the coupling constants are $g$ and $g'$. Experimental evidence shows that only left-handed fermions (or right-handed anti-fermions) are present in the charged weak currents. Left-handed components of the $i$th family are arranged into $SU(2)_L$ doublets:

$$\begin{pmatrix} \nu_i \\ l_i \end{pmatrix}_L, \begin{pmatrix} u_i \\ d'_i \end{pmatrix}_L \tag{1.9}$$

And right-handed components are singlets:

$$(u_i)_R, \quad (d'_i)_R, \quad (l_i)_R \tag{1.10}$$

To describe masses of fermions and gauge bosons without breaking the $SU(2)_L \times U(1)_Y$ gauge symmetry, scalar Higgs fields are introduced. In the Minimal Standard Model, only one complex weak isospin doublet of Higgs fields is introduced:

$$\phi = \begin{pmatrix} \phi^+ \\ \phi^0 \end{pmatrix} \tag{1.11}$$

where the superscript denotes the electric charge of the two complex components. When the Higgs field acquires a non-zero vacuum expectation value, the symmetry of the Lagrangian is spontaneously broken. Three of the gauge bosons receive masses

($W^{\pm}$ and Z), while the photon remains massless. The physics (or massive) charged and neutral weak boson fields are linear combinations of $W^i_\mu$ and $B_\mu$:

$$\begin{aligned} W^{\pm} &= \frac{W^1_\mu \pm iW^2_\mu}{\sqrt{2}} \\ Z_\mu &= W^3_\mu cos\theta_W - B_\mu sin\theta_W \end{aligned} \tag{1.12}$$

While the electromagnetic massless boson field can be written as:

$$A_\mu = W^3_\mu sin\theta_W + B_\mu cos\theta_W \tag{1.13}$$

where $\theta_W$ is the weak mixing angle. Because the vacuum state of the Higgs field is electrically neutral, the $U(1)$ symmetry is left unbroken and the photon, described by the $A_\mu$ field, remains massless.
Fermion masses are generated through Yukawa couplings between the Higgs doublet and the fermion fields. The Lagrangian describing the coupling of $W^{\pm}$ bosons to quarks, written in the weak eigenstate basis is:

$$\mathcal{L}_{CC} = \frac{g}{\sqrt{2}} \left[ \bar{u}_i \gamma^\mu \frac{1-\gamma^5}{2} d_i \right] W^+_\mu + h.c. \tag{1.14}$$

where $(1-\gamma^5)/2$ is the projector operator on the left chirality. The Lagrangian written in the mass eigenstate basis is:

$$\mathcal{L}_{CC} = \frac{g}{\sqrt{2}} \left[ \bar{u}_i \gamma^\mu \frac{1-\gamma^5}{2} V_{CKM} d_i \right] W^+_\mu + h.c. \tag{1.15}$$

where $V_{CKM}$ is the Cabibbo-Kobayashi-Maskawa CKM matrix. This matrix is an extension of the Cabibbo matrix, to the case of three $SU(2)$ isospin doublets of quarks. It connects the weak eigenstates $(d', s', b')$ and the corresponding mass eigenstates $(d, s, b)$:

$$\begin{pmatrix} d' \\ s' \\ b' \end{pmatrix} = \begin{pmatrix} V_{ud} & V_{us} & V_{ub} \\ V_{cd} & V_{cs} & V_{cb} \\ V_{td} & V_{ts} & V_{tb} \end{pmatrix} \begin{pmatrix} d \\ s \\ b \end{pmatrix} = V_{CKM} \begin{pmatrix} d \\ s \\ b \end{pmatrix} \tag{1.16}$$

The CKM matrix is a complex matrix of $3 \times 3$ elements, for 3 quarks doublets. The diagonal elements correspond to transitions within a same family, and the probability of transition from a quark $q$ to a quark $q'$ is proportional to $|V_{qq'}|^2$. There are

9 complex elements of the type $|V_{ij}|exp(-i\,\theta_{ij})$, therefore 18 values are needed to describe the matrix. Unitarity introduces 9 relations between the elements. Furthermore, out of 6 relative phases between the quarks, 5 can be redefined without changing the Lagrangian. With these constraints, only 4 parameters of the CKM matrix remain independent: 3 real rotation angles $\theta_i$ and one phase $\delta$, responsible for the violation of the CP symmetry. These 4 values are not predicted by the SM.

### 1.2.4 Parametrizations of the CKM matrix

There are many possible parametrizations of the CKM matrix, but the most popular ones are the Kobayashi-Maskawa (KM), the Chau-Keung-Maiani (CKM, a.k.a. standard) and the Wolfenstein parametrizations. The physics is independent of a particular parametrization of the CKM matrix. Their theoretical motivations are different and one of them may turn out to be more convenient for some specific problem.

#### 1.2.4.1 The KM parametrization

Using three mixing angles $\theta_i$ and a CP violating phase $\delta$, we can write:

$$V_{CKM} = R_1(\theta_2)R_3(\theta_1)C(0,0,\delta)R_1(\theta_3) \tag{1.17}$$

where $R_i$ is the rotation matrix around the $i$ axis:

$$R_1(\theta_i) = \begin{pmatrix} 1 & 0 & 0 \\ 0 & c_i & s_i \\ 0 & -s_i & c_i \end{pmatrix}, \quad R_3(\theta_i) = \begin{pmatrix} c_i & s_i & 0 \\ -s_i & c_i & 0 \\ 0 & 0 & 1 \end{pmatrix} \tag{1.18}$$

with $c_i = cos\theta_i$, $s_i = sin\theta_i$ and

$$C(0,0,\delta) = \begin{pmatrix} 1 & 0 & 0 \\ 0 & 1 & 0 \\ 0 & 0 & e^{i\delta} \end{pmatrix} \tag{1.19}$$

With this, the $V_{CKM}$ matrix can be explicitly written:

$$V_{CKM} = \begin{pmatrix} c_1 & s_1c_3 & s_1s_3 \\ -s_1c_2 & c_1c_2c_3 - s_2s_3e^{i\delta} & c_1c_2s_3 + s_2c_3e^{i\delta} \\ s_1s_2 & -c_1s_2c_3 - c_2s_3e^{i\delta} & -c_1s_2s_3 + c_2c_3e^{i\delta} \end{pmatrix} \tag{1.20}$$

The values of the three mixing angles can only be determined from experiments. The phase $\delta$, which is responsible for CP violation, cannot be removed by the redefinition of quark fields. This phase disappears only if one of the angles is zero, which leads to a rotation matrix equal to the identity matrix. Therefore, we can end with a matrix of the form [28]:

$$V_{CKM} = \begin{pmatrix} 1 & 0 & 0 \\ 0 & a & b \\ 0 & c & d \end{pmatrix} \tag{1.21}$$

Where the $2 \times 2$ submatrix can be made real by a suitable re-phasing, just as in the case of two quark families.

#### 1.2.4.2 The standard parametrization

The Chau-Keung-Maiani parametrization has been advocated by the Particle Data Group (PDG) to be the standard parametrization. For this parametrization, three angles $\theta_{ij}(\ i,j \in [1,3], i \neq j)$ and one CP violating phase $\delta_{13}$ are also used. The indices $i,j$ = 1,2,3 stand for the quark families. With $c_{ij} = cos\theta_{ij}$ and $s_{ij} = sin\theta_{ij}$ (i,j = 1,2,3), the standard parametrization is [29]:

$$V_{CKM} = \begin{pmatrix} c_{12}c_{13} & s_{12}c_{13} & s_{13}e^{-i\delta_{13}} \\ -s_{12}c_{23} - c_{12}s_{23}s_{13}e^{i\delta_{13}} & c_{12}c_{23} - s_{12}s_{23}s_{13}e^{i\delta_{13}} & s_{23}c_{13} \\ s_{12}s_{23} - c_{12}c_{23}s_{13}e^{1\delta_{13}} & -s_{23}c_{12} - s_{12}c_{23}s_{13}e^{i\delta_{13}} & c_{23}c_{13} \end{pmatrix}$$

The angles $\theta_{12}, \theta_{13}$ and $\theta_{23}$ can be chosen to lie in the first quadrant, so $s_{ij}, c_{ij} \geq 0$. It was experimentally observed that $s_{12} \gg s_{23} \gg s_{13}$. From phenomenological studies, we know that $s_{12} \approx \mathcal{O}(10^{-3})$, $s_{23} \approx \mathcal{O}(10^{-2})$ [30]. The four independent parameters can be selected as following:

$$s_{12} = |V_{us}| \quad s_{13} = |V_{ub}| \quad s_{23} = |V_{cb}| \quad \text{and } \delta. \tag{1.22}$$

#### 1.2.4.3 The Wolfenstein parametrization

The current average values of the modules of the CKM elements are obtained from a global fit considering the latest experimental and theoretical constraints in the quark flavour sector [31]:

$$V_{CKM} = \begin{pmatrix} 0.97427 \pm 0.00014 & 0.22536 \pm 0.00061 & 0.00355 \pm 0.00015 \\ 0.22522 \pm 0.00061 & 0.97343 \pm 0.00015 & 0.0414 \pm 0.0012 \\ 0.00886^{+0.00033}_{-0.00032} & 0.0405^{+0.0011}_{-0.0012} & 0.99914 \pm 0.00005 \end{pmatrix} \quad (1.23)$$

We can notice a hierarchical pattern in the values of the CKM elements, with:

$$\begin{aligned} V_{ud} \approx V_{cs} \approx V_{tb} \approx 1 \\ V_{us} \approx V_{cd} \approx 0.22 \\ V_{cb} \approx V_{ts} \approx 0.04 \end{aligned} \quad (1.24)$$

Expressing $V_{us} = \lambda = sin(\theta_C)$, then $V_{cb} = A\lambda^2$ and $V_{ub}$, $V_{td}$ can be written in terms of $A\lambda^3$. The Wolfenstein parametrization up to order $\lambda^3$ was introduced as [32]:

$$V_{CKM} = \begin{pmatrix} 1 - \frac{1}{2}\lambda^2 & \lambda & \lambda^3 A(\rho - i\eta) \\ -\lambda & 1 - \frac{1}{2}\lambda^2 & \lambda^2 A \\ \lambda^3 A(1 - \rho - i\eta) & 1 - \frac{1}{2}\lambda^2 & 1 \end{pmatrix} + \mathcal{O}(\lambda^4) \quad (1.25)$$

Here, the CP violation source is carried by the most off-diagonal elements $V_{ub}$ and $V_{td}$. It is an approximate parametrization of the CKM matrix in which each element is expanded as a power series of the parameter $\lambda \approx 0.22$. In this parametrization, the four parameters from 1.22 needed to describe the CKM matrix are replaced by:

$$\lambda,\ A,\ \rho,\ \text{and}\ \eta \quad (1.26)$$

It was pointed out in [33] that in any perturbative expansion, the higher orders for $\lambda$ are not unique. This non-uniqueness of the expansion will lead to different possible numerical values of the parameters in Eq. 1.26. But the physics is independent on the parametrization, and this can be seen when all the terms are summed up.

In the B factories era, a level of accuracy of the order $\mathcal{O}(\lambda^3)$ was enough to observe CP asymmetry effects, and corresponded to the level of experimental precision. With the precision reached with LHCb and expected with Belle II, a higher order of the expansion of the CKM matrix becomes necessary. The terms of the order $\mathcal{O}(\lambda^4)$ or $\mathcal{O}(\lambda^5)$ have to be included now in the expansion. There are several ways of doing

this in the literature, depending on the definition of the four parameters. As the physics does not rely on a particular definition of these parameters, we will adopt the most frequent definition [32, 34, 35] to link the parameters of the Wolfenstein parametrization to the ones of the standard parametrization:

$$s_{12} = \lambda = \frac{|V_{us}|}{\sqrt{|V_{ud}|^2 + |V_{us}|^2}}, \quad s_{23} = A\lambda^2 = \lambda \left|\frac{V_{cb}}{V_{us}}\right|$$
$$s_{13}e^{i\delta} = V_{ub}^* = A\lambda^3(\rho + i\eta) = \frac{A\lambda^3(\bar{\rho} + i\bar{\eta})\sqrt{1 - A^2\lambda^4}}{\sqrt{1-\lambda^2}[1 - A^2\lambda^4(\bar{\rho} + i\bar{\eta})]} \tag{1.27}$$

Where we introduced the parameters:

$$\bar{\rho} = \rho\left[1 - \lambda^2/2 + \cdots\right], \quad \bar{\eta} = \eta\left[1 - \lambda^2/2 + \cdots\right] \tag{1.28}$$

It follows that:

$$\rho = \frac{s_{13}}{s_{12}s_{23}} cos\delta, \quad \eta = \frac{s_{13}}{s_{12}s_{23}} sin\delta \tag{1.29}$$

The relations from Eq.1.27 ensure exact unitarity of the CKM matrix as expressed in terms of $\lambda, A, \rho, \eta$. The CKM matrix written up to $\lambda^5$ expansion is [36]:

$$V_{CKM} = \begin{pmatrix} 1 - \frac{1}{2}\lambda^2 - \frac{1}{8}\lambda^4 & \lambda & \lambda^3 A(\rho - i\eta) \\ -\lambda + \frac{1}{2}\lambda^5 A^2[1 - 2(\rho + i\eta)] & 1 - \frac{1}{2}\lambda^2 - \frac{1}{8}\lambda^4(1 + 4A^2) & \lambda^2 A \\ \lambda^3 A[1 - (1 - \frac{1}{2}\lambda^2)(\rho + i\eta)] & -\lambda^2 A + \lambda^4 A[1 - 2(\rho + i\eta)] & 1 - \frac{1}{2}\lambda^4 A^2 \end{pmatrix} + \mathcal{O}(\lambda^6) \tag{1.30}$$

CP is not necessarily violated with 3 quark families in the SM. In fact, there are 14 conditions to be satisfied in order to have CP violation. 6 conditions arise from the requirement that if two up-type quarks or two down-type quarks have the same mass, there is no CP violation:

$$\begin{array}{lll} m_u \neq m_c & m_c \neq m_t & m_u \neq m_t \\ m_d \neq m_s & m_s \neq m_b & m_d \neq m_b \end{array} \tag{1.31}$$

And 8 additional conditions are related to the angles and the phase. We can write for the KM parametrization (but another parametrization will imply a similar set of conditions) [37]:

$$\theta_j \neq 0, \frac{\pi}{2} \quad \delta \neq 0, \pi \quad j = 1, 2, 3 \tag{1.32}$$

All these conditions can be merged into one only, independent on the CKM matrix parametrization, using the Jarlskog invariant J [38]:

$$det[M^u, M^d] = -2iF_u F_d J \tag{1.33}$$

Eq. 1.33 characterizes the determinant of the commutator of the up-type and down-type unitary mass matrices $M^u$ and $M^d$, with:

$$F_{u(d)} = \frac{(m_{t(b)} - m_{c(s)})(m_{t(b)} - m_{u(d)})(m_{c(s)} - m_{u(d)})}{m^3_{t(b)}} \tag{1.34}$$

J represents a measure of the CP violation (CPV occurs only if $J \neq 0$), and can be written as:

$$Im[V_{ij} V_{kl} V^*_{il} V^*_{kj}] = J \sum_{m,n=1}^{3} \epsilon_{ikm} \epsilon_{jln} \tag{1.35}$$

Where $V$ are the CKM matrix elements and $\epsilon$ is the antisymmetric tensor. The Jarlskog parameter can be expressed in the standard parametrization as:

$$J = c_{12}\ c_{23}\ c^2_{13}\ s_{12}\ s_{23}\ s_{13}\ sin\delta \tag{1.36}$$

or in the Wolfenstein parametrization as [39]:

$$J \approx A^2 \lambda^6 \eta (1 - \lambda^2/2) \tag{1.37}$$

### 1.2.5 The unitarity triangles

The CKM matrix permits to switch from the mass eigenstates basis to the flavour eigenstates basis. Unitarity of the CKM matrix leads to 9 constraints on its matrix

elements. The 3 diagonal relations are:

$$\begin{aligned} V_{ud}^2 \quad &+V_{us}^2 + V_{ub}^2 = 1 \\ V_{cd}^2 \quad &+V_{cs}^2 + V_{cb}^2 = 1 \\ V_{td}^2 \quad &+V_{ts}^2 + V_{tb}^2 = 1 \end{aligned} \tag{1.38}$$

And the off-diagonal relations are the 6 ones shown in Table 1.1. For each term of each relation, the magnitude is presented in terms of $\lambda$. Each off-diagonal relation can be symbolized in a complex plane by a so-called unitarity triangle. The sides of these triangles are given in terms of the moduli of the elements of the mixing matrix.

| Unitarity triangle | Relation |
|---|---|
| b-s | $V_{us}V_{ub}^* + V_{cs}V_{cb}^* + V_{ts}V_{tb}^* = 0$<br>$\lambda^4 \quad \lambda^2 \quad \lambda^2$ |
| b-d | $V_{ud}V_{ub}^* + V_{cd}V_{cb}^* + V_{td}V_{tb}^* = 0$<br>$\lambda^3 \quad \lambda^3 \quad \lambda^3$ |
| s-d | $V_{ud}V_{us}^* + V_{cd}V_{cs}^* + V_{td}V_{ts}^* = 0$<br>$\lambda \quad \lambda \quad \lambda^5$ |
| t-c | $V_{td}V_{cd}^* + V_{ts}V_{cs}^* + V_{tb}V_{cb}^* = 0$<br>$\lambda^4 \quad \lambda^2 \quad \lambda^2$ |
| t-u | $V_{td}V_{ud}^* + V_{ts}V_{us}^* + V_{tb}V_{ub}^* = 0$<br>$\lambda^3 \quad \lambda^3 \quad \lambda^3$ |
| c-u | $V_{ud}V_{cd}^* + V_{us}V_{cs}^* + V_{ub}V_{cb}^* = 0$<br>$\lambda \quad \lambda \quad \lambda^5$ |

**Table 1.1:** The six unitarity triangles, their corresponding off-diagonal unitarity relations and magnitudes of the sides of the triangles in terms of $\lambda$.

All the six unitarity triangles feature the same area, even though their appearance is very different. The area of each triangle equals to half of the Jarlskog invariant, related to CP violation in a phase convention independent way.
Out of these six unitarity relations, two represent triangles where the lengths are of the order of $\lambda^3$ (see Table 1.1: the $b-d$ and the $t-u$ triangles). These triangles are more accessible for measurements of their sides and angles. The one represented by the $b-d$ relation contains the relevant matrix elements for the $B^0 - \bar{B}^0$ mixing. If

we divide this relation by the experimentally best known sides, $V_{cd}V_{cb}^*$, then we end up with the so-called Unitarity Triangle, displayed in Fig. 1.3.

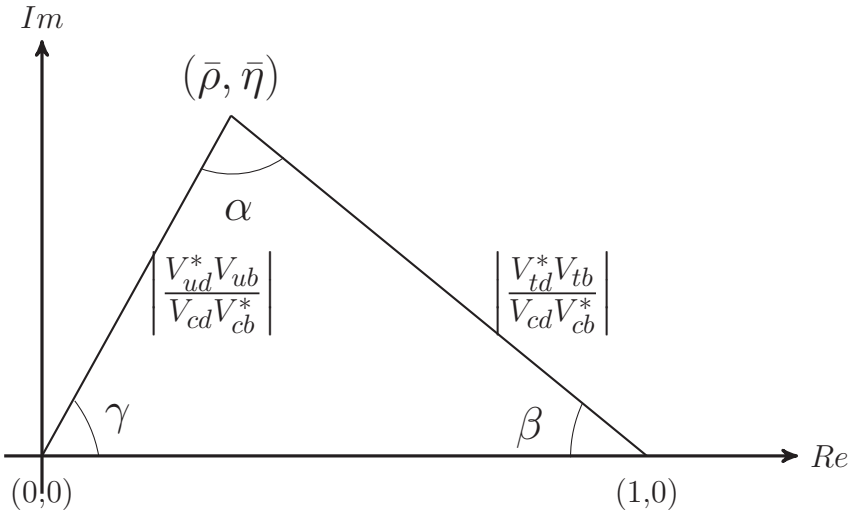


**Figure 1.3:** The Unitarity Triangle representation in the complex plane.

The three angles of this triangle are called $\alpha, \beta$ and $\gamma$ as displayed in Fig. 1.3, but another notation can also be found, especially in Asia: $\phi_1 = \beta$, $\phi_2 = \alpha$ and $\phi_3 = \gamma$. The two triangles defined by the first and the fourth off-diagonal relation of Table 1.1 have a squashed appearance with the lengths of two sides of the triangle of $\lambda^2$ order, and the third one of $\lambda^4$ order. The remaining two triangles, the $s - d$ and the $c - u$ triangles, are even more squashed, with lengths of two sides of order $\lambda$, and the third one of order $\lambda^5$. These four triangles are more difficult to measure experimentally. But, in the SM framework, measuring only one triangle gives access to the four parameters needed to describe the CKM matrix, and further to predict all the other triangles.

### 1.2.6 The $c - u$ unitarity triangle

In this thesis, we are particularly interested in the $c - u$ unitarity triangle, which contains the CKM matrix elements involved in charm transitions. This triangle has not been studied yet because of its shape, having a flat appearance, with a very small side and a very small $\beta$ angle, and two long sides, as illustrated in Fig. 1.4.
We can also represent the $c - u$ triangle in the $(\bar{\rho} - \bar{\eta})$ plane, as we did with the Unitarity Triangle, dividing the terms of the last relation of Table 1.1 by $V_{us}^*V_{cs}$. We obtain the normalized charm unitarity triangle, which is represented in Fig.1.5. This rescaled unitarity triangle is completely determined by the location of its apex

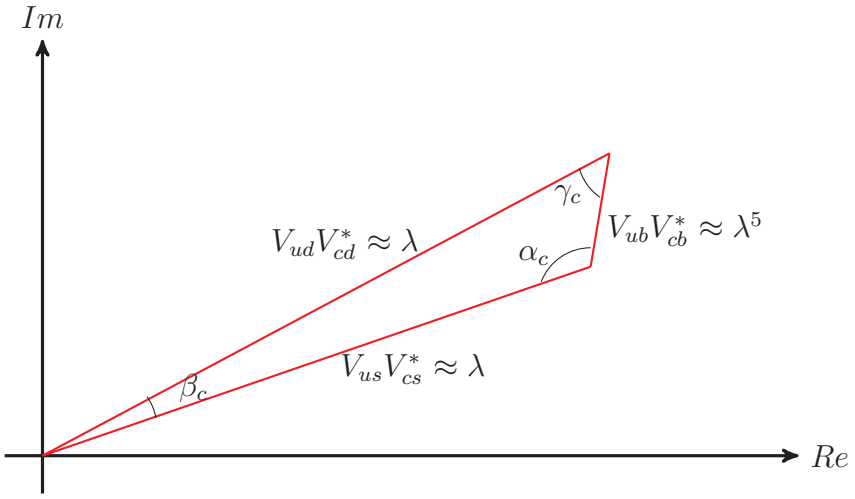


**Figure 1.4:** The $c-u$ unitarity triangle (not to scale).

$(\bar{\rho}, \bar{\eta})$. The triangle can be rotated in the $(\bar{\rho} - \bar{\eta})$ plane because the physics and the triangle remain invariant under a phase transformation. But the angles and the sides of the triangle will still be the same because they are independent on the phase convention. They represent physical observables that can be measured in dedicated experiments.

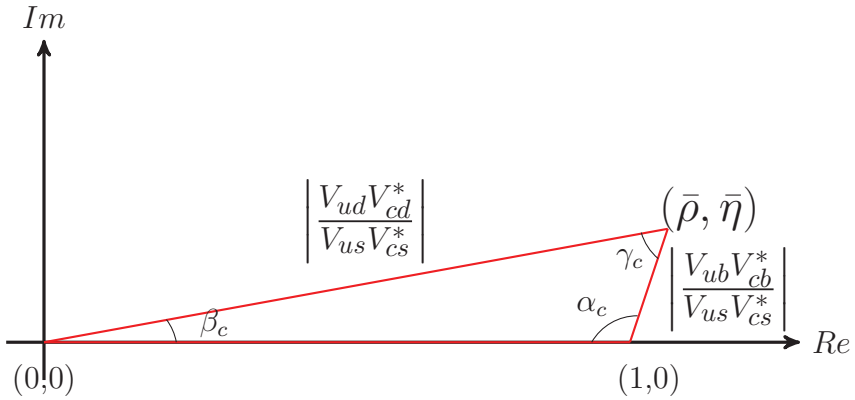


**Figure 1.5:** The normalized $c-u$ unitarity triangle. Triangle not to scale.

The angles of the $c-u$ unitarity triangle are:

$$\alpha_c = arg\left[\frac{-V_{ub}^* V_{cb}}{V_{us}^* V_{cs}}\right]$$

$$\beta_c = arg\left[\frac{-V_{ud}^* V_{cd}}{V_{us}^* V_{cs}}\right] \tag{1.39}$$

$$\gamma_c = arg\left[\frac{-V_{ub}^* V_{cb}}{V_{ud}^* V_{cd}}\right]$$

In the SM, assuming that there is only one unique complex phase, the $c-u$ unitarity triangle can be related to the Unitarity Triangle in a simple way. It was pointed out in [40] that $\gamma_c \approx \gamma$, and $\alpha_c = 180° - \gamma_c + \mathcal{O}(\lambda^4)$. Existing constraints on the Wolfenstein parameters can contribute to give predictions of the $c-u$ triangle parameters. The average values of CKMFitter [41] and UTFit [42] values for $A$, $\lambda$, $\bar{\rho}$ and $\bar{\eta}$ combined with an expansion up to $\lambda^5$ of the CKM matrix are used in [43] to predict the angles of the $c-u$ triangle to be:

$$\begin{aligned} \alpha_c &= (111.5 \pm 4.2)°, \\ \beta_c &= (0.0350 \pm 0.0001)°, \\ \gamma_c &= (68.4 \pm 0.1)° \end{aligned} \tag{1.40}$$

In this thesis, we are interested in measuring $\beta_c$, the smallest angle of the charm unitarity triangle. Any significant deviation from its expected value (for more details, see Chapter 3) could be a manifestation of new physics (NP), e.g. a fourth family of quarks or an additional phase violating the CP symmetry.

## 1.3 $D^0$ mixing and oscillations

Neutral meson mixing was observed for the first time in the $K^0$ systems in 1956 [44], after being theoretically predicted two years before [45]. Indeed, because $K^0$ and $\bar{K^0}$ can decay to the same final state $\pi^+\pi^-$, therefore $K^0 \leftrightarrows \pi^+\pi^- \leftrightarrows \bar{K^0}$ should be possible. It was later understood that this oscillation is due to the charged weak interaction, oscillations being described by a box Feynman diagram.
Mixing was also observed in $B^0$ systems in 1987 by UA1 [46] and since then in many other experiments. After this, it was also revealed in $B_s^0$ [47] and $B_d^0$ systems [48],

with better sensitivity in time-dependent analyses aiming at direct measurements of the oscillation frequencies $\Delta m_d$ and $\Delta m_s$.
Finally, mixing in $D^0$ systems was measured in 2007 by Belle, BaBar and CDF[49–51]. The combined measurement excludes the non mixing hypothesis with more than 11 standard deviations [52].

### 1.3.1 Formalism

In this section we derive the probability for a $D^0$ meson to oscillate to its anti-particule, using the quantum mechanics formalism. The neutral D mesons are produced as flavour eigenstates, but they evolve as physics eigenstates which are a superposition of $D^0$ and $\bar{D}^0$. There are furthermore contributions from long distance processes which correspond to all possible hadronic decays $f_1$, $f_2$, etc.:

$$|\Psi(t)\rangle = a(t)\,|D^0\rangle + b(t)\,|\bar{D^0}\rangle + \sum_i c_i(t)\,|f_i\rangle \tag{1.41}$$

The time scales of the weak interaction (that causes particle-antiparticle oscillations) is much larger than the one of strong and electromagnetic interactions. Therefore, we can treat the time evolution in a simplified formalism (with the effective Hamiltonian that does not explicitly contain the couplings to the final states $f_i$), where the time evolution of $|\Psi(t\rangle)$ is described by the Schrödinger equation:

$$i\frac{d}{dt}\,|\Psi(t)\rangle = \left(M - \frac{i\Gamma}{2}\right)|\Psi(t)\rangle \tag{1.42}$$

where $H = M - \frac{i\Gamma}{2}$ is the effective $2\times 2$ Hamiltonian matrix. To define the evolution with time of an unstable particle, the Hamiltonian does not have to be hermitian, however $M$ and $\Gamma$ are both hermitian.
The matrix $M$ is the dispersive part and describes the mass components of the Hamiltonian, and the matrix $\Gamma$ symbolizes the decay rate component and corresponds to the absorptive part of the Hamiltonian:

$$M = \begin{pmatrix} M_{11} & M_{12} \\ M_{12} & M_{22} \end{pmatrix} \qquad \Gamma = \begin{pmatrix} \Gamma_{11} & \Gamma_{12} \\ \Gamma_{12} & \Gamma_{22} \end{pmatrix} \tag{1.43}$$

CPT conservation implies $M_{11} = M_{22} = M$ and $\Gamma_{11} = \Gamma_{22} = \Gamma$.
The matrix element $M_{12}$ corresponds to virtual $D^0/\bar{D}^0$ transitions and the matrix element $\Gamma_{12}$ describes real transitions due to decays to a common final state, accessible to both $D^0$ and $\bar{D}^0$.

The neutral D meson mass eigenstates $D_1$ and $D_2$ are expressed as a linear combination of the flavour (and weak interaction) eigenstates:

$$\begin{aligned} |D_1\rangle &= p\,|D^0\rangle + q\,|\bar{D^0}\rangle \\ |D_2\rangle &= p\,|D^0\rangle - q\,|\bar{D^0}\rangle \end{aligned} \tag{1.44}$$

where the complex coefficients $p$ and $q$ satisfy the normalization condition $|p|^2 + |q|^2$=1. We can write:

$$\frac{q}{p} = \sqrt{\frac{M_{12}^* - \frac{i}{2}\Gamma_{12}^*}{M_{12} - \frac{i}{2}\Gamma_{12}}} \tag{1.45}$$

The Hermitic operators are introduced in the Schrödinger equation:

$$|D_{1,2}(t)\rangle = e^{-i(\lambda_{1,2})t}\,|D_{1,2}(0)\rangle \tag{1.46}$$

with:

$$\lambda_{1,2} = M_{1,2} - i\frac{\Gamma_{1,2}}{2} \tag{1.47}$$

Expressing the flavour eigenstates in terms of mass eigenstates from Eq.1.44, we can derive the proper time evolution of a state which is initially a pure $D^0$ or a pure $\overline{D}^0$:

$$\begin{aligned} D^0(t) &= \tfrac{1}{2}(g_+\,|D^0\rangle + \tfrac{q}{p} g_-\,|\overline{D}^0\rangle) \\ \bar{D^0}(t) &= \tfrac{1}{2}(g_+\,|D^0\rangle + \tfrac{p}{q} g_-\,|\overline{D}^0\rangle) \end{aligned} \tag{1.48}$$

with:

$$g_\pm = e^{-i\lambda_1 t} \pm e^{-i\lambda_2 t} \tag{1.49}$$

We introduce the mass and width differences, which are:

$$\begin{aligned} \Delta M &= M_1 - M_2 \\ \Delta\Gamma &= \Gamma_1 - \Gamma_2 \end{aligned} \tag{1.50}$$

where $M_{1,2}$ and $\Gamma_{1,2}$ are the masses and decay widths of the $D^0$ mass eigenstates.

Their dimensionless equivalents are often used:

$$\begin{aligned} x &\equiv \frac{\Delta M}{\Gamma}, \\ y &\equiv \frac{\Delta\Gamma}{2\Gamma} \end{aligned} \tag{1.51}$$

where $\Gamma = (\Gamma_1 + \Gamma_2)/2$ is the mean decay width.

Finally, the probabilities of obtaining a $D^0$ ($\bar{D^0}$) state at proper time t, starting from an initially pure $D^0$ ($\bar{D^0}$) state are:

$$\begin{aligned} |\langle D^0|D^0\rangle|^2 &= |\langle \bar{D^0}|\bar{D^0}\rangle|^2 = \tfrac{1}{2}e^{-\Gamma t}\,[cosh(y\Gamma t) + cos(x\Gamma t)] \\ |\langle D^0|\bar{D^0}\rangle|^2 &= \tfrac{1}{2}|\tfrac{p}{q}|^2 e^{-\Gamma t}\,[cosh(y\Gamma t) - cos(x\Gamma t)] \\ |\langle \bar{D^0}|D^0\rangle|^2 &= \tfrac{1}{2}|\tfrac{q}{p}|^2 e^{-\Gamma t}\,[cosh(y\Gamma t) - cos(x\Gamma t)] \end{aligned} \tag{1.52}$$

This formalism is also correct to describe $K^0$, $B^0$ and $B_s^0$ oscillations. But the induced phenomenology is specific to each neutral meson oscillating system, because of different lifetimes and CKM matrix element module values involved. For instance, in the $B^0$ system, it may be convenient to neglect $\Delta\Gamma$.

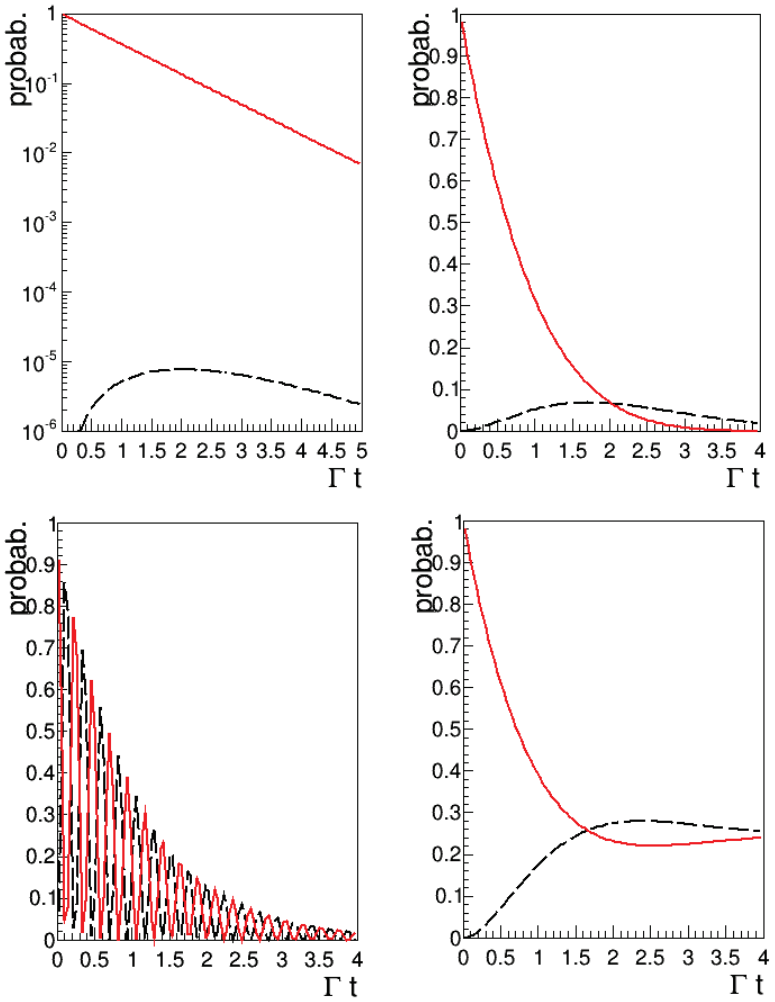


**Figure 1.6:** The unmixed (equivalent to the pure decay rate, represented by a continuous line) and the mixed (dashed line) amplitude as a function of $\Gamma t$ in case of an initially pure $D^0$, $B^0$, $B_s^0$ and $K^0$ state. For each neutral meson it was considered that $q/p = 1$ (i.e. indirect CP violation effects are neglected). The scale used for the $D^0$ system is logarithmic.

Using the equations from 1.52, we can characterize the no-mixing and the mixing probabilities as a function of the proper decay time for an initially pure meson sample, for respectively the $D^0$, $B^0$, $B_s^0$ and $K^0$ systems, as shown in Fig. 1.6. We observe that the $D^0$ system features the lowest probability of mixing. In contrary, the $B_s^0$ system presents a high oscillation frequency. Experimentally, this translates to different challenges for these two systems. In the $B_s^0$ system, the proper time resolution is crucial, while in the $D^0$ system, the statistics play an important role because many mesons decay before having oscillated.

### 1.3.2 Current knowledge of mixing parameter values

It was estimated in [53–57] that $D^0 - \bar{D}^0$ mixing in the SM should be of the order of 1% or less. The current world average values of the $x, y$ mixing parameters, taken from the Heavy Flavour Average Group (HFAG) [52] are:

$$\begin{aligned} \mathrm{x}(\%) &= 0.49^{+0.14}_{-0.15} \\ \mathrm{y}\ (\%) &= 0.62 \pm 0.08 \end{aligned} \tag{1.53}$$

Allowing CP violation, the values become:

$$\begin{aligned} \mathrm{x}\ (\%) &= 0.41^{+0.14}_{-0.15} \\ \mathrm{y}\ (\%) &= 0.63^{+0.07}_{-0.08} \\ \left|\frac{q}{p}\right| &= 0.93^{+0.09}_{-0.08} \end{aligned} \tag{1.54}$$

The two dimensional probability contours, which include both statistical and systematical uncertainties and allow for CP violation are shown in Fig.1.7 $(x, y)$ and Fig. 1.8 $(|\frac{q}{p}|)$.

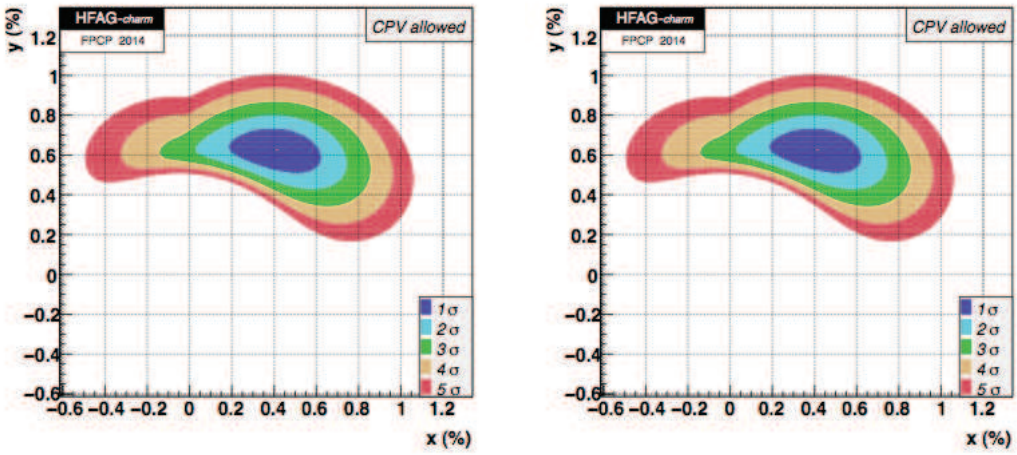


**Figure 1.7:** One to five $\sigma$ contours of allowed regions for x and y, taken from [52].

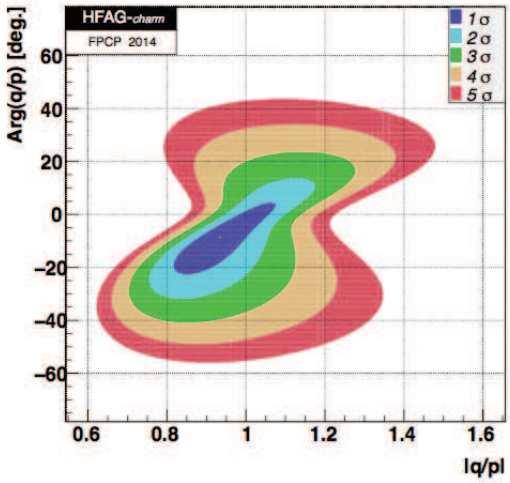


**Figure 1.8:** One to five $\sigma$ contours of the allowed region for $q/p$, taken from [52].

### 1.3.3 Phenomenology of $D^0$ -$\overline{D}^0$ oscillations

$D^0$ oscillations, i.e. mixing as a function of time, can occur in the SM through two possible ways: through short distance contributions, involving a double weak boson exchange, or through long distance contributions, implying hadronic intermediate states that are both accessible to $D^0$ and $\overline{D}^0$.

The short distance contributions are expected to be very small, because of the CKM matrix elements involved and because of the GIM suppression. Their box diagrams are displayed in Fig. 1.9. We observe that only down-type quarks are present in the box diagram. This leads to an unique way to test models beyond the SM, with possible new particles in the box coupling to up-type quarks.

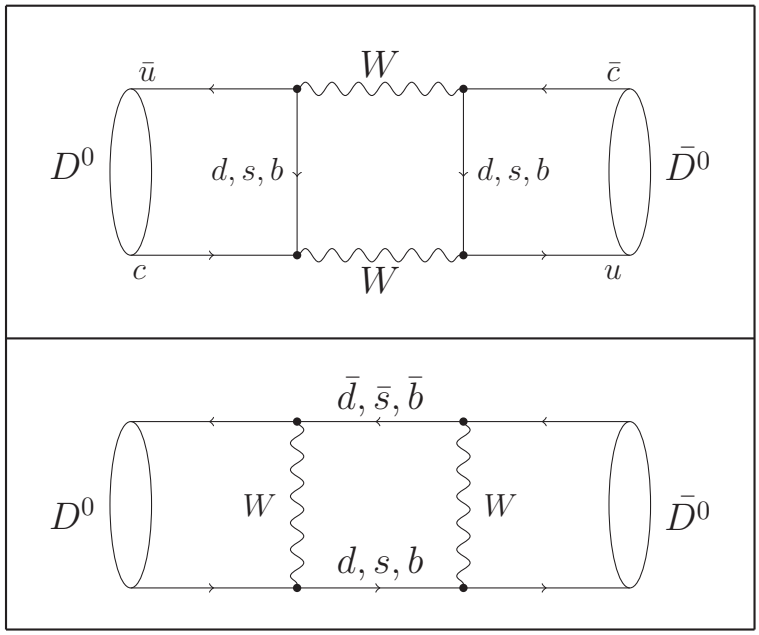


**Figure 1.9:** Box diagrams contributing to $D^0$ oscillations.

In addition to these box diagrams, it was shown in [58] that the di-penguin box diagram represented in Fig. 1.10 contributes to the short distance amplitude, at the same order of magnitude as the box diagram.

Long distances exist because only down-type quarks are present in the box, whose masses are small so that they hadronise faster than the $W^{\pm}$ propagation. They are difficult to calculate since they involve non-perturbative QCD calculations.

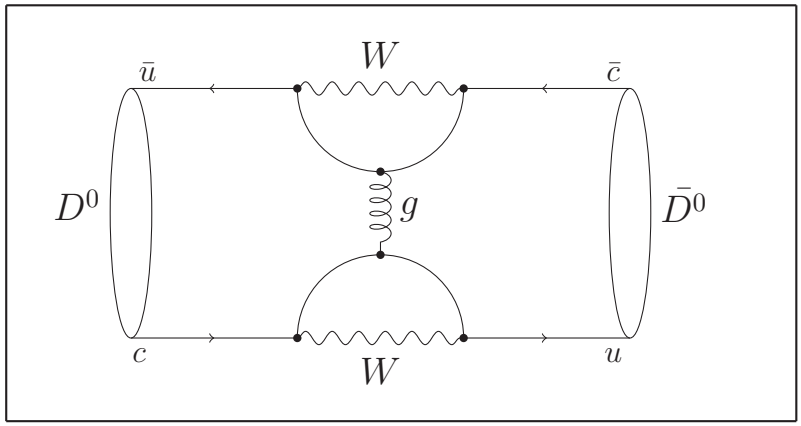


**Figure 1.10:** Di-penguin diagram contributing to $D^0$ oscillations.

## 1.4 CP violation

CP violation in the SM of electroweak interactions is caused by a single irreducible complex phase in the CKM matrix. There are 3 types of CP violation, as illustrated in Fig. 1.11. The direct CP violation describes processes with $\Delta F = 1$ and is accessible to both charged and neutral mesons. The indirect CP violation can be of two types: in mixing and in interference between mixing and decay.

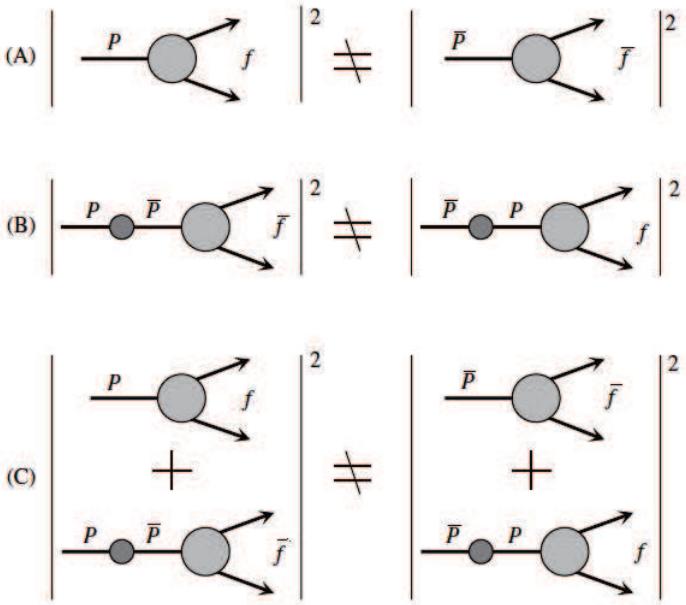


**Figure 1.11:** The three types of CP violation for $D^0$ mesons (and for other neutral mesons): (A) in decay, (B) in mixing and (C) in interference between mixing and decay. Image taken from [19].

### 1.4.1 Indirect CP violation due to mixing

The CP violation due to mixing, which is an indirect type of CP violation, occurs when the probability of transition of a meson to its anti-meson is different from the one of the reverse process:

$$P(D^0 \to \overline{D}^0) \neq P(\overline{D}^0 \to D^0) \tag{1.55}$$

This type of CP violation only depends on the mixing parameters, and not on the final state of the decay. It occurs when the physical states are not the same as the

CP eigenstates. From the equations of $D^0$ meson mixing 1.52, it results that the condition for the CP violation in mixing is:

$$\left|\frac{q}{p}\right| \neq 1 \tag{1.56}$$

### 1.4.2 Direct CP violation in decay

If the probability of a $D^0$ to decay to a final state $f$ is different from the probability for the charge conjugate process to occur, then we refer to direct CP violation, or CP violation in the decay:

$$\Gamma(D^0 \to f) \neq \Gamma(\bar{D^0} \to \bar{f}) \tag{1.57}$$

This type of CP violation is the only one also possible for charged mesons, which cannot mix due to charge conservation. It requires the existence of at least two interfering decay amplitudes, with different weak and strong phases.
For charged D, meson mixing can not occur, therefore CP violation in decay is characterized by non-zero values in the time integrated CP asymmetry:

$$A_f^{\pm} = \frac{\Gamma(D^- \to f^-) - \Gamma(D^+ \to f^+)}{\Gamma(D^- \to f^-) + \Gamma(D^+ \to f^+)} = \frac{|\bar{A}_{f^-}/A_{f^+}|^2 - 1}{|\bar{A}_{f^-}/A_{f^+}|^2 + 1} \tag{1.58}$$

where $A_f$ and $\bar{A}_{\bar{f}}$ are the amplitudes of the corresponding decay. With $\delta_{1,2}$ being the strong phases and $\phi_{1,2}$ the weak phases, they can be expressed as following:

$$\begin{aligned} A_f &= |a_1|e^{i(\delta_1+\phi_1)} + |a_2|e^{i(\delta_2+\phi_2)} \\ \bar{A}_{\bar{f}} &= |a_1|e^{i(\delta_1-\phi_1)} + |a_2|e^{i(\delta_2-\phi_2)} \end{aligned} \tag{1.59}$$

The sign of $\phi_{1,2}$ will change under CP, while the sign of $\delta_{1,2}$ will not change, as CP is conserved by the strong interaction. The CP asymmetry can also be rewritten as:

$$A_f^{\pm} = -\frac{2|a_1||a_2|sin(\delta_2 - \delta_1)sin(\phi_2 - \phi_1)}{|a_1|^2 + |a_2|^2 + 2|a_1||a_2|cos(\delta_2 - \delta_1)cos(\phi_2 - \phi_1)} \tag{1.60}$$

The CP asymmetry $A_f^{\pm} = 0$ only if the difference between the strong phases or the difference between the weak phases (of the two amplitudes) is zero or a multiple of $\pi$.

For neutral D meson decays, the CP asymmetry can be written as:

$$A_D = \frac{|A_f/\bar{A}_f|^2 - |\bar{A}_{\bar{f}}/A_{\bar{f}}|^2}{|A_f/\bar{A}_f|^2 + |\bar{A}_{\bar{f}}/A_{\bar{f}}|^2} \tag{1.61}$$

and this CP asymmetry is different from zero if:

$$\left|\frac{\bar{A}_f}{A_f}\right| \neq 1 \tag{1.62}$$

### 1.4.3 Indirect CP violation due to interference between mixing and decay

The third type of CP violation is also called mixing induced CP violation. If the probability that a particle oscillates and decays to a final state $f$ is different from the probability that the antiparticle oscillates and decays to the same final state $f$, there is a CP violation due to interference between mixing and decay. A sketch illustrating a mixing induced CP violation is shown in Fig. 1.12.

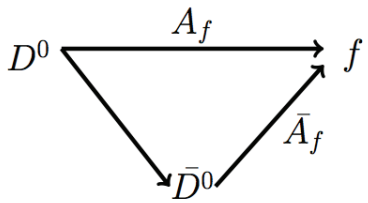


**Figure 1.12:** Interference between mixing and decay amplitudes.

This CP violation in the interference is present if the complex quantity $\lambda_f$, defined as:

$$\lambda_f = \frac{q}{p}\frac{\bar{A}_f}{A_f} = -\eta_{CP}\left|\frac{q}{p}\right|\left|\frac{\bar{A}_f}{A_f}\right| e^{i\phi} \tag{1.63}$$

has a non-zero imaginary part. It implies that we can observe mixing induced CP violation even if the amplitudes for both flavour oscillations and physical decays have the same magnitude for CP-conjugate states, meaning $|q/p| = 1$ and $|\bar{A}_f/A_f| = 1$. In Eq. 1.63, $\eta_{CP} = \pm 1$ is the eigenvalue of the CP eigenstate $f_{CP}$ and $\phi$ is the CP violating relative phase between $q/p$ and $\bar{A}_f/A_f$.
In this thesis, we study the potential of the Belle experiment to measure the time-dependent CP asymmetries of $D^0$ decaying to $h^+h^-$ final states ($h^+h^- = \pi^+\pi^-$ and $K^+K^-$). We will explain in Chapter 3 how the $\beta_c$ angle of the charm unitarity triangle can be estimated thanks to these two measurements.

# 2. Experimental Framework

This chapter details the experimental framework of the work presented in this thesis. Section 2.1 briefly describes the previous KEKB collider. Section 2.2 explains how the machine parameters of KEKB are being modified for SuperKEKB in order to achieve an instantaneous luminosity 40 times higher. Then, in Section 2.3, SuperKEKB is presented, its operation schedule is given and the induced background sources that will affect the Belle II detector are introduced. The interaction region is defined in Section 2.4. Each sub-detector of Belle II and the necessary improvements to operate the new colliding scheme are exposed in Section 2.5. Finally, the Belle II analysis framework is briefly presented in Section 2.6.

## 2.1 The KEKB collider

KEKB was an asymmetric $e^+e^-$ circular collider, composed of a High Energy Ring, referred to as HER, where an 8 GeV electron beam circulated, and a Low Energy Ring, referred to as LER, where a 3.5 GeV positron beam circulated. Electrons and positrons were produced and accelerated in a Linac, then fed to the 3 kilometers rings. At the interaction point (IP), the beams collided with a crossing angle of 22 mrad. This scheme presented several advantages, like an easier beam separation with no need for a bending magnet to separate the beams and limiting beam-beam background, a simpler design around the IP with few components and in the end limited synchrotron radiation. But the price to pay is a limited instantaneous luminosity. To overcome this issue, a scheme with crab crossing was introduced in 2007 [59].

With the crab crossing scheme, KEKB holds the intensity world record for colliders, by reaching in 2009 an instantaneous luminosity of $2.1 \times 10^{34}$ cm$^{-2}$s$^{-1}$. Fig. 2.1 shows the integrated luminosity delivered by KEKB and PEP-II (a similar collider hosted at SLAC, USA), at center-of-mass energies corresponding to the different $\Upsilon$ resonances and off-peak. The Belle and the BaBar detectors have registered together 1.5 ab$^{-1}$ of data, corresponding to more than 1 billion of $B\bar{B}$ pairs.

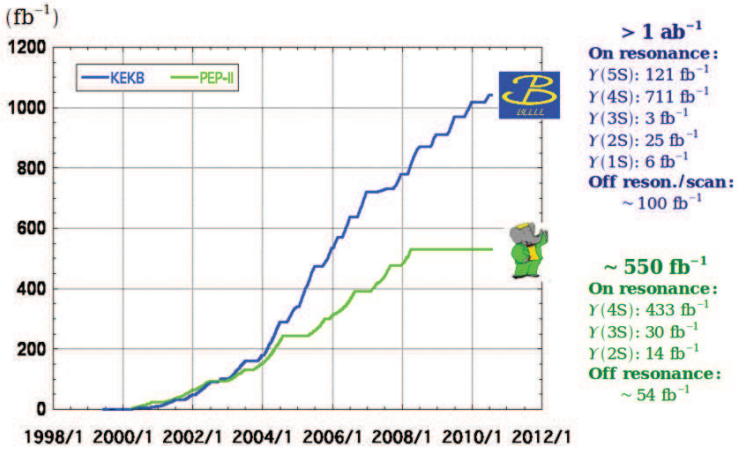


**Figure 2.1:** Integrated luminosity registered respectively by Belle at KEKB and by BaBar at PEP-II [60].

## 2.2 The upgrade scheme

### 2.2.1 The $\beta$-function and betatron oscillation

Under the influence of the focusing and defocusing forces in a ring, the differential equation of the trajectory of one particle in the beam is the Hill's equation:

$$x''(s) + k(s)x(s) = 0 \tag{2.1}$$

Where $k(s)$ is the quadrupole strength and the trajectory function x(s) is known as the betatron oscillation. $x(s)$ describes the oscillation around the orbit (or the distance of a single particle to the center of the beam) and its amplitude and phase depend on the position $s$ along the orbit.
The general solution of the trajectory has the form [61]:

$$\begin{aligned} x(s) &= \sqrt{\epsilon\beta(s)}cos(\Psi(s) + \Phi) \\ x'(s) &= -\frac{\sqrt{\epsilon}}{\sqrt{\beta(s)}}\left[\alpha(s)cos(\Psi(s) + \Phi) + sin(\Psi(s) + \Phi)\right] \end{aligned} \tag{2.2}$$

Where $\alpha(s) = -\frac{\beta(s)}{2}$, $\beta(s)$ term is called the $\beta$-function, $\epsilon$ is called the emittance, $\Psi(s)$ is the amplitude and $\Phi$ is the phase. $\beta(s)$ depends on the beam focusing which varies with the longitudinal position $s$ and $\sqrt{\epsilon\beta(s)}$ is the envelope of the beam. It is very hard to describe a beam by tracking all its particles in a 3D space. Therefore, the beam envelope is used, where the particle with the highest emittance will have a motion describing an ellipse in the x-x' phase space (for systems where

the beam energy stays constant, where x'= $\frac{dx}{ds}$ is the horizontal slope of the particle trajectory), as showed in Fig. 2.2. All the other particles in the beam will describe smaller ellipses, inside of this outermost ellipse. This is illustrated in Fig. 2.3, with a simulation for 2 and 18 particles respectively.

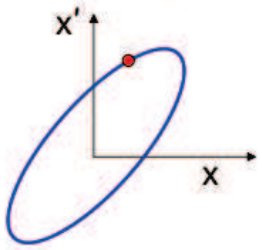


**Figure 2.2:** An example of a phase-space plot. The area of the ellipse is always constant, equal to $\pi\epsilon$. The emittance $\epsilon$ cannot be changed by the focusing properties, it remains constant throughout the whole beam transport system.

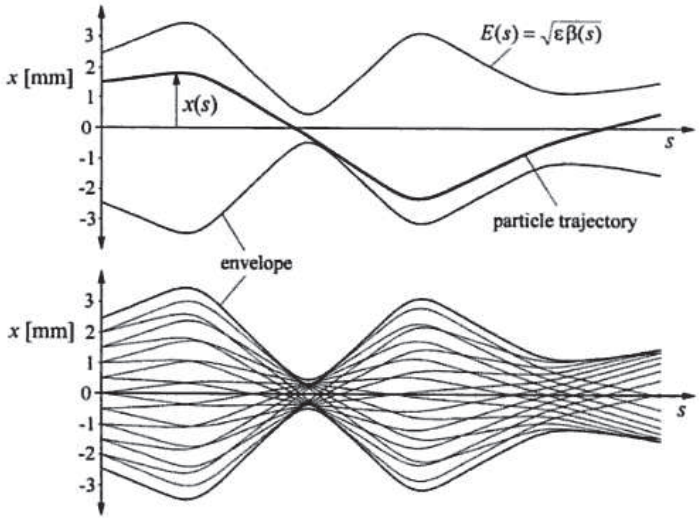


**Figure 2.3:** Particle trajectories x(s) and the beam envelope E(s), in the upper image for 2 particles in the beam and in the lower image for 18 particles [61].

### 2.2.2 The luminosity of a collider

The simplest expression of the instantaneous luminosity, considering a Gaussian particle distribution, is:

$$\mathcal{L} = \frac{N_1 N_2 f}{4\pi\sigma_x^*\sigma_y^*} \tag{2.3}$$

where the superscript * means that the value is considered at the interaction point (IP) and the terms are:

| | | | |
|---|---|---|---|
| $N_{1,2}$ | = number of particles per bunch | $f$ | = bunch collision frequency |
| $\sigma^*_{x,y}$ | = horizontal (vertical) beam size | | |

But this expression does not include effects due to the bunch length or a non-zero crossing angle. Therefore, we can look at the following equation of the luminosity of a collider, expressed in terms of the betatron function and the beam current:

$$\mathcal{L} = \frac{\gamma}{2e \cdot r_e}\left(1 + \frac{\sigma^*_y}{\sigma^*_x}\right)\left(\frac{I_{beam} \cdot \xi_y}{\beta^*_y}\right)\left(\frac{R_L}{R_{\xi y}}\right) \tag{2.4}$$

where

| | | | |
|---|---|---|---|
| $\gamma$ | = Lorentz factor | $\xi_y$ | = vertical beam-beam tune shift parameter |
| $r_e$ | = classical electron radius | $R_L$ | = reduction factors of luminosity |
| $e$ | = elementary charge | | (due to crossing angle) |
| $I$ | = beam current | $R_{\xi y}$ | = tune shift reduction factor |
| $\beta^*_y$ | = vertical $\beta$ function | | (due to hourglass effect) |

We can analyze the Eq. 2.4 in the perspective of boosting the luminosity. First of all, we look how to reduce the hourglass effect. This effect appears when the bunch length is comparable to $\beta^*_{(x,y)}$, and the effect is a variation of the transverse beam size along the length of a bunch. If the condition for a small hourglass effect is fulfilled ( $\beta^*_y \gg \sigma_z$), then we have:

$$\frac{R_L}{R_{\xi y}} \approx 1 \tag{2.5}$$

One way to amplify the luminosity is to increase the beam currents $I_{beam}$. This scheme was considered for the future SuperKEKB before 2009, but it is suffering from coherent synchrotron radiation and from an increased power consumption heating the vacuum chamber. The target instantaneous luminosity with this technique was therefore limited to $2 \times 10^{35}$ cm$^{-2}$s$^{-1}$, i.e. 20 times more than the KEKB design value but only 10 times more than the world record. With such an instantaneous luminosity, assuming $1.5 \times 10^7$ $s$ of operation per year, 17 years of running at the $\Upsilon(4S)$ center-of-mass energy would have been needed to deliver 50 $ab^{-1}$ of data.

Another way to intensify the luminosity is to use round beams, where:

$$\left(1 + \frac{\sigma_y}{\sigma_x}\right) \approx 2 \tag{2.6}$$

The primary advantage of the round beams is their stability, particularly against the detrimental effects of beam-beam interactions. But since no consistent design was found with an acceptable dynamic aperture and with feasible separation of the two beams at IP, this scheme was abandoned [62].
Fortunately, a new technique of so-called nano-beam with large crossing (also called Piwinski) angle was proposed by P. Raimondi in 2006 for the italian SuperB project [63]. This scheme was successfully tested at the DAΦNE ring by Raimondi and his team in 2010 [64]. In the nano-beam scheme, we have:

$$\left(1 + \frac{\sigma_y}{\sigma_x}\right) \approx 1 \tag{2.7}$$

With the nano-beam scheme, the vertical $\beta$-function at the IP will be reduced to 1/20 of KEKB's one, therefore squeezing the beam in the transverse direction, increasing the beam density and hence the colliding probability. The beam currents $I_{beam}$ will be moderately increased from 1.6 / 1.2 A in KEKB to 3.6 / 2.6 A in SuperKEKB, for LER and HER respectively. As far as the beam-beam tune shift $R_{\xi y}$ parameter is concerned, it is assumed to be similar to the one of KEKB. With all these modifications, an improvement factor of 40 is expected for the instantaneous luminosity, with respect to KEKB.
Despite this nano-beam scheme, the dynamic aperture remains a considerable issue of SuperKEKB, because a narrow dynamic aperture shortens the beam lifetime due to the Touschek effect, and the lost particles cannot be restored by the injector if the lifetime is too short [65].
To reduce the problem of emittance growth due to high intra-beam scattering, the beam asymmetry is decreased from 3.5 / 8.0 GeV (in KEKB for LER/HER) to 4.0/ 7.007 GeV (in SuperKEKB) [77]. This decreased asymmetry results in a lower boost of the collision products at SuperKEKB with respect to KEKB. The disadvantage is a reduced separation between the two B meson decay points, but the advantage is an improved acceptance in the detector.
As a conclusion, a comparison between the machine parameters of KEKB and SuperKEKB is provided in Table 2.1.

| Parameters (LER / HER) | KEKB crab cavities | SuperKEKB phase 2 | SuperKEKB phase 3 |
|---|---|---|---|
| En. (GeV) | 3.5 / 8.0 | 4.0 / 7.007 | 4.0 / 7.007 |
| $\epsilon_x(nm)$ | 18 / 24 | 2.2 / 5.2 | 3.2 / 4.6 |
| $\sigma_x^*$ $(\mu m)$ | 147 / 170 | 16.8 / 22.8 | 10 / 11 |
| $\sigma_y^*$ $(\mu m)$ | 0.94 / 0.94 | 0.308 / 0.5 | 0.048 / 0.062 |
| $\beta_x^*$ $(mm)$ | 1200 / 1200 | 128 / 100 | 32 / 25 |
| $\beta_y^*$ $(mm)$ | 5.9 / 5.9 | 2.16 / 2.4 | 0.27 / 0.30 |
| $\xi_y$ | 0.129 / 0.09 | 0.0240 / 0.0257 | 0.088 / 0.081 |
| $2\phi(mrad)$ | 22 | 83 | 83 |
| $I_{beam}$ (A) | 1.64 / 1.19 | 1.0 / 0.8 | 3.6 / 2.6 |
| Nb bunches | 1584 | 2500 | 2500 |
| $\mathcal{L}(10^{-34}cm^{-2}s^{-1})$ | 2.11 | 1 | 80 |

**Table 2.1:** Beam parameters of KEKB using the crab cavitiy scheme and SuperKEKB based on the nano-beam scheme. Phase 2 corresponds to the commissioning, discussed later in this chapter and phase 3 to the physics run. Values taken from [66, 67].

## 2.3 The SuperKEKB collider

In order to build SuperKEKB, several modifications were undertaken and new parts were added to KEKB: a new Damping Ring was added for positrons, the Linac was upgraded with a new positron capture section and a new low emittance RF gun, monitors and control systems were also improved, the RF system was reinforced to cope with the higher beam currents, new TiN-coated beam pipes with antechambers were installed, a new LER lattice was designed to squeeze the emittance (replacing short dipoles with longer ones, increasing wiggler cycles) and new superconducting final focusing magnets were placed near the IP [68]. The main upgrades are summarized on the schematic view of SuperKEKB shown in Fig. 2.4. Several facilities will be reused in order to minimize the cost, like most of the magnets and the tunnel.

The commissioning of SuperKEKB is scheduled to start in January 2016 and the physics run in 2018.

SuperKEKB is planned to achieve an integrated luminosity of about 50 $ab^{-1}$ in approximately 6 years of operation, which represents about 50 times more than KEKB.

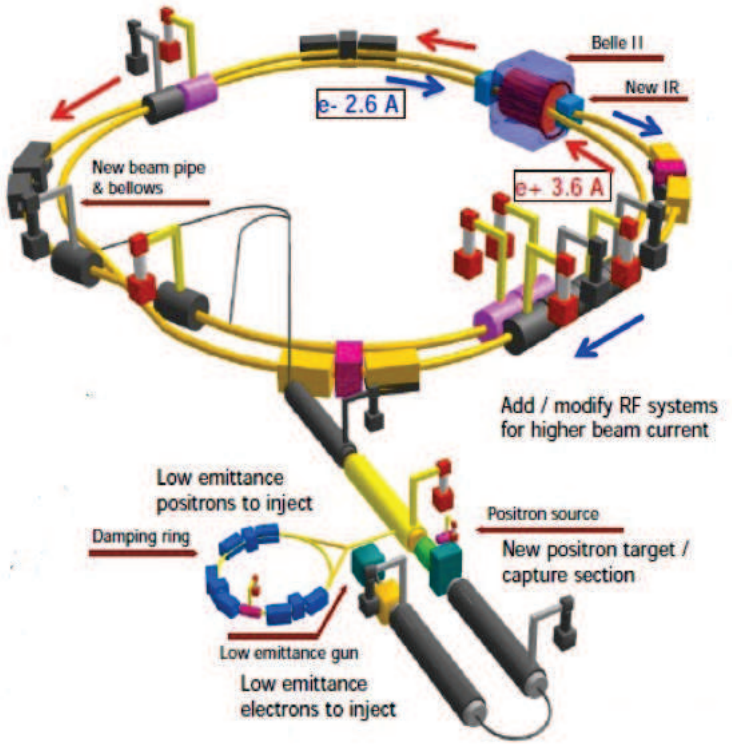


**Figure 2.4:** Schematic plan of SuperKEKB summarizing the main upgrades undertaken, taken from [69].

### 2.3.1 SuperKEKB operation schedule

The operation schedule of SuperKEKB is detailed in Fig. 2.5, also presenting the targeted instantaneous and integrated luminosities. It contains three phases, two of commissioning and the third, of the physics run. The first phase was recently postponed for economical reasons to early 2016, while the physics run is scheduled to start in October 2018.

The increase in instantaneous luminosity will be performed prudently, with a smooth slope at the beginning, to reach the nominal value after about 2 years.

SuperKEKB will be operated 9 months every year, with a summer shutdown scheduled each year from July to September. After one year of running, about twice as much data as already existing from BaBar and Belle should already be registered. The next milestone will be achieved after 2 years of running, with 10 $ab^{-1}$ of data registered at the $\Upsilon(4S)$, i.e. about 10 times more than Belle and BaBar. Finally, the targeted 50 $ab^{-1}$ should be obtained in about 6 years of running. Beside the run at the $\Upsilon(4S)$ center-of-mass energy, data will also be collected at other $\Upsilon$ resonance energies and off-peak.

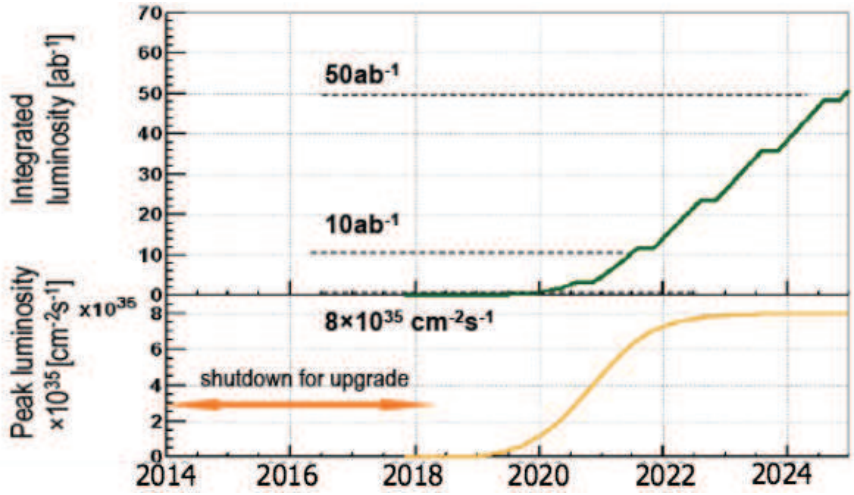


**Figure 2.5:** Targeted integrated and instantaneous luminosities of SuperKEKB, taken from [70]. A shift of about 1 year has been applied with respect to the plot, to account for the latest calendar.

Following its switch-on, SuperKEKB is expected to be fully operational after three phases. The first two are called BEAST II (standing for Beam Exorcism for A STable BELLE Experiment) and correspond to the experiment commissioning.

- BEAST II phase 1: During this phase, the aim is to tune each beam independently and to test the vacuum scrubbing inside the rings. Belle II detectors will not be in place at the IP, but another set of detectors are installed there to provide appropriate measurements of the environment, ionizing and non-ionizing radiation levels, occupancy rates and bring fast feedback to tune the beam parameters. Neither the final focus magnets will be available nor the Belle II solenoid. The beam pipe at the IP will not be the final one but a thicker one of larger radius. This phase is scheduled to last 5 months from January to May 2016.

- BEAST II phase 2: This period will be useful to tune the collision scheme. Objectives are numerous: to characterize the machine induced background, to be able to extrapolate accurately background simulation predictions at the nominal instantaneous luminosity, to ensure a safe operation of all detectors as far as radiation level and occupancy levels are concerned, to check the integration (data acquisition) of all detectors and to place background shields.

  At this stage, Belle II will be set up ready and all magnets participating to the final focus in place and switched on (QCS and the Belle II solenoid). The

vacuum will almost be reached in the beam pipe and the beam pipe at the IP has been changed to the quasi-final one (made of beryllium, with a radius of 1 cm). With respect to the one which will be used during the data taking, the gold coating of the beam pipe will be only 6.6 $\mu m$ thick, in order to study more accurately the synchrotron radiation. During the physics run, the gold coating is foreseen to be 10 $\mu$m thick to stop photons more efficiently.

Belle II will not be fully assembled during the phase 2 of BEAST II: in particular the inner tracker volume will only be equipped with one ladder of each layer type (4 double-sided silicon strip layers and 2 DEPFET pixel layers, see next section), placed at one $\phi$ position. The rest of the inner tracker volume will be used to set other devices meant to characterize the background produced by SuperKEKB and to make sure that the inner tracker can be safely operated.

The Strasbourg group proposes to use 2 PLUME ladders during this phase to contribute to the background characterization. The idea is to compare measurements with different beam and colliding conditions, to validate the MC simulation predictions and to be confident in their extrapolation at higher luminosities. This is essential since a new collision technique will be used for the first time, for which no background measurements exist. Even if the fundamental processes are mainly electromagnetic and well known, it is not easy to predict the impact of these backgrounds in the interaction region (IR) because such a prediction would need a very precise propagation of the particles produced, sometimes along the entire 3 km ring. Moreover, while within the Belle II detector the magnetic field is uniform, being mainly the one produced by the solenoid, it shows a non-linear behaviour outside of the Belle IR. The background is impacted by the field outside Belle II detector, outside the solenoid, where there are contributions from the magnetic fields produced by the collider components. Finally, the background prediction also relies on a very precise description of all the material budget in a wide region around the IR.

This phase is supposed to end when the instantaneous luminosity reaches $10^{34}$ $cm^{-2}s^{-1}$, which is the target to start the physics run. It is scheduled to last during 5 months between May 2017 and January 2018.

- Phase 3: corresponds to the physics run. The vertex detector is installed and the final version of the beam pipe is placed in the IR. The beam current and the luminosity will continue to gradually increase. This phase is planned to

start in October 2018, after the summer shutdown.

### 2.3.2 Background particles produced by SuperKEKB

Electrons and positrons composing the two beams will interact, within the same beam and from one beam to the other. Furthermore, particles may escape the bunch or hit a remaining atom or molecule in the beam pipe. This machine induced background will be higher at SuperKEKB than at KEKB, because of the reduced beam cross section and the increased beam intensity. All the particles produced by these processes, either the primary or the secondary ones, may hit the detector and overwhelm the signal produced by the collision final state products. They may degrade the detector performances, on one side by significantly raising the detector occupancy and on the other side by ionizing and non-ionizing radiation effects on the detectors.
We refer to SuperKEKB induced background when speaking of all particles produced by the beams but not produced by an $e^+e^-$ collision in the center of the Belle II detector. Several types of backgrounds will impact the experiment, they are categorized as single-beam background processes, beam-beam background processes (proportional to the luminosity) and injection noise. The energy, spatial and angular distributions of background particles are strongly dependent of the process that produces them. As a consequence, the dominant source of background depends on which detector is considered.

#### 2.3.2.1 Single-beam background processes

- **Synchrotron radiation**

  In SuperKEKB, electrons and positrons are bent with a magnetic field and the emitted photons can escape or hit the beam pipe wall and produce electromagnetic showers. In the vicinity of the IR, photons and the produced $e^+$ and $e^-$ may reach the detector. The photons are produced with a rate proportional to the square of the beam energy and the square of the magnetic field. Therefore, the HER (High Energy Ring) is the main source of synchrotron radiation background. It is produced at very small angles with respect to the beam and impact in particular the inner tracker layers. During the Belle experiment, the inner layer of the vertex detector was seriously damaged by X-rays of about 2 keV produced by the HER [71], and this was not properly predicted by simulation studies. To absorb the synchrotron radiation before reaching the inner tracking system, the inner surface of the double-wall beryllium beam pipe will

be equipped with a 10 $\mu$m gold plating. The new SuperKEKB scheme with an increased crossing angle also reduces the synchrotron radiation, because the final focus quadrupole magnets will be independent for each beam.

- **Beam-gas Coulomb scattering**

  This source of background is due to the collision between a particle from the beam and a remaining atom within the beam pipe. It includes the Coulomb scattering (that changes the direction of the beam particle) and the bremsstrahlung scattering (that decreases the energy of the beam particle). Its rate is therefore proportional to the beam pipe pressure and the beam current. At SuperKEKB, the targeted pressure in the beam pipe is the same as the one achieved at KEKB, about $10^{-7}$ Pa, but the beam current will be twice as high. As a consequence, the rate of this background is expected to increase. Simulations revealed an increased rate of about 100 times compared to KEKB [72], considering also the different vertical beta function and the reduced beam pipe aperture.

- **Touschek effect**

  The Touschek effect consists in an intra-bunch scattering effect due to particles with slightly lower or higher momentum than the bunch average. These particles can escape the bunch, hit the beam pipe and produce secondary particles. This effect is proportional to the number of bunches and the beam currents, and inversely proportional to the horizontal (vertical) beam size and the cubic of beam energy ($E^3_{beam}$). Therefore, with the nano-beam scheme, the Touschek rate is expected to be larger by a factor of 20 with respect to KEKB.

  To reduce this background rate, two countermeasures are proposed: movable collimators and heavy-metal shielding. The movable collimators will be located along the ring, in order to stop the particles before they reach the detectors. The heavy metal shield is made of tungsten-alloy and will be placed outside the detector acceptance, between the beam pipe and the inner detectors. This will help stopping the background showers before reaching the inner tracker of Belle II.

#### 2.3.2.2 Beam-beam background processes

- **2 photons QED-pair production**

  This background is luminosity dependent and generated by QED processes. One of the dominant Feynman diagrams for this process is represented in Fig. 2.6, where an $e^+$ and an $e^-$ interact via two photons $\gamma$ and produce two $e^+e^-$ pairs in the final state.

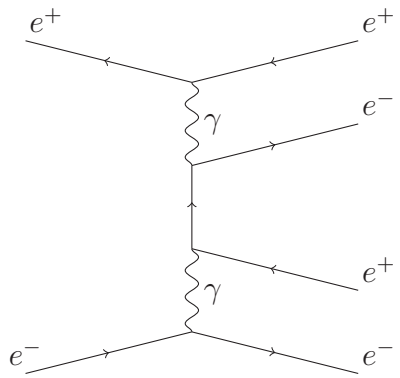


**Figure 2.6:** Feynman diagram of a 2 photons QED-pair production, with 2 $e^+e^-$ pairs in the final state.

  The two-photons background particle density increases with $1/r^2$ (where $r$ = the distance from the IP), due to the fact that the momentum spectrum of these particles is in the MeV range. Therefore, these particles tend to curl in the innermost detector layers and significantly increase their occupancy rate. At SuperKEKB, since the instantaneous luminosity will grow with respect to KEKB, and because the innermost detector layers will be placed closer to the interaction point, the rate of this background will become the dominant one in the pixel detector.

- **Radiative Bhabha**

  Radiative Bhabha is also a QED interaction between an $e^-$ of one beam and an $e^+$ of the other beam, producing photons in the final state, as illustrated by the Feynman diagram shown in Fig. 2.7.

  This effect is proportional to the luminosity, therefore it can be used in measurements of the instantaneous luminosity and to provide on-line feedback to the collider to tune the beam parameters. These photons created can interact with the iron of the magnets and produce neutrons. The cross-section of this process is much larger than those of all other background processes, but

since photons are created at very small angles with respect to the beam axis, acceptance considerations lead to the fact that it mainly affects the outermost detectors. The beam electron or positron energy will decrease after the radiation of photons, therefore the scattered particle will be over-bent by the magnets, hit the wall of magnets and produce electromagnetic showers.

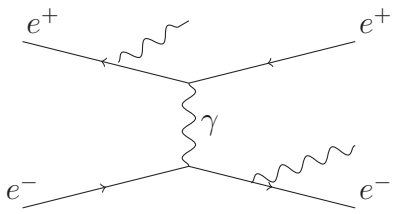


**Figure 2.7:** Example of a radiative Bhabha Feynman diagram with initial state and final state radiations.

#### 2.3.2.3 Injection noise at SuperKEKB

To ensure a reasonable beam lifetime in presence of a high induced background, SuperKEKB will work with a continuous injection scheme, also called top-down injection scheme. Injection occurs at every 20 ms (i.e. with a total rate of 50 Hz) and a bunch will need 10 $\mu$s to perform a complete revolution in the 3 km ring. During the accelerator beam injection, the beam is unstable and will produce a high background in the Belle II detector. Two processes will occur during this stage: particle losses because of the noisy bunch and "cooling" (radiation damping) from synchrotron radiation. The first effect causes a very short beam lifetime of about 600 s for the LER.

As far as the second effect is concerned, the damping scheme of SuperKEKB is not known, but it is assumed to be the same one as KEKB's one, as shown in Fig. 2.8 right. At KEKB, a new injected bunch needed 100 turns in the ring (which corresponds to about 1 ms) in order to start to stabilize, and after about 4 ms it got relatively stable. This information can be used by the vertex detector for instance in order to veto the trigger during the passage of a noisy bunch, each 10 $\mu$s necessary to a complete one turn around the ring, during the first 4 ms. But this will only be possible if the damping scheme is the same as at KEKB, otherwise the vertex detector can be damaged or saturated by the produced background. For this reason also, BEAST II is a crucial program, in order to study both coherent and incoherent damping mechanisms.

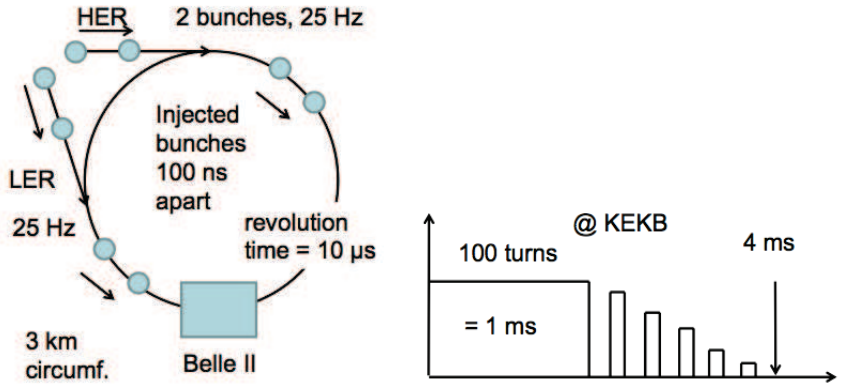


**Figure 2.8:** In the left image the continuous injection scheme at SuperKEKB is presented. The right image illustrates the particle rate induced by the collider background. The damping due to the feedback system at KEKB, which is about 1 ms (in the image, the square representing 1 ms contains in fact data every 10 $\mu$s), appears much shorter than the radiation damping (incoherent damping). This prediction is empirically determined, and it represents the damping of the center of gravity of the bunch, but there can still be particles with high oscillations amplitude during about 20-40 ms. Images taken from [73].

#### 2.3.2.4 Conclusion on backgrounds produced by SuperKEKB

The machine induced background is studied with simulations in order to predict its impact on the Belle II detectors. This impact depends on the considered detector and Table 2.2 shows the expected occupancy rates in the two pixel layers, which reach the % level if synchrotron radiation is added. These simulations suffer from large uncertainties and the BEAST II commissioning will be employed to perform measurements to validate them.

## 2.4 The interaction region (IR)

The success of the SuperKEKB and Belle II experience will strongly rely on the architecture of the IR. The main modifications brought to KEKB were driven by the requirements of the nano-beam scheme and the necessity to maintain the background as low as possible. These changes include: a larger crossing angle, from 22 mrad to 83 mrad, a smaller beam pipe radius from 15 mm to 10 mm, magnets placed closer to the IP (Interaction Point) and additional shields.
A non-zero $\phi$ crossing angle at the IP reduces the effective bunch length by a factor $2/\phi$ and decreases the hourglass effect. In the new scheme there will not be any

| Background | | Layer 1 (%) | Layer 2 (%) |
|---|---|---|---|
| Touschek | LER | 0.1 | 0.07 |
| Touschek | HER | 0.0 | 0.0 |
| Beam-gas Coulomb | LER | $2{\cdot}10^{-4}$ | $1{\cdot}10^{-4}$ |
| Beam-gas Coulomb | HER | 0.0 | 0.0 |
| Radiative Bhabha | LER | $5{\cdot}10^{-3}$ | $2{\cdot}10^{-3}$ |
| Radiative Bhabha | HER | 0.03 | 0.01 |
| Two-photon QED | | 0.8 | 0.2 |
| TOTAL | | 0.9 | 0.3 |

**Table 2.2:** Predicted occupancy rates in the two pixel layers, for different background sources except synchrotron radiation and injection noise [74].

bending of the beams near the IP to reduce the emittance and the synchrotron background [75].

However, the background can remain an issue, especially for the innermost detectors. Therefore additional measures have to be taken. In order to stop the background originating from a distance greater than 65 cm in both forward (the side of incoming $e^+$) and backward (the side of incoming $e^-$) directions, thick tungsten shields will be mounted outside of the IR [76]. But in the region within 65 cm around the IP, the shield is limited due to the narrow space and the restricted weight that can be supported. To protect the inner tracker detector from showers coming from upstream, heavy metal shields will be placed outside of the acceptance region.

An important part of the IR will be occupied by the focusing and steering magnets. In order to reduce the dispersion of the beams, the back-scattering background and the over-bent $e^+e^-$ after radiative Bhabha, the final focus magnets will be used independently for each ring.

The beam pipe at IR is a double-wall made of beryllium (0.6 mm), with an inner diameter of 10 mm. Its design minimizes the creation and the trap of HOM (Higher Order Modes) and it will have a ridge structure on the inner surface of collimation part to hide the beryllium pipe from reflected or scattered synchrotron radiation. Another measure to reduce the synchrotron radiation is the 10 $\mu$m gold plating. The beam pipe is required to operate at room temperature, while the magnets will work at 4.5 K. In order to reduce the heating due to radiation, the beam pipe will have a new structure with two small antechambers, on the left and on the right sides. Knowing that beryllium is reactive, a cooling system with water is not recommended.

A beam pipe made of titanium would be a better solution but much more expensive. Instead of water, paraffin will be used to keep the temperature rise below 10° C.
The magnetic field is globally well known in the detector area, and Fig. 2.9 is displaying its profile around the IR. This profile is dominated by the field produced by the Belle II solenoid and it is relatively constant in the vicinity of the interaction point.

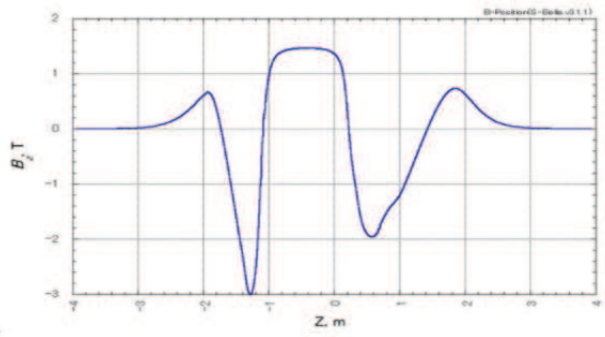


**Figure 2.9:** The magnetic field B (T) as a function of z (m) in the IR, between -4 m and +4 m around the collision point [77].

## 2.5 The Belle II detector

### 2.5.1 Introduction

The Belle II detector consists in different detectors arranged in cylindrical barrels around the beam in forward and backward positions around the IP in order to improve hermeticity. Each one is dedicated to a particular measurement. The tracking is performed with an inner tracking silicon detector followed by a central gaseous detector. At larger distance from the IP, the particle identification and the electromagnetic calorimeter detectors are placed, surrounded by a superconducting solenoid which produces a 1.5 T magnetic field. Outside the solenoid the $K_L^0$ and muon detector is placed.
Since the collisions are not symmetric, the detector also shows an asymmetry to optimize the acceptance. The asymmetric coverage of the tracker corresponds to a polar angle of 17° in the forward part and 150° in the backward part. A global figure of the detector is displayed in Fig. 2.10.

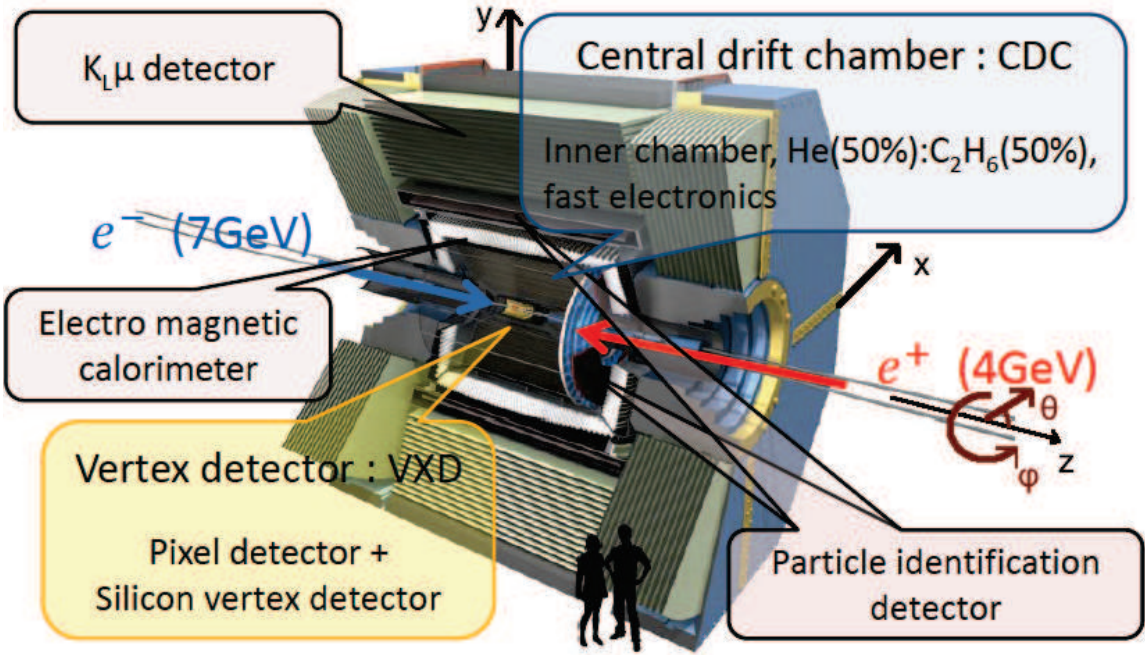


**Figure 2.10:** A general view of Belle II detector with the main improvements indicated with respect to the Belle detector, taken from [70].

### The coordinate system

In this thesis report we often refer to the coordinate system of Belle II introduced here. Two global coordinate systems are used in Belle II: the Cartesian one (x,y,z) and the spherical one (R,$\phi$,$\theta$). The origin of both systems is located at the center of the detector.

The x-axis is horizontal and goes towards outside of the accelerator ring, the y-axis is pointing vertically upward, lastly the z-axis is pointing along the magnetic solenoid axis with the same direction as the $e^-$ beam.

The $\rho$ coordinate is defined as the radius in the x-y plane, $\rho = \sqrt{x^2 + y^2}$, and R is the radius in three dimensions, R $= \sqrt{x^2 + y^2 + z^2}$, $\phi$ is the azimuthal angle and $\theta$ is the polar angle. The forward direction denotes z $> 0$ and the backward direction indicates z $< 0$.

When discussing the instrumental devices, it is convenient to locate each component with a number. The numbering scheme follows the simple rule, applied both for hardware and software considerations (with some exceptions for hardware): a component (or a sub-component within one physical component) with the smallest $R$ has the smallest number; similarly for a component with a smaller $\phi$, or smaller $\theta$.

### SuperKEKB main challenges

With respect to the KEKB collider, the operating conditions at SuperKEKB will be more challenging, in particular:

- the occupancy rate due to machine induced background will be higher. An extrapolation from the working conditions of Belle at KEKB, considering both the machine parameters changes and a modified IR, gives a background rate 20-40 times higher, depending on the detector considered;
- the radiation damage caused by machine induced background will be worse;
- the data acquisition system needs to fulfill the requirements of a considerably higher event rate;
- the beam energy asymmetry is 2/3 lower, resulting in a smaller center-of-mass boost and thus less separation between both B mesons decays vertices.

In such an experimental environment, the Belle II detector is designed in order to keep at least as good performances as achieved with the Belle detector.

**In that context, the main modifications with respect to the Belle detectors are:**

- a pixel detector (PXD) based on a DEPFET technology will be added as close as possible to the beam pipe, whose radius will be decreased in the IR. This detector will have a major contribution on the vertex resolution: to maintain a time resolution on the B flight distance at least equivalent to that measured at Belle, despite of the reduced boost in Belle II.
- the silicon vertex detector (SVD) will be extended to a larger radius. It will be equipped with a faster readout, and a standalone SVD track can be reconstructed and extrapolated to the pixel layers.
- the ability to identify particles is very important in flavour physics. Therefore, a particular effort is made to improve the Particle Identification Detectors (or PID).
- new electronics for the Electromagnetic Calorimeter (ECL) and the old CsI(Tl) crystals will be replaced with new pure CsI crystals.

| | Layer | Radius [mm] | Number of ladders | Material budget % $X_0$ |
|---|---|---|---|---|
| PXD | 1 | 14 | 8 | 0.21 |
| | 2 | 22 | 12 | |
| SVD | 3 | 38 | 7 | 0.57 |
| | 4 | 80 | 10 | |
| | 5 | 115 | 12 | |
| | 6 | 140 | 16 | |

**Table 2.3:** Description of each silicon layer of the inner tracking system of Belle II [77–79].

- a completely new acquisition system is designed to cope with a high event rate.

- a new trigger system called HLT (Belle II High Level Trigger) in order to reduce the beam background events and to enhance the physics-oriented events.

In the following, the different detector parts are described, with a particular emphasis on the inner tracking system. It has to be mentioned that at a B-Factory, we are interested in estimating a B meson flight distance, and this mainly relies on the z-projected flight distance because B mesons are boosted mostly along z-axis. Therefore, contrary to LHC-types of tracking detectors, the z spatial resolution is very important.

### 2.5.2 The Inner Tracking System

The inner tracking system consists of two silicon detectors, arranged in cylindrical barrels around the beam pipe. The innermost one is the pixel detector PXD, which includes two silicon layers of DEPFET sensors, and the outermost one is the strip detector SVD which is composed of four double-sided silicon layers.

The radii and the material budget of the different layers of the inner tracking system are presented in Table 2.3. The material budget is related to the thickness and properties of a given material. This thickness is usually expressed in units of radiation length $X_0$ which corresponds to the material thickness where a high energy electron loses all but 1/e of its energy.

#### 2.5.2.1 The PXD detector

The closest detector to the IP will face the highest background rate. Therefore it has to be pixellated to maintain the occupancy rate at an acceptable level. Furthermore, the energy spectrum of final state particles produced at SuperKEKB is particularly low (with respect to the one at LHC) and multiple scattering would cause serious problems if the same detectors were used, i.e. hybrid pixel detectors (for more details, see Chapter 5). This is the reason why a new type of pixel detectors will be used, based on the DEPFET (DEPleted Field Effect Transistor) technology, where the sensitive area of the sensors are thinned down up to 75 $\mu$m, leading to a material budget of 0.21 % $X_0$ per layer, as indicated in Table 2.3. To reduce even more the material budget, the readout chips are placed outside of the acceptance region (therefore these pixel detectors are not monolithic).

In order to avoid being saturated by the injection noise, the PXD detector uses a trigger veto lasting a couple of $\mu$s until the noise has calmed down. The integration time of the DEPFET sensor is 20 $\mu$s, and this veto leads to a 20% dead time [80].

**Detector layout**

The PXD consists of two layers, arranged in a cylindrical shape around the beam pipe as shown in Fig. 2.11. The first layer is composed of 8 ladders while the second layer is composed of 12 ladders. Furthermore, each ladder includes two half modules (splitting the modules in half is necessary due to size limitations of the wafer production [81] ). The modules are mounted on a metallic support including a cooling structure. The sensitive area of a module is 15 mm large and 90 mm long for the first layer and 123 mm long for the second layer [82].

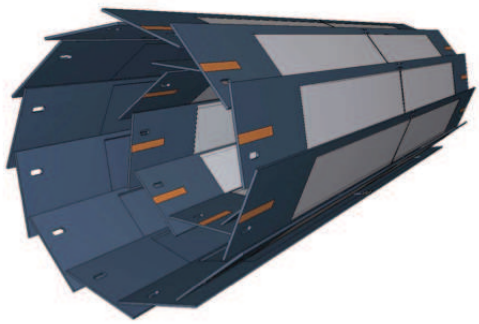

**Figure 2.11:** Geometry of the PXD detector, with the first layer placed at 14 mm and the second layer at 22 mm from IP [77].

The modules of the inner layer are pixelated with a 50×50 $\mu$m$^2$ granularity while the modules of the outer layer feature pixels of 50×75 $\mu$m$^2$. In total, there are about 8 million pixels, arranged in a matrix of 768×250 pixels in each DEPFET module. The PXD will be operated in the so-called rolling shutter mode. In order to minimize the readout time, four rows of pixels will be simultaneously read out so that only 20 $\mu$s are needed to read a module in a frame.

**DEPFET principle**

The DEPFET pixel cell is a field effect transistor (FET) operating in a fully depleted silicon bulk. The silicon bulk is of high resistivity n-type, with a p+ backside contact. Under the FET gate, a potential minimum for electrons is created by an additional n-implant called internal gate. Fig. 2.12 displays the layout of a single pixel. The DEPFET operation can be separated into three stages: charge collection, readout and clear.

A traversing charged particle produces electron-hole pairs, the holes drift to the back contact while the electrons accumulate in the potential minimum located at approximately 1 $\mu$m below the sensor surface. Due to the capacitive coupling of the internal gate to the transistor channel, when the transistor is switched on, the charge collected modulates the transistor current proportionally to the collected charge. Thus, the read out source-drain current of the transistor turns out to be an amplified signal. The readout is non-destructive, therefore it can be repeated many times.

The full depletion and the fact that the signal is amplified just above the position of its generation avoid a lateral charge spread where losses could occur.

After the charge collection and the read-out process, the charge from the internal gate is removed by applying a positive voltage to the n+ clear contact. A pedestal charge can be measured even without charge accumulated in the internal gate of the pixel, caused by leakage currents through the silicon. A sustained radiation dose can increase this effect. Moreover, the leakage currents tend to differ for each pixel.

The measured current (drain current) $I_d$ equals to the sum of the signal current $I_{sig}$ and the pedestal current $I_{ped}$. To extract $I_{sig}$, $I_d$ has to be corrected for the pedestal and noise offline, once after each integration time, before clearing the internal gate. The sample and reset of the signal happens within a 100 ns window.

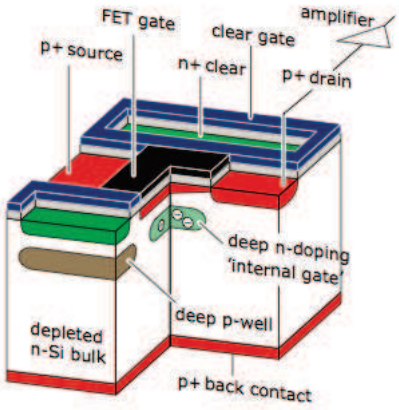


*Figure 4.3: Operating principle of a DEPFET*

**Figure 2.12:** Schematic view of a DEPFET cell taken from [77].

### Auxiliary ASICs

A module consists of an active area with the DEPFET pixels, surrounded by a support structure with Application Specific Integrated Circuits (ASICs) on it. ASICs are located outside of the acceptance region, where the material budget can be higher and effective active cooling is possible. The DEPFET matrix is operated by three kinds of ASICs bump bonded on a half ladder: six SwitcherB, four Drain Current Digitizers (DCD) and four Data Handling Processors (DHP), as shown in Fig. 2.13.

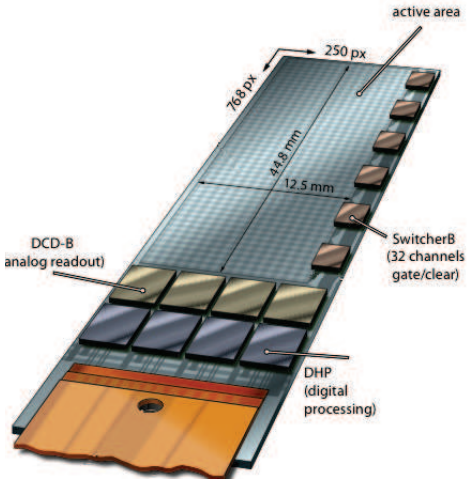


**Figure 2.13:** The layout of a DEPFET half ladder [81].

- The SWITCHER
  The SWITCHER chips are located along the long side of the half ladder (along

the magnetic field axis, or $z$ axis), on a 2 mm wide unthinned rim. For each line of the matrix, the gate and clear contacts of single pixels are connected together and controlled by switchers. These ASICs are able to deliver high pulses up to 20 V to clear the internal gate of the DEPFET in a short time.

- The Drain Current Digitizer (DCDB)
  These chips consist of 256 channels and they process the currents from a row of pixels and digitize the analog values.

- The Data Handling Processor (DHP)
  The DHP chips perform the data processing, compression, buffering and fast serialization. The raw data are corrected for pedestal fluctuations and noise and then the data rate is reduced by zero-suppression. The reduced data together with a time stamp are stored in hit buffers. The triggered hit data will be transmitted to the data handling hybrid (DHH) at a rate of 1.25 Gbit/s per chip.

A readout time of 100 ns for each row is achieved using the ASICs steering and reading out the DEPFET pixels. For DEPFET pixels with 50× 50 $\mu$m$^2$ pitch, an intrinsic resolution of 12 $\mu$m (RMS) was measured in [83].

#### 2.5.2.2 The SVD detector

The four double-sided silicon strip layers of the SVD detector are placed after the PXD detector, between 38 mm and 140 mm, as displayed in Fig. 2.14. The asymmetry allows optimizing the acceptance, since the center-of-mass of the collision products is boosted.
The hits measured in the SVD will be combined into tracks and SVD track candidates will be reconstructed with a SVD standalone tracking algorithm. These SVD tracklets will be used online and extrapolated to the 2 PXD layers to define regions of interest (ROI). Those will be useful to look for hits in the PXD and therefore significantly limit the data flow to be read out in the PXD. All the hits inside a ROI are considered as being part of the physics event while the ones outside are discarded as being background. This method will reduce the overall data volume from the PXD by at least a factor of ten, otherwise the PXD readout chips would be saturated. The procedure is particularly efficient thanks to the favorable time stamp of 2-4 ns in the SVD (depending on the strip size and the pitch).
SVD tracklets will also be extrapolated towards outside, on the CDC wall plane, to look for a corresponding CDC tracklet extrapolated outside-in on the same plane at

the same location, and then merge the CDC track candidate with the SVD track candidate, and refit the global track. If the momentum of the incident particle is too low, the track is too bent in the magnetic field and does not reach the CDC, then only the PXD and SVD are used to reconstruct the track with reduced performances. This is why, in order to improve these performances, we propose in this thesis a new estimator of low momenta, as explained in Chapter 4.

The spatial resolution of the SVD may suffer from ghost hits. These ghost hits correspond to ambiguities due to multiple hit strips on each sensor side. In a double-sided strip detector, N particles produce N! possible crossing positions. Even with a detector with strips differently oriented in each layer, solving these ambiguities can pose problems.
Furthermore the spatial resolution of the SVD deteriorates around $\theta = 90^{o}$ in the radial direction, because the probability of single strip clusters, therefore the exact position estimation, suffers from the absence of charge sharing between neighboring strips.
According to what was observed in the Belle experience, the occupancy rate has to be maintained below 10 % in order to enable the correct association of hits to tracks reconstructed in the CDC [77].

### Detector layout

The long strips are on the p-side, parallel and facing the beam pipe. The short strips are perpendicular to the long strips and are situated at the exterior of the detector. As we can observe from Fig. 2.14, sensors are overlapping from one layer to the other. The overlapping area represents a proportion of 8-10% of the sensor area, and even if this aspect increases the material budget, it is useful for the alignment procedure. This alignment is done with cosmic muons, and that is why there is an overlapping of all sensors at the 12 o'clock position.
It can also be noticed from Fig. 2.14 that the sensors are slanted in the forward region. The use of slanted sensors is a way to optimize the acceptance with a given length of sensors. In the slanted part, the sensors will have a trapezoidal shape. The trapezoidal sensors are only used for the slanted part of layers 4 to 6. For the rest of the detector, rectangular sensors are employed. There are two types of rectangular sensors, differing in pitch and number of channels, one type is for the layer 3 and the other type is used for layers 4 to 6.
Fig. 2.15 displays the two types of sensors, both made of n-type bulk with high

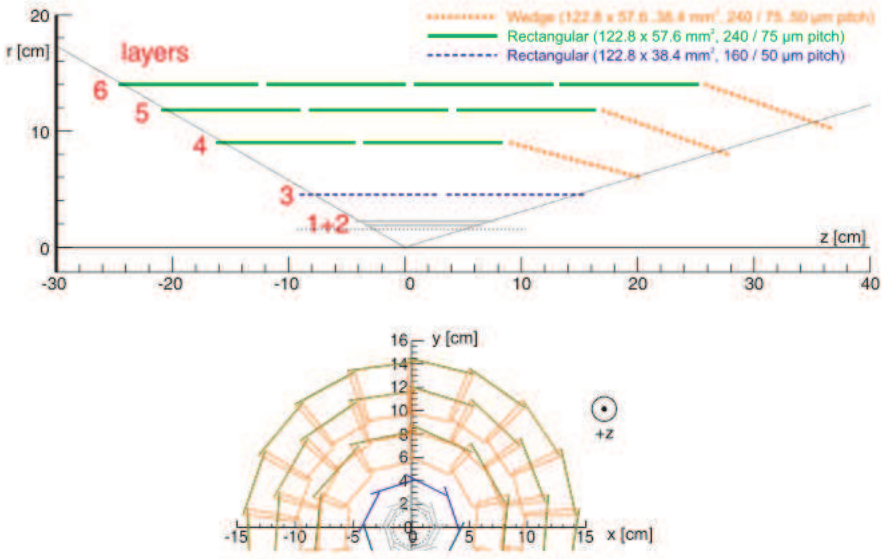


**Figure 2.14:** A cross section of the SVD detector, on the top in the Rz plane and on the bottom in the xy plane [84].

resistivity, the trapezoidal one with a thickness of 300 $\mu$m and the rectangular one with a thickness of 320 $\mu$m. In Fig 2.15 only the larger type of rectangular sensors is represented.

The Lorentz force acts on the charge carriers moving in the magnetic field. Both electrons and holes will spread in the semiconductor, but electrons will spread three times more than holes (due to a higher mobility). To reduce the electron spread, a tilt of the sensor is proposed, referred to as Lorentz tilt. This tilt will increase the hole spread. In Chapter 4, we will show that there is a resulting difference in the charge collection between the p-side and the n-side of SVD sensors.
Fig. 2.16 explains how the Lorentz tilt reduces the spread of electrons. The holes spread over the segmented p-side strips, but electrons moving towards the n-side strips induce image currents on the p-side. According to the Ramo theorem, the currents are induced by the motion of carriers, not by their collection on electrodes [85]. Since electrons and holes move in opposite directions, they induce currents of the same sign on a given electrode, despite their opposite charge [86], therefore both carriers have to be considered regardless of the p or n side readout.

For the front-end electronic readout, the APV25 chip was chosen because of its fast readout and its good resistance to radiation. All sensors made of 6 inch wafers will

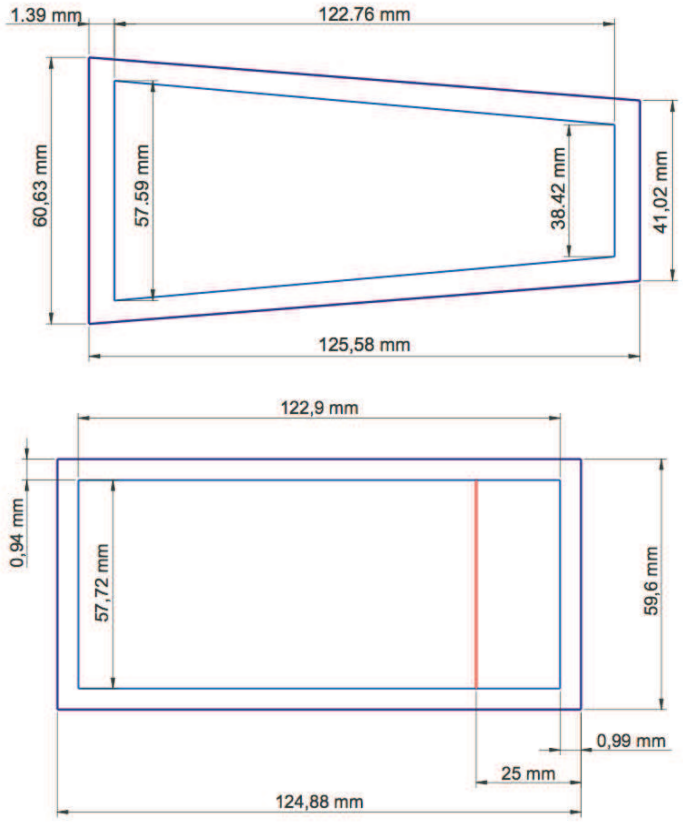


**Figure 2.15:** The two shapes of sensors equipping the SVD sensor: trapezoidal sensors in the slanted part and rectangular sensors for the rest of the detector. With light blue color is represented the active area. [77].

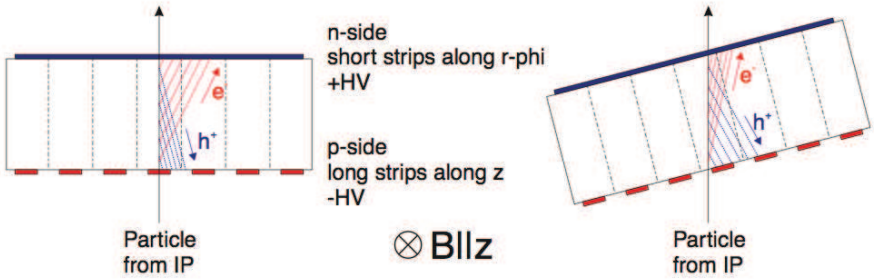


**Figure 2.16:** The effect of Lorenz tilt on electron and hole spreading [77].

be read individually by APV25 chips. In total, the Belle II SVD will consist of 172 sensors read out by 1748 APV25 chips [87]. The fast readout of 50 ns reduces the off-trigger background in Belle II and allows to keep a low occupancy, but the counterpart is a low signal-to-noise ratio (SNR). The signal is limited by the silicon thickness and the noise is determining the SNR. The only way to increase the SNR is to reduce the capacitive load at the front-end and this can only be done by approaching as close as possible the APV25 chip to the sensor strips, which leads to use the Origami chip-on-sensor concept. The Origami sensors are used for the inner sensors, while the sensors located at the edge of the acceptance are conventional hybrid sensors. The chip-on-sensor method adds material to the sensitive volume at the gain of significantly improved SNR. The APV25 chips are placed on flexible circuits and glued on top of the sensors.
The signals are transmitted by cable links of about 12 meters and in the back-end the data is digitized and processed by FADC modules which are capable of precisely measuring the hit time stamp and to discard the off-time background.

#### 2.5.2.3 Conclusions

The PXD detector features a good spatial resolution but a large integration time of 20 $\mu$s, resulting in a significant amount of background hits. It is complemented, to increase the lever arm, by the SVD detector which provides an excellent time stamp of 2-4 ns (depending on the strip size and the pitch) but a lower spatial resolution. The impact parameter resolution along the z-axis of the inner tracking system estimated with simulation studies is displayed in Fig. 2.17. The predicted impact parameter resolution reaches an asymptote of 15 $\mu$m at high momenta, which is twice better than what was measured in Belle. This is due to the lower radius of the innermost layers in Belle II and their higher granularity. At low momenta, the impact parameter resolution is also improved with respect to Belle thanks to a decreased material budget of the first tracking layers.

### 2.5.3 The CDC detector

The Central Drift Chamber detector (CDC) is the largest tracking detector in Belle II, surrounding the SVD in a barrel structure, with the inner radius starting at 160 mm and ending at 1130 mm from the beam pipe. With respect to Belle, the inner radius of the CDC is augmented. This allows to extend the SVD detector to a larger lever arm and to decrease the impact of radiation and background (which decreases with the radius). A new wire configuration is also used.

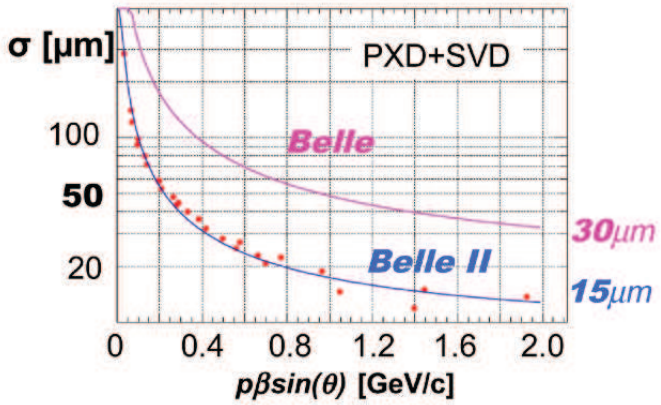


**Figure 2.17:** The impact parameter resolution along z axis of the Belle II inner tracking system, estimated from simulation and compared with the Belle measured vertex detector performances [88].

| | Belle | Belle II |
|---|---|---|
| Radius of inner cylinder (mm) | 77 | 160 |
| Radius of outer cylinder (mm) | 880 | 1130 |
| Radius of innermost sense wire (mm) | 88 | 168 |
| Radius of outermost sense wire (mm) | 863 | 1111.4 |
| Number of layers | 50 | 56 |
| Number of sense wires | 8,464 | 14336 |

**Table 2.4:** The main characteristics of the CDC detector of Belle II, compared to those of the former Belle CDC [77].

In Belle II, the global structure of the Belle CDC is kept given that it worked more than 10 years without any serious problem. The main differences between Belle II and Belle CDC are summarized in Table 2.4. In addition to the number of wires which has almost been doubled in the Belle II CDC, a new readout electronic system is installed, in order to handle higher trigger rates and to provide a lower dead time. Another modification is the z-trigger based on a 3D tracking method using axial (aligned with the solenoid magnetic field) and stereo wires (featuring alternating positive and negative angles with respect to the axial wires).
The CDC has to provide three important quantities: an estimated momentum of the reconstructed charged track, a particle identification using energy deposition in the gas volume and an efficient and reliable trigger signal.

The CDC consists of two parts, the inner chamber and the main chamber. The inner

chamber is composed of 8 layers grouped in a superlayer, featuring smaller cells and with an extent from a radius of 168 mm to 238 mm. The main chamber features 8 superlayers with 6 layers in each. The total number of layers is therefore 56 for the whole CDC.
The sensing wires are suspended in 8000 $l$ of gas mixture of 50% helium and 50% ethane. This gas was chosen because of its low Z number, in order to minimize the multiple Coulomb scattering.
The main concern related to the CDC is the tension on the end plates due to the wires. In the Belle CDC, the thirty thousands wires induced a force equivalent to 3 tons, displacing the location of the endplates by as much as 3 millimeters. The endplates of the Belle II CDC will have to endure a force equivalent to 4 tons. Tapered aluminum is therefore used for the outer region to reduce the deformation (by a factor of two compared to the Belle CDC) and conical aluminum endplates are used in the inner region to match the detector polar angle acceptance of 17-150°.
A test chamber of 30 cm long and containing 5 layers was tested at KEK using a 2 GeV electron beam. The measured overall spatial resolution was 100 $\mu$m [77] in the $R\phi$ plane. The dE/dx resolution was found to be 11.9 % for an incident angle of 90° and about 8.5 % for an incident angle of 30°.

### 2.5.4 The barrel TOP counter

The time-of-propagation (TOP) barrel detector is located between the CDC and the ECL detectors. Its role is to identify charged particles using a combination of time-of-flight and Cherenkov angle measurements.

The number of photons emitted by a single charged particle crossing the TOP detector is between 20 and 30 photons, therefore a precise time measurement of single photons is required. Particles of different velocities will produce photons with different angles. The cosine of the angle at which the Cherenkov photons are emitted is inversely proportional to the speed of the particle and the refractive index of the material. It also depends on the mass of the particle that created the track.
In order to identify the particle that crossed the TOP detector, the spatial coordinates (x,y) and the time information are combined to form a likelihood for a given particle hypothesis and the most probable particle hypothesis is associated to the track.
Fig. 2.18 shows a schematic view of a TOP counter with a kaon and a pion crossing the quartz radiator. A time reference $t_0$ is used to perform a time measurement and

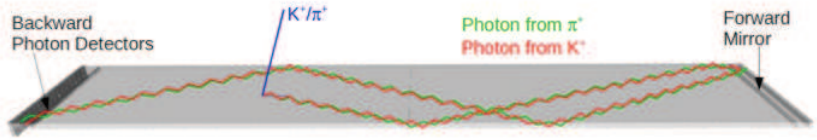


**Figure 2.18:** Schematic view of a TOP counter showing photons emitted by a charged kaon (red) and a charged pion (green). The photons are emitted at different angles therefore they will be detected at different times [89].

determine the velocity of the particle. The Cherenkov image is reconstructed from two spatial coordinates (x,y) and the time information. A photon originating from a kaon will, on average, be detected later than one originating from a pion of the same momentum.

The TOP detector consists of 16 modules composed of a quartz radiator, each module containing two quartz bars with a total length of approximately 2.5 m. There are 32 micro-channel-plate photomultiplier tubes (MCP-PMTs), each with 4×4 channels in an active area of 23×23 $mm^2$.
The intrinsic time resolution on $t_0$ is 25 ps and the time resolution of the readout system was measured to be approximately 50 ps.
The predicted efficiency of identifying a kaon or a pion is typically 95% and the fake rate probability is about 5%, depending on the momentum [90].

### 2.5.5 The end-cap ARICH detector

In the forward endcap of the Belle II detector, the Aerogel Ring Imaging CHerenkov detector (ARICH) aims at separating pions from kaons in the momentum range 1-4 GeV, and at discriminating pions, muons and electrons below 1 GeV. The detector has to endure high neutron and gamma rates and to work properly in a 1.5 T magnetic field.
The ARICH detector is made up of the following elements: an aerogel radiator where charged particles emit Cherenkov photons, an expansion volume where Cherenkov rings gain size, an array of position sensitive photon detectors, capable of detecting single photons with a good resolution, and a readout system.
The design is led by two main criteria: to detect enough photons for each ring image and to keep the emission point uncertainty small.
The number of detected photons depends on the detection efficiency, the active surface fraction of the photon detectors, the radiator thickness, the quantum efficiency

of the photon detector and the aerogel transmission. The silica aerogel Cherenkov radiator should be highly transparent not to lose photons inside the medium due to absorption or Rayleigh scattering. The optimal thickness of the silica aerogel layers was found to be 20 mm. The problem which remains is how to get enough photons without degrading the Cherenkov angle resolution due to emission point uncertainty. The solution is to stack together two layers of aerogel with the appropriate refractive index in a focusing configuration.
A reliable photon detector is the Hybrid Avalanche PhotoDetector (HAPD) which provides measurements of Cherenkov angles. It consists of 144 channels with high single photon detection efficiency. Results of beam tests with an ARICH prototype show that it is capable to separate pions from kaons over a wide range of momenta up to 4 GeV/c with more than 4 $\sigma$ [91].

### 2.5.6 The ECL detector

The Belle ECL detector is being upgraded for the new requirements of SuperKEKB. The barrel part is the same as in Belle, while endcaps will be changed with a new type of crystals (of the same sizes and shapes) and the electronics will be upgraded to be faster.
The detector is placed inside the super conducting magnetic coil and encloses both TOP and ARICH. It consists of a 3 m long barrel section with an inner radius of 1.25 m and the annular endcaps at z = -2.0 m and z = -1.0 m from the interaction point [92]. The polar angle covered by the calorimeter is varying from 12.4° to 155.1°. Two gaps of approximately 1° are situated between the barrel and endcaps. The ECL contains 8736 CsI(Tl) (caesium iodide doped with thallium) scintillating crystals: 6624 in the barrel and 2112 in the endcaps. The total weight of this detector is 43 tons.
The purpose is to ensure an efficient detection of photons with a good measurement of their position and energy, electron identification and $K_L^0$ detection, together with the KLM detector. The Belle ECL detector worked without problems for more than 10 years, and even after this period all its 736 channels are still working. However, with the new operating conditions, several effects may occur: a degradation of the CsI(Tl) crystals because of the higher radiation dose, an increased dark current in the photodiode related to the neutron flux and an increased pile-up noise resulting from soft background photons with average energy of about 1 MeV. Therefore, several improvements are made, and the Belle II ECL is expected to reach the same or even better performances than Belle's one.

For an improved immunity to the beam-background, it was decided that the CsI(Tl) crystals in the endcaps will be replaced with pure CsI crystals of the same shape and size. The CsI(Tl) crystals will still be used in the barrel. They are very bright with an average output signal of about 5000 photoelectrons per 1 MeV. The disadvantage is that they are slow, with a scintillation decay time of about 1 $\mu$s. The energy resolution for photons was measured for this kind of crystals and varies between 2.5 % at 100 MeV to 1.7 % at 5 GeV [92].
The pure CsI crystals are fast, providing a scintillation decay time of 16 ns [94]. But they are less bright, with ten times less photoelectrons per 1 MeV than the doped crystals. They require photo-detectors with internal gain in order to keep the electronic noise at the same level as the electronics of the CsI(Tl) crystals. And since the photoemission has a wavelength of about 300 nm, these photo-detectors must be UV sensitive.
The pure CsI crystals were tested, together with the new faster electronics and provided a better time resolution than CsI(Tl) crystals, and the same measured energy resolution [92, 95]. The photo-detectors will be produced by Hamamatsu, two options were proposed in [92, 93].

### 2.5.7 The KLM detector

The Belle $K_L^0$ and muon detector (KLM) contained a barrel part and two planar endcap sections. It was designed to detect $K_L^0$ mesons and muons in a polar range from 20° to 155° using resistive plate chambers (RPC). With the harder operating conditions of SuperKEKB, a significant efficiency drop is expected in the innermost layer of the barrel and in endcaps. Therefore, these parts are changed for the Belle II KLM with a new system based on scintillation strips readout by silicon photo-multipliers SiPM [96]. This technology allows to reach a time resolution at the level of 1 ns [97].

## 2.6 Belle II on-line and off-line software tools

### 2.6.1 The Belle II analysis framework

To perform simulation studies and future data analysis, an analysis framework was developed, called basf2. It is a completely new framework with respect to what was used in Belle, incorporating in its design concepts of other HEP experiments, like ILC, LHCb, CDF and ALICE [98]. The data management is implemented in ROOT

[99], the analysis framework developed at CERN.
With basf2, one is able to simulate the whole Belle II detector and the physics processes produced by SuperKEKB. The framework can be used for both online and offline data handling and for simulation, reconstruction, analysis and data acquisition.
It is based on the concept of modularity. The user writes a Python steering script where a linear chain of modules is declared. Modules are executed in the order of their declaration. They are performing simple tasks like reading data from a file, but also more complex tasks like the full detector simulation.
These modules are arranged in a container in a strict linear order, and are executed one at a time. An example of a path containing 4 modules is represented in Fig. 2.19. Each module has read and write access to the common storage of the data, the DataStore.

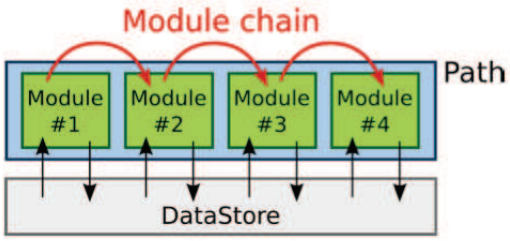


**Figure 2.19:** A chain of modules with common DataStore access (taken from [100]).

Important modules are:

- **EventInfoSetter**
  In this module the user defines the number of simulated experiments and events.

- **ParticleGun**
  This module generates one or more particles. The user decides the type of particles to be shot in the Belle II detector, their number per event, the generated momentum, their polar and azimuthal angles and their production vertices.

- **EvtGenInput**
  This module is a generator of generic $\Upsilon(4S) \to B\bar{B}$ events and $c\bar{c}$ continuum. The decay chain is set in a user decay file. The generators used are Pythia [101] and EvtGen [102].

- **Simulation**
  This module processes the information from EventInfoSetter and from the gen-

erator. It simulates all the detectors or, if the user requests otherwise, only some of the Belle II detectors, and the physics events in the detectors. All detector parameters are stored in XML files. The detector simulation is performed with Geant4, which treats the passage of particles through matter (and the energy deposition) and the digitization process. In the basf2 framework, the package SVDDigitizer (or PXDDigitizer) converts the simulated energy deposition from Geant4 into the real SVD (PXD) detector response of single strips (pixels). These packages are responsible for simulating the drift of the charge with different mobilities for electrons and holes in the electric field.

- **Reconstruction**
  The reconstruction code is the same for online and offline processing, in order to keep consistency between experimental and simulated data. This module is responsible, among others, for the hit reconstruction and tracking. Tracks reconstructed in the CDC are merged with the corresponding tracks in the inner tracking system. Final state particles and vertices are reconstructed and the information are saved in a root file for future analysis.

- **EventDisplay**
  This module enables the user to visualize an event in the Belle II detectors. It will also be used for online data monitoring [103].

- **Output**
  The output can be saved in a root file, with the format of a root tree with a branch for each collection of objects. This module provides a GUI interface for plotting and access content via root scripts.

In basf2, there is a separation between the modules and their functionalities. Each functionality is encapsulated in a shared, reusable library. A module can resort to one or more libraries, for example the tracking algorithm can be used by the tracking module but also by other modules.

Basf2 allows parallel processing. Because the raw data amount is expected to be larger than those corresponding to the sum of all LHC experiments at CERN, it will be stored at KEK. After being processed, the resulting output (mDST) will be distributed worldwide.

At the time of writing the thesis, the framework is under development and therefore still quickly evolving.

### 2.6.2 The Belle II High Level Trigger

The Belle II High Level Trigger (HLT) is designed for online data processing. Its goal is to reduce the data by a factor of 1/3 to 1/5. Since the input rate of HLT is expected to be 30 kHz with 100 kB being the size of one event, assuming that 3 GB of data will come into HLT every second, the output will be lower than 1 GB /of data per second. This system is using basf2 (and hbasf2 frameworks) with the same architecture as the one used for offline data processing.

# 3. Sensitivity of Belle II to the $\beta_c$ angle of the charm unitarity triangle

## 3.1 Introduction

To date, CP violation in charm decays has not been experimentally established [104]. It is predicted by the standard model (SM) to be very small, of the order of $10^{-4}$ (though theoretical predictions have varied in the last years, as shown later in this chapter) but can be enhanced by the presence of contributions of particles beyond the standard model. Because $D^0$ mixing is firmly measured by several experiments [49–51] and now settled with more than 11 standard deviations [52], it is interesting to search for indirect CP violation: in mixing alone or in interference between mixing and decays. This can be done with time-dependent analyses: either with two-body decays, as for example with the singly Cabibbo suppressed decays (SCS) $D^0 \to K^+K^-$ and $D^0 \to \pi^+\pi^-$ or with three-body decays, with time-dependent Dalitz plot analyses, as $D^0 \to K^0_s\pi^+\pi^-$ and $D^0 \to K^0_s K^+K^-$. In this work we are interested only in the SCS two-body decays.

This chapter is devoted to a prospective study estimating the ability of Belle II to measure the CP asymmetry in $D^0$ decays as a function of time, and to extract the $\beta_c$ angle of the c-u unitarity triangle from this measurement. A similar study was already performed [105], focusing mainly on $D^0$ produced in SuperB with a collision energy at $\Psi(3770)$ center-of-mass.

After this introduction, we present in Section 3.2 the last measurements of CP violation in $D^0$ decays performed by LHCb, CDF, BaBar and Belle. In Section 3.3, we investigate how the $\beta_c$ angle can be extracted from the measurement of CP asymmetry as a function of time in the two decay channels $D^0 \to K^+K^-$ and $D^0 \to \pi^+\pi^-$. In Section 3.4, the ingredients of the measurement of the time-

dependent CP asymmetry studied here are introduced.
We explain how to simulate and reconstruct the asymmetry in Section 3.5. The impact of the ingredients affecting the measurement is studied in Section 3.6 and the expected Belle II sensitivity to $\beta_c$ is given. And finally, the conclusion is given in Section 3.7.

## 3.2 Experimental results on CP violation in $D^0 \to h^+h^-$ decays

Searches for CP violation in $D^0 \to K^+K^-$ and $D^0 \to \pi^+\pi^-$ decays were already pursued in $pp$ collisions by LHCb, in $p\bar{p}$ collisions by CDF and in $e^+e^-$ collisions at BaBar and Belle.
Two types of measurements were performed: time-integrated, mainly sensitive to direct CP violation and time-dependent, sensitive to indirect CP violation. The direct CP violation can be caused by different magnitudes in $D^0$ and $\bar{D}^0$ decay rates or by a different phase of these two amplitudes. The indirect CP violation is generated by the asymmetry in mixing rates, or by the weak phase.
The direct CP violation in the SCS double body decays will be expressed as the difference $\Delta A_{CP}$ between the time-integrated asymmetries of $D^0 \to K^+K^-$ and $D^0 \to \pi^+\pi^-$ decay rates (with the notation $A_{CP}(h^+h^-)$).
The indirect CP violation will be refered to in two different ways: through the asymmetry $A_\Gamma$ between $D^0$ and $\bar{D}^0$ effective lifetimes or, by the deviation of $y_{CP}$ from the value of the mixing parameter $y$.
It was pointed out in [106, 107] that the direct CP violation contribution to $A_\Gamma$ may not be negligible. Therefore, it is important to perform both time-integrated and time-dependent measurements in order to disentangle direct and indirect CP violation contributions.

### 3.2.1 Time-integrated CP asymmetry measurements

In 2011, LHCb reported an unexpected high difference in time-integrated CP asymmetries measured with $D^0 \to K^+K^-$ and $D^0 \to \pi^+\pi^-$ decays, with 0.62 fb$^{-1}$ of data [108]. The $D^0$ meson flavour was identified by the charge of the slow pion in the $D^{*+} \to D^0\pi^+_{slow}$ and $D^{*-} \to \bar{D}^0\pi^-_{slow}$ decay channels (with prompt $D^{*\pm}$ production, meaning $D^{*\pm}$ produced at the primary vertex, i.e. not coming from B meson decays). At that time, the measured value of $\Delta A_{CP}$ showed a 3.5 standard deviations

discrepancy with the CP conservation hypothesis. Whether this measurement was due to a manifestation of new physics or not remains an open question. Various theoretical articles predicted different values of $\Delta A_{CP}$ in the SM: below $\mathcal{O}(10^{-3})$ in [109, 110], with an observation of a CP asymmetry of the order of $\mathcal{O}(10^{-2})$ being considered a sign of new physics (NP) in [110], or even SM expectations up to $\mathcal{O}(10^{-2})$ in [111].
However, further results of LHCb on time-integrated CP asymmetry in $D^0$ decays, with an increased data set did not confirm this large CP asymmetry. The latest measurement is based on 3 fb$^{-1}$ of integrated luminosity and on another flavour tagging method. In this analysis, $D^0$ mesons are produced through semileptonic b-meson decays such as $B^- \to D^0\mu^-\bar{\nu}_\mu X$ and $\bar{B}^0 \to D^0\mu^-\bar{\nu}_\mu X$, where the charge of the muon delivered in association with the $D^0$ meson is used to know the $D^0$ flavour. The result is now compatible with zero [104]:

$$\Delta A_{CP} = A_{CP}(K^+K^-) - A_{CP}(\pi^+\pi^-) \quad = (+0.14 \pm 0.16(stat) \pm 0.08(syst))\ \% \tag{3.1}$$

In 2012, the CDF collaboration also reported a measurement of time-integrated CP asymmetry based on their full 9.7 $fb^{-1}$ dataset registered at Tevatron. Their result shows a 2.7$\sigma$ excess with respect to the CP conservation hypothesis [112]:

$$\Delta A_{CP} = (-0.62 \pm 0.21(stat) \pm 0.10(syst))\ \% \tag{3.2}$$

And finally, the result released by the Belle collaboration, also based on their full 976 fb$^{-1}$ dataset, corresponds to [113, 114]:

$$\Delta A_{CP} = (-0.87 \pm 0.41(stat) \pm 0.06(syst))\ \% \tag{3.3}$$

These results are all largely statistically limited, although based on all the data available. To drive to a conclusion, this measurement needs to be re-investigated with increased statistics at future experiments. This will be possible with Belle II and LHCb Run 3, which will start taking data in the end of 2018 and in 2021 respectively.

### 3.2.2 Time-dependent CP asymmetry measurements

Time-dependent CP asymmetry measurements, sensitive to indirect CP violation, can be measured from the asymmetry $A_\Gamma$ between the effective $D^0$ and $\bar{D}^0$ lifetimes [115]:

$$A_\Gamma = \frac{\tau^{eff}(\bar{D}^0) - \tau^{eff}(D^0)}{\tau^{eff}(\bar{D}^0) + \tau^{eff}(D^0)} \tag{3.4}$$

The latest measurements from LHCb are [116]:

$$\begin{aligned} A_\Gamma(K^+K^-) &= (-0.134 \pm 0.077^{+0.026}_{-0.034})\ \% \\ A_\Gamma(\pi^+\pi^-) &= (-0.092 \pm 0.145^{+0.025}_{-0.033})\ \% \end{aligned} \tag{3.5}$$

where the first uncertainty is statistical and the second is systematic. This result is compatible with CP conservation, but is also largely statistically limited.
CDF measured indirect CP-violating asymmetries in 2014 based on their full data set (9.7 fb$^{-1}$) integrated luminosity [10]:

$$\begin{aligned} A_\Gamma(K^-K^+) &= (-0.19 \pm 0.15 \pm 0.04)\ \% \\ A_\Gamma(\pi^+\pi^-) &= (-0.01 \pm 0.18 \pm 0.03)\ \% \end{aligned} \tag{3.6}$$

BaBar measured the amplitude of indirect CP violation in $D^0$ decays with their full dataset of 468 fb$^{-1}$ in 2013. Lifetimes of CP-even SCS $D^0 \to K^+K^-$ and $D^0 \to \pi^+\pi^-$ modes were compared with the ones of CP-mixed doubly Cabibbo suppressed (DCS) $D^0 \to K^+\pi^-$ and Cabibbo favoured (CF) $D^0 \to K^-\pi^+$ decays in order to measure $y_{CP}$. Their result is [117]:

$$y_{CP} = (0.72 \pm 0.18(stat) \pm 0.12(syst))\ \% \tag{3.7}$$

The result is consistent with the world average value of the mixing parameter $y$ obtained from time-dependent Dalitz plot analyses of $D^0 \to K^0_s\pi^+\pi^-$ and $D^0 \to K^0_sK^+K^-$ [52]. Therefore, a possible CP violation in $D^0$ decays is excluded in this measurement.

Finally, Belle presented a measurement in 2012 with their full data set of $\sim$1 ab$^{-1}$.

The reconstructed number of neutral D mesons is [118]:

$$\begin{aligned} 242 \times 10^3 \ D^0 \to K^+K^- \\ 114 \times 10^3 \ D^0 \to \pi^+\pi^- \end{aligned} \tag{3.8}$$

Leading to the result:

$$A_\Gamma \quad = (-0.03 \pm 0.2 \pm 0.08)\% \tag{3.9}$$

These numbers of reconstructed neutral D mesons in Belle (relation 3.8) will be used in this study to estimate the number of $D^0$ mesons that will be reconstructed in Belle II with 50 $ab^{-1}$ of integrated luminosity.
The world average of all the measurements of the asymmetry $A_\Gamma$ due to different decay amplitudes is displayed in Fig. 3.1.

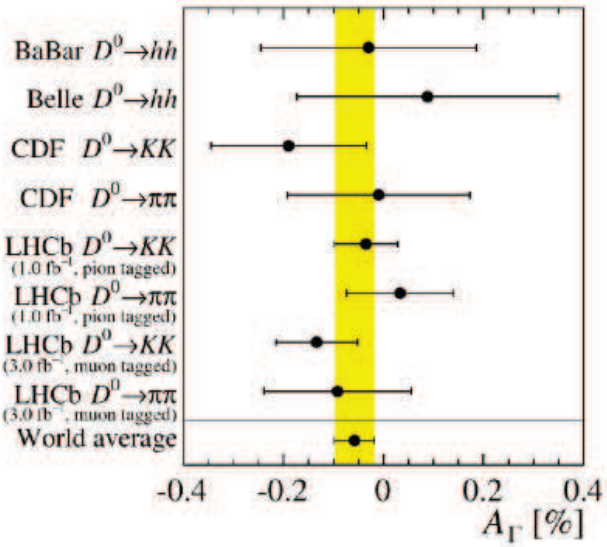


**Figure 3.1:** Results from Belle, BaBar, CDF and LHCb on time-dependent CP asymmetries in $D^0$ decays, yielding an average asymmetry $A_\Gamma = (-0.58 \pm 0.04)\%$. From [115].

As a conclusion of all these time-dependent measurements of CP asymmetries in $D^0$ decays, the world average is compatible with the SM expectations at the $1\sigma$ level. But all the measurements are limited statistically and the average is largely driven by LHCb results. Therefore, only future measurements at Belle II and LHCb Run 3 may help concluding.

## 3.3 Principle of the $\beta_c$ measurement

In this section, the extraction of the $\beta_c$ angle of the $c-u$ unitarity triangle from the measurement of the time-dependent asymmetries in $D^0 \to h^+h^-$ decays is explained.

The time-dependent CP asymmetry in $D^0$ decay rates is defined by the normalized decay rate difference between mesons and anti-mesons:

$$A_{CP}(t) = \frac{\bar{\Gamma}(t) - \Gamma(t)}{\bar{\Gamma}(t) + \Gamma(t)} \tag{3.10}$$

The $D^0$ and $\bar{D^0}$ decay widths $\Gamma$(t) and $\bar{\Gamma}$(t) are defined by:

$$\begin{aligned}
\Gamma(t)(D^0 \to f) &= e^{-t/\tau}\ [\ \cosh(\frac{\Delta\Gamma t}{2})\ -\ \frac{2Re(\lambda_f)}{1+|\lambda_f|^2}\sinh\ (\frac{\Delta\Gamma t}{2}) \\
&\quad + \frac{1-|\lambda_f|^2}{1+|\lambda_f|^2}cos(\Delta M t) - \frac{Im(\lambda_f)}{1+|\lambda_f|^2}sin(\Delta M t)\ ] \\
\bar{\Gamma}(t)(\overline{D}^0 \to f) &= e^{-t/\tau}\ [\cosh\ (\frac{\Delta\Gamma t}{2})\ -\ \frac{2Re(\lambda_f)}{1+|\lambda_f|^2}\sinh\ (\frac{\Delta\Gamma t}{2}) \\
&\quad - \frac{1-|\lambda_f|^2}{1+|\lambda_f|^2}cos(\Delta M t) + \frac{Im(\lambda_f)}{1+|\lambda_f|^2}sin(\Delta M t)\ ]
\end{aligned} \tag{3.11}$$

for an uncorrelated $D^0$ production (this point will be explained in Section 3.4.2) and assuming there is no production asymmetry between $D^0$ and $\bar{D^0}$ . These two decay widths depend on the mass difference $\Delta M$, the width difference $\Delta\Gamma$ and on the complex parameter $\lambda_f$ defined in Eq. 1.63.

In order to violate CP, several amplitudes contributing to a given process are needed, one is a tree dominant amplitude and one can be a sub-leading contribution from SM amplitudes suppressed by their CKM elements, or even from new physics. Therefore, the amplitude can be split in a leading and a sub-leading part, with a relative magnitude $r_f$. For two-body decays to CP eigenstates, the amplitudes can be written as [107]:

$$\begin{aligned}
A_f &= A_f^T e^{+i\phi_f^T}(1 + r_f e^{i(\delta_f+\phi_f)}) \\
\bar{A}_{\bar{f}} &= \eta_{CP} A_f^T e^{-i\phi_f^T}(1 + r_f e^{i(\delta_f-\phi_f)})
\end{aligned} \tag{3.12}$$

where $A_f^T$ stands for the leading tree amplitude, $\phi$ is the weak phase which can violate CP and $\delta$ the strong CP conserving phase. For $D^0 \to h^+h^-$, besides the tree-level (T) dominated decays, different other topologies can also participate, like colour suppressed (CS), weak exchange ($W_{ex}$) and penguin ($P_q$). These contributions are not necessarily related to one angle of the $c-u$ unitarity triangle. All these contributions can be summed as [43]:

$$A = |T|e^{i(\phi_T+\delta_T)} + |CS|e^{i(\phi_{CS}+\delta_{CS})} + |W_{ex}|e^{i(\phi_{W_{ex}}+\delta_{W_{ex}})} + \sum_{q=d,s,b} |P_q|e^{i(\phi_{P_q}+\delta_{P_q})} \quad (3.13)$$

The different Feynman diagrams implied in $D^0 \to \pi^+\pi^-$ and $D^0 \to K^+K^-$ decay amplitudes are shown in Fig. 3.2 and Fig. 3.3.

The $\beta_c$ angle can be obtained from the measurement of the phase of the complex parameter $\arg(\lambda_f)$ from Eq. 5.3, which is for the $\pi\pi$ and $KK$ decay modes:

$$\begin{array}{lll} \arg(\lambda_f)_{\pi\pi} = & \phi_{mix} \text{ - } 2\beta_{c,eff} & \text{if measured with } D^0 \to \pi^+\pi^- \text{ decays} \\ \arg(\lambda_f)_{KK} = & \phi_{mix} & \text{if measured with } D^0 \to K^+K^- \text{ decays} \end{array} \quad (3.14)$$

Since the mixing phase is the same in both modes, we obtain :

$$\beta_{c,eff} = \frac{1}{2}\sqrt{(arg(\lambda_f)^2_{\pi\pi} + arg(\lambda_f)_{KK})^2} \quad (3.15)$$

In Eq. 5.6, $\beta_{c,eff}$ appears instead of $\beta_c$ to account for higher order contributions discussed with Eq. 3.13. The effective $\beta_{c,eff}$ includes theoretical uncertainties induced by the amplitudes contributing to the $h^+h^-$ final state with a different weak phase [120]. The two values of $\arg(\lambda_f)$ as measured in the $D^0 \to \pi^+\pi^-$ and $D^0 \to K^+K^-$ decay channels, enable to eliminate the $\phi_{mix}$ phase, which is currently only poorly determined. In this way, the study of the time-dependent asymmetry tests the $c-u$ unitarity triangle and the CKM mechanism as the origin of CP violation.

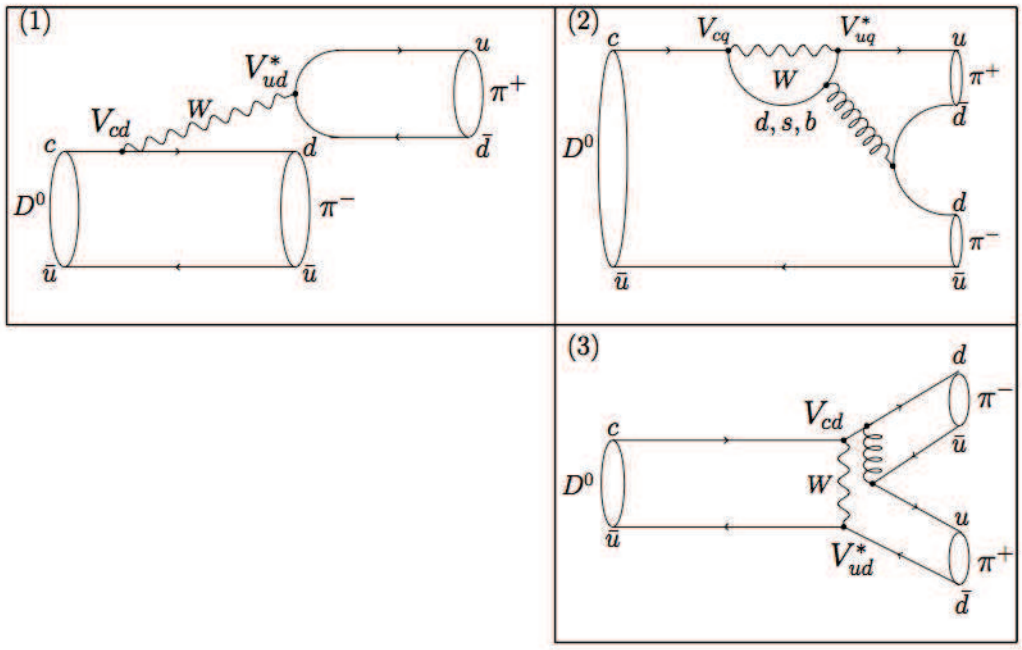


**Figure 3.2:** Two body hadronic $D^0$ decays to $\pi^+\pi^-$: (1) tree, (2) penguin and (3) W exchange topologies, together with the CKM matrix elements involved in the transitions.

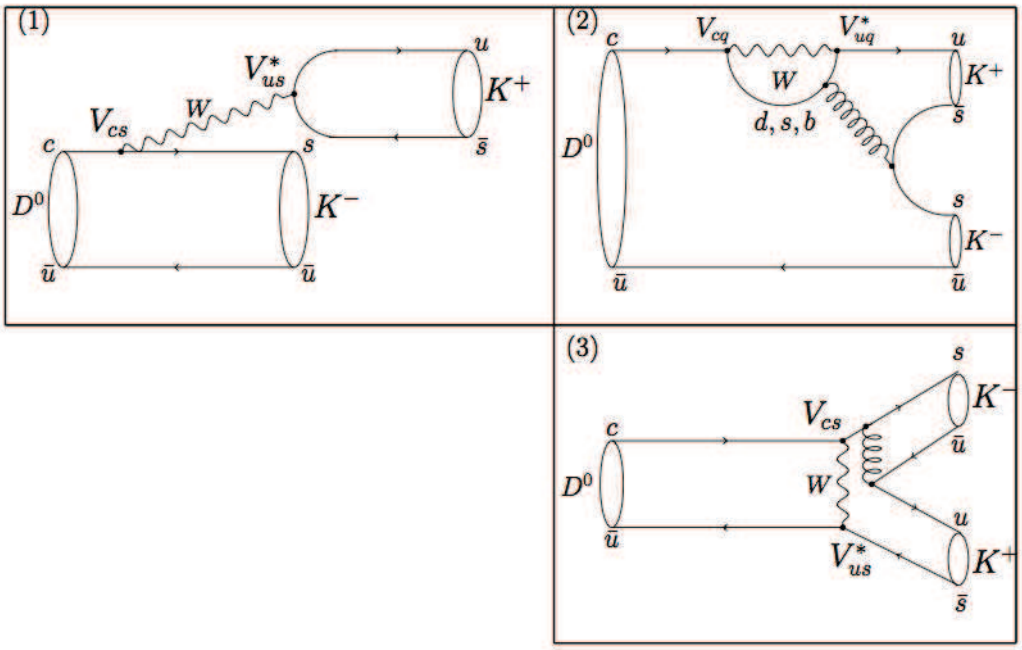


**Figure 3.3:** Two body hadronic $D^0$ decays to $K^+K^-$: (1) tree, (2) penguin and (3) W exchange topologies, together with the CKM matrix elements involved in the transitions.

## 3.4 Ingredients of the time-dependent CP asymmetry measurement

### 3.4.1 Analysis overview

To measure the difference between the number of $D^0$ and the number of $\bar{D}^0$ decaying to a CP eigenstate final state as a function of time, the following quantities have to be detemined:

- A $D^0$ candidate has to be reconstructed in the considered CP eigenstate decay mode, $D^0 \to K^+K^-$ or $D^0 \to \pi^+\pi^-$. This is discussed in Section 3.4.2.
- The flavour of the reconstructed $D^0$ needs to be known. This is called the flavour tagging and is presented in Section 3.4.3.
- Finally, the flight time of the reconstructed $D^0$ has to be measured. Experimentally, only a flight distance can actually be measured in the detector. The way to measure this flight distance and how it can be translated to a flight time is explained in Section 3.4.4.

Once all these quantities are known, we are able to reconstruct the CP asymmetry as a function of time. From that, $arg(\lambda_f)$ can be measured by fitting the function 5.1 with $arg(\lambda_f)$ as a free parameter in the fit, to investigate indirect CP violation in the interference between mixing and decay. The module $|\lambda_f|$ is fixed to 1 in order to neglect direct CP violation.

### 3.4.2 Reconstruction of $D^0$ candidates

$D^0$ mesons are produced through various processes in $e^+e^-$ collisions. At the $\Upsilon(4S)$ center-of-mass energy, they can originate from $B^\pm$ or $B^0$ mesons decays. Considering this case, as far as our analysis is concerned, we would need to reconstruct with very good accuracy the $B$ meson decay vertex (which is also the $D^0$ production vertex) separately from the $D^0$ decay vertex. The $D^0$ meson flavour has to be determined. That can be done for instance by reconstructing $\bar{B}^0 \to D^{*+}\ell^-\nu$ decays, followed by $D^{*+} \to D^0\pi_{soft}$ decays, the $D^0$ flavour being given by the $\pi_{soft}$ charge. In that case, the statistics are reduced by the $B^0\bar{B}^0$ event selection and the signal full decay chain reconstruction.
A second process can be mentioned, occurring at $e^+e^-$ collisions at the $\Psi(3770)$ center-of-mass energy. This scenario was considered by the SuperB project and

studied in [43]. The $\Psi(3770)$ decays to $D^0\bar{D}^0$ in more than 50 % of the cases, producing 2 quantum correlated $D^0$ mesons. It means that the oscillation of one meson leads to the oscillation of the second meson at the same time. This is a very powerful tool to tag the meson's flavour, and is equivalent to the method used to measure $\sin 2\beta$ with quantum correlated $B^0 - \bar{B}^0$ produced by the $\Upsilon(4S)$ decay. The time information (needed to do a time-dependent analysis) is extracted from the flight distance between the 2 meson's decay vertices rather than between one meson's production vertex and its decay vertex. It can easily be shown that it is equivalent.

In this analysis, we choose as working hypothesis the production process through $e^+e^- \to c\bar{c}$ hadronization, producing $D^{*\pm}$ mesons decaying to $D^0\pi_{soft}$. A graphical example is found in Fig. 3.4. The production cross section of $e^+e^- \to c\bar{c}$ is roughly the same as $e^+e^- \to b\bar{b}$, around 1 nb. Details on the decay flight time reconstruction and the expected statistics in that case are given in [113].

In our study, we did not particularly investigate the $D^0$ reconstruction. $D^0$ mesons have been extensively reconstructed in $e^+e^-$, $p\bar{p}$ and $pp$ collisions for several decades. For instance, to measure $D^0$ - $\bar{D}^0$ oscillation in Belle, their reconstruction relies on the following selection criteria [118]:

- Two $D^0$ daughter candidates with opposite charges are identified with standard particle identification criteria [121] and refitted to a common vertex which is the decay vertex of the $D^0$ candidate.

- Reconstructed $D^0$ candidates are selected using two kinematic variables: the invariant mass of the $D^0$ decay products ($1.81\ \mathrm{GeV/c^2} < M_{D^0} < 1.91\ \mathrm{GeV/c^2}$), as displayed in Fig. 3.5 and the energy Q released in the $D^{*\pm}$ decay ($\mathrm{Q} = (M_{D^*} - M_{D^0} - M_\pi)c^2 < 20$ MeV), as displayed in Fig. 3.6. This cut is very efficient thanks to the limited phase space in the $D^{*\pm} \to D^0\pi^\pm$ decay.

- The $D^0$ production vertex is obtained from the fit of the $\pi_{soft}$ track and the reconstructed $D^0$ flight direction to a common point.

- The $D^{*\pm}$ momentum measured in the center-of-mass system of $e^+e^-$ collisions is required to be greater than a certain threshold to reject $D^*$ from B decays. For Belle measurements this threshold is usually 2.5 GeV/c, and only in case of data taken at $\Upsilon(5S)$, the threshold was increased at 3.1 GeV/c.

We have to estimate the expected statistics of reconstructed $D^0 \to K^+K^-$ and $D^0 \to \pi^+\pi^-$ from prompt production in the Belle II experiment with the full

dataset. This estimation is based on Belle measured performances. We scale the number of reconstructed $D^0$ candidates used to perform $D^0$ -$\bar{D}^0$ mixing and time-dependent CP asymmetry measurements in Belle with 1 $ab^{-1}$ to 50 $ab^{-1}$ and obtain [49, 118]:

$$\begin{array}{ccc} 5 \times 10^6 & \text{tagged} & D^0 \to \pi^+\pi^- \\ 1.2 \times 10^7 & \text{tagged} & D^0 \to K^+K^- \end{array} \tag{3.16}$$

This difference in the number of $D^0 \to K^+K^-$ and $D^0 \to \pi^+\pi^-$ comes from the CKM matrix elements implied in each decay channel. Tagged means here that the flavour of these mesons is known.

### 3.4.3 Flavour tagging

The goal of flavour tagging is to unambiguously identify the flavour of the meson, i.e. whether it is a meson or an anti-meson. This is important in order to measure the asymmetry 5.1. Flavour tagging can be performed thanks to various methods featuring different purities and efficiencies. For instance, in a reconstructed jet (in case of hadronization at Tevatron or LHC), the charge of the $K^{\pm}$ accompanying the $B_s^0$ production during the b-quark hadronization indicates the flavour of the produced $B^0$s. The charge of a lepton originating from the B semileptonic decay indicates the flavour of the meson at decay time.

In our study, we identify the flavour of the $D^0$ meson at production time using the charge of the soft pion produced together with the $D^0$ meson from $D^{*+}$ decay, as displayed in Fig. 3.7. A positive pion is associated with a $D^0$ and a negative pion with a $\bar{D}^0$ .
Experimentally, the guess of the flavour may be incorrect. The possible mis-identification of the flavour has to be taken into account in the measurement of the CP asymmetry. This is done by translating the theoretical decay rates of Eq. 5.2 to experimental decay rates as following:

$$\begin{array}{ll} \Gamma_{phys}(t) & = (1-\omega)\Gamma(t) + \bar{\omega}\bar{\Gamma}(t) \\ \bar{\Gamma}_{phys}(t) & = (1-\bar{\omega})\bar{\Gamma}_{phys}(t) + \omega(\Gamma(t)) \end{array} \tag{3.17}$$

where $\omega$ (respectively $\bar{\omega}$) stands for the mis-identification probability of a $D^0$ (respectively $\bar{D}^0$) as a $\bar{D}^0$ (respectively $D^0$).

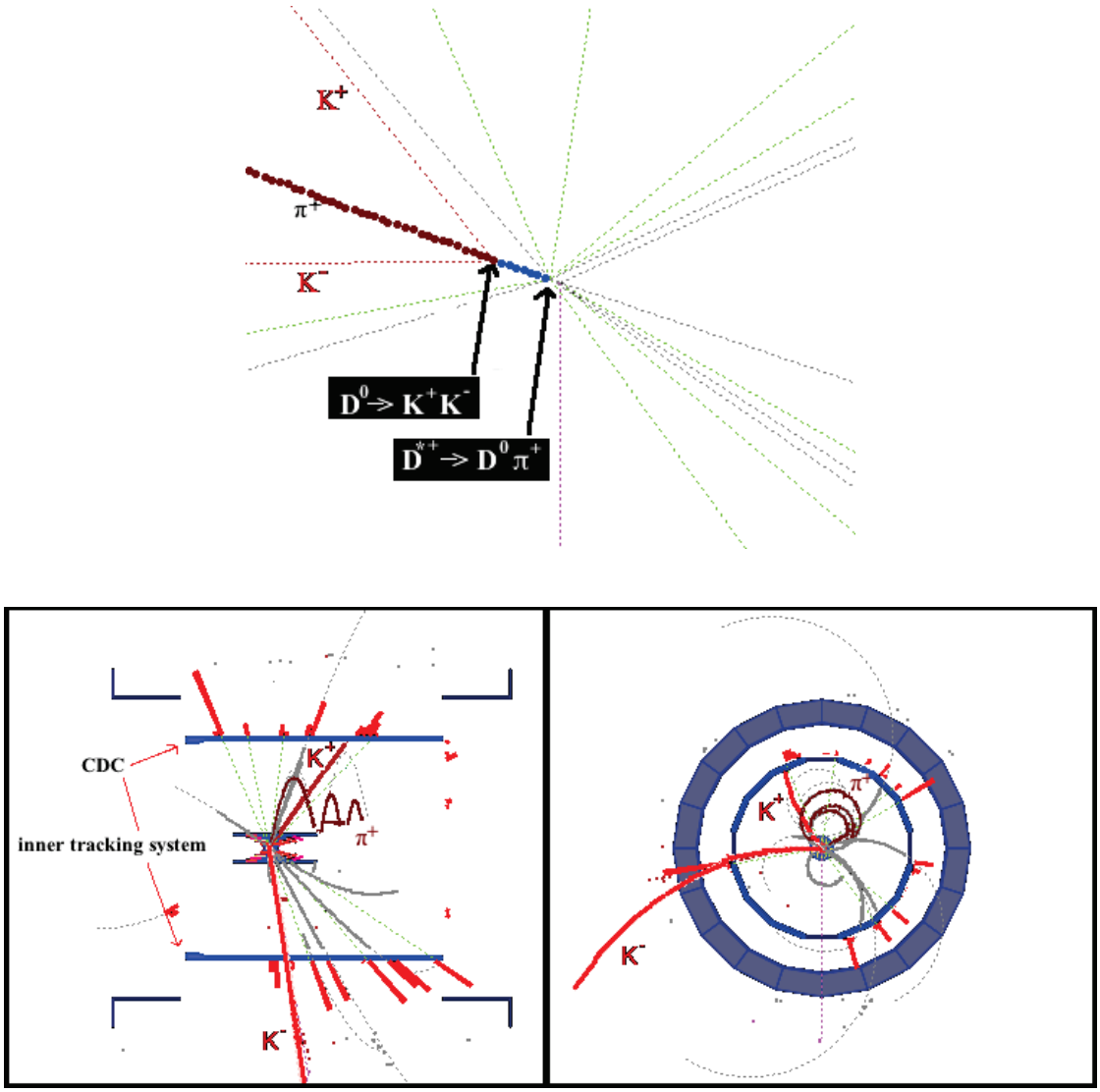


**Figure 3.4:** Event display view of a $D^{*\pm}$ originating from the hadronization of $c\bar{c}$ continuum events, decaying to $D^{*\pm} \to D^0\pi^+$ followed by $D^0 \to K^+K^-$. The charged pion is represented in brown, neutral particles but photons in violet, photons in green and charged kaons in red. The upper picture displays the extrapolated tracks inside the vacuum chamber, where the blue dotted line represents the $D^0$ flight distance. The bottom pictures show the soft pion curled track in the CDC, and tracks of the $K^+$ and $K^-$ decay products of the $D^0$ meson. This event was simulated in the Belle II detector with the basf2 framework.

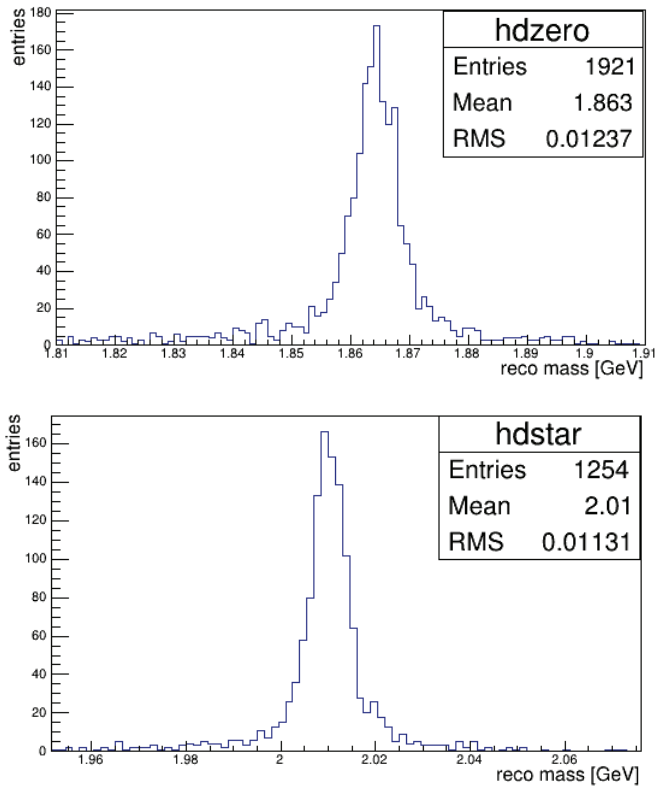


**Figure 3.5:** Distribution of the reconstructed mass of $D^0$ mesons (upper image) and $D^{*+}$ (lower image).

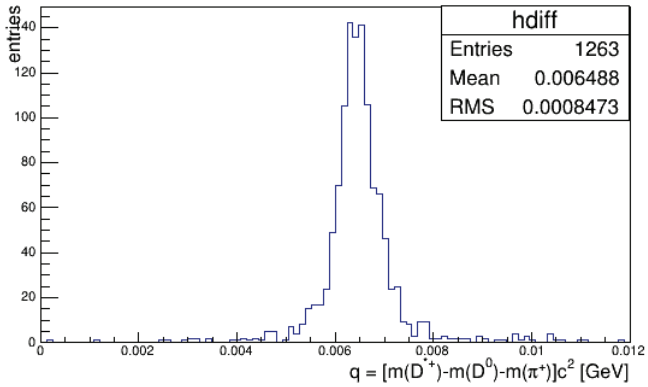


**Figure 3.6:** Distribution of the energy released in the $D^{*\pm}$ decay, as Q = $(M_{D^*} - M_{D^0} - M_\pi)c^2$.

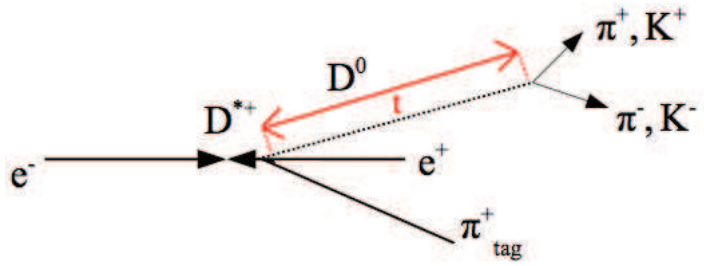


**Figure 3.7:** Sketch of the $D^{*\pm}$ production from $c\bar{c}$ continuum (prompt production). The $D^{*\pm}$ can decay to a $D^0$ and a slow pion. The flavour identification relies on the charge of the soft pion: a positive slow pion corresponds to a $D^0$ , while a negative pion to a $\bar{D}^0$.

Considering that mistag probabilities are the same to $D^0$ and $\bar{D^0}$ , we can define the dilution factor $D = 1 - 2\omega$, which impacts the asymmetry as following:

$$A_{CP}^{phys}(t) = 2D\,\frac{\bar{\Gamma}(t) - \Gamma(t)}{\bar{\Gamma}(t) + \Gamma(t)} \tag{3.18}$$

Or, by inserting Eq. 5.2 in Eq. 3.18, we can write the asymmetry as:

$$A_{CP}^{phys}(t) = 2D \cdot \frac{\dfrac{Im(\lambda_f)}{1+|\lambda_f|^2} sin(\Delta M t) - \dfrac{1-|\lambda_f|^2}{1+|\lambda_f|^2} cos(\Delta M t)}{cosh(\dfrac{\Delta\Gamma t}{2}) + \dfrac{-2Re(\lambda_f)}{1+|\lambda_f|^2} sinh(\dfrac{\Delta\Gamma t}{2})} \tag{3.19}$$

In our study we will take this dilution factor into account and analyze the impact of the flavour mis-identification on the reconstruction of the asymmetry.

These mistag probabilities can be estimated with a good accuracy using $D^0 \to K^-\pi^+$ decays. The dominant contribution to this process is the CF process, in which the charges of the $K$ and $\pi$ indicate the flavour of the $D^0$ meson. In addition to this, there is a very small contribution from processes involving an oscillation $D^0$ -$\bar{D}^0$ followed by the DCS decay $D^0 \to K^+\pi^-$, with opposite $K$ and $\pi$ charges with respect to the CF process. Assuming the same reconstruction performances as in the previous Belle experiment [118], we can expect the signal purities to be of the order of 98 % for $D^0 \to K^+K^-$ and 93 % for $D^0 \to \pi^+\pi^-$. In this thesis, the impact of flavour mis-identification is studied up to the value of 10 %.

### 3.4.4 $D^0$ flight time estimation

In the function used to fit the reconstructed CP asymmetry 5.1, the variable $t$ stands for the proper flight time elapsed between the $D^0$ production and its decay, as expressed in the $D^0$ rest frame. Actually, what is accessible experimentally is the flight distance expressed in the laboratory frame. The translation of the observed flight distance to the proper flight time depends on the $D^0$ momentum, and is obtained from the simulation. It is displayed with Fig. 3.8.

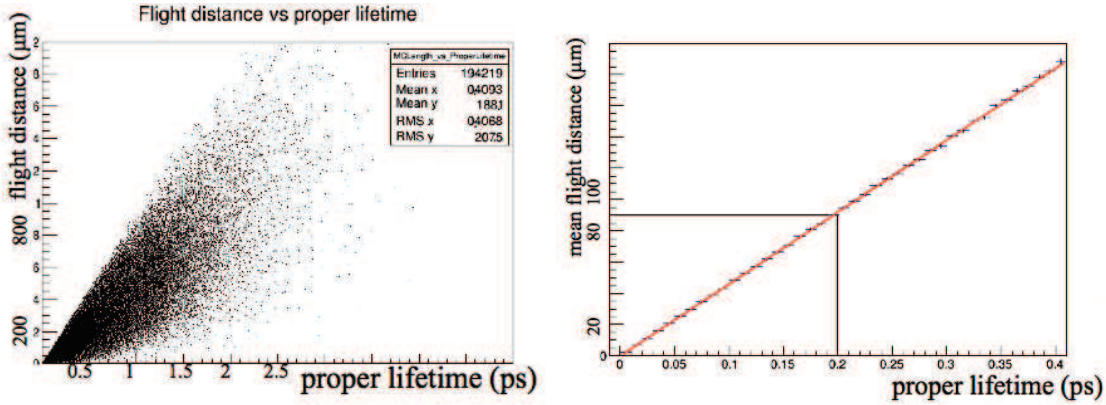


**Figure 3.8:** Distribution of the flight distance of $D^0$ mesons in the laboratory frame displayed as a function of the flight time in the $D^0$ rest frame (left) and mean values of this distribution (right).

To build this distribution, $e^+e^- \to c\bar{c}$ events producing at least one $D^{*+} \to D^0\pi^+$ (and c.c.) were simulated with the basf2 framework. The $D^0$ flight distance is computed between its generated decay point and production point. We observe that the 0.4 ps mean lifetime of the $D^0$ mesons corresponds to an observed flight distance of 188 $\mu$m in the detector.

To have a first idea on the spatial resolution expected in Belle II on the $D^0$ reconstructed flight distance, we simulated $e^+e^- \to c\bar{c}$ events with basf2. In these events, we reconstructed (after track finding and fitting) $D^0$ candidates selected according to criteria presented in Section 3.4.2. The estimated spatial resolution used in our study was obtained by comparing the reconstructed flight distances of $D^0$ mesons with their generated ones, as displayed in Fig. 3.9. We observe a spatial resolution of about 45 $\mu$m, which is translated into a time uncertainty $\sigma_t$ of about 0.1 ps. This time resolution is better than in Belle, where it was on average equal to half of the $D^0$ lifetime [119].

Fig. 3.10 shows the contributions to these 45 $\mu$m separately from the resolution on the reconstructed decay and production $D^0$ vertices. The observed resolutions are equivalent in the 3 dimensions x, y, z, thanks to the innermost tracking layer, which is equipped with square 50 $\times$ 50 $\mu$m$^2$ pixels. These decay and production vertices resolutions are correlated since the $D^0$ reconstructed from two daughter tracks candidates is used together with an additional $\pi$ candidate to determine the production vertex. They are of the order of 25-30 $\mu$m.

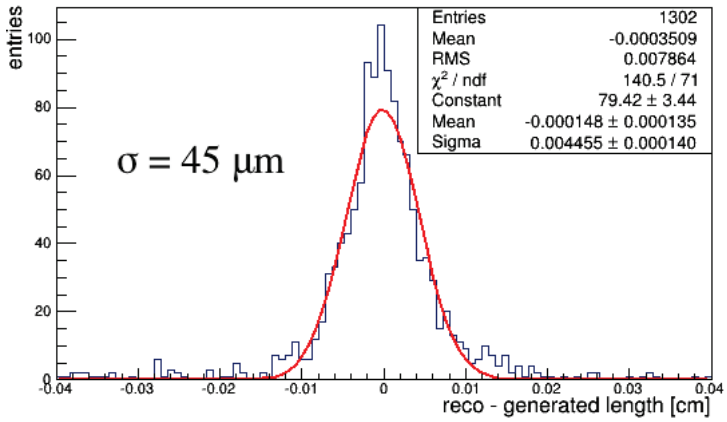


**Figure 3.9:** The Belle II expected resolution on the reconstructed $D^0$ flight distance.

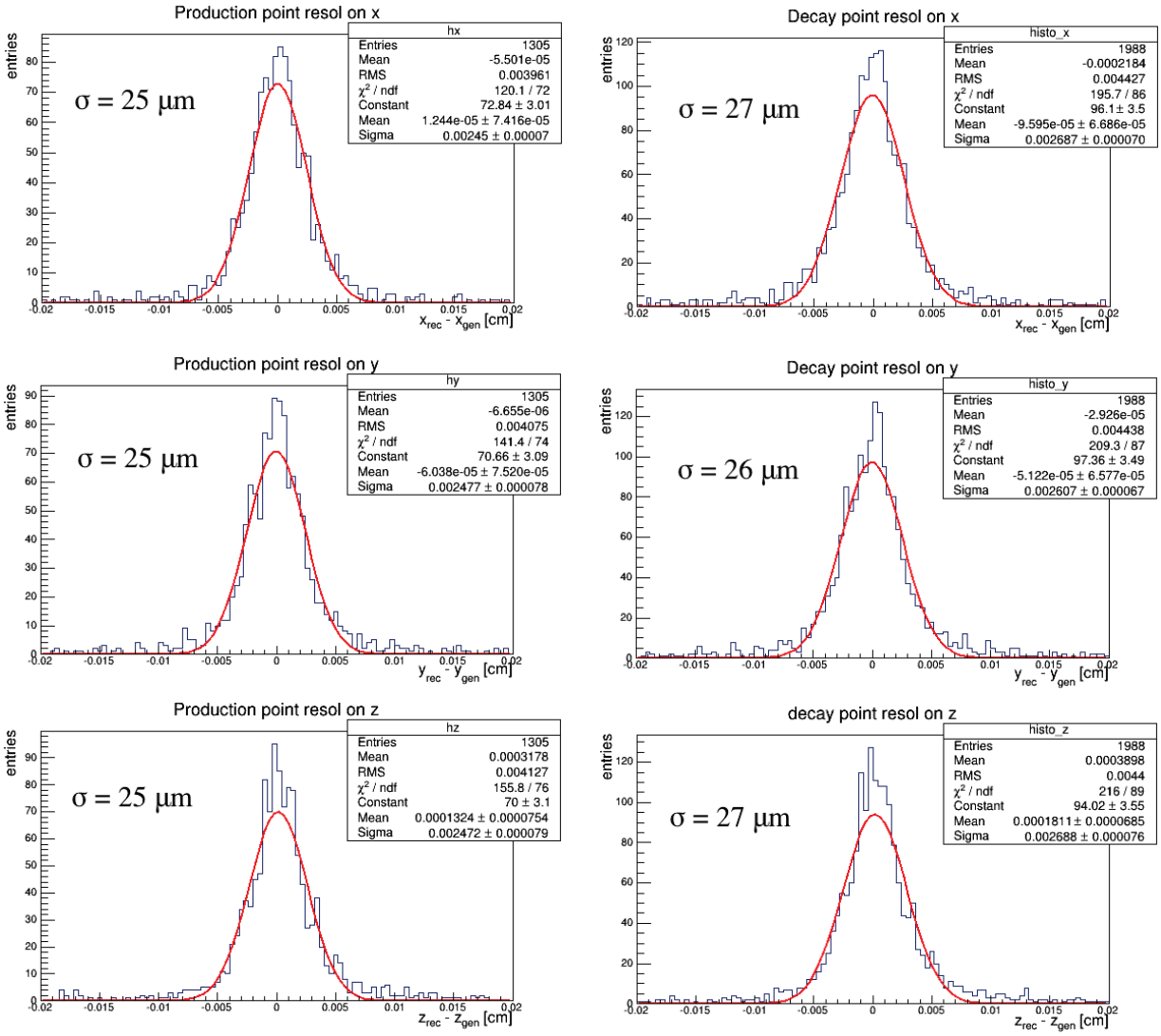


**Figure 3.10:** Expected resolutions on the reconstructed $D^0$ production vertex (left column) and decay vertex (right column).

## 3.5 Simulation and reconstruction of the CP asymmetry in $D^0$ decays

### 3.5.1 Simulation of the CP asymmetry in $D^0$ decays

The tool to generate different CP violation amplitudes in $D^0$ decays within the basf2 framework is not yet available. Therefore, we developed a fast simulation tool to generate $D^0$ and $\bar{D}^0$ with different $\lambda_f$ values. $D^0$ time distributions are created using a Monte-Carlo technique, following Eq. 5.2. The flavour of the meson at time $t$ is decided according to Eq. 5.1. The proper time distributions of one generated dataset of $D^0$ and $\bar{D}^0$ obtained with our simulation are displayed in Fig. 5.3, in this case for $D^0 \to \pi^+\pi^-$.

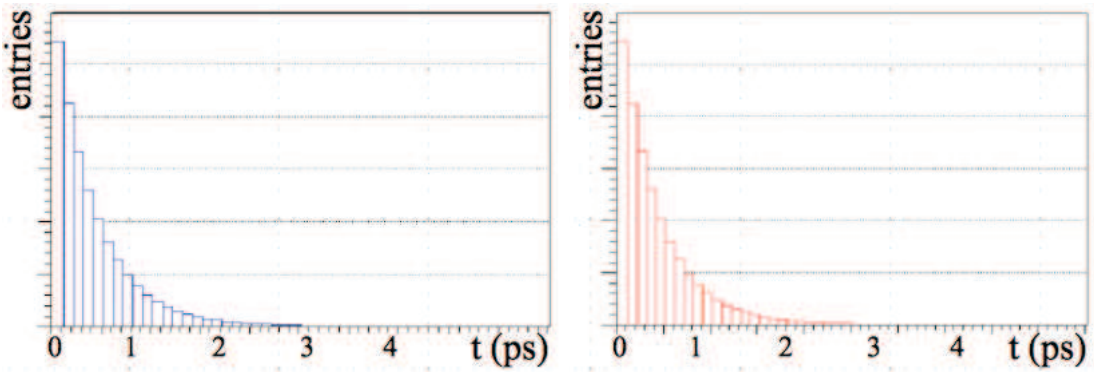


**Figure 3.11:** The proper time distributions of $D^0$ (left) and $\bar{D}^0$ (right) generated with our fast simulation tool, here with $arg(\lambda_f) = 10^o$, $|\lambda_f| = 1$ and a dataset of $5{\times}10^6$ $D^0$ - $\bar{D}^0$.

From these distributions, the generated asymmetry can be built according to Eq. 5.1, as displayed in Fig. 5.4.

The distributions shown in Fig. 5.3 and Fig. 5.4 were generated supposing an ideal detector. This means that the $D^0$ flavour tagging and its flight time, needed to reconstruct the CP asymmetry 5.1 are perfectly known.

In our prospective study of the Belle II ability to reconstruct this CP asymmetry reported in the next section, the flavour tagging performances are taken into account by including the dilution factor D, according to Eq. 3.19. A time resolution $\sigma_t$ can also be considered by smearing the flight time $t$ according to a Gaussian distribution centered in $t$ with a width $\sigma_t$.

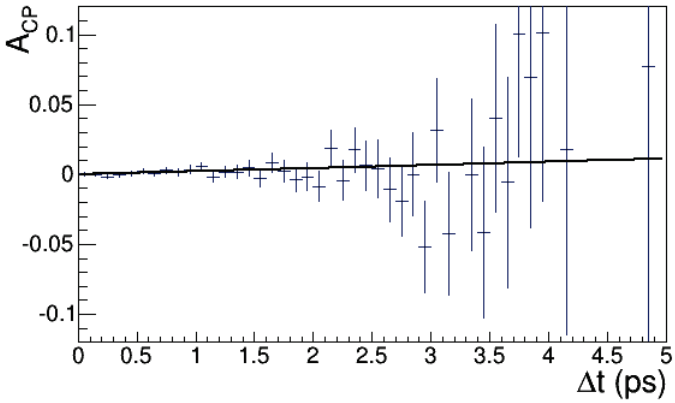


**Figure 3.12:** Simulated asymmetry with $arg(\lambda_f) = 10^o$, $|\lambda_f| = 1$ and a dataset of $5{\times}10^6$ $D^0$ - $\bar{D}^0$.

### 3.5.2 Reconstruction of the CP asymmetry in $D^0$ decays

The CP asymmetry can be measured with a binned likelihood fit depending on the parameter $\lambda_f$ to the time distribution shown on Fig. 5.4. To illustrate the difficulty of this fit, asymmetries generated with different values of $|\lambda_f|$ and $arg(\lambda_f)$ are shown in Fig. 3.13.

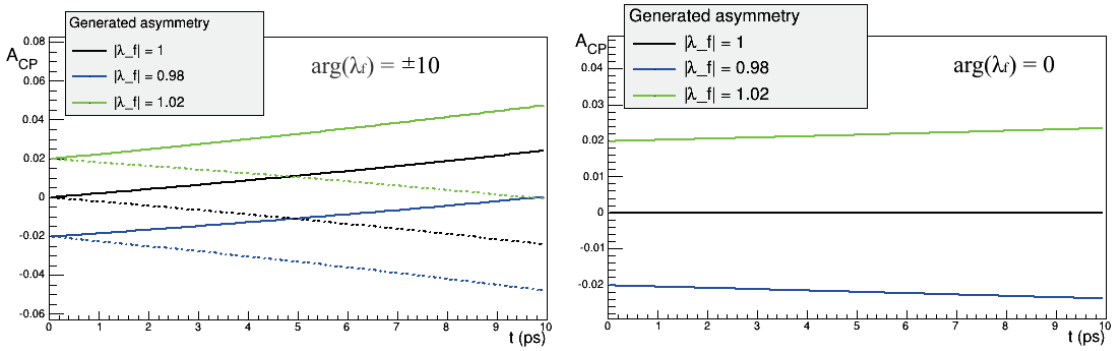


**Figure 3.13:** CP asymmetries as a function of time, generated with different values of $|\lambda_f|$ and $arg(\lambda_f)$. Continuous lines correspond to generated asymmetries with different values of $|\lambda_f|$, while dotted lines correspond to generated asymmetries with different values for $arg(\lambda_f)$. On the left plot we see the variation of the asymmetry as a function of time, with the influence of both $|\lambda_f|$ and $arg(\lambda_f)$, while on the right plot only the influence of $|\lambda_f|$ is considered.

The slope of the asymmetry is related to $arg(\lambda_f)$, while its curvature and offset is related to $|\lambda_f|$. We observe that the asymmetry is almost linear for values of $|\lambda_f|$ close to unity.

In our study, we focus on the CP violation due to interference between mixing and decay. This is legitimated by the fact that new physics is not expected to appear at first order in tree processes. Therefore, we fix $|\lambda_f| = 1$ in the fit and measure only $arg(\lambda_f)$. An example of the reconstructed asymmetry for one simulated experiment is displayed in Fig. 3.14 with a generated $arg(\lambda_f) = 10^o$. For high values of the flight time $t$ we observe large statistical uncertainty bars, which is obviously expected because of the exponential decay law. However, it is precisely at high values of $t$ that we get the sensitivity to indirect CP violation effects. Moreover, we benefit from a larger lever arm to measure $arg(\lambda_f)$, whose value is given by the slope of this curve.

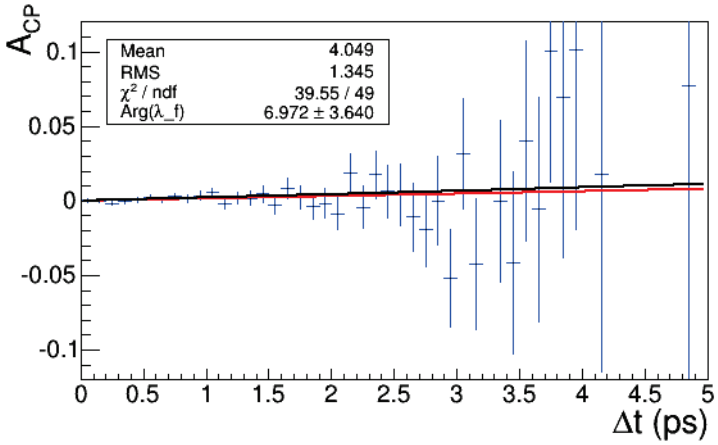


**Figure 3.14:** Time-dependent CP simulated asymmetry with $arg(\lambda_f) = 10^o$, $|\lambda_f| = 1$ and a dataset of $5{\times}10^6$ $D^0$ - $\bar{D}^0$ . The fit to the asymmetry is superimposed (red). Here, a measured value of $arg(\lambda_f) = 6.97^o \pm 3.6^o$ is obtained from the fit.

### 3.5.3 Estimation of the statistical uncertainty

Figure 3.14 shows the measurement of $arg(\lambda_f)$ obtained from the fit to the reconstructed asymmetry with one simulated data set. The statistical uncertainty estimated by the fit is $\sigma_{stat} = 3.6^o$.

In our study, we estimate the actual statistical uncertainty from the Gaussian dispersion of 1000 measurements (1000 data sets), as shown with Fig. 5.5. In this example, a value of $arg(\lambda_f) = 10^o$ was generated, and the mean measured value is about $9.9^o$, with a statistical uncertainty of $3.7^o$ (here still with $5{\times}10^6$ $D^0$ -$\bar{D}^0$ generated mesons).

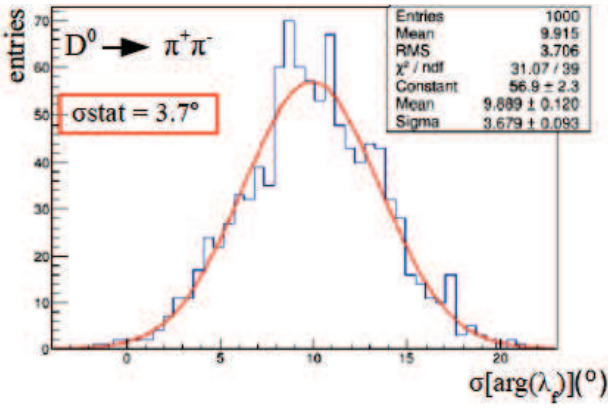


**Figure 3.15:** The statistical dispersion of the measured value of $arg(\lambda_f)$ in 1000 experiments. $5{\times}10^6$ $D^0$ -$\bar{D}^0$ mesons were generated, with $arg(\lambda_f) = 10^o$.

## 3.6 Study of the sensitivity of Belle II to $\beta_{c,eff}$

### 3.6.1 Impact of the main ingredients on the measurement

As a starting point to our study, we verified the method and investigated the impact on the accuracy of $arg(\lambda_f)$ as a function of the main ingredients to this analysis, to identify the most limiting factors.

First, we check that the statistical uncertainty on the measurement of $arg(\lambda_f)$ does not depend on the value of $arg(\lambda_f)$, as it is demonstrated with Fig. 3.16. We observe a flat dependency as long as $arg(\lambda_f)$ is smaller than $20^o$ (it is reminded that very small values of the asymmetry are expected).

Then, we look at the improvement of the statistical uncertainty with increasing statistics, displayed with Fig. 3.17. As expected, the statistical uncertainty on the measurement of $arg(\lambda_f)$ improves with $\sqrt{N}$.

We examine also the evolution of the statistical uncertainty as the flavour tagging performance degrades, displayed with Fig. 3.18. We observe that for values of mistag below 5%, as it is conservatively expected in Belle II, the mistag factor presents a much lower influence on the measurement than the meson statistics.
Finally, the binning of the histogram used to reconstruct the asymmetry may significantly impact the measurement. Several studies to optimize the binning were performed, also with variable bin width as a function of the flight time. However, the conclusion is difficult to draw because it depends significantly on all the other pa-

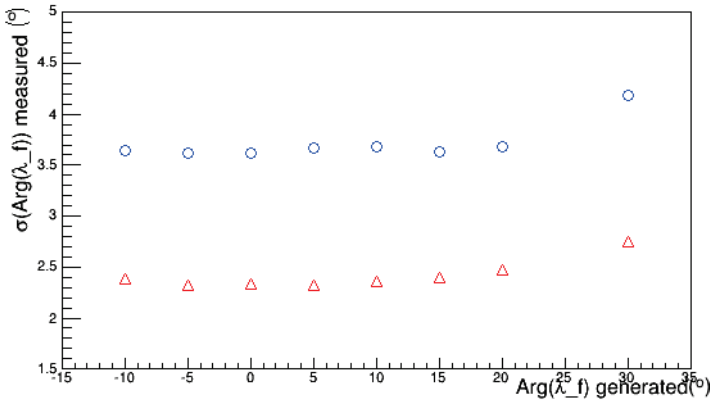


**Figure 3.16:** Estimated statistical uncertainty on the measured value of $arg(\lambda_f)$ as a function of the generated value of $arg(\lambda_f)$, observed for the expected $D^0 \to K^+K^-$ decay statistics (red triangles) and for the expected $D^0 \to \pi^+\pi^-$ decay statistics (blue circles) in Belle II.

rameters (statistics, values of $arg(\lambda_f)$). Moreover, we wanted to include also a time resolution in the fit method, so it appeared much easier to switch to an unbinned likelihood method, as proposed in RooFit [122].

### 3.6.2 Sensitivity of Belle II to $arg(\lambda_f)$ and $\beta_{c,eff}$

To estimate the Belle II sensitivity to $arg(\lambda_f)$ measured with $D^0 \to K^+K^-$ and $D^0 \to \pi^+\pi^-$ decays, and finally to $\beta_{c,eff}$, we take into account:

- the expected statistics of $5 \times 10^6$ reconstructed $D^0 \to \pi^+\pi^-$ and $1.2 \times 10^7$ reconstructed $D^0 \to K^+K^-$
- the flavour tagging purities: 98 % for $D^0 \to K^+K^-$ and 93 % for $D^0 \to \pi^+\pi^-$
- a resolution of 0.1 ps on the reconstructed flight time

To include the flight time resolution in the fitting method, we switch to an unbinned likelihood method. We adapt the RooFit method used to measure $sin(2\beta)$ in BaBar [123] with $B^0 \to J/\Psi K^0_s$ decays, to study $D^0$ decays from $e^+e^- \to c\bar{c}$ events. To do so, we have to modify the $x, y$ mixing parameters and the $\Gamma(t)$ functions because $\Delta\Gamma$ is neglected in Eq. 5.2 for $B^0$ oscillations.
The expected uncertainties on $arg(\lambda_f)$ measured with this unbinned likelihood fit

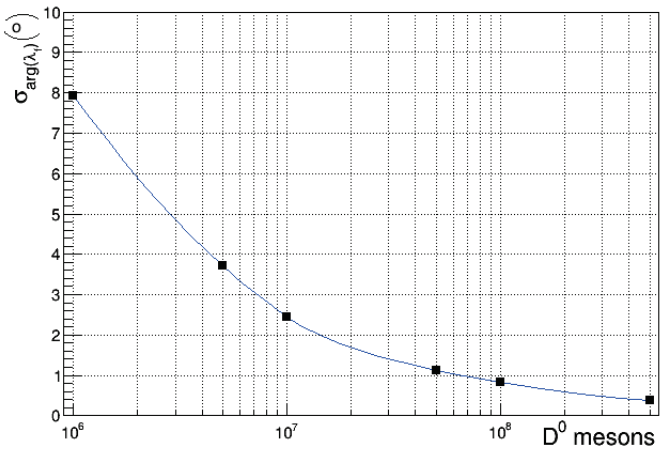


**Figure 3.17:** Estimated statistical uncertainty on the measured value of $arg(\lambda_f)$ as a function of the number of reconstructed mesons, here displayed for a generated value $arg(\lambda_f) = 10^o$.

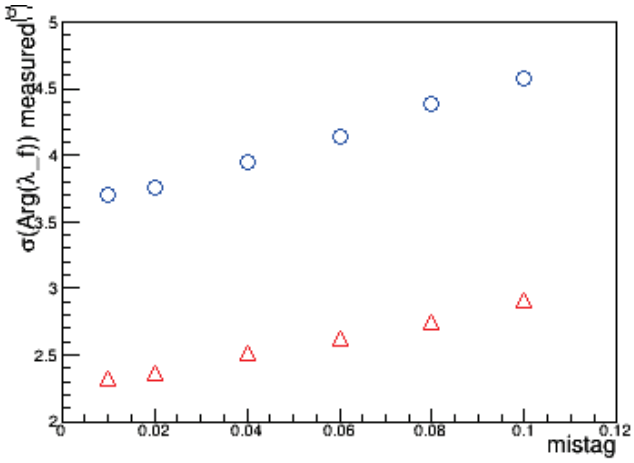


**Figure 3.18:** Estimated statistical uncertainty on measuring $arg(\lambda_f)$ as a function of the flavour mis-identification (here displayed for a generated value $arg(\lambda_f) = 5^o$). The red triangles correspond to the $D^0 \to K^+K^-$ decay channel and the blue circles to the $D^0 \to \pi^+\pi^-$ decay channel.

to the reconstructed CP asymmetry in $D^0$ decays with Belle II conditions, are :

$$\begin{array}{lll} \sigma_{stat}(arg(\lambda_f)) & \approx 2.1^o \text{ in the } D^0 \to K^+K^- & \text{decay channel} \\ \sigma_{stat}(arg(\lambda_f)) & \approx 3.7^o \text{ in the } D^0 \to \pi^+\pi^- & \text{decay channel} \end{array} \quad (3.20)$$

Using these two decay channels, we can add in quadrature (for two independent measurements) the uncertainties, and with Eq. 5.6, we determine an expected uncertainty on $\beta_{c,eff}$ as being $\sigma_{stat}(\beta_{c,eff}) \approx 2.1^o$.

### 3.6.3 Discussion on systematic uncertainties

From the studies presented in Section 3.6.1 it is obvious that the time-dependent measurement of the CP asymmetry in $D^0$ decays in Belle II will still be largely statistically limited, even if using the full 50 $ab^{-1}$ dataset. To corroborate this statement, we evaluated the impact on the measurement of $arg(\lambda_f)$ caused by the uncertainty in the measurement of the mixing parameters $x = \frac{\Delta M}{\Gamma}$ and $y = \frac{\Delta\Gamma}{2\Gamma}$, which are key inputs to this measurement. They are currently known with a precision of $\pm 0.18\%$ and $\pm 0.08\%$ respectively [124]. At the end of the Belle II data taking, this precision is expected to have improved to $\pm 0.09\%$ and $\pm 0.05\%$ respectively [77]. The contributions to the systematic uncertainties on the measured $arg(\lambda_f)$ from these inputs are listed in Table 3.1. These values can be directly compared to the statistical precision, of the order of a 2-4 °, and they are completely negligible with respect to them. Therefore, other possible sources of uncertainties were not investigated, since their impact is expected to be reduced with respect to the statistical uncertainty.

| Source of uncertainty | $D^0 \to K^+K^-$ | $D^0 \to \pi^+\pi^-$ |
|---|---|---|
| mixing parameter x | +0.0025° | 0.03° |
| | -0.0347° | -0.014 ° |
| mixing parameter y | +0.0137° | 0.0003° |
| | -0.0004° | -0.00275° |

**Table 3.1:** Systematic uncertainties on $arg(\lambda_f)$ due to uncertainties on the mixing parameters $x$ and $y$.

## 3.7 Conclusion

The most precise measurements of CP violation in the charm sector are currently obtained by the LHCb experiment, which benefits from the largest sample of $D^0$ mesons. However, their result is still statistically limited and it does not allow to draw any conclusion yet. This measurement will have to wait for a larger $D^0$ dataset, which will be produced by LHC Run 3 for LHCb (starting in 2021) and by SuperKEKb for Belle II (starting in 2018).
Anticipating the availability of a large dataset of reconstructed $D^0$ mesons in Belle II, we performed a first prospective study of a time-dependent measurement of the CP asymmetry in $D^0$ decays, aiming at extracting for the first time the $\beta_c$ angle of the $c-u$ unitarity triangle.
We showed that even at SuperKEKB, such a measurement would still be largely statistically limited. A statistical accuracy of about $2.1^o$ on $\beta_{c,eff}$ seems to be reachable taking into account Belle II expected performances (mistag, statistics and flight time resolution). This can be compared to the estimated precision on the same measurement performed in LHCb Run3 which is $1.7^o$ [105] if considering only mistag but a perfect flight time reconstruction.

Performing this measurement at both experiments would be very interesting, since the experimental conditions are completely different. Belle II has the advantage of a very low background and a very good flavour tagging, with a drawback of smaller boosts of the mesons. However, this measurement may benefit from an upgraded inner tracker.
But actually, the key ingredient to improve the sensitivity to $\beta_{c,eff}$ through such an analysis remains the $D^0$ statistics. For this, other decay channels should be investigated, though the translation of the measured value of $arg(\lambda_f)$ to $\beta_c$ is delicate. The theoretical uncertainty on $\beta_c$ due to hadronic corrections from penguin diagrams are estimated in [120] to be about $2.7^o$. Another way to increase the statistics could be also investigated, for instance by adding other tagging methods or by using $D^0$ meson originating from B decays.

# 4. Estimation of low momenta using energy deposition in Belle II silicon detectors

In this chapter, an alternative way to estimate low momenta in Belle II is proposed, in order to improve the estimation based on the helix fit of the track. This method uses the charged particle energy deposition in Belle II inner tracking detectors. To begin with, the importance of low momentum particles in the physics program of Belle II and the difficulties to reconstruct them are discussed in Section 4.1. The principle of the estimation of low momenta using energy deposition is explained in Section 4.2. Details on the building procedure of the proposed estimator are given in Section 4.3 and a study on its performances is presented in Section 4.4. Finally, Section 4.5 concludes on this study and expound the expected outlooks.

## 4.1 Low momentum tracks in Belle II

Low momentum tracks (which do not penetrate enough into the CDC, with a momentum below 150 MeV) are generally difficult to reconstruct, first because of the pattern recognition which looks for all clusters belonging to the same track, and also in terms of fitting the helix track formed by these clusters. Indeed, soft charged particles tightly curl in the magnetic field, which reaches 1.5 T in Belle II. Therefore they do not cross all tracking layers, but curl several times in the innermost ones. Clusters corresponding to a same curling track may be associated to different tracks, or different tracks can be reconstructed instead of one, one for each loop of the helix track, as illustrated with Fig. 4.1.

Along with the problem of knowing which clusters should be associated to a same track, the energy loss is more significant with curling tracks because of the Bethe-Bloch $1/\beta^2$ and also because more layers of the same detector are crossed. As a consequence, the momentum is more significantly decreasing along the track path,

making the helix fit more difficult to converge.

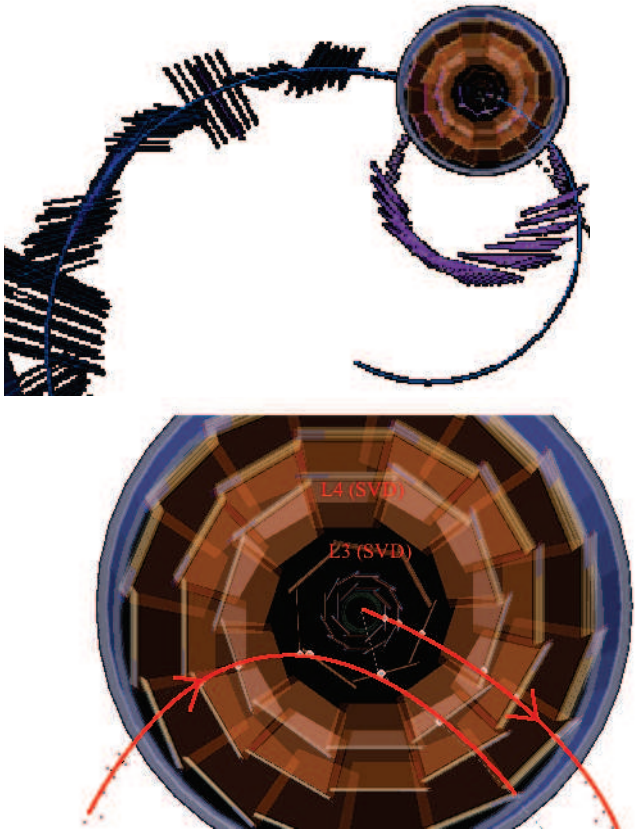


**Figure 4.1:** Illustration of the difficulty to reconstruct low momentum tracks. These two pictures are event displays of the Belle II detector, showing a transversal view of the detector. Two tracks were reconstructed by mistake instead of one curling track. On the upper view, the two reconstructed tracks are represented in blue and in the zoom below, we represent in red how the reconstructed track should have looked like.

If we do not consider the energy loss in the PXD and SVD detectors, but only the curvature in the magnetic field, a charged particle would need about 40 MeV to reach the first layer of the CDC at a radius of 16.8 cm from the beam axis, and about 150 MeV to reach the middle of the CDC, at a radius of 64 cm. In addition to this geometrical aspect, the charged particle loses energy in each layer crossed, and the softer the particle is, the more energy it loses. In the end, the curvature radius of the track decreases rapidly, and the helix track has to be reconstructed using only few hits and with a small lever arm. The momentum resolution will be poorer than the one of a track revealing lots of hits in the CDC. At small momenta,

multiple scattering also limits the resolution of momentum estimation.

SuperKEKB is a collider delivering collisions at the $\Upsilon$ center-of-mass energies, producing relatively soft final state particles. As an illustration, Fig. 4.2 shows the momentum spectrum of all final state particles produced in generic $\Upsilon(4S) \to B\bar{B}$ events, where about 10% of the pions are produced with a momentum below 150 MeV.

In particular, the soft pion from $D^{*\pm} \to D^0\pi^{\pm}_{soft}$ decays, whose electrical charge is used to identify the flavor of neutral B and D mesons, plays an important role in the Belle and Belle II physics program. Soft pions were extensively employed for flavor tagging in Belle, with major results such as the measurement of $sin2\beta$ [125] and the measurement of $D^0$ oscillations [49].

Fig. 4.3 presents the $\pi_{soft}$ momentum spectrum for two different production processes, $e^+e^- \to c\bar{c}$ continuum producing $D^{*\pm} \to D^0\pi^{\pm}_{soft}$, and $e^+e^- \to \Upsilon(4S) \to B\bar{B}$ events producing $D^{*\pm} \to D^0\pi^{\pm}_{soft}$. The first decay channel is the one selected to study the sensitivity of the Belle II experiment to the $\beta_c$ angle of the $c-u$ unitarity triangle, presented in Section 3. About 60 % and 15 % respectively of the soft momentum pions from these examples have a momentum below 150 MeV.

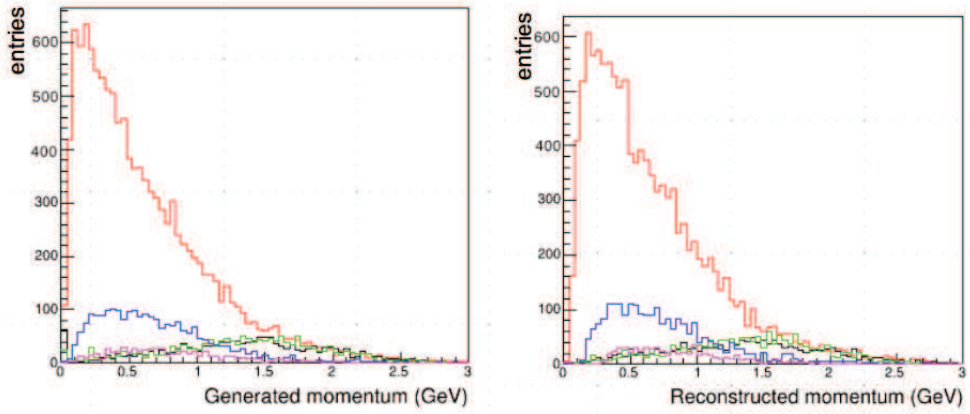


**Figure 4.2:** Momentum distribution of final state particles in generic $\Upsilon(4S) \to B\bar{B}$ events. The left figure displays generated momenta and the right one displays reconstructed momenta. Pion spectrum is represented in red, electron with black, kaon with blue, muon with green and proton with violet.

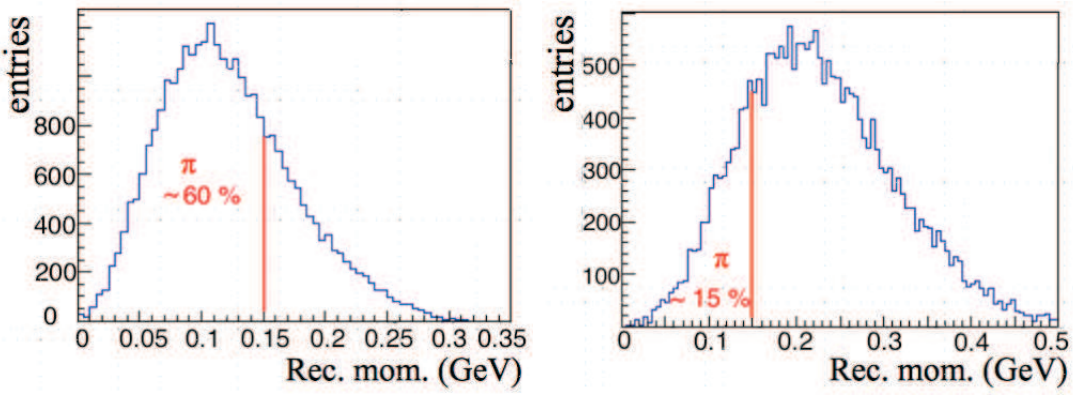


**Figure 4.3:** Momentum distribution of soft pions originating from $\Upsilon(4S) \to B\bar{B}$ events with one $B$ decaying to a $D^{*\pm}X$ followed by $D^{*\pm} \to \pi^{\pm}D^0(\bar{D}^0)$ (on the left), and originating from continuum $c\bar{c}$ events producing $D^{*\pm} \to \pi^{\pm}D^0(\bar{D}^0)$ (on the right).

The accuracy of the reconstruction of the soft pion momentum may impact the following two aspects:

- This $\pi_{soft}$ is selected thanks to a cut on $Q$, which is narrow because of the limited phase space ($M_{D^*} - M_{D^0} \approx M_\pi$). To reconstruct this invariant mass difference, the momentum of the soft pion is an input. The narrower this reconstructed mass difference peak is, the lower the background selected in a given mass window will be.

- In time dependent analyses, the $B$ meson decay point in $\Upsilon$(4S) events (or the $D$ meson production point in $c\bar{c}$ events) is estimated from a vertex fit of its daughter tracks including the soft pion track. But low momentum tracks are more impacted by multiple scattering and the $D^0$ production vertex resolution is degraded due to the soft pion.

The motivation of tis study, aiming at improving the momentum estimation for soft tracks in Belle II, is the importance of these low momentum particles in Belle II physics program and the difficulty in estimating accurately low momenta.

## 4.2 Principle of the momentum estimation based on energy loss

### 4.2.1 The Bethe-Bloch formula

Fast charged particles moving through matter lose energy mainly through ionization and atomic excitation. Their mean linear energy loss is described by the Bethe-Bloch formula [126]:

$$-\left\langle \frac{dE}{dx} \right\rangle = Kz^2 \frac{Z}{A} \frac{1}{\beta^2} \left[ \frac{1}{2} \ln \frac{2m_e c^2 \beta^2 \gamma^2 T_{max}}{I^2} - \beta^2 - \frac{\delta(\beta\gamma)}{2} \right] \tag{4.1}$$

where:

| | | | |
|---|---|---|---|
| z | = charge of the incident particle | c | = speed of light |
| Z | = charge number of the medium | $m_e$ | = electron mass |
| I | = mean excitation energy of the medium | $\delta(\beta\gamma)$ | = density effect correction related to the polarization of the medium |
| A | = atomic mass of the medium | $\beta$ | = $v/c$, the boost |
| K | = $4\pi N_A r_e^2 m_e c^2$ | $\gamma$ | = $(1-\beta^2)^{-2}$, the Lorentz factor |
| $N_A$ | = Avogado's number | $T_{max}$ | = maximum energy transfer in a single collision |
| $r_e$ | = classical electron radius | | |

The maximum energy transfer in a single collision parameter can be expressed by the formula:

$$T_{max} = \frac{2m_e c^2 \beta^2 \gamma^2}{1 + 2\gamma \frac{m_e}{M} + (\frac{m_e}{M})^2} \tag{4.2}$$

where M is the mass of the incident particle.

This mean linear energy loss is also called the stopping power. It is a function of the boost $\beta$ of the incident particle. At very low and very high energies, several additional corrections need to be applied to this function [127, 128]. In the end, the Bethe-Bloch function roughly varies as $1/\beta^2$ at low boosts and increases as the logarithm of $\gamma$ at high boosts. This is illustrated by Fig. 4.4 which displays the stopping power of pions crossing a 300 $\mu$m layer of silicon. In thin layers, the estimated linear energy loss is usually lower than the real one because a fraction of the energy lost by the charged particle is carried off by energetic knock-on electrons, the so-called $\delta$ electrons. This leads to the restricted energy loss, displayed with the

thick line in Fig. 4.4, expressed with the following formula:

$$-\left\langle \frac{dE}{dx} \right\rangle = Kz^2 \frac{Z}{A} \frac{1}{\beta^2} \left[ \frac{1}{2} \ln \frac{2m_e c^2 \beta^2 \gamma^2 T_{cut}}{I^2} - \beta^2 \left( 1 + \frac{T_{cut}}{T_{max}} \right) - \frac{\gamma}{2} \right] \tag{4.3}$$

Where $T \leq T_{cut} \leq T_{max}$, and with $T_{cut}$ depending on the material and the incident particle momentum. Since $T_{cut}$ replaces $T_{max}$ in the argument of the logarithmic term of Equation 4.3, the $\beta\gamma$ term is replaced by a constant and the density effect correction $\gamma$ eliminates the explicit $\beta\gamma$ dependence. For low momenta pions, there is no difference between the standard and the restricted form of the Bethe-Bloch functions, since knock-on electron production is improbable.

In the $1/\beta^2$ low momentum region, two pions of different momenta can be distinguished through their energy deposition in the material. We propose to use this feature to estimate the momentum of soft pions crossing silicon layers in Belle II. One important point to keep in mind is that for a given momentum, the energy deposition is a stochastic process and its distribution is described by a Landau distribution. Furthermore in thin layers, only few collisions will take place between the incident charged particle and the electrons of the material, resulting in a large variance of the total energy loss distribution [129].

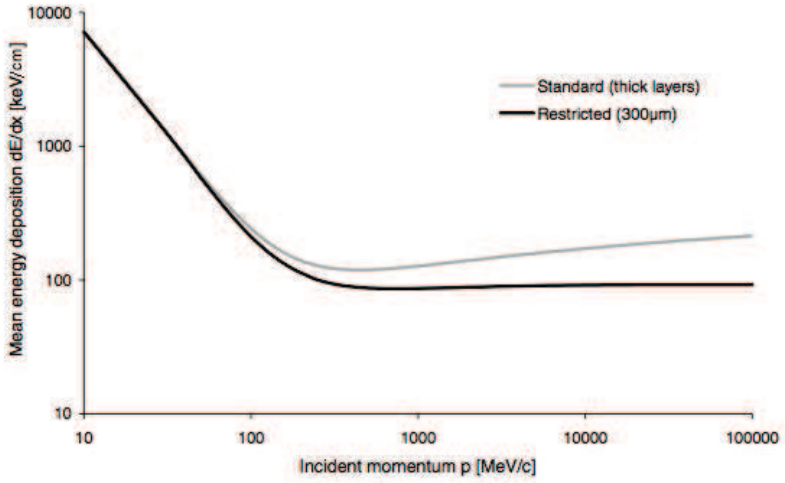


**Figure 4.4:** Stopping power of pions in silicon. Figure taken from [130].

Such an idea of making use of the energy loss in silicon detectors to build an estimator of the momentum has already been studied in the frame of the STAR [131] and ALICE [132] experiments. The method consists in using as inputs the measured

charges of the clusters associated to the reconstructed track.
We propose here to study this same idea in the frame of the Belle II inner tracker, which is composed of two silicon pixel layers of 75 $\mu m$ thickness (PXD) and four double-sided silicon strip layers of 320 $\mu m$ thickness (SVD). In addition, track parameters and the momentum estimated from the track helix fit are also used to compute the actual path into matter in each detector layer by the crossing soft particle, taking into account the track $\theta$ polar angle and its curvature in the transverse plane due to the magnetic field.
Fig 4.5 gives a qualitative idea on the sensitivity of the mean energy loss to the momentum. The separation between the most probable values (MPVs) of the Landau distributions degrades with increasing momentum. Above 200 MeV at most, there is no significant sensitivity to the momentum anymore, because we are no more in the $1/\beta^2$ regime of the Bethe-Bloch curve.

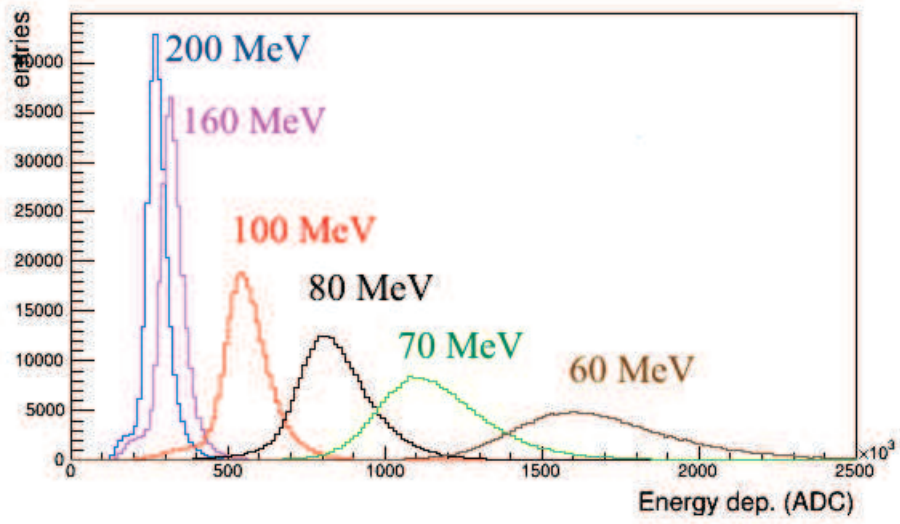


**Figure 4.5:** Distributions of energy deposition (ADC counts) measured in silicon layers in Belle II, of pions produced with different soft momenta ranging from 60 MeV to 200 MeV.

### 4.2.2 Application of this method to Belle II

In this study we are interested in particles which do not penetrate significantly the CDC. In the Belle II inner tracking system, we can potentially make use of 6 energy deposition: 2 are measured by the PXD detector and 4 are measured by the SVD detector. In practice we can have more than 6 energy deposition from a charged particle crossing the inner tracking system, on one hand due to curling in the mag-

netic field and on another hand because of the overlap between the ladders of a same detector layer.

**PDX versus SVD inter-calibration**

In this section, we first take care of inter-calibrating all the cluster charges measured from these 6 silicon layers. To do that calibration, we compare $\Delta E/\Delta x$ distributions observed in each layer, $\Delta E/\Delta x$ being here a cluster charge divided by the layer width. This cluster is associated to a perpendicular track crossing this layer.

Informations provided by the PXD and by SVD are measured with different precisions due to the different ADC ranges, in addition to the different layer widths. The analogue signal created by the charge deposition in the PXD is digitised by a 5 bit ADC, and by a 10 bit ADC in the SVD.

As mentioned in Chapter 4.2, distributions of energy loss in thin material layers feature a large variance. Furthermore, the PXD signal is encoded with only 5 bits. Therefore, we have to check if the PXD detector can bring useful information to the estimator we are building. We first have to calibrate for the different ADC dynamic ranges in the PXD with respect to the SVD. To do so, the MPV (Maximum Probable Value) of the Landau distributions of $\Delta E/\Delta x$ in PXD and SVD layers are compared, as displayed in Fig. 4.6 for pions generated with momentum of 450 MeV, high enough to simulate a Minimum Ionizing Particle (MIP). Because of detection effects, the distribution of mean energy deposition does not exactly follow a Landau distribution for both PXD and SVD. A convoluted Gauss and Landau function is used for the fit. A correction factor of 0.61 is derived from the comparison of PXD and SVD $\Delta E/\Delta x$ distributions, it will be applied to the cluster charges measured in the PXD.

**SVD double-sided layers inter-calibration**

Each layer of the SVD is double sided, providing two reconstructed clusters. The two clusters are correlated because they are induced by the same charge cloud in the silicon wafer. In simulated data, we observe that the cluster charges measured on p-side strips and the cluster charge measured on n-side strips of a SVD silicon wafer are not exactly equal, though they are induced by the same energy loss. The measured correction factor is about 0.93, as we can see from Fig. 4.7. In the following, we correct for this difference to narrow the mean linear energy loss Landau

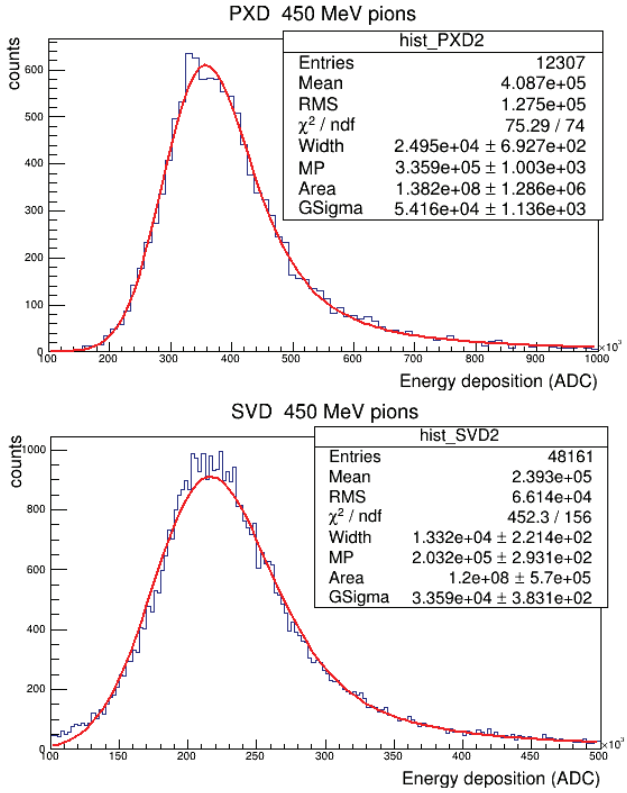


**Figure 4.6:** Mean energy deposition $\Delta E/\Delta x$ (ADC counts) for the PXD detector encoded with 5 bits (up) versus the SVD detector, encoded with 10 bits (down).

distributions. This factor is interpreted as a combination of two causes. The first one is the influence of the drift field and the Lorentz force on the mobility of charges. The second one is the integration over time of the currents produced by these charges, for each type of strips, in order to obtain the measured charge. More details on the charge collection are provided in Chapter 2.

## 4.3 Proposition of a low momentum estimator in Belle II

In this section, the principles behind the low momentum estimator that we are trying to develop are described. In the subsection 4.3.1 we detail the parameters used to generate the data used in our study. In the two following subsections, we explain how to build up the $< \Delta E/\Delta x >$ of a particle, by taking into account the path in silicon, in subsection 4.3.2, and the truncation of the largest deposition is handled in subsection 4.3.3. The two aspects to take care of when building the estimator

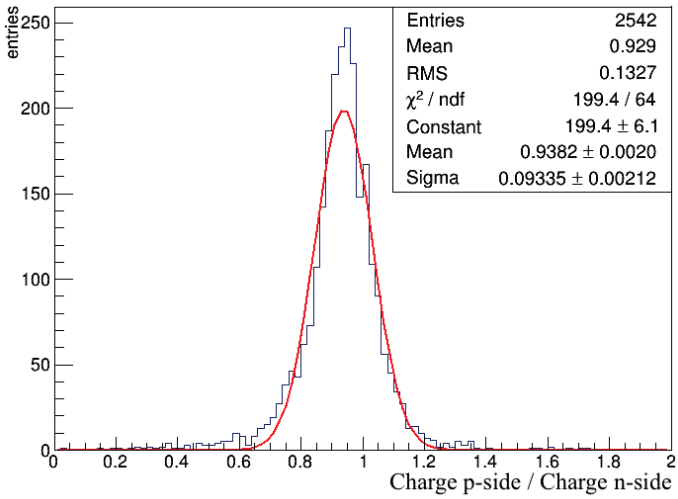


**Figure 4.7:** Ratio between the charge collected on the p-side strips and on the n-side strips of a same wafer of the SVD detector and for a same crossing particle.

are: the increasing energy loss along the path of a track (subsection 4.3.3.1) and the curling tracks (subsection 4.3.3.2). A preliminary conclusion is drawn in subsection 4.3.4. However the final estimator will be only chosen in Section 4.4, based on a performance study.

### 4.3.1 Simulation study parameters

To simulate the interaction of only one or several particles with the Belle II detectors, we resort to the generator named ParticleGun, described in Chapter 2. In this study, exactly one charged pion per event is generated with the ParticleGun module of basf2, with the following parameters of the track, depending on the considered study:

- Fixed or uniformly distributed momentum in the range [0.05, 0.2] GeV.
- Fixed or uniformly distributed $\theta$ polar angle in the acceptance of the Belle II detector, i.e. in the range [17, 150]°.
- Uniformly distributed $\phi$ azimuthal angle in the range [0, 360]°.

### 4.3.2 Building a momentum estimator based on energy deposition in the inner tracking system

The energy lost by a particle crossing the 6 silicon layers in Belle II can be estimated from the total charge measured in these layers. In practice, clusters are reconstructed, and then associated to a given track with a pattern recognition algorithm.
The basic idea, to estimate $\Delta E/\Delta x$ as expressed with the Bethe-Bloch formula 4.1, is to sum over all the charges of clusters associated to the track, and to divide this sum $\Delta E$ by the total length $L$ of the path of the particle in the silicon layers:

$$\frac{\Delta E}{L} = \frac{\sum charge\_clusters}{\sum d_{PXD} \times n_{PXD} + \sum d_{SVD} \times n_{SVD}} \tag{4.4}$$

In this formula, $n_{PXD}$ and $n_{SVD}$ correspond to the number of PXD and SVD layers crossed by the charged particle and $d_{PXD}$, $d_{SVD}$ represent the distance travelled by the particle in each silicon layer. Without magnetic field, these distances are:

$$\begin{aligned} d_{PXD} &= 75\,\mu m/sin\theta \\ d_{SVD} &= 320\,\mu m/sin\theta \end{aligned} \tag{4.5}$$

for an incident particle with polar angle $\theta$.
However, to reproduce with more accuracy the path of the charged particle through the silicon layers, we also have to consider the curvature in the transverse plane due to the magnetic field. The path $L$ through all silicon layers becomes in this case:

$$L = \frac{\sum d_{PXD} \times n_{PXD} + \sum d_{SVD} \times n_{SVD}}{\sqrt{sin^2\theta - (0.3RB/2p)^2}} \tag{4.6}$$

where the magnetic field $B = 1.5$ T, $R$ is the radius of the layer with respect to the beam axis as given in Table 2.3, $p$ and $\theta$ are respectively the momentum and the polar angle of the track. In practice, $p$ and $\theta$ inputs are obtained from the helix fit of the track and clusters are known from the pattern recognition. Details about how equation 4.6 was obtained can be found in Appendix A.

In addition to what was presented in Section 4.2, we have to consider that different particle types will feature a different dE/dx curve while crossing a given material.

Therefore, to determine the momentum thanks to $\Delta E/\Delta x$ , we also have to know which particle is considered.
However, this is not a real issue if we consider particles of momentum in the range 50-120 MeV (where 50 MeV is the minimum momentum of a track to be reconstructed in Belle II). Indeed, we show with Fig. 4.8 that the mean energy loss measured in the Belle II inner tracking silicon detector features distinct distributions for each type of particle, for momenta below 120 MeV. All final state charged particles produced from $B\bar{B}$ events in Belle II were simulated to produce this figure and protons are outside of the displayed range. Therefore, in the considered momentum range, except muons, no particle can be mis-identified as a pion from its energy deposition.

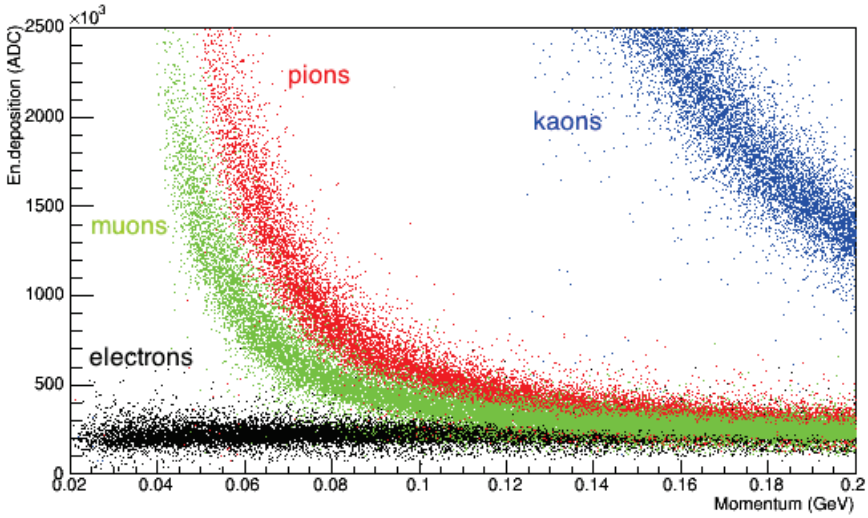


**Figure 4.8:** Energy deposition (ADC counts) of low momentum particles as a function of the momentum (GeV).

Actually we have seen in Section 4.1 and we can observe in Fig. 4.2 that only pion tracks were reconstructed with such a low momentum. Indeed, we observe from Fig 4.9 (with generated clusters) that, because of their energy loss, protons need more than 220 MeV to cross all the SVD layers (and produce at least 8 clusters), kaons need about 150 MeV, while pions can cross the whole SVD if their momentum is greater than 55 MeV.

### 4.3.3 Truncated mean

To define the mean energy loss ΔE, computing the mean value of all the clusters is not a good approach since the energy loss distribution is described by a Landau distribution, whose tail is experimentally truncated by the finite number of recon-

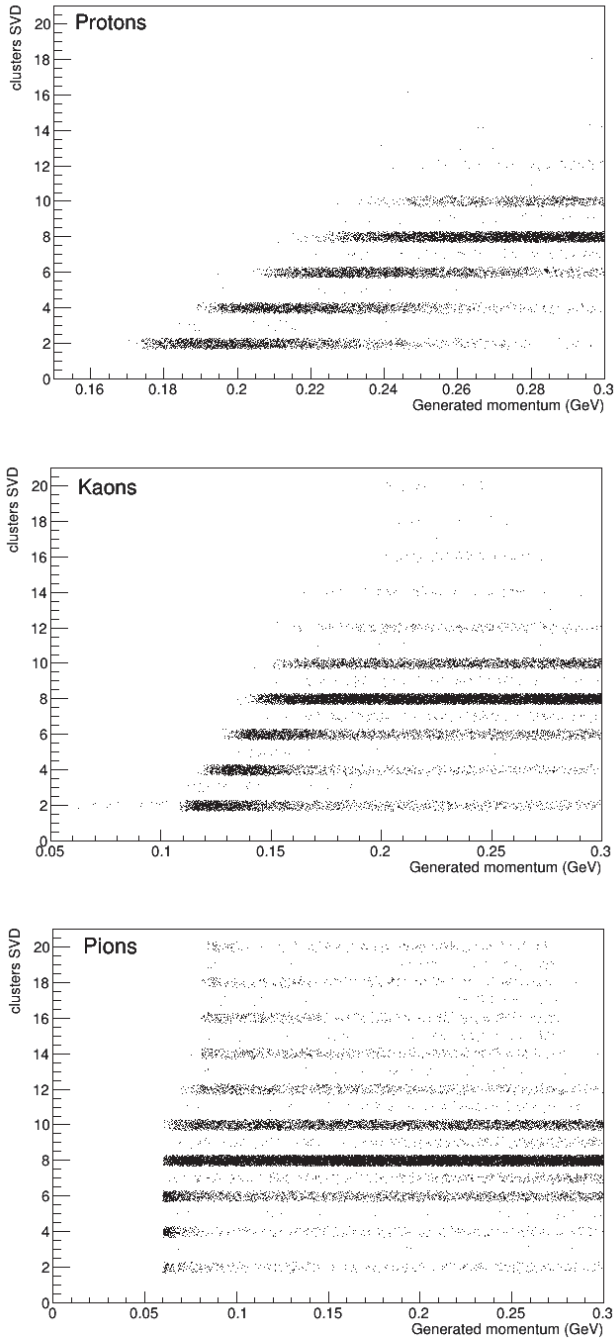


**Figure 4.9:** Cluster multiplicity in the SVD vs. the momentum, for protons, kaons and pions produced with a polar angle $\theta \in [17, 150]°$.

structed hits. This issue is a classical problem faced in particle identification based on $\Delta E/\Delta x$ measurements. To avoid such statistical fluctuations of the estimated mean energy loss, the set of measurements is usually truncated in some well defined way. The simplest truncation method consists in eliminating the highest charge value of all cluster charges, to reduce the tail of the distribution. Actually, in this analysis, this translates in the elimination of the two highest values since these two clusters are measured from the same wafer and are fully correlated (it was checked that the two highest charge values always correspond to a same wafer). This truncation indeed narrows the Landau distribution as it can be seen from Fig. 5.6 that compares the "mean energy loss" to the "truncated mean energy loss" of 70 MeV generated pions.

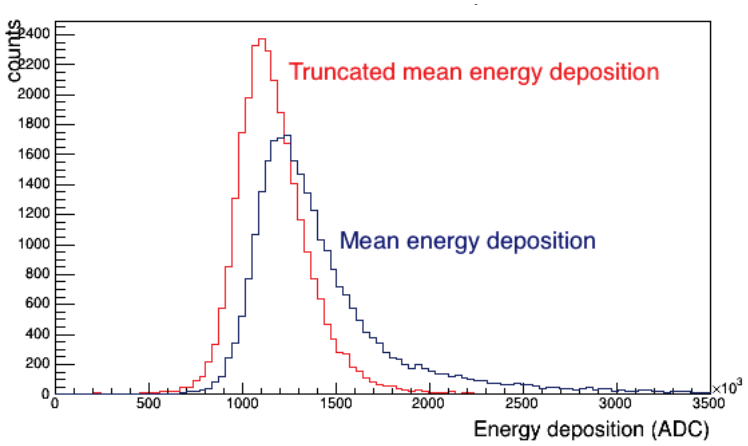


**Figure 4.10:** Distribution of truncated mean energy deposition compared to the one of raw mean energy deposition, of 70 MeV generated pions.

However in our case, contrary to the particle identification situation, energy loss measurements are performed in very thin silicon layers, resulting in significant statistical fluctuations as already mentioned in Section 4.2.1. In addition to that, low momentum tracks may curl several times in the detector, losing energy each time they cross a material layer.

Therefore, a study was performed to refine the truncation procedure and optimize the estimation of the measured mean energy loss. In the following, the different aspects which impact the mean energy loss distribution are discussed. The final conclusion about the truncation method will be drawn in Section 5.8 by looking at performances of the different methods investigated.

#### 4.3.3.1 Increasing energy loss along the track path

The risk of simply using all associated clusters is to bias the estimator towards lower momenta. The lower the momentum of a particle is, the more energy it will lose in each layer, depending also on the polar angle (i.e. the track path in silicon). The energy loss of the particle after crossing several layers is illustrated with Fig. 4.11 and Fig. 4.12, where the energy deposition distributions of 80 MeV pions are displayed in case of 45° (long path of the particle in the layers, therefore more energy is lost) and 90° incident polar angles (short path of the particle in the layers). The fitted MPVs (most probable values) of the Landau energy deposition distributions are compared, for pions generated with different momenta, after each crossed layer. We observe that, for a low momentum pion, the energy deposition measured in the last two layers significantly fake a lower momentum pion (i.e. higher $\Delta E/\Delta x$ values), therefore it seems better not to make use of these measurements to build the low momentum estimator.

#### 4.3.3.2 Curling tracks

Due to the 1.5 T magnetic field, low momentum particles may curl back several times in the detector, losing energy at each passage. This is illustrated with Fig. 4.13, showing the cluster multiplicity of charged pions generated in Belle II with a momentum equal to 100 MeV and a polar angle $\theta = 90°$ or $\theta = 30°$, and with a momentum equal to 1 GeV and $\theta = 90°$. If produced in the transverse plane, the particle may even cross several times the same sensor, while if produced with a small polar angle, it may escape the detector acceptance.
Due to the increasing energy loss of curling low momentum particles, we would like to eliminate clusters produced by the track after the particle loses too much energy, hence clusters corresponding to several loops, maybe even as soon as the second loop. Unfortunately, no chronological information is provided with the clusters, meaning that they are not ranked along the track path. The set of clusters associated to a same track has therefore to be truncated according to an empirical method which we have to develop.
For curling tracks, we first considered to take into account the lowest energy deposition in each layer (out of several). This method assumes that this deposition corresponds to the first passage of a curling particle. But there can be a scenario where a particle curls back before crossing all the layers of the SVD. Thus, in such a case, using more than two energy deposition for a layer can be useful in order to

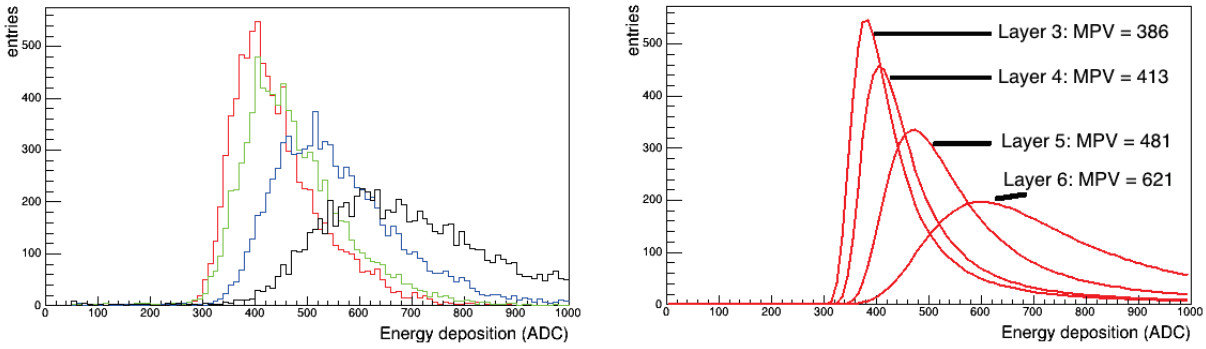


**Figure 4.11:** Energy deposition distributions in the SVD layers (left), and the corresponding fits (right) for pions generated with momentum of 80 MeV and an incident polar angle of $\theta = 45°$.

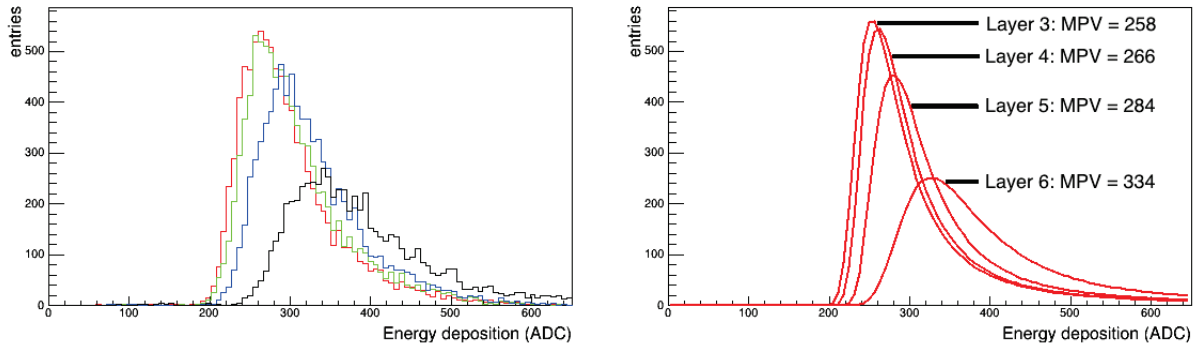


**Figure 4.12:** Energy deposition distributions in the SVD layers (left) and the corresponding fits (right) for pions generated with momentum of 80 MeV and an incident polar angle of $\theta = 90°$.

determine the momentum.

### 4.3.4 Conclusions

The truncation method and the decision to use or not the PXD detector are correlated. The PXD detector can provide two more cluster energy deposition for the final mean energy deposition. But since the layers of the PXD detector are only 75 $\mu$m thin, the energy deposition fluctuations are larger. An estimator using this detector measurement will also have to use a truncation method, which may not be the same as for an estimator considering the SVD detector alone. Therefore, the conclusion on using or not the PXD detector can be drawn only by comparing the final relative resolution of the estimator using only SVD information and the estimator using both the PXD and SVD information.
The curling tracks pose problems because the clusters are not stored along the track path and, moreover, two or more tracks can be reconstructed from a curling track. The increasing energy loss along the path has to be taken into account. This is a delicate issue, because the purpose is to build a general low momentum estimator, not an estimator tuned for particular momentum and path (a specific $\theta$ polar angle) through silicon.
Therefore, by analyzing all these aspects, it was decided to apply several technics to compute the mean value of the energy deposition:

- using all the cluster energy deposition except for the 2 highest values;
- as the mean value of the first 4 cluster energy deposition;
- as the mean value of the first 6 cluster energy deposition.

The final conclusion of which estimator provides a better resolution is driven in the next section after comparing the resolution obtained with each method to the one obtained with the helix fit.

## 4.4 Performances of the proposed low momentum estimator

### 4.4.1 The final proposed low momentum estimator

To build the momentum estimator, the parameterization of the momentum as a function of the measured energy loss is derived. To do so, we first produce the

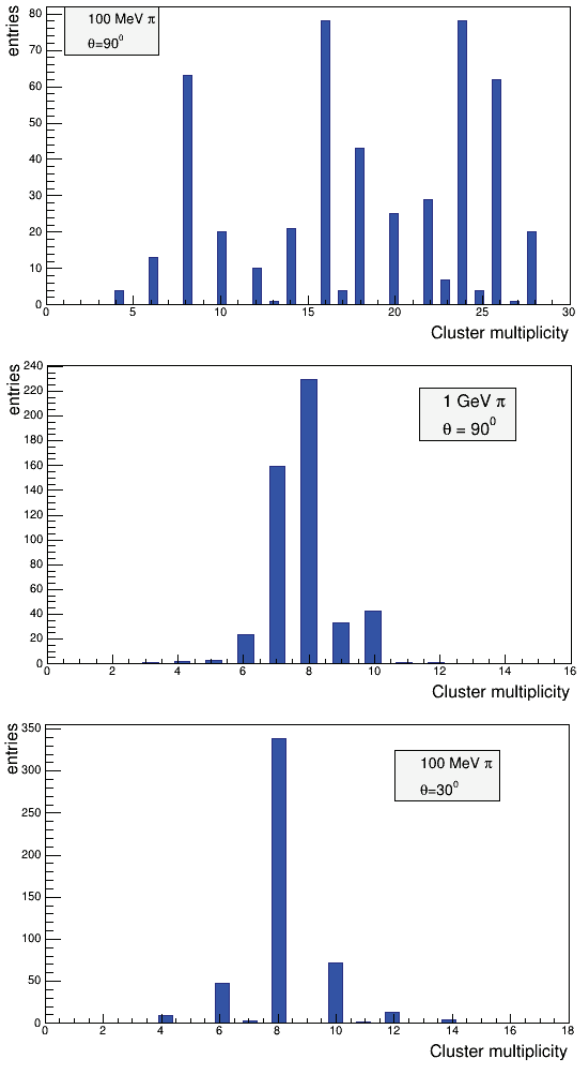


**Figure 4.13:** SVD cluster multiplicities observed for pions generated with different momenta and $\theta$ polar angles.

distribution of the mean truncated energy loss as a function of the momentum, by generating 300 000 $\pi^{\pm}$ with basf2, in the geometrical acceptance of the detector and with momenta ranging from 50 MeV to 200 MeV. The mean truncated energy loss $< \Delta E/\Delta x >$ is computed using the selected clusters as described in the previous section. For each truncation scenario presented in Section 4.3.4, a 2D histogram with the distribution $< \Delta E/\Delta x >$ versus generated momentum is created, as displayed (for one case of truncation method) in Fig. 4.14.

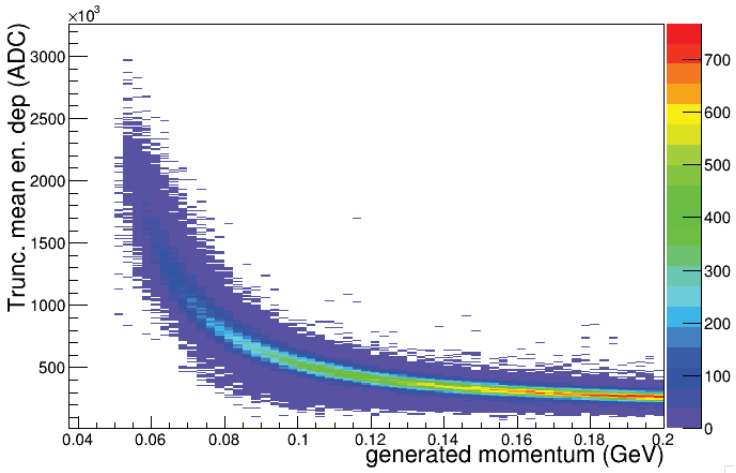


**Figure 4.14:** Truncated mean energy deposition $\Delta E/\Delta x$ (ADC counts) versus the charged particle momentum.

In a second step, distributions of $< \Delta E/\Delta x >$ are produced for each momentum bin of the histogram from Fig. 4.14. We want to estimate a "mean value" of each distribution, keeping in mind that the mean value of a Landau distribution is not the relevant variable. Hence, several ways to estimate the "mean value" were tried: the bin with the largest population, the mean obtained from a Gauss fit, the MPV obtained from a Landau fit and finally the MPV of a Moyal fit.
The mean of the Gaussian fit is not always at the same position as the MPV value observed in the distribution, therefore this method was not used any more. For the Moyal fit, the normalization parameter is free in the fit, but it needs as input a relatively well fine tuned value to converge properly. Since this method requires of carefully choosing the initial values of MPV and the normalization constant, and in the end the results are similar with a simpler Landau fit, the latter one was preferred for the estimations of the mean $< \Delta E/\Delta x >$.
A Landau fit example is displayed in Fig.4.15 for one bin in momentum. The $\chi^2$ / n.d.f of the fit may be sometimes high, generally because of a bad description of the starting slope or of the tail of the distribution, as illustrated by this example.

This does not harm our purpose which is a good determination of the MPV of the distribution.

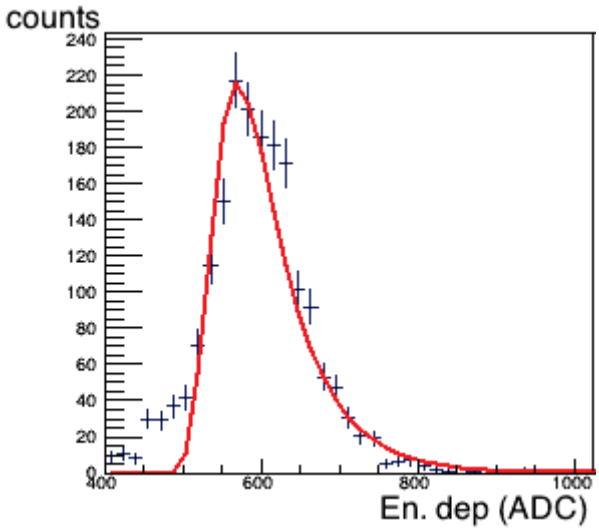


**Figure 4.15:** Estimation of the "mean value" (see text) of the $\Delta E/\Delta x$ for one momentum bin of the 2D histogram of the mean truncated $\Delta E/\Delta x$ as a function of the momentum.

From these estimated $< \Delta E/\Delta x >$ values we build the histogram shown in Fig. 4.16 displaying the momentum as a function of the mean $< \Delta E/\Delta x >$, with the parameterization of this curve superimposed. The parameterization is a function of $A/\sqrt{x}$ (corresponding to the $1/\beta^2$ dependence of the Bethe-Bloch function) where $A$ is the parameter of the fit to be determined. The fit is performed only up to a momentum of 120 MeV to stay in the $1/\beta^2$ region of the Bethe-Bloch curve. It appears that replacing the constant $A$ by a function of the momentum A($p$) could slightly improve this fit. At the level of this prospective study, this refinment is not considered being useful.
As a conclusion, our final estimator of low momenta is:

$$p = A/\sqrt{< \Delta E/\Delta x >} \tag{4.7}$$

where the fitted parameter $A$ was determined to be 73.3±1 for the final estimator.

### 4.4.2 Performances of the low momentum estimator

To fine-tune the $< \Delta E/\Delta x >$ estimated momentum, we look at the relative resolution obtained with each investigated algorithm. To conclude on the interest to

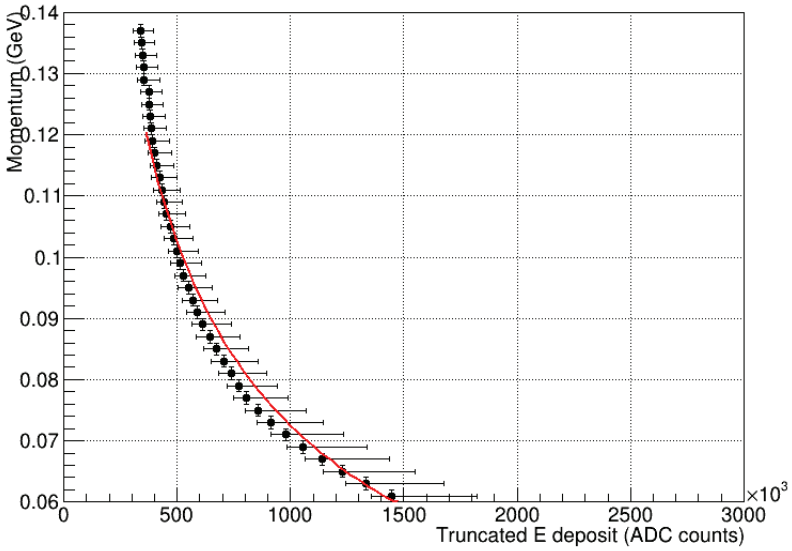


**Figure 4.16:** Momentum as a function of the mean truncated $\Delta E/\Delta x$ (as the MPV obtained from a Landau fit) with the parametrization 4.7 superimposed. The uncertainty error bars are asymmetric, one for the left and one for the right part of the MPV.

use this estimator, we compare its performances to the resolution obtained with the momentum estimated by the helix fit to the track.

#### 4.4.2.1 Momentum estimated from the helix fit

To estimate the resolution found on the momentum obtained with the helix fit to the track, we generate sets of 100 000 $\pi^{\pm}$, each set corresponding to a given momentum, ranging from 50 MeV to 140 MeV with steps of 10 MeV. The momentum reconstructed by the Belle II tracking algorithm is compared to the true generated momentum. The results are displayed as $(p_{rec} - p_{true})/p_{true}$ and are shown in Fig. 4.17 for each set of a momentum.

To compare with the resolution obtained with the proposed estimator based on $< \Delta E/\Delta x >$ we are here interested in the resolution on the momentum module rather than on the transverse momentum, which is the one directly collected from the helix fit. The resolution is estimated as one standard deviation of the obtained distribution, which is expected to be Gaussian. Actually, momentum resolution distributions are nicely Gaussian at high momenta, but we observe distortions of the distributions at low momenta.

We consider that 2 or even 3 distinct populations of events exist, described each by the corresponding Gaussian distribution. One set represents events for which the

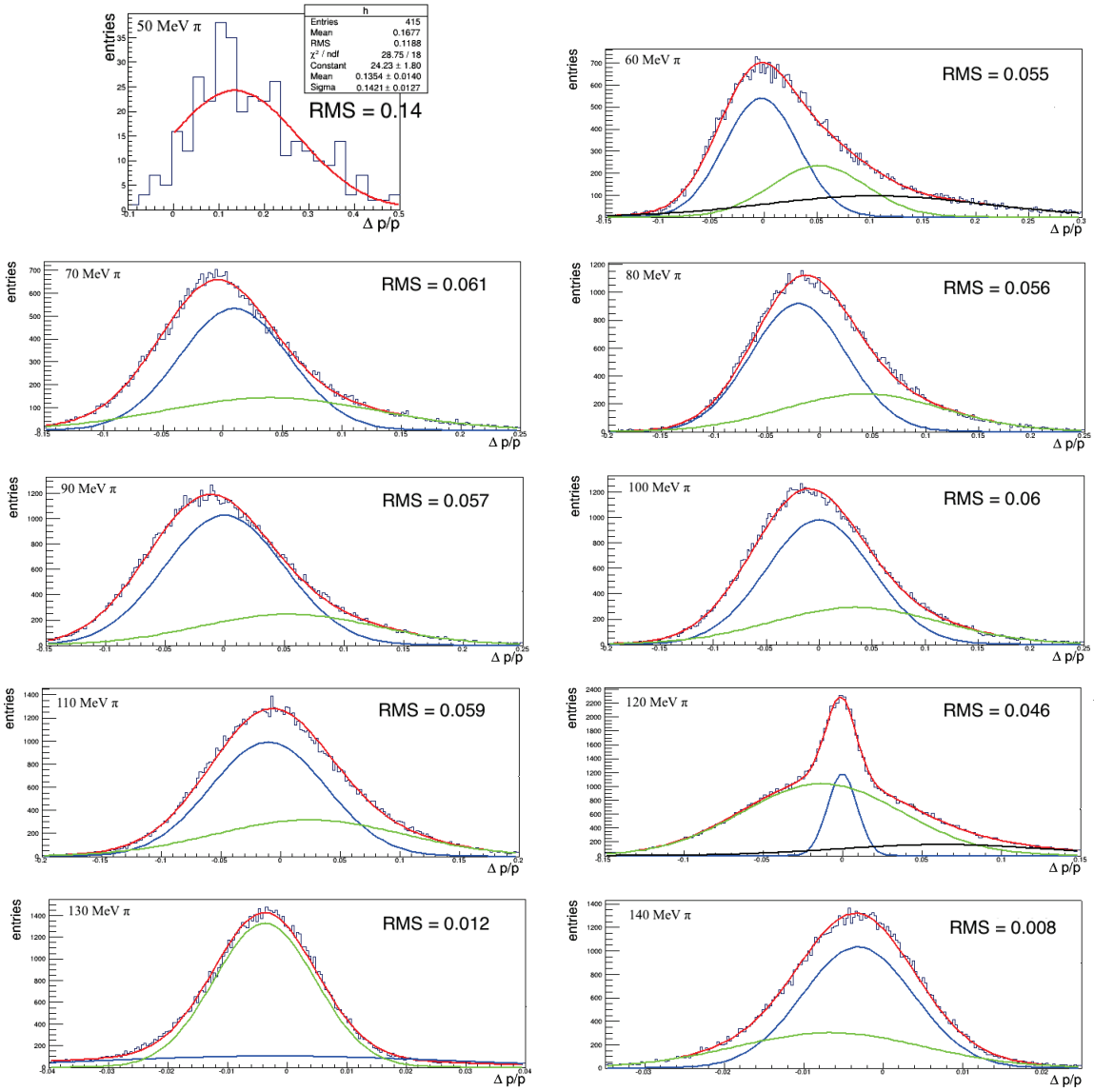


**Figure 4.17:** Helix-estimated momentum resolution for pions generated with an incident polar angle $\theta = 45°$. For 50 MeV pions, the fit was realized with half of a Gaussian, because no tracks with momentum below 50 MeV are reconstructed in Belle II. For reconstructed tracks of pions with momenta between 60 and 140 MeV, a sum of two or three Gaussians is used: each individual Gaussian is represented in blue, green or black and the sum in red.

momentum is correctly reconstructed, the other sets correspond to events for which the multiple scattering and the energy loss might not be properly taken into account, or even clusters belonging to another track might be improperly associated to the track. The conditions described in the latter case will result in a poor momentum resolution. Therefore, the resolution from the helix fit estimated momentum is defined as the population weighted mean of 2 (or more) Gaussian functions. The observed resolutions are displayed on each distribution on Fig. 4.17.

#### 4.4.2.2 Resolution on the momentum estimated by the $< \Delta E/\Delta x >$

In the same way as we operate for the classical estimation of the momentum based on the helix fit to the track, we study the resolution $(p_{rec} - p_{true})/p_{true}$ of our low momentum estimators based on $< \Delta E/\Delta x >$. In Fig. 4.18 the resolution distributions are displayed for pions with generated momenta ranging from 50 MeV to 140 MeV and a polar angle of 45°. Two Gaussian functions are also used to fit these distributions, and an effective resolution is defined in the same way as in the previous section. Resulting estimated resolutions are displayed on each distribution on Fig. 4.18.
After building the low momentum estimators with the different truncation methods introduced in Section 4.3.4, we can finally compare the best estimator using cluster informations from both PXD and SVD detectors and the best estimator using the SVD detector alone. This is displayed in Fig. 5.7. We observe that the energy deposition in the PXD detector provide useful information to improve the momentum estimation, as expected in paticular for the lowest momenta.

Then, we can finally compare the resolution of our proposed estimator, with the one obtained from the helix fit. The observed relative resolution is displayed in Fig. 5.8, for pions generated with a polar angle $\theta = 45°$. For the helix based estimator, we observe that the relative resolution improves with increasing momentum at very low momenta, because the Coulomb multiple scattering dominates the resolution at very low momenta. Then, the resolution reaches a plateau between 60-110 MeV, featuring a relative resolution of about 6 %. Finally, a significant improvement occurs at 120 MeV, which is the momentum enabling the track to significantly penetrate the CDC. Below 120 MeV, the momentum is estimated from a helix fit to a standalone-VXD reconstructed track. These numbers slightly vary with the polar angle of the incident track, and the ones shown here to illustrate our results correspond to $\theta = 45°$.
The tracking algorithm is still under development in Belle II and its performances are still evolving and improving. Currently, the relative momentum resolution reaches

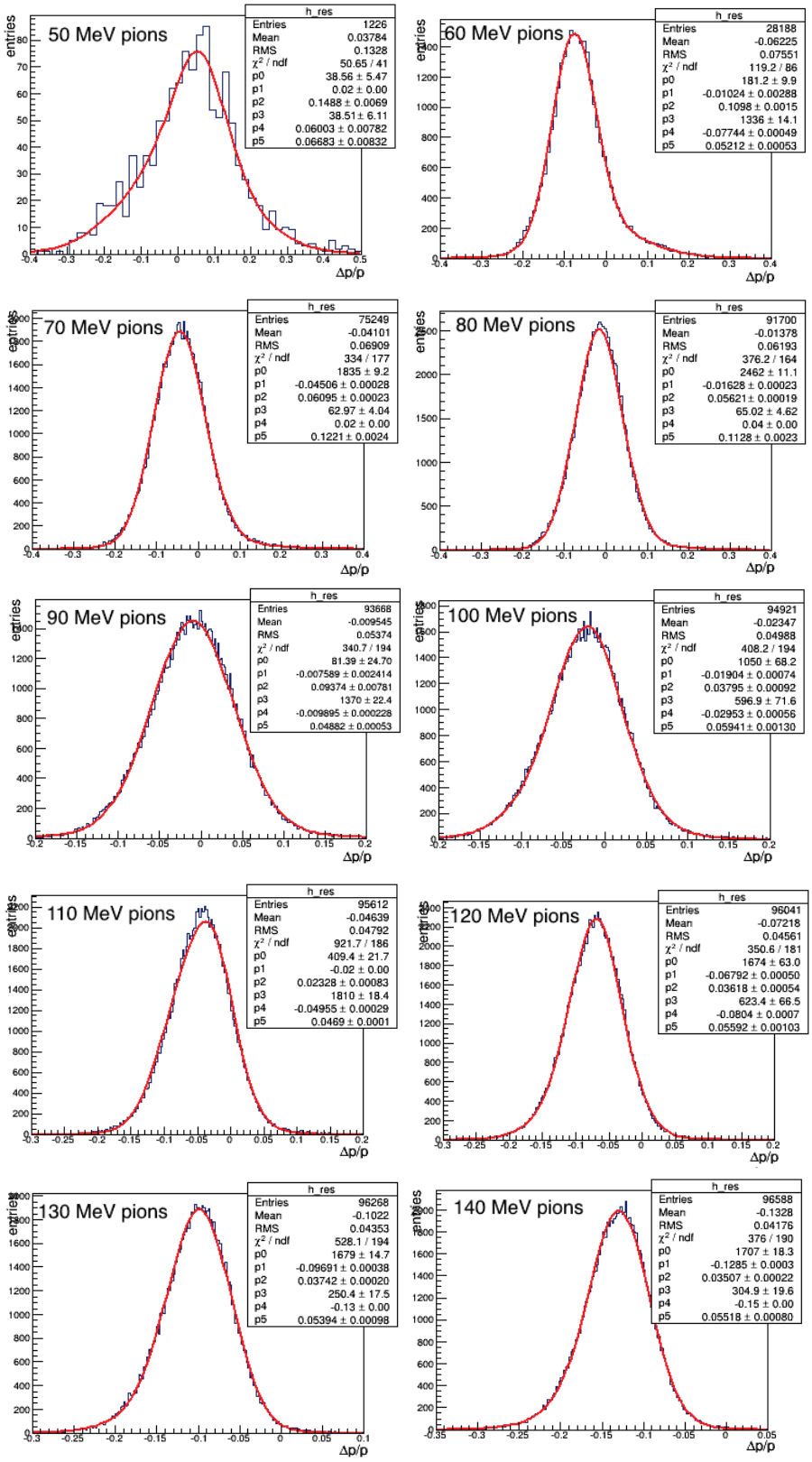


**Figure 4.18:** Relative momentum resolution observed in different momentum bias, of the estimator considering both PXD and SVD detectors, for pions generated with an incident polar angle $\theta = 45°$.

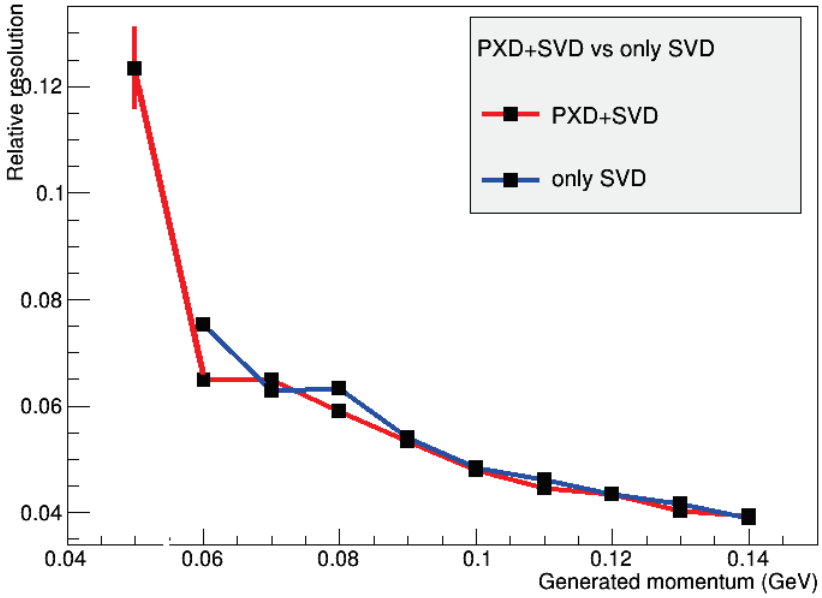


**Figure 4.19:** Comparison of the momentum resolution observed with a $\Delta E$-based estimator considering the 6 minimum energy deposition in both PXD and SVD detectors and an estimator considering the 4 minimum energy deposition only in the SVD detector. The pions were generated with uniform momentum distribution between 0.05 and 0.14 GeV, uniform azimuthal angle $\theta$ in the acceptance of the detector and an incident polar angle $\theta = 45°$. The error bars are smaller than the black squares for momenta higher than 0.05 GeV.

0.02 around 500 MeV - 1 GeV, then it degrades smoothly to reach about 0.05 at 4 GeV. We can see by comparing our method of low momentum estimation with the one from the helix fit that our proposed method gives slightly better to equivalent results for momentum in the range 0.05 - 0.12 GeV. All the figures and the results are shown here for $\theta = 45°$ incident angles, but all the angles were studied and the conclusion is unchanged.

## 4.5 Conclusions and outlooks

Low momentum tracks are particularly difficult to reconstruct, because they are very impacted by multiple scattering, they lose energy in the medium crossed as $1/p^2$ and they are curled in the magnetic field, resulting in a small lever arm of the track.

Since collisions are performed at a center of mass energy of about 10 GeV, final state particles are relatively soft, in the 1 GeV range. A significant fraction of

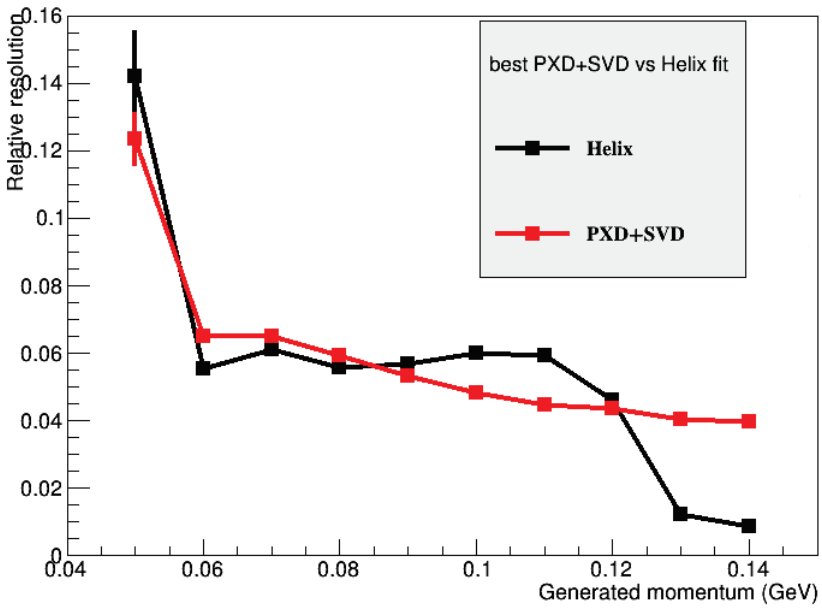


**Figure 4.20:** Relative momentum resolutions observed with the helix-based estimation (red colour) and with the dE/dx-based estimator (blue colour) for low pions generated with incident polar angle $\theta = 45°$. The error bars are smaller than the black / red squares for momenta higher than 0.05 GeV.

these particles are even produced with momenta below 150 MeV, hence they do not penetrate significantly the CDC and their reconstruction relies only on the VXD. However, they play an important role in the Belle II physics program.
In this chapter, we have showed an alternative method to estimate the momentum of a track, focusing on low momenta, below 150 MeV. For this we make use of the energy deposition in the 6 layers of the silicon detectors of the inner tracking system. We have shown that in this momentum range, the momentum resolution can be slightly improved with the $< \Delta E/\Delta x >$ estimator.
These results are encouraging and the Belle II collaboration considers making use of this information to improve the tracking algorithm in the very low momentum range. Several ways can be investigated to go further:

- The momentum resolution can be simply improved by combining the helix fit estimator, which is sensitive to the transverse momentum $p_t$ and the $< \Delta E/\Delta x >$ estimation, which is sensitive to the module $p$. The resolution will be improved roughly by a factor of $\sqrt{2}$.

- The track could be refitted with this input, improving the fit and possibly the impact parameter resolution in the end.

- The information of the cluster charges can be used to build a track index quality, helping the pattern recognition algorithm to choose among several cluster associations to build a track. This is of particular importance because of the pollution due to SuperKEKB induced background hits particularly impacting silicon layers detectors.

During this thesis, the tracking algorithm has always been evolving. As a consequence, our study is based on the clusters truly belonging to a same track, i.e. not the ones associated (with some efficiency and purity) by the tracking algorithm. Moreover, the SuperKEKB background influence was not taken into account. It would be then interesting to carry out this study again once the tracking algorithm is fully developed.

# 5. Performance studies of a PLUME ladder

## 5.1 Introduction

In Belle II, an important part of the physics program relies on time dependent measurements and on an accurate determination of decay vertices. Since the boost is lower than it used to be in the former Belle experiment, an improved vertex detector is needed, providing measurements closer to the collision point. Strip detectors are not able to sustain the high particle rate caused by the SuperKEKB induced background in the innermost detector layers. Indeed, the ghost hit rate is too high, up to radii of around 3.5-4 cm so these detector layers have to be pixelated. Several pixel technologies exist, such as hybrid, CCD, DEPFET and CMOS Pixels.

In Belle II, the vertex detector will be equipped with DEPFET pixels, as already described in Chapter 2. However, for the commissioning of the experiment, a pixelated device will be used to characterize the SuperKEKB induced background and to validate its simulation.

This chapter is devoted to the presentation of PLUME beam test studies. It introduces CMOS pixel sensors in Section 5.2 and the MIMOSA-26 CMOS chip equipping the PLUME ladder, in Section 5.3. In Section 5.4 the PLUME ladder is presented. The beam test setup is sketched in Section 5.5. The last two sections are dedicated to the beam test studies conducted in this thesis: the measurement of the gap between two sensors mounted on the ladder in Section 5.6 and tracking performances with tilted tracks in Section 5.7.

## 5.2 CMOS Pixel Sensors

The development of CMOS (Complementary Metal-Oxide-Semiconductor) pixel sensors, or shortly CPS, started in the early '90s with a demand in simple, low power and cheap imaging devices. Now, they are used for various fields like medical imaging, space devices and consumer electronics. One of their purpose is to replace CCDs in the visible imaging [133]. In 1999, the Strasbourg group proposed to use these sensors for charged particle tracking [134]. This development was driven by the requirements of the future experiment TESLA linear collider (now, International Linear Collider or ILC).

### 5.2.1 General considerations

The vertex resolution is directly related to the impact parameter resolution $\sigma_{IP}$ which can be written with the compact relation:

$$\sigma_{IP} = a \oplus \frac{b}{p \cdot sin^k\theta} \tag{5.1}$$

The impact parameter $\sigma_{IP}$ is defined as the distance of closest approach of the track to the colliding point. In Eq. 5.1, $p$ is the momentum of the particle, $k = 3/2$ for the $R-\phi$ projection and $k = 5/2$ for the $z$ projection and $\theta$ is the track polar angle. We consider a two layers detector, with the first layer along the particle direction situated at a distance $R_1$ and the second layer situated at a distance $R_2$ to the collision point. The term $a$ is related to the detector layers intrinsic resolution ($\sigma_1$ and $\sigma_2$) and their distance to the collision point. The term $b$ accounts for the resolution degradation due to multiple scattering and includes the distance $R_1$ and the path of the particle in the first layer. Neglecting the magnetic field, we can write the two terms as:

$$\begin{aligned} \mathrm{a} &= \frac{R_1\sigma_2 \oplus R_2\sigma_2}{R_2 - R_1} \\ \mathrm{b} &= R_1 \cdot \frac{Z \cdot 13.6\ \mathrm{MeV}}{\beta \mathrm{c}} \cdot \sqrt{\frac{x}{X_0 \cdot sin\theta}} \left[1 + 0.038 \cdot ln\left(\frac{x}{X_0 \cdot sin\theta}\right)\right] \end{aligned} \tag{5.2}$$

where $Z$ is the charge of the particle, $\beta = v/c$, $x$ the thickness of the detector layer, $\theta$ is the polar angle of the incoming particle and $X_0$ is the material budget.

Particularly for low momenta particles, as it is the case at SuperKEKB, multiple scattering may significantly degrade the vertex resolution. Therefore, pixel detectors featuring the lowest material budget are the most appropriate. This criteria eliminates the hybrid pixel technology, since the material budget is too high, at the 1 % level. The CCD technology is not suitable neither, because of two aspects. The first one is the long integration time (at the ms level) with respect to the background rate accumulated during the whole integration time. Faster CCD exists, but at the cost of a very high power dissipation, requiring heavy cooling devices and increasing the material budget. The second aspect is the radiation tolerance of the CCD sensors which is not good enough for the Belle II requirements. As a conclusion, only DEPFET [77] and CMOS pixel technologies can currently work in the Super KEKB environment.

### 5.2.2 Benefits of CMOS Pixel sensors

CMOS pixel sensors (CPS) feature advantageous performances to equip Flavour Factory experiments, offering a low material budget. The useful signal is created in a thin epitaxial layer, with a typical width between 10 to 20 $\mu m$. Because the thick silicon substrate does not participate to the detection, it can be reduced without affecting the sensor performances. Therefore the sensor can be thinned down to 50 $\mu m$ or even less, corresponding to a material budget below 0.05 % $X_0$. Taking advantage of the sub-micron CMOS technology, the signal processing (amplification, noise subtraction, discrimination, digitization, etc.) can be integrated on the same substrate. Therefore, CPS are truly monolithic sensors, with the electronics incorporated in the pixel.

Another advantage of CPS is the high granularity. The typical pixel size varies between 10 and more than 100 times the minimal feature size of the fabrication process. This means that a pixel pitch smaller than 10 $\mu m$ can be built with a submicron technology. This is a real asset in order to limit the occupancy rate. A small pixel pitch also reduces the spatial resolution as long as the multiple scattering is not too high. For demanding applications, with analog readout, a spatial resolution of less than 1 $\mu m$ can be achieved [135], but for a detector with many pixels, this leads to difficulties in reading all the pixels in a short time.

Another type of asset of the CMOS technology is that it relies on an industrial technology, implying low cost and good fabrication yields. Moreover, driven by the market, the technology keeps improving.

### 5.2.3 Finding the optimal working point

Constraints put on a vertex detector are governed on one side by running conditions, as in the case of LHC, where the detectors have to be fast and radiation hard. On the other hand, their characteristics are driven by the targeted physics performances, as in the case of Belle II. All these performances are correlated, e.g. a fast read-out of a huge number of pixels can be obtained by reading them at least partially in parallel, implying a high dissipation and requiring active cooling, i.e. increasing the material budget. This correlation between the detector performances is illustrated in Fig.1 with a "squaring the circle" problem. In the end, the design of an inner tracker always results from a compromise between all the performances.

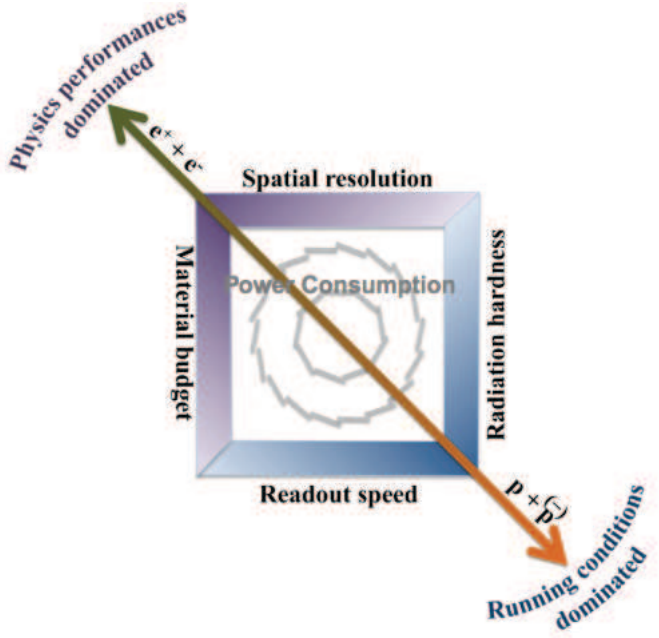


**Figure 5.1:** Illustration of the correlation between all the performances which looks like a problem of squaring the circle. Image taken from [136].

As an example, we give the ILC case, since the *R&D* of CPS for charged particle tracking was driven many years by their requirements. The physics goals of ILC impose very strong conditions on the performances of the vertex detector, beyond what was achieved until now. The ILD Letter of Intent [137] ambitiously demands parameters $a$ and $b$ of the Formula 5.1 to be below 5 $\mu$m and 10 $\mu$m·GeV/c respectively. This implies a material budget of 0.3 % and 0.15 % $X_0$ per layer for the double- and single-sided layer option respectively, a single point accuracy below 3 $\mu$m and a vertex detector as close as 15 mm from the IP.

In the following we will explain how CMOS sensors are particularly flexible to choose the best suited working point as a function of all these performances.

### 5.2.4 CMOS sensors working principle

Two types of CMOS sensors exist today: passive and active. For passive sensors, a photodiode is integrated in a pixel together with selection switches. The latter connects the photodiode directly to the readout output line. For active sensors, each pixel includes an integrated amplifier which buffers the charge signal. Because of their better performances (superior noise performances, electron noise can be as low as 4.5 electrons r.m.s. at room temperature [138]), most of the CPS are equipped with active pixels.
A cross section with an active CPS is displayed in Fig. 5.2. When a charged particle crosses the semi-conducting sensitive volume, electron-holes are created along the path. About 80 electron-holes / $\mu m$ are produced in case of a minimum ionizing particle (or MIP) crossing a silicon layer. The transport of charges is realized through diffusion and drift. Electrons produced in the epitaxial layer by one charged particle diffuse to adjacent pixels, where they will be collected by the diodes. Clusters can be reconstructed with a cluster reconstruction algorithm from the diode signals, and the pixel that collects most of the signal is identified as the seed pixel.

It is better to work with fully depleted epitaxial layers. Indeed the charge collection is improved in presence of an electric field, the carriers moving faster are less trapped in the lattice defects, and the recombination rate is lower because the electrons and holes are moving in opposite directions. However the standard CMOS processes are usually of relatively low resistivity and not compatible with high electric fields. As a consequence, as it is represented in Fig. 5.2, the electric field is present only in the vicinity of the electrode and the charge from the undepleted active volume is collected through thermal diffusion. This aspect can be overcome by using a high resistivity epitaxial layers, which will lead to a deeply depleted region. Depleted CPS prototypes do exist now and the concept was already validated for small prototypes [139].

### 5.2.5 Basic pixel architectures

The basic cell architecture is the ”three transistors” or 3T architecture, and the pixel operation requires three transistors: a reset switch M1, which resets the photodiode

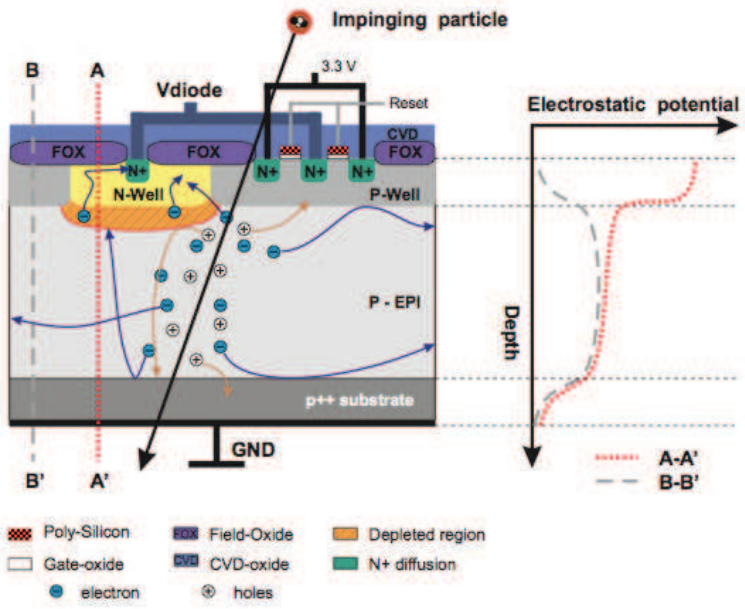


**Figure 5.2:** Transverse cross section of an active CPS (left) and the electrostatic potential through the sensor substrate (right), taken from [140]. Charges are created along the path of the particle in the epitaxial layer, where the doping is low enough to allow these charges to diffuse thermally towards the sensing element. The depleted region, in brown, represents a small part of the whole sensitive volume.

to reverse bias, the input M2 of a source follower and a row selection switch M3, as displayed in Fig. 5.3 (a).

Because of the leakage current, the voltage will drop in the sensing diode. To compensate for this drop, the sensing diode is periodically connected to the reference potential $V_{diode}$. The signal is integrated within the time separating two consecutive reset operations.

Another pixel architecture is the self-biased architecture, which was proposed for applications with low or moderate occupancies. The charge sensing diode $D_1$ is reverse biased, while the diode $D_2$ is biased in the forward direction. This device features a logarithmic response, but for small input signals, the response can be approximated by a linear behaviour [141]. When the reverse biased diode collects the charge, the voltage on the diode drops and a slow recovery follows. At equilibrium, the forward-biased diode only conducts the leakage current from the sensing diode. This current is usually small, in the range of 1 fA, and the diode dynamic resistance R is very high. The structure operates as a constant reverse bias and this is why

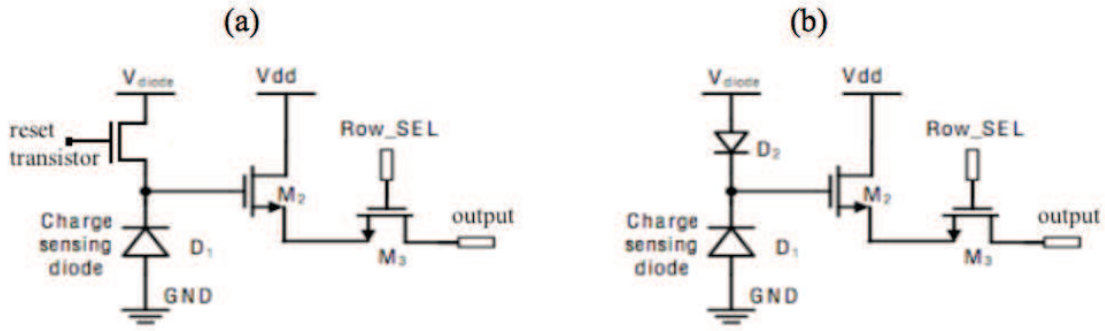


**Figure 5.3:** Schematic view of the 3T baseline pixel architecture (a) and of the SB baseline architecture (b).

it is referred to as self-biased (SB) diode. The pixel architecture of the SB diode appears in Fig. 5.3 (b).
This structure presents some advantages with respect to the 3T architecture. First of all, no periodical reset is needed to compensate for the sensing diode voltage drop, therefore there is no pedestal to be removed during the signal extraction (but correlating double sampling is needed, and this will is explained in the next section). Furthermore, since no reset transistor is used, the fixed pattern noise originating from the reset-transistor non-uniformities is eliminated. Last but not least, there is more space to implement in-pixel electronics.

### 5.2.6 Conclusion

The physics objectives of the existing or of the future particle physics experiments demands vertexing and tracking performances calling for a specific pixel technology. But the performances of a vertex detector result from a compromise between different conditions. Thanks to their low cost, precision, lightness and low power consumption, CPS are good candidates to be used in particle physics experiments. The CPS developed in Strasbourg have already been used to equip operating devices in subatomic physics: TAPI, a general purpose beam telescope [142–144], EUDET, a two arms (each with three measurement planes equipped with MIMOSA-26 sensors) telescope [145–147], the pixel detector of STAR-RHIC, operating since 2014 (equipped with MIMOSA-28 sensors, with similar characteristics as MIMOSA-26) [148]. A non exhaustive list with the upcoming projects based on or considering CPS developped by the Strasbourg group includes the upgrade of the ALICE inner tracker [149, 150], BEAST II [151], CBM [152] and ILC [153].

## 5.3 MIMOSA-26 Sensors

### 5.3.1 Introduction

The first prototype of the MIMOSA (Minimum Ionising particle MOS Active pixel sensor) series was fabricated in 1999. It was successfully and extensively tested, providing a detection efficiency of 100 % [154]. Other prototypes followed since then, with several fabrication processes, a full list can be found here [155].
MIMOSA-26 is the first full scale digital sensor (the output is 0 if the collected charge is lower than a certain threshold and 1 otherwise) of the MIMOSA series with integrated signal processing. The chip layout is displayed in Fig. 5.4.

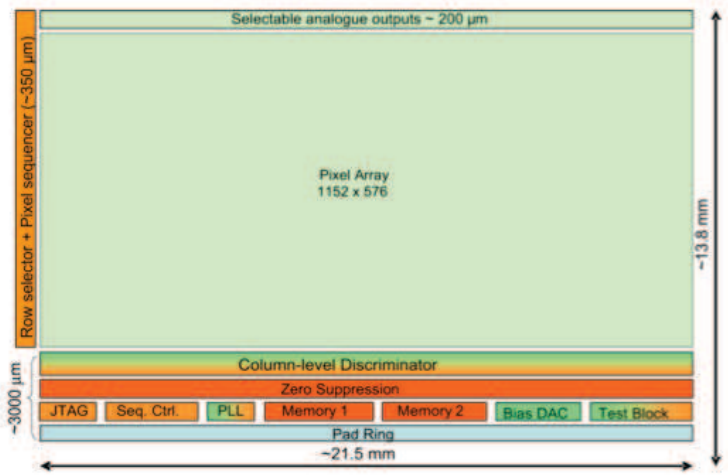


**Figure 5.4:** MIMOSA-26 layout.

The fabrication process is based on an AMS 0.35 $\mu$m technology, providing an epitaxial layer of thickness 14 $\mu$m. The sensors studied in this chapter have epitaxial layers of moderate resistivity (standard epitaxial), lower than 0.1 k$\Omega$ cm. This technology is mature, already being used for previous MIMOSA pixel sensors.

### 5.3.2 Working principle

The MIMOSA-26 sensor contains 576 rows and 1152 columns, with square pixels pitch of 18.4 $\times$ 18.4 $\mu$m$^2$ based on the SB architecture. Each pixel contains a preamplifier and circuits performing the correlated double sampling. At the end of each column, there is a column level discriminator. The amplified signals are compared to a fixed threshold with the help of the column level discriminators. Their binary output is sent to the zero suppression logic.

### Correlated double sampling

The Signal to Noise Ratio (SNR) is an important figure of merit of a sensor, being directly related to basic performances like efficiency versus rate interplay and spatial resolution [156]. One way to improve the SNR is to use a correlated double sampling (CDS). This method consists in collecting two signal samples during the readout of the sensor, afterwards the signal is calculated as the difference between the first and the second sample. The different types of noise of the sensor are either completely removed or diminished with the correlated double sampling. The process can be performed inside the pixel or at the sensor periphery. The first method aims at eliminating the reset noise and the second at minimizing pixel to pixel dispersions caused by mismatches of the threshold voltage of the in-pixel source follower.

### Read-out architecture

Reading all the pixels can become a complicated task for sensors with many pixels, like MIMOSA-26 consisting in $6.6\times10^5$ pixels. The detector will be slow and dissipate a lot of power. A solution for this issue is to group pixels in arrays of pixels and to multiplex the signal to an individual bus line. For MIMOSA-26 sensors, the pixels are grouped in lines, and one line is read at a time, in the so-called rolling shutter mode. Since only a single line of pixels is turned on at the time, this architecture allows to limit the power consumption. This procedure is explained in Fig. 5.5. Once all the lines in the matrix are read out, the process restarts from the first line.

### Zero suppression

The zero suppression of the MIMOSA-26 chip is named SUZE-02 (acronym of SUppression de ZEro No 2). Because of the large number of pixels composing a sensor (about 660 000) and of their read-out frequency of about $10^4$ frames/s, the data flow is very high. In order to reduce the data flow and to relax the requirements on the data acquisition system, the zero suppression circuitry is located just after the discriminators [157]. The discriminators select all the pixels presenting a charge above a chosen threshold and transfer this information to the zero suppression circuitry. Only the address of fired pixels and their neighbours are used. This procedure is based on a Priority Lock Ahead (PLA) algorithm, more details on the algorithm can be found in [158] .
SUZE-02 is advantageous because it is fabricated with the same process as the

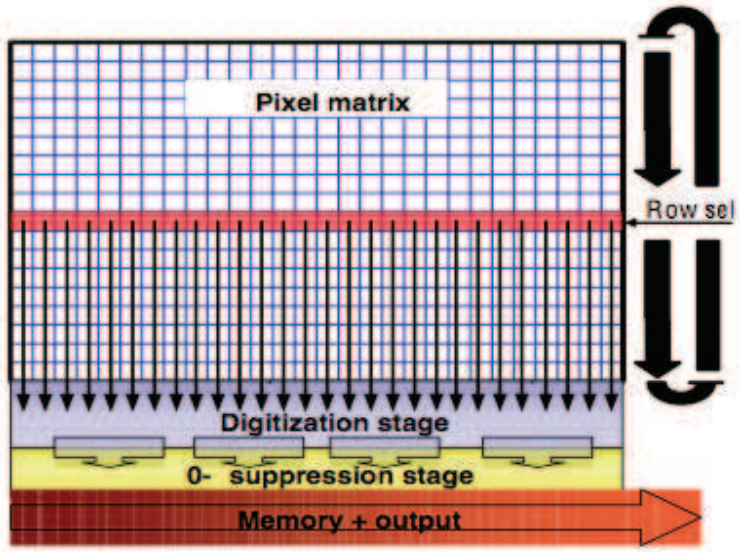


**Figure 5.5:** The readout scheme consisting in reading a column at a time. Figure taken from [159] .

sensing part, therefore integrated on the same chip. It is located at the bottom of the 1152 discriminators, occupying an area of 21.5×0.62 $mm^2$, as displayed in Fig. 5.4. The data flow can be suppressed by a factor of 10 to 1000, depending on the occupancy.

### 5.3.3 Performances

The MIMOSA-26 sensor features a readout time of 112 $\mu$s, with a low dissipated power of 350 $mW/cm^2$. The sensor chip was validated to sustain a 300 kRad ionizing dose in order to be used in the STAR experiment. But the sensor can work even up to 500 kRad, using a higher discriminator threshold, or by cooling the device.

Its performances (observed in a beam test) in terms of efficiency, fake hit rate and spatial resolution as a function of the discriminator threshold are displayed in Fig. 5.6. For thresholds below 6 mV (see Section 5.7.1 for the corresponding noise units) the sensor presents an efficiency better than 98 % and a spatial binary resolution of about 3.5 $\mu$m.

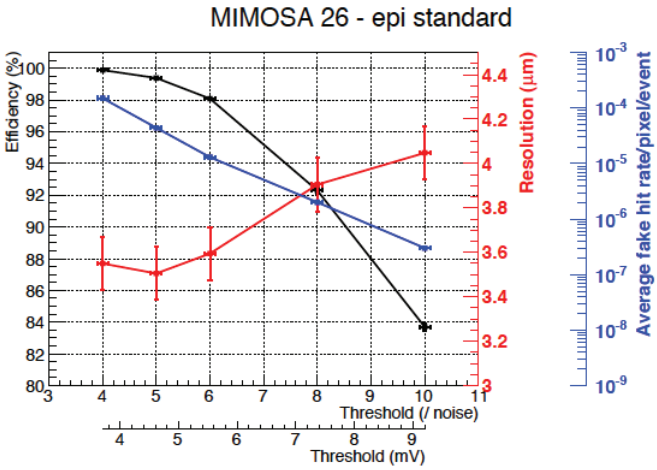


**Figure 5.6:** Performances of the MIMOSA-26 sensor with a standard epitaxial layer 14 $\mu$m thick. [160].

## 5.4 The PLUME ladder

System integration of pixel sensors is a key point to limit the material budget, in order to keep the advantages of CPS. Two projects explore the integration of CMOS pixel sensors into ladders:

- PLUME, a double-sided pixelated ladder with a sensitive length of 12.5 cm and a thickness of 2 mm, targeting a total material budget of 0.3 % $X_0$ [161].
- SERNWIETE, a single-sided ladder where the sensors are wrapped in a polymide-based micro-cable, with a material budget around 0.15 % $X_0$ [162].

We focus here on the PLUME ladder.
PLUME stands for Pixel Ladder using Ultra-low Material Embedded. The laboratories implied in its R&D are: DESY-Hamburg, University of Bristol, IPHC-Strasbourg and formerly University of Oxford.
In order to settle the fabrication and the beam test procedure, a first prototype of material budget 0.6 % $X_0$ was fabricated in 2009. It was composed of 2 MIMOSA-20 analog output sensors on each side, thinned down to 50 $\mu m$, providing a 1×4 cm$^2$ large sensitive area. This prototype was tested in November 2009 at CERN-SPS with a 120 GeV pions beam and confirmed an expected improved spatial resolution by associating the hits on the two sides [153].
Following this prototype, a design called PLUME-1 has been fully validated. This prototype still features a material budget of 0.6 % $X_0$, because the stress was put on electrical operation and tracking performances, and not on the material budget

(which is the goal of the future prototype). It consists of a double-sided ladder equipped with six MIMOSA-26 epi-standard sensors of standard resistivity on each side. The sensors are thinned down to 50 $\mu m$ and glued on a kapton-copper cable, as displayed in Fig. 5.7. This cable is then fixed on a 2 mm silicon carbide foam (SiC of density 8 %). This foam presents several advantages: low material budget, stiffness, it is commercially available and macroscopically uniform. Therefore, the foam density can be decreased even below 8 % in the future.
Most of the stiffness of this device comes from a sandwich effect between the sensors and the foam rather from the foam itself, which serves essentially as a spacer.

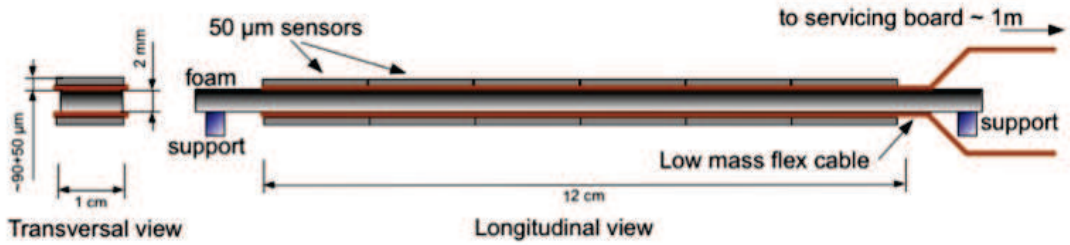


**Figure 5.7:** The layout of the PLUME-1 ladder, composed of 6 MIMOSA-26 sensors thinned down to 50 $\mu m$ placed on each side of a foam.

Such a double-sided pixelated device presents several important added values. Because the two layers are close to each other, it is easy to associate the two hits induced by a same crossing charged particle, improving the spatial resolution by a factor of $1/\sqrt{2}$. A mini-vector can also be reconstructed with the two associated hits, as detailed later in this chapter. This procedure using mini-vectors provides an angular information on the incident track, with particularly interesting applications in fast and robust detector alignment as well as in (collider induced) background hits identification.
In the following, results obtained with data recorded during the November 2011 beam tests and analyzed as part of this thesis will be presented:

- An estimation of the gap between two adjacent sensors on the PLUME ladder.
- A study of tracking performances with tilted tracks.

The first point is related to the fabrication procedure, and the results will be used to build the next PLUME prototype. The results of the second point may be used to account for the added value of the prototype. Currently, an improved ladder is being produced, PLUME-2. This new ladder will be equipped with a lighter flex cable (where the copper is replaced with aluminum) and a lower 4 % density foam.

These improvements will allow to reach the targeted material budget of 0.3 % $X_0$ for the double-layer. This new ladder is the one that will be used during the BEAST II commissioning of the Belle II experiment.

## 5.5 The PLUME beam test setup and the analysis procedure

### 5.5.1 Beam test setup

The data taking was performed in November 2011 at CERN-SPS, with a beam of 120 GeV negative pions. The bench setup of the beam test consists of a pixel telescope, a 7×7 $mm^2$ scintillator and the PLUME ladder, from now on referred to as the DUT (Detector Under Test). The layout of the DUT, with the numbering scheme, is displayed in Fig. 5.8. In order to keep the temperature of the sensors stable, an air flow cooling system (containing a fan) was used for the DUT.
The pixel telescope is composed of two arms, each arm containing two 120 $\mu$m-thin MIMOSA-26 sensors, separated by a 5 mm distance, as shown in Fig. 5.9.
The data acquisition is triggered by the scintillator, placed on the beam axis. Several data runs were registered, varying one or more parameters at a time (like DUT threshold, air flow cooling) for the same or a different configuration of the bench setup.

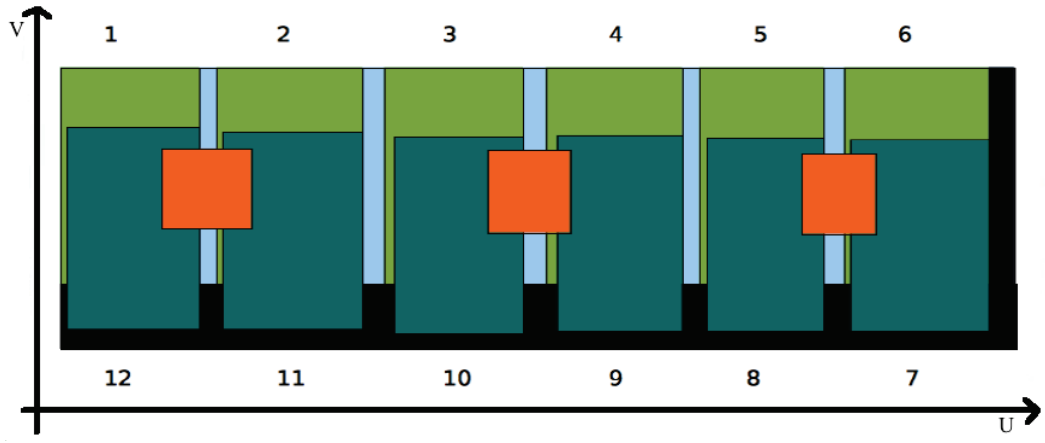


**Figure 5.8:** The PLUME ladder equipped with 12 sensors, 6 on each side. The 6 sensors of one side of the ladder (dark green) are slightly shifted along the $V$-axis with respect to the sensors from the opposite side of the ladder (light green). The beam spot on the sensors is illustrated in orange.

Two Cartesian coordinate systems are employed: one global, including all the sensors of the telescope, and one local, attached to each individual sensor. The global coordinate system uses $(x, y, z)$ notation, where $+z$ is along the beam axis, $+y$ is taken as the vertical up direction and $+x$ is the horizontal direction, according to the right-hand rule. In the local coordinate system the $(u, v)$ notation is used, where $u$ is the horizontal axis along the sensor (defined by the read-out direction along the pixel lines) and $v$ is the vertical axis along the sensor (along the pixel columns). The origin $(0, 0, 0)$ of the global coordinate system is fixed in the center of one sensor of the telescope that is referred to as the primary reference plane. For each studied sensor, the origin $(0, 0)$ in the local coordinate system is taken in the center of the pixel matrix. For alignment purpose (detailed in Section 5.7.5.1), six parameters are defined for each sensor of the telescope or the DUT: three are spatial translations along $Ox$, $Oy$ and $Oz$, and three are rotations around these axes.

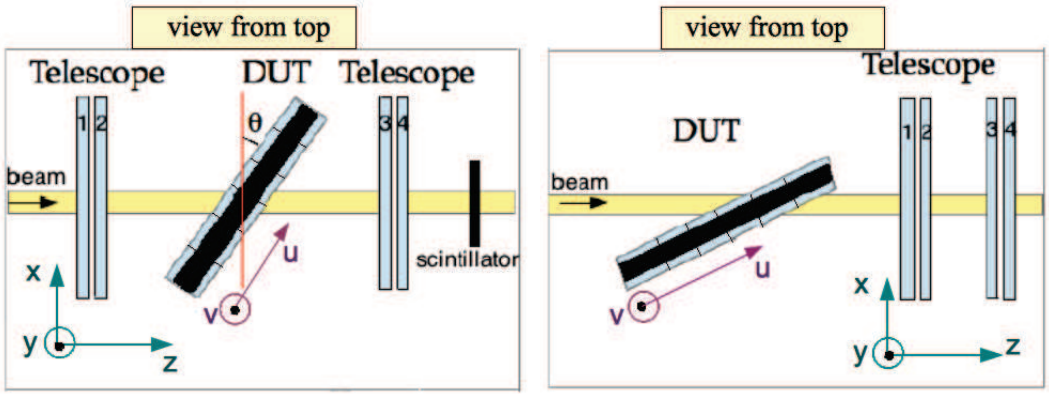


**Figure 5.9:** Views from the top of the setup used for the runs registered with DUT tilts $\theta$=0°, 36° (top) and 60° (bottom). The distances are measured from the center of the PLUME device to the center of each telescope arm. The numbering scheme used for the telescope sensors increases from the beam side. The telescope planes, DUT and the distances between them are not in scale.

In the two studies reported in this chapter, the position of the DUT during the data taking was the following:

- To estimate the gap between two adjacent sensors, the DUT was placed in the center of the telescope, at $z = 0$ and $\theta = 0°$ (perpendicular to the beam). The DUT was translated along $Ox$ so that two sensors are crossed by the beam, as displayed in Fig. 5.8.

- For the second study, the position of the DUT is shown in Fig. 5.9. For $\theta = 36^o$, the DUT was placed at the center of the telescope, but for $\theta = 60^o$ the DUT was lodged outside the telescope arms, because there was not enough space to keep it between the two arms. The DUT was also translated along $Ox$ so that the beam spot was always centered on one sensor.

The beam test data analysis is performed with TAF v 2.8.1. TAF stands for Télescope à Pixels de l'IPHC Analysis Framework. It is an analysis framework created at IPHC to characterize CPS from data acquired with different sources, like X-,$\alpha$-,$\beta$-rays, laser, electron or proton beams. The documentation on TAF can be found in [163].

### 5.5.2 Alignment of the telescope

In order to study the DUT, we have to align the telescope sensors and the DUT itself. This means knowing precisely all positions in a common coordinate system. The relative position of the sensors composing the telescope and the DUT are obtained $in-situ$ at the mm level from a metric survey done during the beam test. But a precision at the $\mu$m level can only be achieved with a software alignment, as, in our case, with TAF software. Three parameters will be used to align the telescope sensors: one accounting for the position along the $x$-axis, one for the $y$-axis and one rotation around the $z$-axis. The $z$ position of each telescope sensor is fixed to the position measured during the metric survey. The alignment is less sensitive to the $z$-position, therefore the millimetric precision provided by the metric survey is satisfactory.

#### 5.5.2.1 Prerequisites of the alignment procedure

The alignment of the test bench and the beam test analysis relies on hits measured in the sensors and reference tracks reconstructed with the telescope.

**Hit reconstruction**

After the signal extraction and the data processing, pixels measuring a signal greater than the chosen threshold (set on the signal level or on the signal-to-noise ratio) are grouped in clusters. Because MIMOSA-26 is a digital sensor, we do not have direct access to the seed pixel (the pixel with the highest charge collection). To register a hit candidate, an additional condition can be put on the number of pixels in a cluster. Studies done on the IPHC CMOS pixel sensors showed that all the charge is

collected within 5×5 pixels around the pixel which was the closest to the traversing particle. The hit position is finally obtained from the center-of-gravity calculation [164, 165] (using a simple average here for a binary output sensor) and registered in the local coordinate system.

**Track reconstruction and residue**

At the beginning of the alignment procedure of the telescope sensors, track candidates are built as perpendicular lines starting from the hits found in the first sensor. This sensor is usually chosen to be the first sensor in the beam direction, and is referred to as the primary reference plane. Its coordinates are taken to be (0,0,0) in the global reference system. Once all the telescope sensors are aligned, as detailed later in this section, the track candidates are reconstructed through a linear fit including the hits reconstructed in all the telescope sensors. A track candidate is dismissed if it is made of less than 4 hits, one in each sensor of the telescope, or if the fit $\chi^2$ is greater than a chosen value.

The alignment procedure is done in an iterative way, by minimizing the residue. This measure represents the difference (it can be taken along $x$ or $y$ axes) between what is considered to be the real (or predicted) hit position and the actual hit position found in the sensor. The real (or predicted) hit position is the extrapolated track candidate position on the sensor we want to align.

**Alignment assumptions**

The alignment procedure is performed in the $(x, y, z)$ reference system and is based on two assumptions:

- The four telescope sensors are parallel. A position of one sensor can be therefore transformed into another through geometrical operations limited to 2 spatial translations ($\Delta x$ and $\Delta y$) and one rotation.
- The tracks are perpendicular to the telescope detector planes. This is true in absence of a magnetic field and if the Coulomb multiple scattering (in a sensor) is negligible which is actually the case with high energy pions.

#### 5.5.2.2 Alignment procedure

**Alignment procedure for one sensor**

The alignment of a sensor is an iterative procedure. A hit found in the sensor is associated to a track candidate only if it is found in a certain window around the predicted hit position. If more than one hit is detected in this window, the closest

one to the predicted hit will be associated to the track. This search window is wide at first iterations, in order to discern large offsets. The process is repeated several times, each time decreasing the search window, in order to minimize the errors due to fake hit associations.

The alignment procedure consists in minimizing the residue along the $x$ and $y$ axes observed for each track. The alignment is obtained when the residual distribution observed with many reference tracks presents a Gaussian shape centered in zero, with a distribution width of the order of a few $\mu$m.

**Alignment procedure for all sensors of the telescope**

The closest sensor to the primary reference plane is the one aligned first with the procedure described above. After alignment, this sensor is defined as a secondary reference plane. Tracks are reconstructed with a simple linear fit starting from the primary and the secondary reference planes and extrapolated towards the second telescope arm. The rest of the telescope planes are aligned with respect to these two planes. After a first alignment of all the telescope sensors, the secondary reference plane is set as one sensor from the second telescope arm and the alignment procedure is re-iterated. In this way we perform a better alignment of the sensors, having a larger lever arm.

Once the alignment is completed, the three parameters defining the position of each sensor are updated in the database with the correct positions and angle.

The distribution of the residues, defined as $x_i$ - $x_{ref}$, where $x$ is the considered coordinate and $i$ the considered sensor obtained after alignment of the telescope, are shown in Fig. 5.10 and in Fig. 5.11. These distributions are centered at zero with a width around 3 $\mu$m.

**Alignment procedure for the DUT placed perpendicular to the beam**

After aligning the telescope, the DUT can also be aligned, using reference tracks reconstructed with the telescope. For the perpendicular position of the DUT (tilt = 0$^o$), the same alignment procedure is used, but with 5 position parameters: three rotation angles and two shifts (z-position is again fixed).

The alignment of the perpendicular DUT is straightforward and the observed residue is about 4 $\mu$m, as we can see from Fig. 5.12, where the residue obtained with the sensor number 2 two is shown. A similar residual distribution width was obtained for sensor 11, included in Appendix B. The DUT alignment in case of DUT tilts

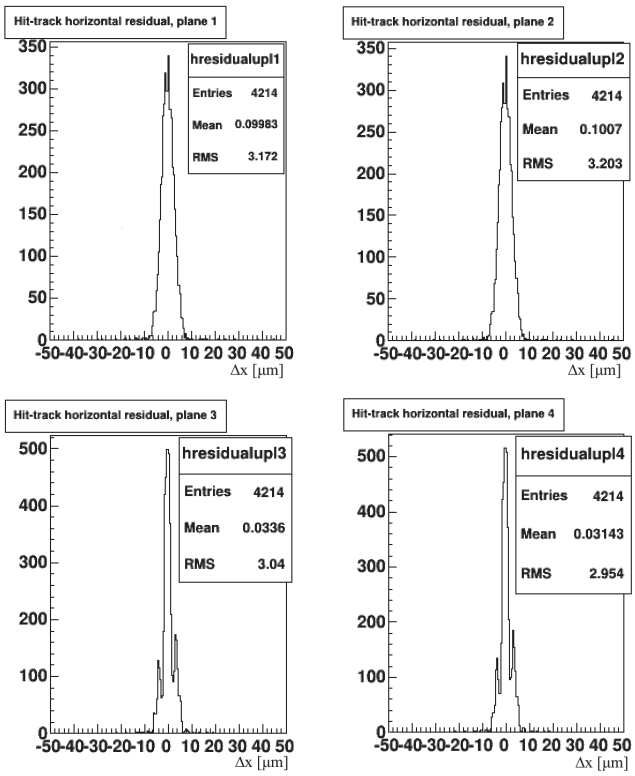


**Figure 5.10:** Distribution of the residues $\Delta x = x_{track} - x_{hit}$ (horizontal axis) after the telescope alignment procedure of the four telescope sensors.

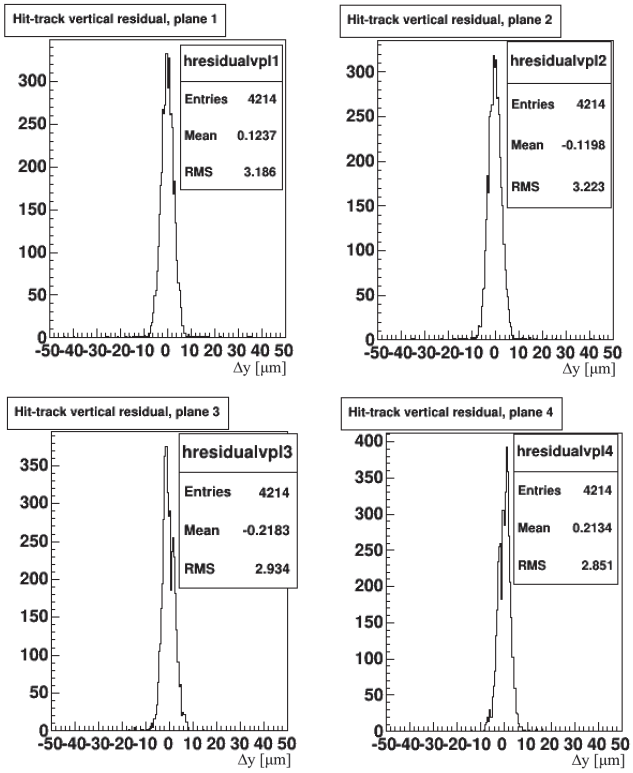


**Figure 5.11:** Distribution of the residues $\Delta y = y_{track} - y_{hit}$ (vertical axis) after the telescope alignment procedure of the four telescope sensors.

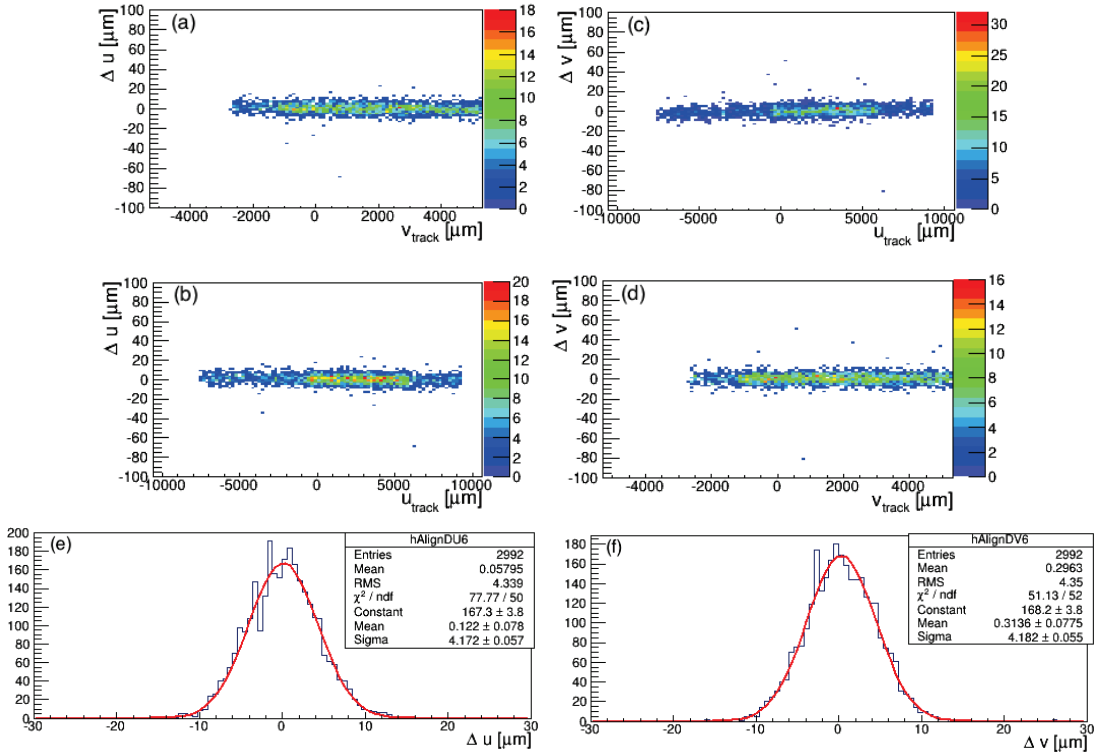


**Figure 5.12:** Distribution of the residues obtained with the DUT placed perpendicularly to the beam (only sensor 2): (a) $\Delta u$ residue as a function of the local $v$ coordinate, (b) $\Delta u$ residue as a function of the local $u$ coordinate, (c) $\Delta v$ residue as a function of the local $u$ coordinate, (d) $\Delta v$ residue as a function of the local $v$ coordinate, (e) $\Delta u$ residue and (f) $\Delta v$ residue.

appears to be more difficult to perform, and is described in Section 5.7.

## 5.6 Estimation of the gap between two adjacent sensors

We are interested in measuring the gap between two adjacent sensors mounted on the PLUME ladder because this insensitive area will affect the tracking efficiency. Sensors were manually glued on the PLUME-1 ladder studied here. The result of this study will contribute to improve the sensors placement of the next prototype PLUME-2, for which an automatic gluing procedure will be employed.

The runs with the beam crossing two adjacent sensors were analyzed, and all the hits found in these planes were represented in the global (x,y) coordinates system. For many tracks, these hits spread on uniformly all the surface of the two adjacent

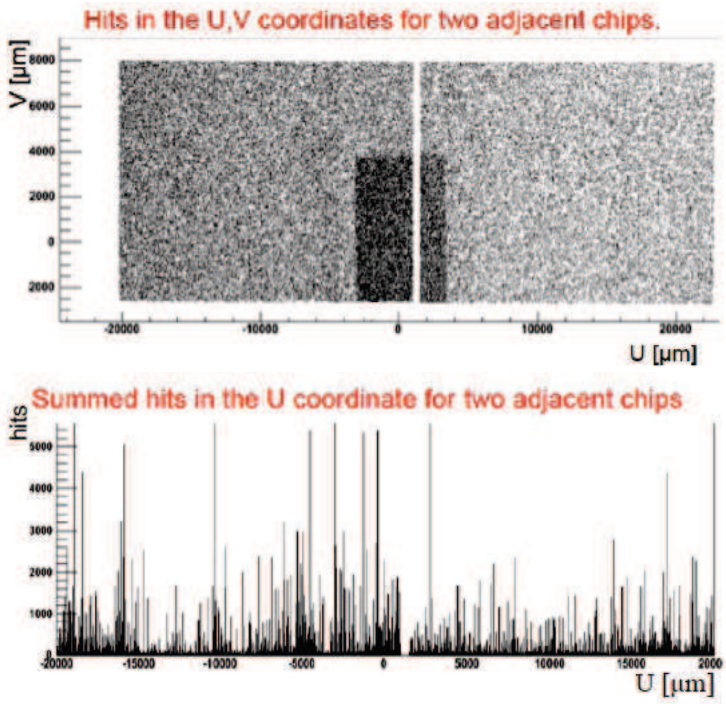


**Figure 5.13:** Distribution of the reference hits (extrapolations of the telescope tracks) on the DUT plane in the global (x,y) coordinates system and projection of this distribution on the x-axis (bottom). Each bin corresponds to 5 $\mu$m.

sensors, as we are able to see in the upper part of Fig. 5.9. Because the acquisition is triggered by signal seen in the scintillator when the beam crosses it, we observe in this image the "shadow" of the scintillator position. The white vertical strip crossing the shadow of the scintillator is the gap between 2 adjacent sensors.

To measure the mean gap, we resort to two step functions, one to fit the hit distribution projection of the left part of the gap and one for the right part of the gap, as displayed in Fig. 5.14. If the margins are not parallel, we divided the sensor's surface in several horizontal parts, and calculate the mean gap for each part individually. The results on the mean gap distance are found in Table. 5.1, with a 5 $\mu$m uncertainty due to binning.

We observe that the mean gap is of the order of 500 $\mu$m, which is not a big gap compared to common distances observed for instance with hybrid sensors. This distance could decrease for future prototypes even to a distance of 100 $\mu m$, mainly by reducing the pads between two adjacent sensors (which now contain the name of the producer) and the dimension of the sequencers (responsible for reading a line of pixels). The next prototype, PLUME-2 prototype, will feature the same distance between the sensors on the ladder because the priority is a decrease in the material

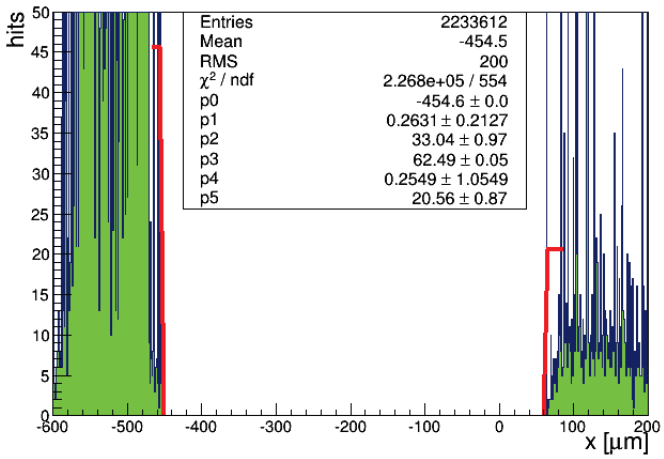


**Figure 5.14:** The mean gap distance measured with two step functions.

budget.

| Sensors | 1-2 | 3-4 | 5-6 | 7-8 | 9-10 | 11-12 |
|---|---|---|---|---|---|---|
| Average gap ($\mu$m) | 550 | 535 | 545 | 555 | 540 | 555 |

**Table 5.1:** Average distances measured between two adjacent sensors of the PLUME device. Uncertainty due to the binning is 5 $\mu$m.

## 5.7 Tracking performances with tilted tracks

### 5.7.1 DUT configurations

The different run configurations considered for this study are presented in Table 5.2. In order to simulate tilted tracks, the DUT was rotated with 36° and 60° with respect to the beam axis, as represented in Fig 5.9. For the 36° tilt, two runs were analyzed, with different temperatures, to check for possible vibrations induced by the cooling system. The DUT sensors were all operated with the same threshold expressed in mV, with 5 mV corresponding to 4.03 noise units and 6 mV standing for 4.84 noise units [166].

### 5.7.2 Alignment of the tilted DUT

The alignment of the DUT with 36° and 60° incoming tracks appears to be more complicated than for perpendicular tracks. Indeed we observe that the sensor surface

| Tilt | Temp [°C] | Threshold [mV] | Air flow speed [m/s] | Sensor number |
|---|---|---|---|---|
| 0° | 45 | 6 | 3 | 2 / 11 |
| 36° | 45 | 6 | 3 | 2 / 11 |
| 36° | 42 | 6 | 7 | 2 / 11 |
| 60° | 45 | 5 | 3 | 4 / 9 |

**Table 5.2:** Different configurations considered for the tilted tracks study.

deformations have visible impacts at large tilts. These impacts are more accentuated along the sensor $u$-axis, as it is illustrated by the left plots of Fig 5.15 (for sensor 2), Fig.5.10 (for sensor 11), Fig. 5.17 (for sensor 4) and Fig. 5.18 (for sensor 9). These residues feature a "banana" shape as well as small bumps. The small bumps are caused by sensor surface deformations. The banana shape may be due to the manual sensor gluing procedure or due to the foam surface. These distributions may also include vibration effects induced by the cooling system.

The right part of these figures displays residues measured for one sub-part of the sensor along the $u$-axis, after alignment. The $\Delta u$ residues as a function of the $u$ and $v$ -coordinates present uniform distributions centered around zero. Their projections are Gaussian, with a width of about 4.5 $\mu$m for $\theta = 36$ ° and 15-17 $\mu$m for $\theta = 60$°. The larger residue width measured for $\theta = 60$° is expected, since the DUT was placed outside the telescope arms. Therefore the residue includes a larger contribution due to the track extrapolation on the DUT.

In order to improve the alignment, the sensor should be mapped in several areas, both along $u$ and $v$ directions. In this study, this was done manually, with the help of the residual distributions obtained for all the sensor surfaces. Since this procedure is time consuming, it should be considered setting up an automatic method to do this. Work in this direction is now being pursued in [167] (ongoing thesis at DESY and IPHC) with a method based on Legendre polynomials.

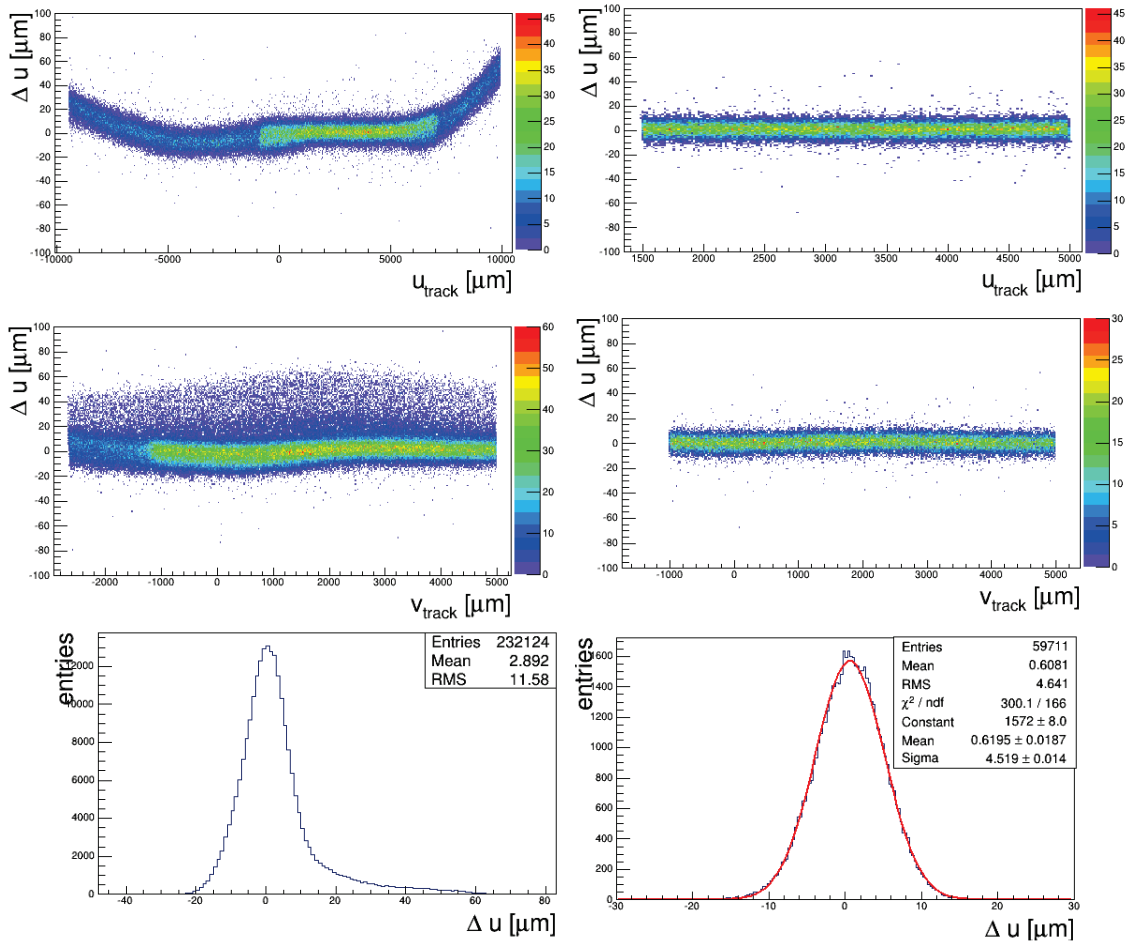


**Figure 5.15:** Distributions of the $\Delta u$ residue obtained with $\theta$=36° tilt (here for sensor 2). Residues are displayed as a function of the $u$ coordinate (top) and of the $v$ coordinate (middle), and integrated along $u$ and $v$ (bottom). Left figures correspond to the residue observed after an alignment performed globally for the whole sensor, while right figures display the distributions observed after the alignment of a small region of the sensor (as it can be seen from the $u$ and $v$ coordinates).

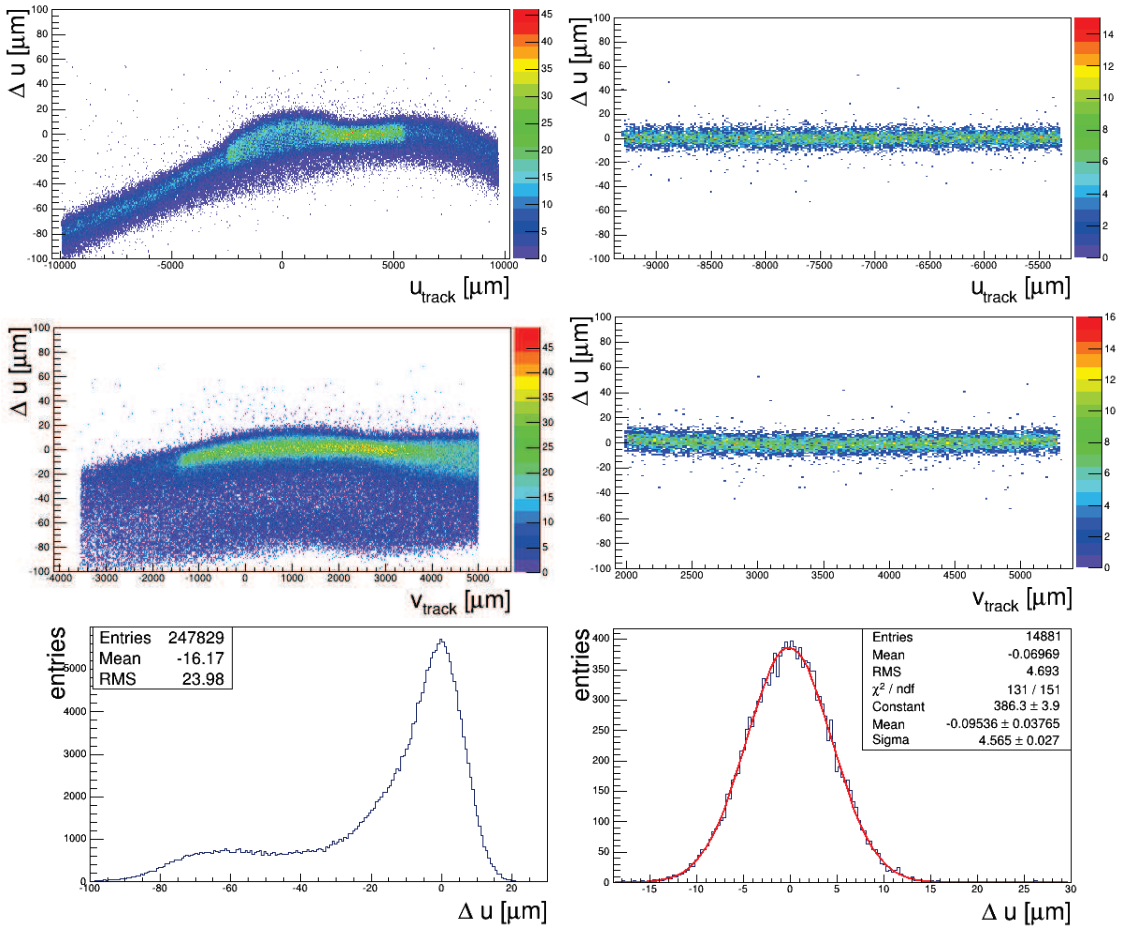


**Figure 5.16:** Distributions of the $\Delta u$ residue obtained with $\theta$=36° tilt (here for sensor 11). Residues are displayed as a function of the $u$ coordinate (top) and of the $v$ coordinate (middle), and integrated along $u$ and $v$ (bottom). Left figures correspond to the residue observed after an alignment performed globally for the whole sensor, while right figures display the distributions observed after the alignment of a small region of the sensor (as it can be seen from the $u$ and $v$ coordinates).

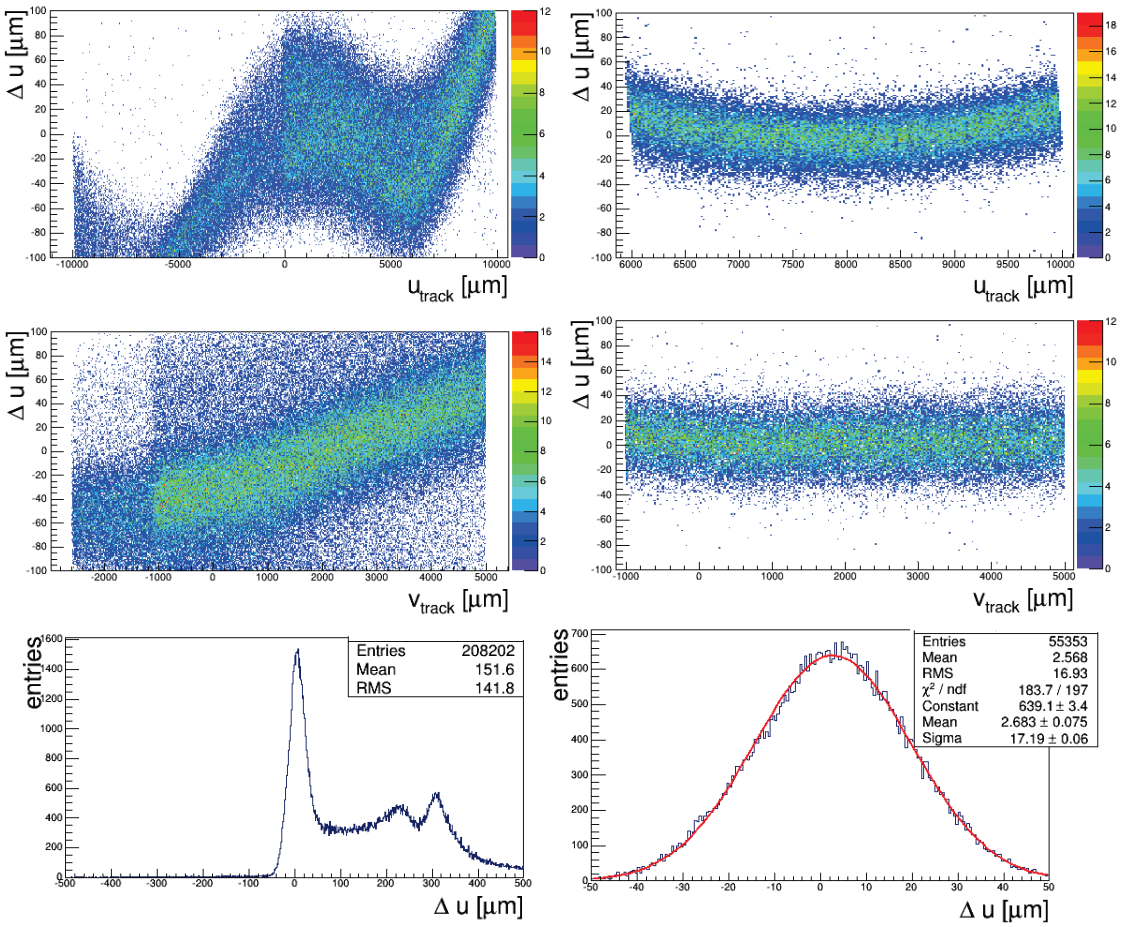


**Figure 5.17:** Distributions of the $\Delta u$ residue obtained with $\theta$=60° tilt (here for sensor 4). Residues are displayed as a function of the $u$ coordinate (top) and of the $v$ coordinate (middle), and integrated along $u$ and $v$ (bottom). Left figures correspond to the residue observed after an alignment performed globally for the whole sensor, while right figures display the distributions observed after the alignment of a small region of the sensor (as it can be seen from the $u$ and $v$ coordinates).

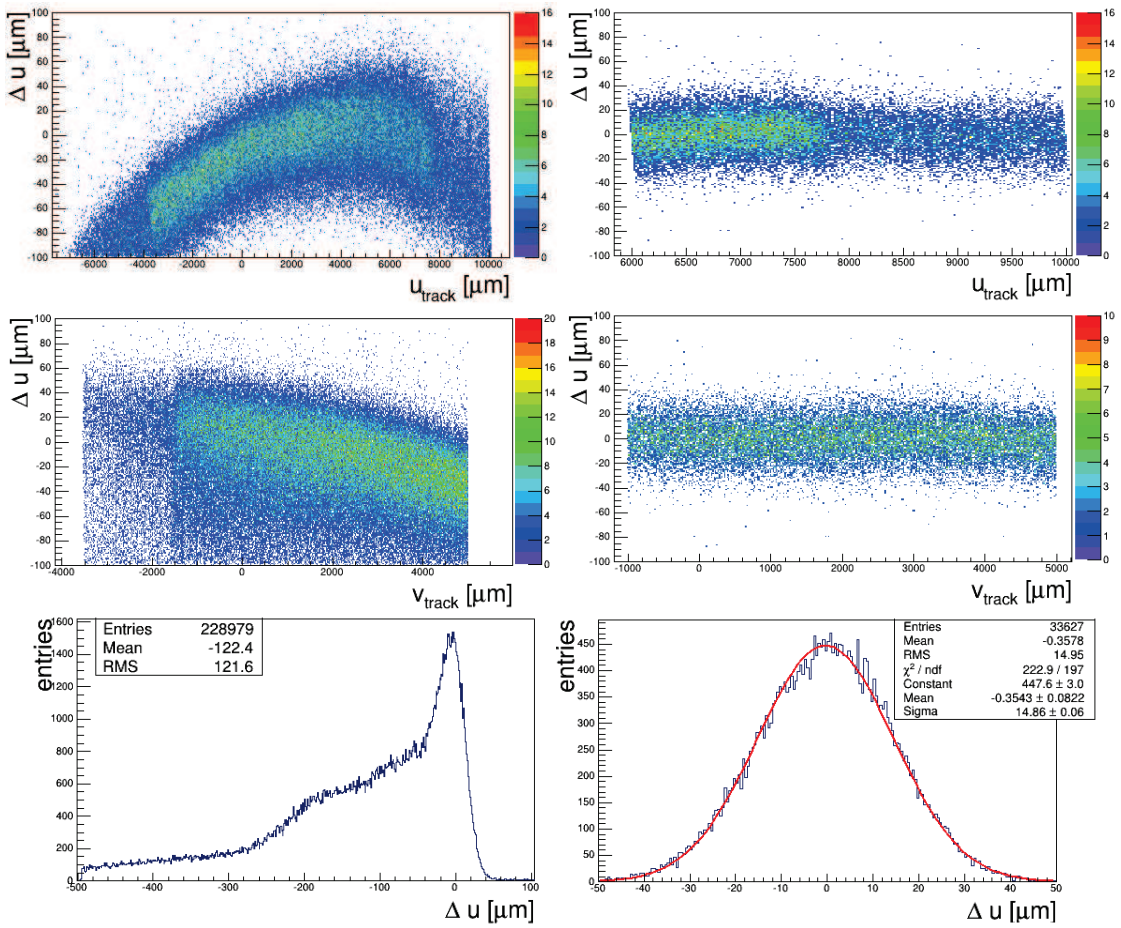


**Figure 5.18:** Distributions of the $\Delta u$ residue obtained with $\theta$=60° tilt (here for sensor 9). Residues are displayed as a function of the $u$ coordinate (top) and of the $v$ coordinate (middle), and integrated along $u$ and $v$ (bottom). Left figures correspond to the residue observed after an alignment performed globally for the whole sensor, while right figures display the distributions observed after the alignment of a small region of the sensor (as it can be seen from the $u$ and $v$ coordinates).

### 5.7.3 Estimation of the sensor deformation dimensions

The sensor surface imperfections cause small bumps (as seen in the residual distributions), while the foam and the gluing procedure used to build the PLUME-1 prototype may lead to a bending of the sensors towards the margins. Studies employing a laser scan of the sensor surface were performed both at IPHC Strasbourg and at Bristol University [168, 169]. They revealed an overall bow, interpreted as due to foam and distortions at the edge of the chips.
We observe the same effects by measuring the spatial residues with tilted tracks. We want to estimate the height of the deformations (or the bending toward the margins of the sensors) from those residual distributions. The deformations introduce a shift of the actual $z$ position of a hit. This shift is estimated as being equal to the height of the deformation $\Delta z$, which can be expressed as a function of the angle $\theta$ of the track of the residue $\Delta u$:

$$\Delta z = \frac{\Delta u}{tan(\theta)} \tag{5.3}$$

Due to this $1/tan(\theta)$ dependence, the larger the angle $\theta$ is, the more sensitive we are to the sensor surface deformation. The effect of these deformations are negligible on residues measured with perpendicular tracks. Using the mean measured $< \Delta u >$ residues and the known track angles $\theta$, we can estimate the deformations from the distributions shown on Fig. 5.19.
On sensor 2 we measure bents rising up to 14 $\mu$ on the left edge and 16 $\mu$m on the right edge. Sensor 11 presents a bent of about 30 $\mu$m at one edge. For sensors 4 and 9, we measure deformations of the order of 100 $\mu$m, to which we are sensitive with $60^o$ tilt.
Special care will be put to reduce as much as possible surface deformations when building the PLUME-2 ladder used in BEAST II. Nevertheless, due to the very good spatial resolution of such sensors, effects caused by surface imperfect flatness will always exist, and they will have to be taken into account to measure spatial position of the hits in future detectors.

### 5.7.4 Cluster shapes induced by tilted tracks

The spatial resolution reached with a sensor depends on the size of the clusters used to estimate the hit position. The center-of-gravity algorithm benefits from the charge sharing between neighbour pixels, to estimate more accurately the hit position. The resolution of clusters reconstructed with signal of too few or too many pixels is degraded. The estimated resolution depends on the cluster size with a parabolic

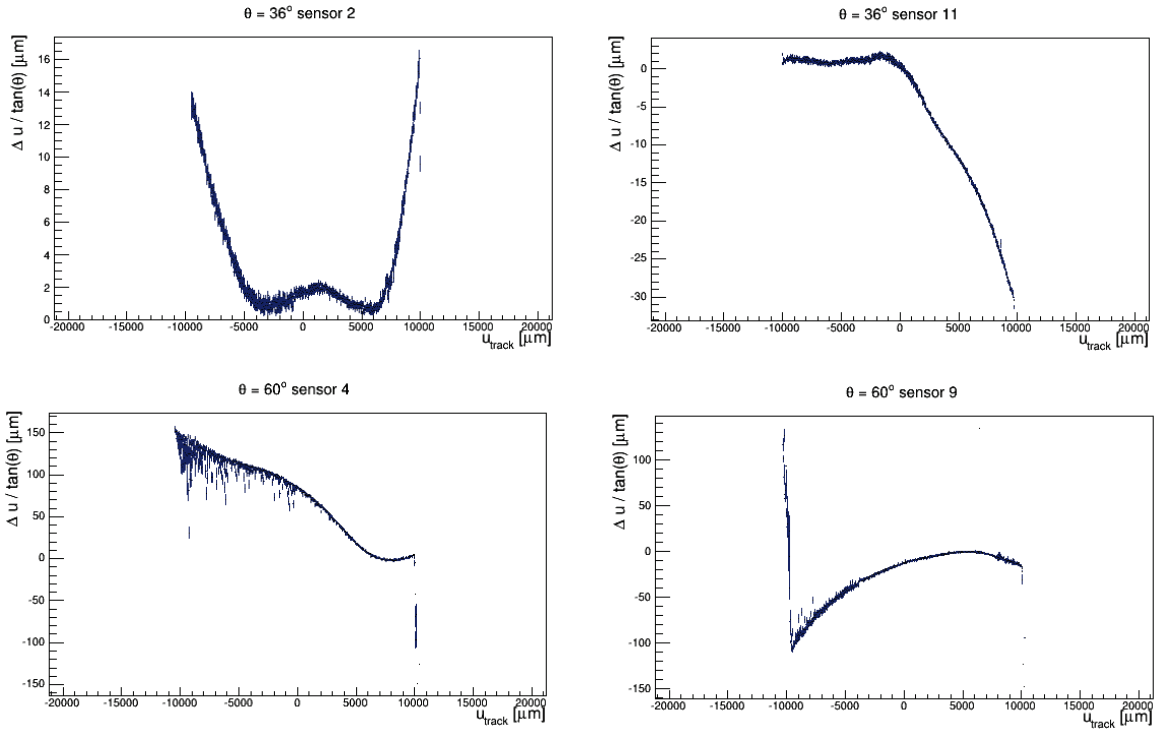


**Figure 5.19:** The sensor deformations measured estimated by the geometrical approximation $\Delta z = \frac{\Delta u}{tan(\theta)}$, where $\Delta z$ is the shift along the z-axis of the reconstructed hit and $\theta$ is the angle of the track.

curve, and there is an optimum cluster size to reach the best possible resolution. In case of tilted tracks (obtained with the rotated DUT), the path of the charged track inside the silicon sensitive layer is increased, resulting in larger cluster dimensions. This effect is confirmed by the comparison of the measured residues and cluster dimensions with $\theta = 0°$, 36°and 60°. Fig. 5.20 represents the distributions of the total cluster dimensions, that means the total number of pixels used to reconstruct the clusters observed at $\theta = 0°$, 36°and 60°. The same distributions are obtained for the sensors on the opposite side of the ladder, found in Appendix C.

Cluster dimensions are also studied in each direction, along the $u$-axis and the $v$-axis separately, as presented in Fig. 5.21. Contrary to what we expected, the cluster dimensions are equivalent and increase with the same rate as the function of the tilt, even though the tilt is done around the $v$-axis.

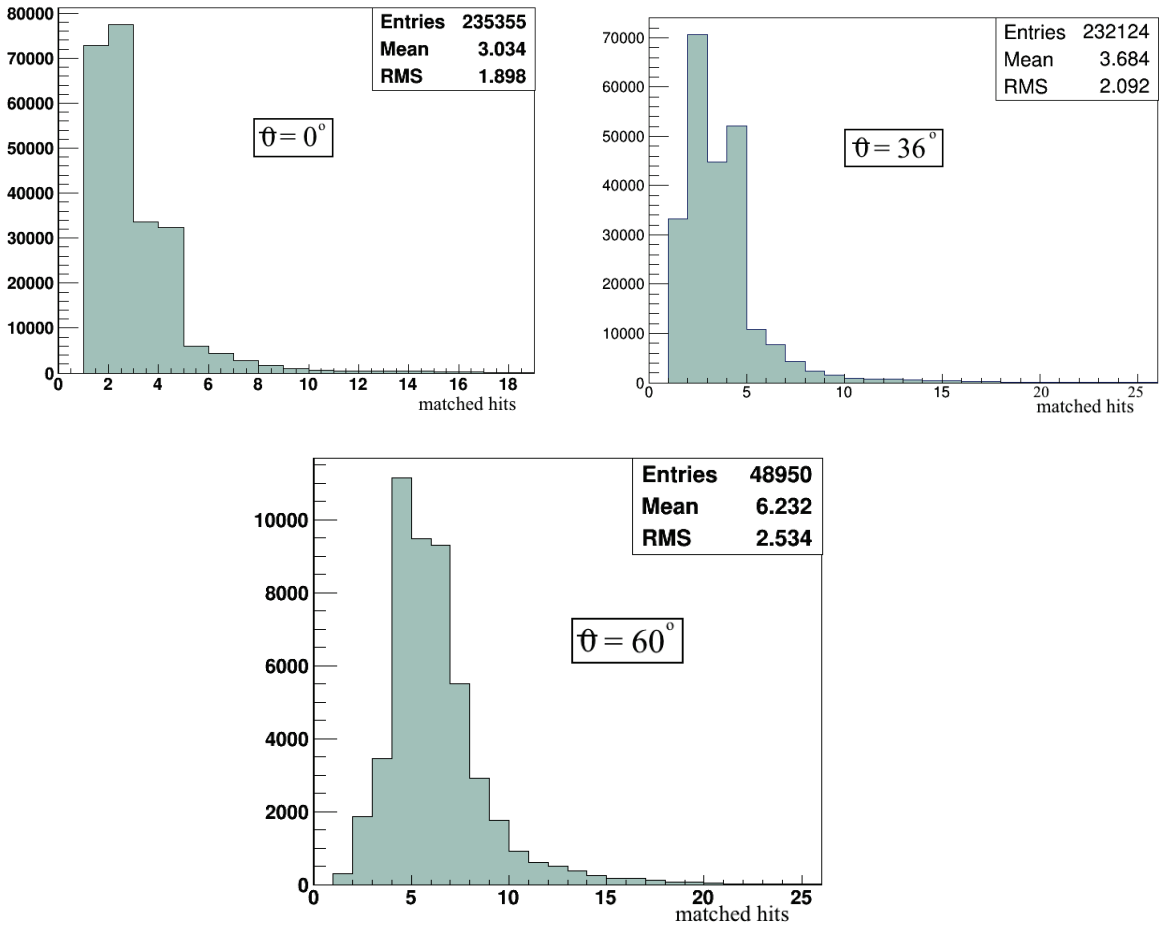


**Figure 5.20:** Distributions of cluster dimensions (total number of pixels used to reconstruct the cluster) observed at tilts $\theta = 0^{o}$ (sensor 2), $\theta$=36$^{o}$ (sensor 2) and $\theta$=60$^{o}$ (sensor 4).

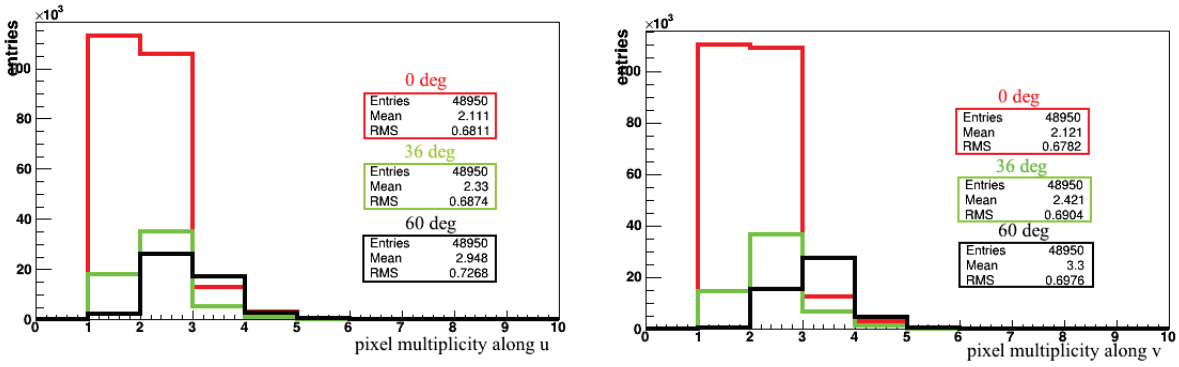


**Figure 5.21:** Distributions of cluster dimensions along the lines ($u$-coordinate, left) and the columns ($v$-coordinate, right) of the pixel matrix.

### 5.7.5 Benefit of double-sided pixelated layers

In this section, the single point resolution of each layer of the double-sided DUT is estimated from the residues measured in Section 5.7.2. The 2 hits measured in the double-sided DUT layer can also be associated to build a mini-vector (or a tracklet) and the corresponding resolution is inferred.

#### 5.7.5.1 Spatial resolution of the DUT

There are three contributions to the measured residue $\sigma_{res}$, as shown by the relation:

$$\sigma_{res}^2 = \sigma_{DUT}^2 + \sigma_{m.s.}^2 + \sigma_{tel}^2 \tag{5.4}$$

where $\sigma_{DUT}$ is the intrinsic spatial resolution of the DUT sensor, $\sigma_{m.s.}$ is the uncertainty induced by Coulomb multiple scattering, which can be neglected here (with a beam of 120 GeV pions), and $\sigma_{tel}$ is the uncertainty on the reference position estimated from the telescope track extrapolation on the DUT.
The latter depends on the intrinsic spatial resolution of the telescope sensors $\sigma_{ref}$ and on the position z of the DUT along the z-axis with respect to the telescope sensor positions ($z_1$,$z_2$, $z_3$,$z_4$). For the DUT placed between the telescope arms, it can be written as:

$$\sigma_{tel}(z) = \frac{\sigma_{ref}}{\sqrt{2}\left|\frac{z_1+z_2}{2} - \frac{z_3+z_4}{2}\right|}\sqrt{\left(z - \frac{z_1+z_2}{2}\right)^2 + \left(\frac{z_3+z_4}{2} - z\right)^2} \tag{5.5}$$

The threshold used to operate the sensors composing the telescope in this beam test was 8 mV, and with the help of Fig. 5.6, we estimate the intrinsic resolution $\sigma_{ref} \simeq 4$ $\mu$m. Knowing the positions along $z$ of the 4 telescope sensors and of the DUT, we can calculate:

- $\sigma_{tel} = 2$ $\mu$m for the runs registered with the tilt $\theta = 0^o$.
- $\sigma_{tel} = 2.5$ $\mu$m for the runs registered with the tilt $\theta = 36^o$.

In the following, these results will be employed to extract the DUT resolution from the measured residue, according to Eq. 5.4. These resolutions will be compared with the ones obtained with mini-vectors.
For runs recorded with a tilt $\theta = 60^o$, the DUT was placed outside the telescope arms, therefore the uncertainty on the reference position estimated from the track extrapolation is higher than the one of the DUT placed between the telescope arms.

Moreover, impact of uncertainties coming from the measurement of the tilt and of the position of the DUT is not negligible anymore, contrary to the former case ($\theta = 0^o, 36^o$). Therefore, with $\theta = 60^o$, we could not properly reconstruct the mini-vectors and the DUT resolution is not estimated in that case.

#### 5.7.5.2 Mini-vectors

For each particle crossing the DUT, the two hits produced in the two layers of the double-sided DUT can be associated to measure the track incidence. For each of the two opposite sensors, the closest hit to the extrapolated tracks is used to reconstruct a mini-vector and the angular residue $\sigma_\theta$ is computed between the reference track direction and the mini-vector dimension, as displayed with Fig. 5.22.
The spatial resolution on the hit position estimated as the mini-vector $z$ position between the two DUT layers is expected to be $1/\sqrt{2}$ better than the spatial resolution on the hit position estimated by a DUT single layer.

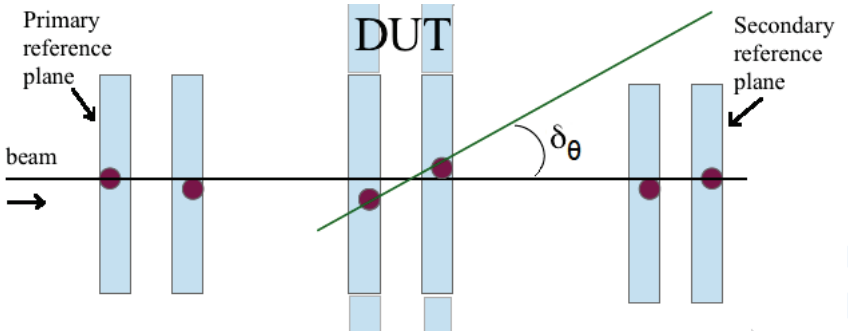


**Figure 5.22:** With the 2 hits measured in the double-sided DUT layer, a mini-vector is reconstructed (represented by the green line). The black line represents the reference track reconstructed with the telescope.

In order to correctly associate the two hits corresponding to one crossing particle and to reconstruct the mini-vectors, we first have to determine the overlapping area of the two sensors. As displayed in Fig. 5.8, two opposite sensors have different vertical position on the ladder. Moreover, we need to check that we registered enough reference tracks passing through this area. Finally, because we are significantly sensitive to sensor deformations with tilted tracks, we have to find two parts of the sensors in this area which are parallel enough (without significant surface deformations).
In Fig. 5.23, the 2D distributions of hits measured in the DUT sensors (with $\theta = 60^o$) are represented. Finding the sub-part of each sensor fulfilling the conditions above is done according to the following procedure. Knowing the position of the

center of the sensor expressed in the $(x, y, z)$ coordinate system and knowing the dimensions of the sensor, we compare Fig. 5.23 with Fig. 5.17 and Fig. 5.18 and we choose the spatial coordinates of the two sub-parts (one for each sensor) that are almost parallel to each other and for which we have enough extrapolated tracks. These sub-parts of the sensors are aligned as described in the previous section, and the mini-vectors are then reconstructed.

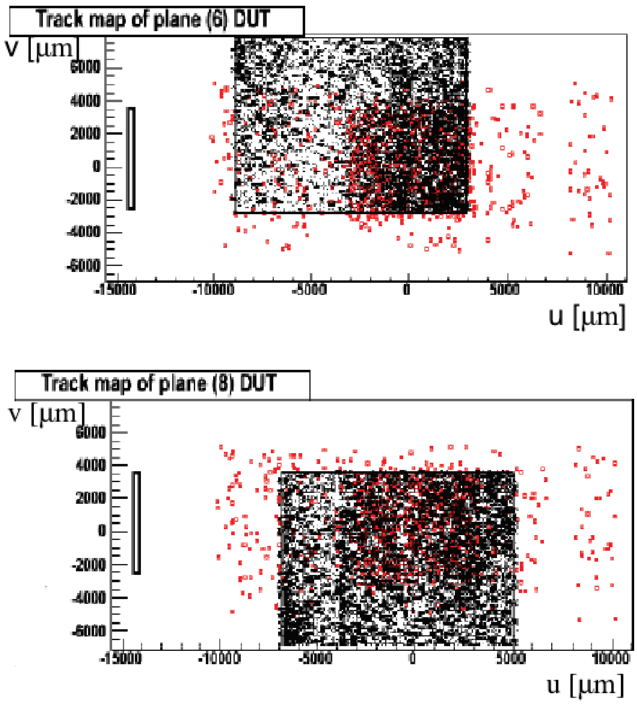


**Figure 5.23:** 2D-distributions ($v$ vs $u$) of the extrapolated positions of the reference tracks (reconstructed with the telescope) on the DUT (red points) and measured hits in the DUT (black points) for two PLUME sensors placed back-to-back on the PLUME ladder.

The spatial resolution of the sensors, obtained with mini-vectors and with single hits, are compared in Fig. 5.24. We observe that for perpendicular tracks the resolution improve from about 3.2 $\mu$m to about 2.3 $\mu$m with mini-vectors. For 36° tracks, the resolution improves from about 4 $mu$m to about 3.3 $\mu$m. This signifies a gaining factor of about $1/\sqrt{2}$ is reachable on the spatial resolution in the center of the ladder is using mini-vectors.

Fig. 5.25 also shows the angular resolution obtained on the track incidence, for tilts = 0° and 36°. Angular resolutions of 0.15° to 0.25° are reached. This performance will be used to disentangle the different background processes during BEAST II.


**Figure 5.24:** Resolution measured along the $v$ direction, for tilts = 0°and 36° (sensor 2).

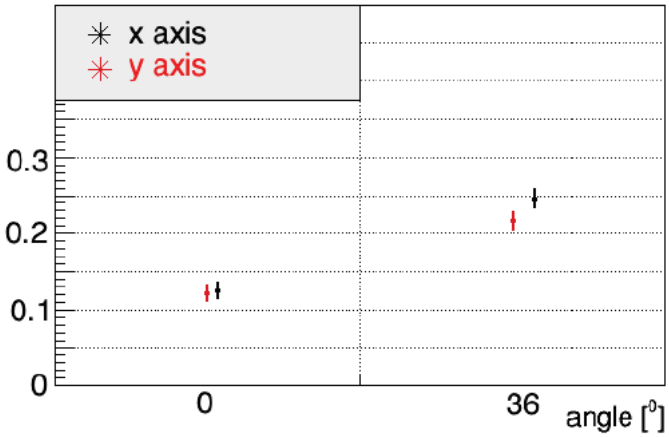


**Figure 5.25:** The angular resolution obtained with mini-vectors.

## 5.8 Conclusions

A device composed of two PLUME ladders will be used during the BEAST II commissioning of Belle II experiment to characterize the SuperKEKB induced background and to validate its simulations. The results obtained in this study show that several improvements have to be brought to the PLUME-1 prototype to design and build the PLUME-2 ladder, which is the one which will be used at BEAST II.

The first study estimated on the insensitive area between adjacent sensors on the ladder. This gap affects the tracking performances. Even if this distance is smaller compared to other pixel technologies, the results obtained will be used to set the automatic method to glue sensors on PLUME-2.

The second study is focused on the tracking performances with tilted tracks. With tilted tracks, because of the excellent spatial resolution of the order of 3 $\mu$m of the sensors, the sensor surface deformation needs to be taken into account. Indeed, impact of the non planar surface of the sensors or of the foam on which sensors are glued, or even of the cooling system, are seen in the spatial residues. From our study, the surface deformation dimensions to which we are sensitive were estimated to be between 15 $\mu$m to 100 $\mu$m. The distortions at the edge of the chips are expected to decrease with the new automatic gluing method, and the overall bow can be reduced by improving the foam planarity. In future analyses, the alignment procedure taking these deformations into account, which was performed step by step and manually in this study, will be made easier based on a parameterization of the surface using Legendre polynomials.

Finally, we also used data recorded during the beam test to investigate the reconstruction of mini-vectors by associating the 2 hits measured in the double-sided PLUME layer with tilted tracks. We show that up to tilts of 36°, we are able to reconstruct the mini-vectors, and the inferred spatial resolution is improved with respect to what is obtained from a single layer hit measurement. Angular resolutions of about 0.1° - 0.25° are reached on the track incidence. However, for extreme track angles (60°), we failed to associate the 2 hits with these data.

# Conclusion and outlook

The work presented in this thesis was performed in the context of the Belle II experiment, which will register the collisions delivered by the SuperKEKB $e^+e^-$ accelerator. The Belle II experiment is in the final preparation stage to start taking data. Our work investigates three topics, all addressing the Belle II inner tracker performances. During the past three years, several algorithms developed by the collaboration and useful for our studies (like tracking and vertexing) were continuously evolving. Therefore, this thesis provides prospective guides for the future Belle II analyses.

First, we studied the Belle II sensitivity to the $\beta_c$ angle of the $c-u$ unitarity triangle. This triangle has not been experimentally investigated yet, and an unexpected high measured value of $\beta_c$ would be an indication of physics beyond the Standard Model. This measurement relies on the reconstruction of the $D^0$ flight distance, thus on the inner tracker resolution. We estimate that a statistical accuracy at the level of 2-3$^o$ can be reached on this angle with the full Belle II dataset. The conclusion of our study is that the statistics will still be the limiting factor for the $\beta_c$ measurement. Another obstruction comes from the neglected higher-order Feynman diagram contributions, which result also in a 2-3$^o$ uncertainty on $\beta_c$. As far as the interpretation of a $\beta_c$ measurement in terms of a potential new physics discovery is concerned, long distance contributions to the $D^0 - \bar{D}^0$ oscillation makes it delicate. Nevertheless, theoretical calculations involving $D^0$ mesons are expected to improve in the future with impoved Lattice QCD predictions.

The second study results in the proposition of a new estimator to improve the low momenta reconstruction in Belle II. Soft momentum particles play an important role in the physics program of Belle II, and in particular in the $\beta_c$ measurement. Currently, the estimation is based on a classical helix fit to the reconstructed track of the charged particle. The low momentum estimator developed in this thesis uses the energy depositions of charged particles in the silicon layers of the inner tracker. Its performances are at least as good, and even better at the lowest momenta, as the currently used estimator. The Belle II collaboration considers using these results

to improve the low momentum track fitting and to reject low momentum machine induced background hits in the inner tracker.

The third work presented in this thesis is an analysis of beam test data of the first PLUME double-sided pixelated device. This analysis aimed at checking several particular features to improve the design and the construction procedure of the second generation of the PLUME ladder. This new PLUME prototype will be used during the commissioning of the Belle II experiment, to characterize the background produced by SuperKEKB collider in the interaction region. In particular, the gap between adjacent sensors was estimated (of the order of 500 $\mu$m), as well as the flatness of the sensor surface, to set up a future automatic gluing procedure of sensors on the ladder.

# A. Approximation of the path of a charged particle through a silicon layer

In this calculus, we will use the following notations:

- $p$, $p_T$ are the momentum and the transversal momentum respectively
- $w$ is the width of the silicon layer considered (75 $\mu$ for the PXD and 320 $\mu$m for the SVD)
- $\theta$ is the polar angle
- $\phi$ is the track parameter related to the curvature of the track; it is estimated by the helix fit
- $\rho$ is the radius of the track curvature in the magnetic field $\vec{B}$
- $R$ is the distance from the impact point to the silicon layer

In Fig. A.1 is just a sketch representing the path of a particle through a silicon layer (PXD or SVD). In the simplest case, without magnetic field, a particle will follow the path $L' = w/sin(\theta)$.
In a magnetic field, the path in the silicon becomes:

$$L' = L \cdot cos\phi \tag{A.1}$$

We can write therefore:

$$L = \frac{w}{cos\phi \cdot sin\theta} \tag{A.2}$$

Using Fig. A.2 we can write:

$$\frac{R}{2} = \rho \cdot cos\left(\frac{\pi}{2} - \phi\right) = \rho \cdot sin\phi \tag{A.3}$$

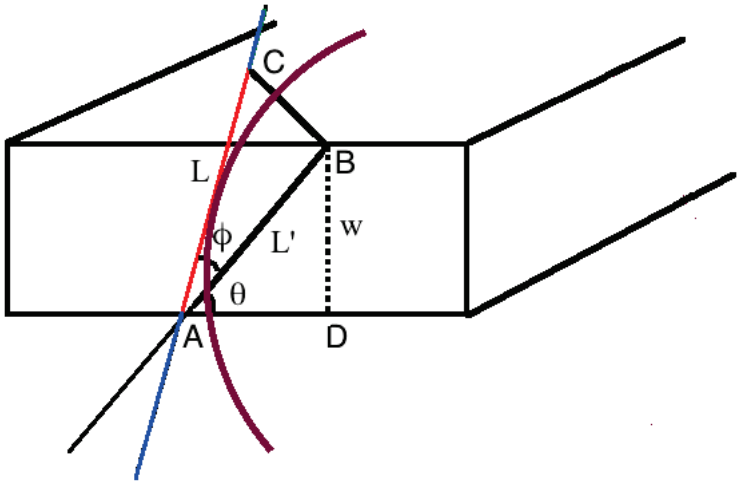


**Figure A.1:** Sketch with the path of a particle through a silicon layer: in the absence of a magnetic field (black), with a magnetic field (purple) and the path estimated by us (red).

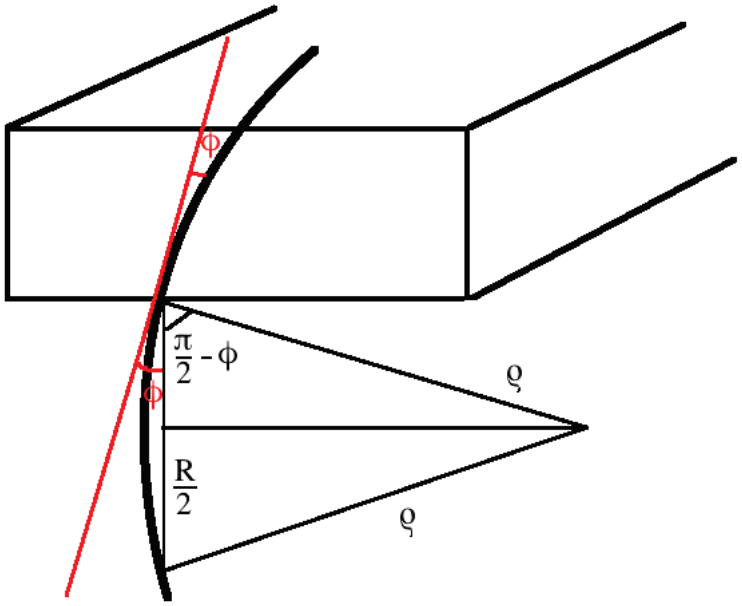


**Figure A.2:** Sketch of the curved path of a charged particle.

Using the relation between the transversal momentum and the magnetic field and $\rho$, $p_T = 0.3\rho$ B, we can extract $sin(\phi)$ as:

$$sin\phi = \frac{0.3RB}{2psin\theta} \tag{A.4}$$

And now, with the help of Eq. A.5 and Eq. A.2 we can approximate the path of a charged particle in a silicon layer as:

$$L = \frac{w}{\sqrt{sin^2\theta - \left(\frac{0.3RB}{2p}\right)^2}} \tag{A.5}$$

# *B.* Alignment of sensor 11, for $\theta = 0^{\circ}$

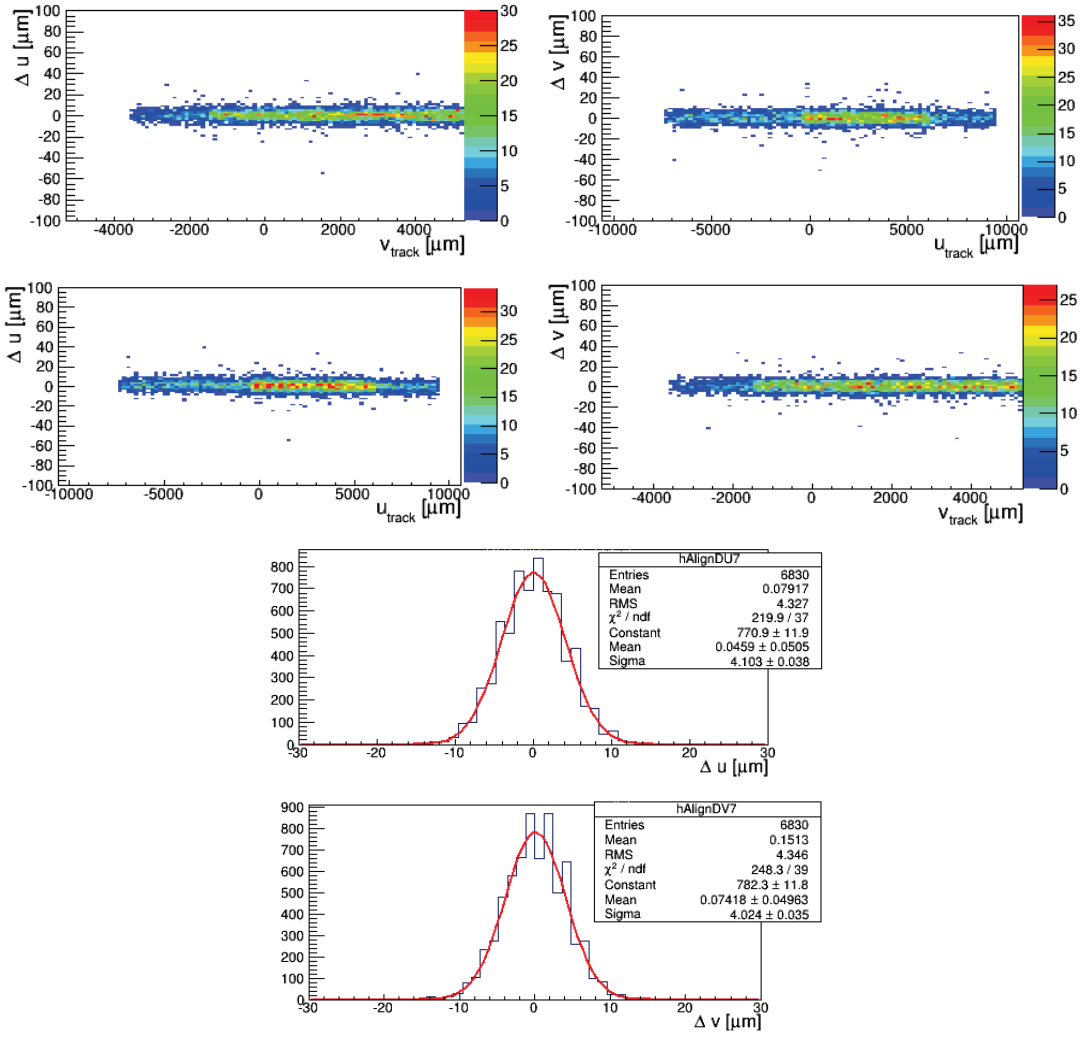


**Figure B.1:** Distribution of the residues obtained with the DUT placed perpendicular to the beam for sensor 11: (a) Residue $\Delta u$ as a function of the $v$ local coordinate, (b) residue $\Delta u$ as a function of the $u$ local coordinate, (c) residue $\Delta v$ as a function of the $u$ local coordinate, (d) residue $\Delta v$ as a function of the $v$ local coordinate, (e) residue $\Delta u$ and (f) residue $\Delta v$.

# *C.* Pixels in matched hits for sensors: 11 and 9

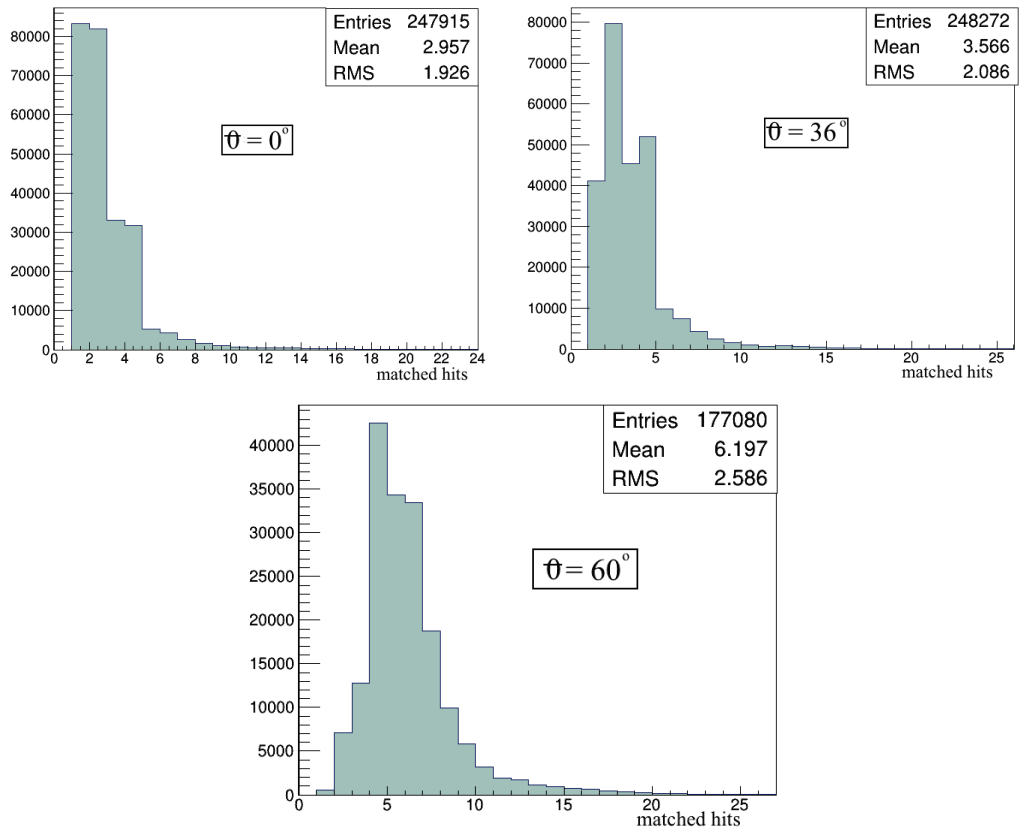


**Figure C.1:** Sum of all pixels (for both $u$ and $v$) in matched hits for $\theta = 0^{o}$ (sensor 2), $\theta$=36$^{o}$ (sensor 2) and $\theta$=60$^{o}$ (sensor 4).

# Résumé en français

## Etude de l'asymétrie de CP en fonction du temps dans les désintegrations du méson $D^0$ dans l'expérience Belle II

## I. Introduction

Cette thèse a pour objectif l'étude des performances du trajectomètre interne de Belle II, en utilisant la mesure de la violation indirecte de CP dans les désintégrations des mésons $D^0$ comme canal de physique particulièrement sensible à ces performances.

Malgré l'immense succès du Modèle Standard (MS) de la physique des particules pour décrire les particules élémentaires et leurs interactions, plusieurs observations expérimentales restent inexpliquées, notamment la dominance de la matière sur l'anti-matière dans l'Univers. A.Sakharov a montré que la disparition de l'anti-matière nécessitait la violation de la symétrie CP. Dans le MS, la violation de CP est décrite par une seule phase complexe apparaissant dans la matrice CKM. Les mesures expérimentales ont cependant montré que la violation de CP décrite par cette phase était trop faible pour expliquer la disparition de l'anti-matière. Nous sommes donc sûrs aujourd'hui qu'il doit exister des sources supplémentaires de violation de CP, mais nous ne les avons pas encore trouvées. Leur découverte annoncerait la présence de nouvelle physique au-delà du MS.

Ces 40 dernières années, la violation de CP a été observée dans les désintégrations des mésons K et B, et toutes ces mesures vérifient les prédictions du MS. Récemment les effets de violation de CP dans les désintégrations du $D^0$ ont été relevés pour la première fois. Cependant ces données sont limitées statistiquement et ne permettent pas actuellement de décider si le résultat est en accord avec le MS ou s'il correspond à une manifestation de physique au-delà du MS.

La mesure de l'asymétrie en fonction du temps considérée dans cette thèse est sensible à des effets de violation de CP intervenant non seulement lors la désintégration

du $D^0$ (violation de CP directe), mais aussi lors de l'oscillation $D^0 - \bar{D}^0$ et dans l'interférence entre les deux (violation de CP indirecte). La violation de CP apparaît dans la description formelle de cette asymétrie sous la forme d'un paramètre complexe $\lambda_f$. L'étude de l'asymétrie de CP effectuée dans cette thèse est basée sur une analyse en fonction du temps où la reconstruction de la distance de vol du $D^0$ est rendue particulièrement difficile par la durée de vie faible du $D^0$ par rapport à celle des mésons B. Cette étude est ainsi très sensible aux performances du trajectomètre interne de l'expérience.

Un autre élément intervient dans cette étude : la présence dans l'état final d'un pion de très faible impulsion. Ce pion permet d'identifier la saveur du $D^0$ produit, ainsi que de reconstruire le point de désintégration du $D^0$. Les trajectoires des particules de faible impulsion sont particulièrement difficiles à reconstruire parce qu'elles sont très courbées par le champ magnétique dans le trajectomètre interne et n'atteignent pas le trajectomètre central de Belle II. Dans cette thèse, une méthode alternative est proposée afin d'améliorer l'estimation de l'impulsion reconstruite à l'aide de l'ajustement de l'hélice de la trajectoire. Pour cela, nous utilisons l'information de l'énergie déposée par la particule dans les détecteurs internes en silicium de Belle II.

Les détecteurs de Belle II vont enregistrer les produits des collisions délivrées par SuperKEKB avec une luminosité instantanée la plus élevée jamais atteinte auparavant, de $0.8\times10^{36}$ cm$^{-2}$ s$^{-1}$. Pour atteindre une telle intensité, une nouvelle technique de collision sera utilisée, basée sur des faisceaux plats de dimension transverse de 50 nm dans une direction. Les interactions entre les particules de ces faisceaux très intenses vont produire un bruit de fond très élevé, qui impactera particulièrement le trajectomètre interne de Belle II car c'est le détecteur le plus proche des faisceaux. Ce bruit de fond sera étudié en détail pendant la mise en route de l'expérience Belle II, prévue en 2016. Des échelles pixellisées PLUME conçues à l'IPHC seront utilisées pour caractériser le bruit de fond produit dans le volume du trajectomètre interne. Dans cette thèse, différentes performances de ces détecteurs PLUME sont mesurées, en analysant les données collectées lors de tests en faisceau.

Dans la suite de ce document sont résumées les trois contributions constituant le travail de cette thèse : l'étude de la sensibilité de Belle II à l'angle $\beta_c$ du triangle d'unitarité $c - u$, l'estimation des faibles impulsions utilisant la mesure de l'énergie déposée dans le trajectomètre interne, et l'étude de performances des détecteurs PLUME qui seront utilisés pour la caractérisation du bruit de fond produit par SuperKEKB dans le trajectomètre interne de Belle II. Ces contributions constituent

des études préliminaires, qui interviennent dans le contexte d'une expérience en construction, dont l'ensemble des outils logiciels sont eux-mêmes en cours de développement.

# II. Sensibilité de Belle II à l'angle $\beta_c$ du triangle d'unitarité $c-u$

Le triangle d'unitarité $c-u$ est quasi plat, ce qui rend son étude difficile et explique pourquoi aucune mesure n'a pu être faite jusqu'à présent. L'angle $\beta_c$ de ce triangle peut être mesuré à partir de mesures d'asymétries de CP en fonction du temps dans les désintégrations du méson $D^0$. L'asymétrie de CP dépendante du temps dans les désintégrations de $D^0$ est définie par la différence normalisée des taux de désintégration entre les mésons et les anti-mésons:

$$A_{CP}(t) = \frac{\bar{\Gamma}(t) - \Gamma(t)}{\bar{\Gamma}(t) + \Gamma(t)} \tag{5.1}$$

Les largeurs de désintégration $\Gamma$(t) et $\bar{\Gamma}$(t) correspondant respectivement à $D^0$ et $\bar{D}^0$ sont définies par:

$$\begin{aligned}
\Gamma(t)(D^0 \to f) &= e^{-t/\tau}\left[cosh(\tfrac{\Delta\Gamma t}{2}) - \tfrac{2Re(\lambda_f)}{1+|\lambda_f|^2}sinh(\tfrac{\Delta\Gamma t}{2}) + \tfrac{1-|\lambda_f|^2}{1+|\lambda_f|^2}cos(\Delta M t) - \tfrac{Im(\lambda_f)}{1+|\lambda_f|^2}sin(\Delta M t)\right] \\
\bar{\Gamma}(t)(\overline{D}^0 \to f) &= e^{-t/\tau}\left[cosh(\tfrac{\Delta\Gamma t}{2}) - \tfrac{2Re(\lambda_f)}{1+|\lambda_f|^2}sinh(\tfrac{\Delta\Gamma t}{2}) - \tfrac{1-|\lambda_f|^2}{1+|\lambda_f|^2}cos(\Delta M t) + \tfrac{Im(\lambda_f)}{1+|\lambda_f|^2}sin(\Delta M t)\right]
\end{aligned} \tag{5.2}$$

Les deux largeurs de désintégration dépendent de la différence de masse $\Delta M$ entre les états propres de masse $D_1^0$ et $D_2^0$, de la différence de largeur $\Delta\Gamma$ et du paramètre complexe $\lambda_f$ défini de la manière suivante:

$$\lambda_f = \frac{q}{p}\frac{\bar{A}_f}{A_f} = -\eta_{CP}\left|\frac{q}{p}\right|\left|\frac{\bar{A}_f}{A_f}\right|e^{i\phi} \tag{5.3}$$

où $\eta_{CP} = \pm 1$ pour les états propres pairs et impairs de CP. Le rapport $q/p$ décrit la violation indirecte de CP dans le mélange. Si $p = q$, les deux états propres des masses sont respectivement CP-pair et CP-impair, sinon la symétrie CP est violée. Le rapport $\bar{A}/A$ définit la violation directe de CP dans la désintégration des $D^0$.

Plusieurs amplitudes de transition sont nécessaires afin que la symétrie CP soit violée. L'amplitude dominante est une amplitude à l'ordre de l'arbre et l'amplitude

sous-dominante peut être une contribution du MS trés supprimée par la hiérarchie des élements de la matrice CKM, ou une contribution de nouvelle physique. Par conséquent, l'amplitude peut être séparée entre une partie dominante et une autre sous-dominante, avec une magnitude relative $r_f$. Pour les désintégrations du méson en deux corps vers des états propres de CP, les amplitudes peuvent être écrites comme ceci:

$$\begin{aligned} A_f &= A_f^T e^{+i\phi_f^T}(1 + r_f e^{i(\delta_f+\phi_f)}) \\ \bar{A}_{\bar{f}} &= \eta_{CP} A_f^T e^{-i\phi_f^T}(1 + r_f e^{i(\delta_f-\phi_f)}) \end{aligned} \tag{5.4}$$

où $A_f^T$ représente l'amplitude arbre dominante, $\phi$ est la phase faible qui peut violer CP et $\delta$ la phase forte qui conserve CP. Pour $D^0 \to h^+h^-$, outre la contribution à l'arbre dominante (T), d'autres topologies peuvent participer, comme la contribution couleur suppressed (CS), les échanges faibles ($W_{ex}$) et pingouin ($P_q$). Ces contributions ne sont pas forcément liées à un angle du triangle d'unitarité $c-u$. Toutes ces contributions doivent être ainsi additionnées:

$$A = |T|e^{i(\phi_T+\delta_T)} + |CS|e^{i(\phi_{CS}+\delta_{CS})} + |W_{ex}|e^{i(\phi_{W_{ex}}+\delta_{W_{ex}})} + \sum_{q=d,s,b} |P_q|e^{i(\phi_{P_q}+\delta_{P_q})} \tag{5.5}$$

L'angle $\beta_c$ peut être déduit à partir de la mesure de $\arg(\lambda_f)$ effectuée dans deux canaux de désintégration du $D^0$ comme suit:

$$\begin{array}{lll} \arg(\lambda_f)_{\pi\pi} = & \phi_{mix} + 2\beta_{c,eff} & \text{si mesurée avec } D^0 \to \pi^+\pi^- \\ \arg(\lambda_f)_{KK} = & \phi_{mix} & \text{si mesurée avec } D^0 \to K^+K^- \\ \hline \multicolumn{3}{c}{\Rightarrow \beta_{c,eff} = \frac{1}{2}\sqrt{(arg(\lambda_f)^2_{\pi\pi} + arg(\lambda_f)_{KK})^2}} \end{array} \tag{5.6}$$

A partir du premier canal de désintégration, nous mesurons la somme de deux quantités: la phase $\phi_{mix}$ du mélange, pas très bien déterminée, et l'angle, $\beta_c$, qui n'a jamais été mesuré mais dont la valeur prédite théoriquement est $\beta_c = 0.035°$. Le deuxième canal de désintégration permet d'éliminer la phase de mélange pour extraire $\beta_c$.

En pratique, nous ne mesurons pas exactement $\beta_c$ à partir de la mesure obtenue avec les équations 5.6, mais un angle effectif $\beta_{c,eff}$ qui inclut des incertitudes théoriques

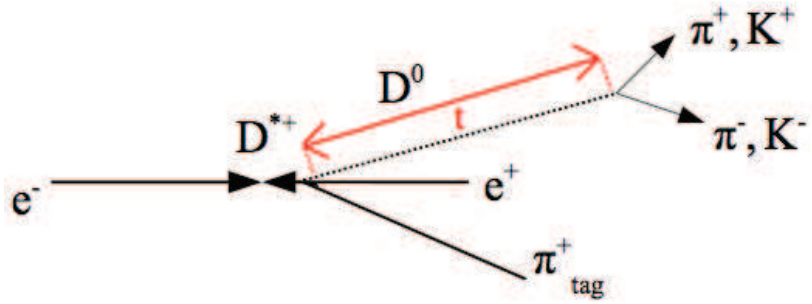


**Figure 5.2:** Production de $D^{*\pm}$ à partir du continuum $c\bar{c}$, le $D^{*\pm}$ se désintègre ensuite en un $D^0$ et un pion mou.

générées par les amplitudes contribuant à l'état final de $h^+h^-$ avec une phase faible $\phi_{mix}$ différente.

L'augmentation de la statistique avec l'expérience Belle II pourrait permettre une première mesure de l'angle $\beta_c$ du triangle d'untarité $c-u$. La mesure sensible à l'angle $\beta_c$ étudiée dans le cadre de cette thèse est l'asymétrie en fonction du temps entre les désintégrations des $D^0$ et celles des $\bar{D}^0$ vers deux états propres de CP différents, $D^0 \to \pi^+\pi^-$ et $D^0 \to K^+K^-$. Pour cela il faut reconstruire les $D^0$ dans chaque canal de désintégration, reconstruire la distance de vol des mésons et identifier leur saveur (méson ou anti-méson) au moment de leur production. Nous considérons les mésons $D^0$ produits dans le continuum $e^+e^- \to c\bar{c}$, dont la saveur est inférée de la charge du pion mou issu de la désintégration $D^{*+} \to D^0\pi^+$ (cf. figure 5.2). La saveur du $D^0$ au moment de sa désintégration est inférée des équations donnant leur évolution temporelle.

Nous reconstruisons ainsi la distribution $A_{CP}(t)$ de la différence entre le nombre de $D^0$ et le nombre de $\bar{D}^0$ qui se désintégrant vers l'état final propre de CP en fonction du temps et nous ajustons cette distribution à partir des équations 5.1 et 5.2.
Dans cette étude, nous nous intéressons à la violation de CP indirecte, c'est-à-dire que nous faisons l'hypothèse que $|\lambda_f|$ =1 et nous étudions la sensibilité de Belle II à la phase $\arg(\lambda_f)$, qui est laissé libre dans l'ajustement.

Les distributions temporelles des mésons $D^0$ et $\bar{D}^0$ sont simulées avec une simulation rapide que nous avons développée. Nous avons étudié la sensibilité de l'expérience Belle II à l'angle $\beta_c$ avec deux méthodes de mesure: une méthode de vraisemblance discréte et une méthode non binnée adoptée de la mesure de sin2$\beta$ dans BaBar,

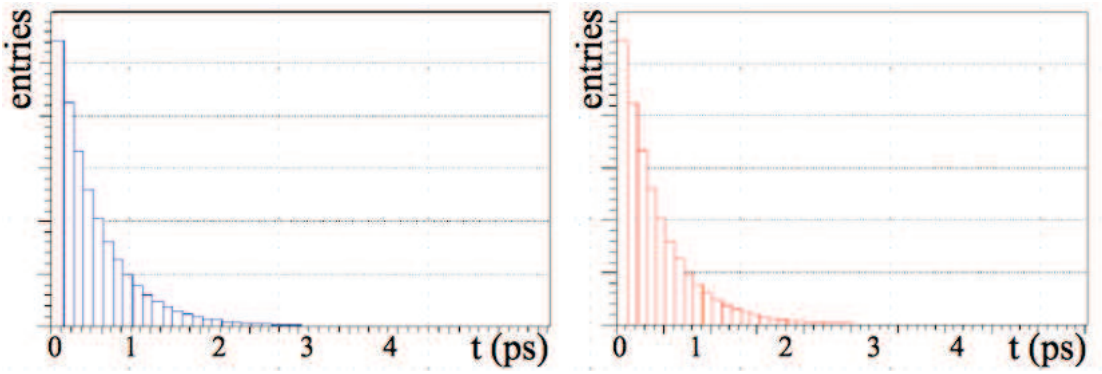


**Figure 5.3:** Les distributions de temps propre des désintégrations de $D^0$ (gauche) et de $\bar{D}^0$ (droite) générées avec une simulation rapide, avec $arg(\lambda_f) = 10°$, $|\lambda_f| = 1$ et $5{\times}10^6$ mésons $D^0$.

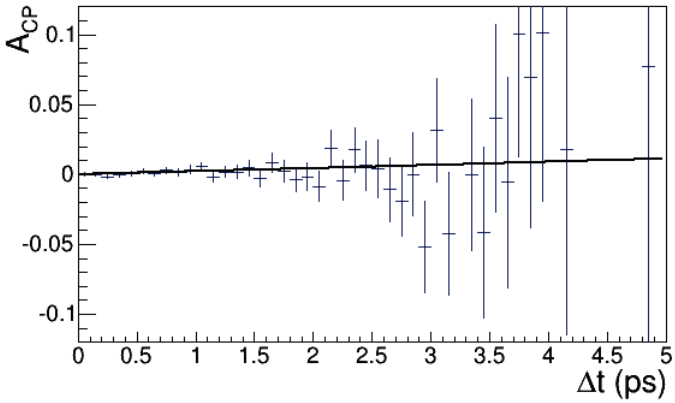


**Figure 5.4:** L'asymétrie simulée avec $arg(\lambda_f) = 10°$, $|\lambda_f| = 1$ et $5{\times}10^6$ mésons $D^0$.

basée sur RooFit. La méthode binnée est plus rapide à mettre en oeuvre en terme de CPU, mais elle est sensible au binning, c'est-à-dire au choix des intervalles en temps choisis pour représenter l'asymétrie en fonction du temps.

Les nombres attendus de $D^0$ reconstruits dans les canaux de désintégration considérés et dont la saveur est identifiée, avec l'ensemble des données de Belle II, c'est-à-dire 50 $ab^{-1}$, sont $5 \times 10^6$ $D^0 \to \pi^+\pi^-$ et $12 \times 10^6$ $D^0 \to K^+K^-$. La figure 5.3 montre les distributions générées du nombre de $D^0$ et $\bar{D}^0$ en fonction du temps. La figure 5.4 montre l'asymétrie de CP en fonction du temps rsultante générée.

La sensibilité à $\arg(\lambda_f)$ est donnée par la sensibilité à la pente de l'asymétrie représentée dans la figure 5.4. On observe que cette sensibilité est limitée par la

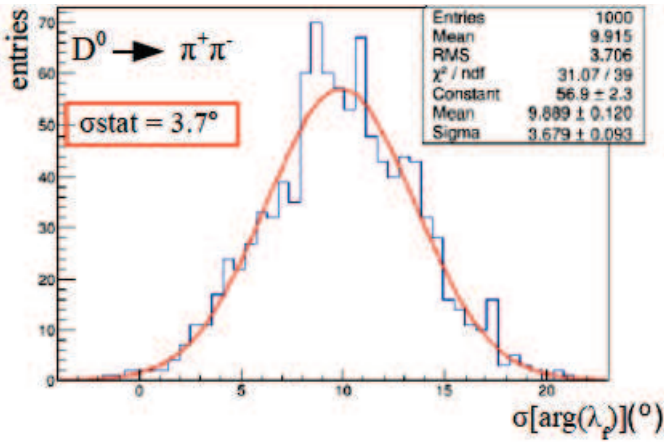


**Figure 5.5:** Dispersion statistique de 1000 mesures de $arg(\lambda_f)$. $5{\times}10^6$ mésons neutres $D^0$ ont été générés avec $arg(\lambda_f) = 10°$.

faible statistique à grand temps de vol des mésons $D^0$, qui ont tendance à se désintégrer plus vite qu'ils oscillent.

L'incertitude statistique est estimée par la largeur de la distribution gaussienne de mesures effectuées un grand nombre de fois, en simulant un grand nombre de lots différénts de données, comme illustré dans la figure 5.5. Notre étude montre que l'incertitude statistique est indépendante de l'amplitude de la violation de CP. Nous avons quantifié la dépendance de cette incertitude en fonction de la pureté de l'étiquetage de la saveur, de la résolution temporelle (traduite en une résolution spatiale) et du nombre de $D^0$ reconstruits.

Avec la statistique et les performances attendues dans Belle II (résolution spatiale, des vertex, pureté et efficacité de l'identification de la saveur de méson), nous prédisons une incertitude statistique de 2.1° sur la mesure de $\beta_c$.

Enfin, nous discutons les sources d'incertitudes systématiques (dont les principales proviennent des paramétres de l'oscillation des $D^0$) que l'on estime négligeables devant l'incertitude statistique.

En conclusion, une première mesure de l'angle $\beta_c$ du triangle d'unitarité $c-u$ pourra être effectuée avec l'ensemble des données de Belle II, avec une sensibilité de 2,1°, à laquelle s'ajoute une incertitude de 2,7° due aux contributions des diagrammes de Feynmann négligées dans la traduction de l'asymétrie de CP en angle $\beta_c$.

# III. Estimation des faibles impulsions basée sur l'énergie déposée dans les détecteurs en silicium de Belle II

Nous proposons d'améliorer la résolution sur les faibles impulsions en utilisant l'information de l'énergie mesurée dans les détecteurs en silicium constituant le trajectomètre interne de Belle II suite au passage de la particule, en adaptant à Belle II une méthode originalement développée dans le cadre des expériences STAR et ALICE.

Les particules de faible impulsion jouent un rôle important dans le programme de physique de Belle II en général, et en particulier pour la mesure de l'angle $\beta_c$ que nous venons de discuter. En effet le pion issu de la désintégration $D^{*+} \to D^0\pi^+$ utilisé pour cette mesure est mou, de l'ordre de 15% d'entre eux ont une impulsion inférieure à 150 MeV. Une estimation basée sur le dépôt d'énergie est susceptible d'améliorer la résolution sur l'impulsion pour les particules d'impulsion inférieure à 150 MeV, dont la reconstruction des trajectoires repose uniquement sur le trajectomètre interne.

La perte d'énergie de particules chargées traversant de la matière est décrite par la formule de Bethe-Bloch, qui varie en $1/\beta^2$ aux impulsions considérées, où $\beta$ est le *boost* de la particule. Cette courbe dépend aussi de la masse de la particule incidente, mais nous montrons qu'à ces impulsions, d'une part il est facile de distinguer un pion d'un kaon et d'un proton par le dépôt dénergie, d'autre part quasiment que des pions sont produits par les collisions dans Belle II.

Nous construisons un estimateur en sommant les dépôts d'énergie mesurés dans chacune des couches du trajectomètre interne et en divisant cette somme par l'épaisseur totale de silicium traversée pour estimer une perte d'énergie linéaire $\Delta E/\Delta x$.
L'épaisseur traversée est calculée en tenant compte de l'inclinaison de la particule au passage d'une couche de détection. Le trajectomètre de Belle II est constitué de deux couches pixellisées en silicium (PXD) de 75 $\mu$m chacune et 4 double-couches à micro-pistes en silicium (SVD) de 320 $\mu$m chacune.

Pour une impulsion donnée, l'énergie déposée relève d'un processus stochastique, et est décrite par une distribution de Landau. Dans le cas particulier de couches fines de silicium, peu de collisions ont lieu entre la particule chargée et les électrons, ce qui se traduit par une grande variance de cette distribution. Nous étudions différentes

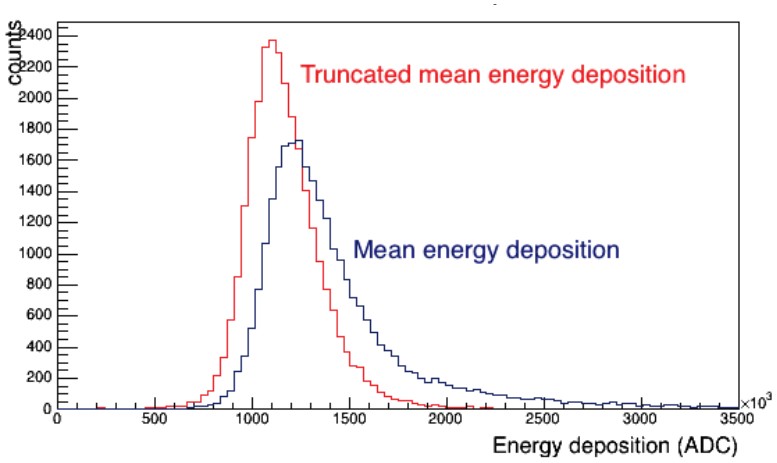


**Figure 5.6:** Distribution de la moyenne tronquée de l'énergie déposée, comparée à la moyenne de l'énergie déposée, pour des pions d'impulsion 70 MeV.

manières d'estimer la perte d'énergie moyenne, qui peut ensuite être paramétrisée en fonction de l'impulsion de la particule par la formule de Bethe-Bloch.

Calculer la valeur moyenne de tous les amas n'est pas la meilleure méthode pour définir la perte moyenne d'énergie ΔE. En effet, la distribution de la perte d'énergie est décrite par une fonction Landau, dont la queue est tronquée par le nombre réduit d'impacts reconstruits expérimentallement. Ce problème est classique dans la procédure d'identification des particules basée sur leur dépôt d'énergie. Pour limiter les variations statistiques de la perte d'énergie moyenne, l'ensemble des données est tronquée d'une manière déterminée.

La méthode la plus simple de troncation consiste à éliminer la charge la plus élevée de tous les amas afin de réduire la queue de distribution. Dans cette analyse, ceci est traduit par l'élimination des deux valeurs les plus élevées, car elles sont correlées. En effet, nous avons vérifié que ces deux charges correspondent toujours à la même couche du détecteur SVD. De fait cette méthode de troncation réduit la queue de la distribution des $\Delta E$ moyens, comme on peut le voir sur la figure 5.6.

Une difficulté supplémentaire dans le cas des faibles impulsions vient de l'importance accrue de la perte d'énergie à chaque passage dans une couche de matière, qui tend à biaiser les estimations de l'impulsion vers des impulsions trop faibles. D'autre part, les particules de faible impulsion ont tendance à boucler dans le trajectomètre interne à cause du champ magnétique. De nombreux amas de charges sont recon-

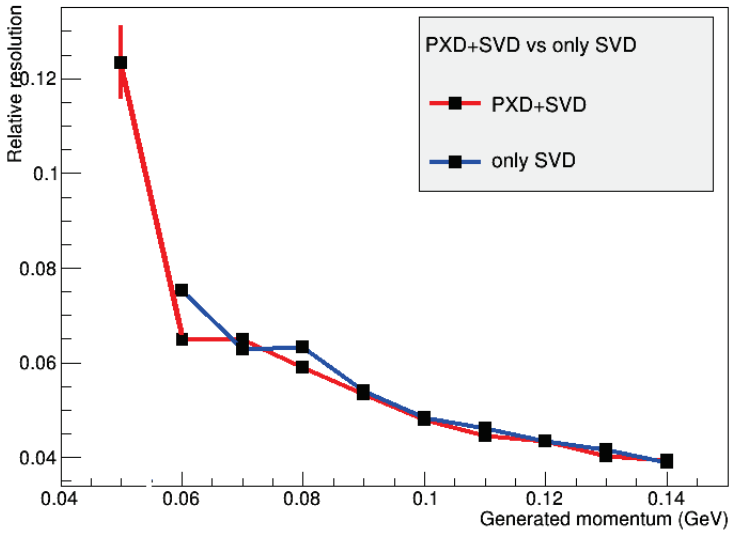


**Figure 5.7:** Résolution sur l'impulsion obtenue avec l'estimateur construit à partir des amas d'énergie reconstruits dans le SVD (courbe bleue) et a partir des amas reconstruits dans l'ensemble du trajectromètre interne SVD + PXD ( courbe rouge).

struits dans le détecteur, mais leur ordre le long de la trajectoire n'est pas connu.

La figure 5.7 présente une comparaison entre la résolution sur l'impulsion obtenue en construisant un estimateur basé uniquement sur les amas de charges reconstruits sans le SVD et sur ceux reconstruits dans l'ensemble du trajectromètre interne (SVD +PXD). Ce dernier estimateur est le meilleur, l'information des couches le plus internes pixelisées étant intéressante pour les plus faibles impulsions.

Les performances de l'estimateur final sont comparées dans la figure 5.8 à la résolution obtenue sur l'impulsion par l'ajustement par une hélice de la trace reconstruite.

Notre estimateur permet d'améliorer la résolution sur les faibles impulsions jusqu'à environ 120 MeV, soit en étant utilisé seul lorsque l'ajustement de la trajectoire par une hélice ne converge pas, soit en combinant les deux informations (ajustement de l'hélice dépendant de l'impulsion transverse et dépôt d'énergie, dépendant du module de l'impulsion).

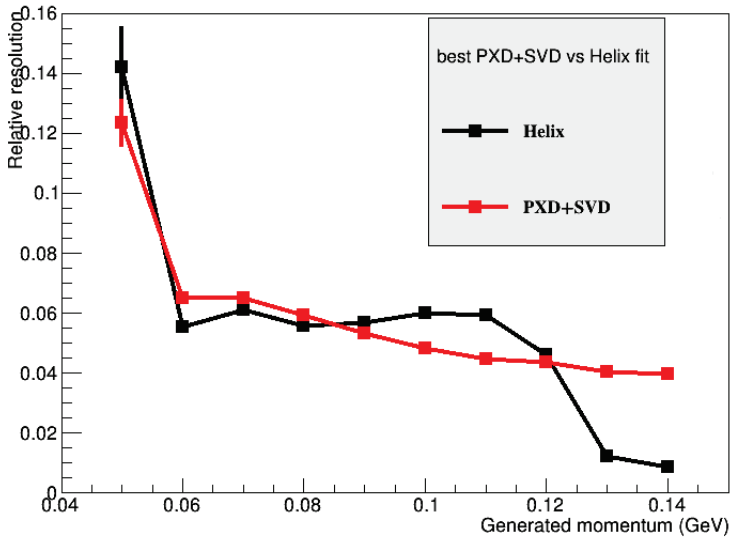


**Figure 5.8:** Les résolutions sur l'impulsion relative obtenues par l'ajustement de la trajectoire par une hélice (noir), et avec notre estimateur utilisant le dE/dx (rouge).

# IV. Etude des performances des détecteurs PLUME équipés de capteurs CMOS

Le détecteur PLUME est une échelle ultra-légére équipée sur chaque face par 6 capteurs pixellisés CMOS. J'ai participé à deux tests en faisceau de capteurs CMOS développés par mon groupe, qui ont eu lieu pendant la thèse : le premier dédié au test de PLUME, le deuxième dédié au test de SALAT (testant la capacité à produire des grandes surfaces pixellisées). Dans mon document de thèse je présente les résultats de l'analyse des données enregistrées lors de tests en faisceau de PLUME: celui auquel j'ai participé ainsi qu'un test effectué en 2011 avant mon arrivée dans le groupe.

Lors de ces tests, un télescope de faisceau constitué de quatre capteurs CMOS a permis de reconstruire les trajectoires des particules du faisceau, constituant un lot de traces de référence que l'on extrapole jusqu'au détecteur étudié (le DUT, Detector Under Test). La première étape de toute étude des performances du DUT est de déterminer les positions des détecteurs du télescope et du DUT dans un référentiel commun, processus appelé alignement. La position relative des capteurs composant le télescope et le DUT ont été obtenus $in-situ$, avec une précision de l'ordre de quelques millimètres. Mais, pour obtenir une précision de l'ordre de 3-4 $\mu$m, il faut utiliser le logiciel TAF développé par le groupe PICSEL de Strasbourg. Nous avons

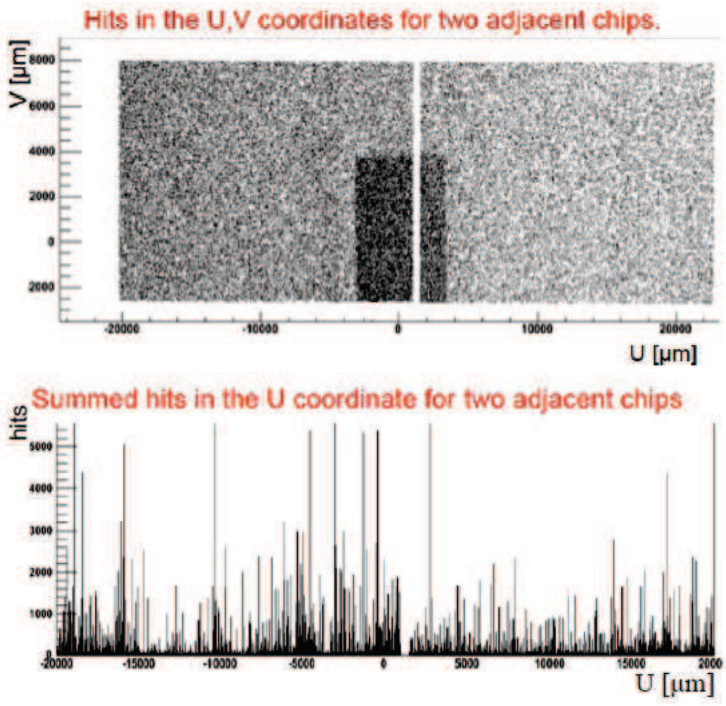


**Figure 5.9:** La distribution des impacts des particules du faisceau sur deux plans adjacents du DUT. Chaque intervalle d'histogramme correspond à une distance de 5 $\mu$m.

donc aligné le DUT avec des traces perpendiculaires au DUT, puis avec des traces inclinées de 36 et 60°. Pour 0 et 36°, le DUT est situé entre les deux bras du télescope et pour 60°, nous l'avons placé en-dehors par manque de place. Une fois l'alignement effectué, nous avons pu étudier les performances de l'échelle PLUME.

La première étude a permis de quantifier la distance effective entre deux capteurs adjacents sur l'échelle PLUME. A partir de l'extrapolation des traces de référence sur la surface des capteurs, nous avons produit des cartes 2D (les 2 dimensions correspondant au plan du capteur) des impacts des particules du faisceau, comme on peut le voir sur la figure 5.9.

Nous avons ainsi mesuré la distance entre deux capteurs adjacents en termes d'efficacité de reconstruction des impacts, qui est en moyenne de 550 $\mu$m. Cette distance est insensible du point de vue de la trajectrométrie. Le résultat obtenu est plutôt satisfaisant si on le compare avec d'autres technologies, comme celle des pixels hybrides.

Cette distance ne vas pas être diminuée pour le prochain prototype PLUME-2, qui va être utilisé pour la mesure du bruit de fond pendant la mise en route de Belle II. Mais, à l'avenir, il sera probablement possible d'atteindre un écart de 100 $\mu m$, notamment en réduisant la bordure protectrice entre deux capteurs adjacents et la dimension des séquenciers (qui permettent de lire une ligne de pixels).

La deuxième étude a consisté à mesurer la résolution angulaire des particules de grande incidence par rapport au détecteur. En effet, PLUME étant un détecteur pixellisé double-face, un mini-vecteur peut être reconstruit en associant les deux impacts reconstruits correspondant au passage d'une particule chargée. En plus de la mesure de la position de l'impact induit par le passage de la particule, ce mini-vecteur donne une information sur l'incidence angulaire de la particule. Nous avons mesuré la résolution angulaire de PLUME pour des particules d'incidence normale par rapport au détecteur, puis d'incidence 36°. Nous avons mis en évidence que l'alignement des détecteurs avec des particules de grande incidence est significativement plus difficile qu'avec des incidences normales. En effet, nous devenons sensibles à la planarité des capteurs, qui est imparfaite à l'échelle du micron, l'ordre de grandeur de la résolution spatiale visée. Pour obtenir une résolution spatiale raisonnable, le processus d'alignement doit être effectué individuellement pour des petites régions du capteur, correspondant à des surfaces qui peuvent être considérées comme planes. Un exemple d'alignement est montré sur la figure 5.10 pour une rotation du DUT de 36°.
La resolution spatiale obtenue est de 1,8 et 3,5 $\mu$m et la resolution angulaire de 0,12 et 0,25° pour, respectivement des traces perpendiculaires et des traces à 36°.

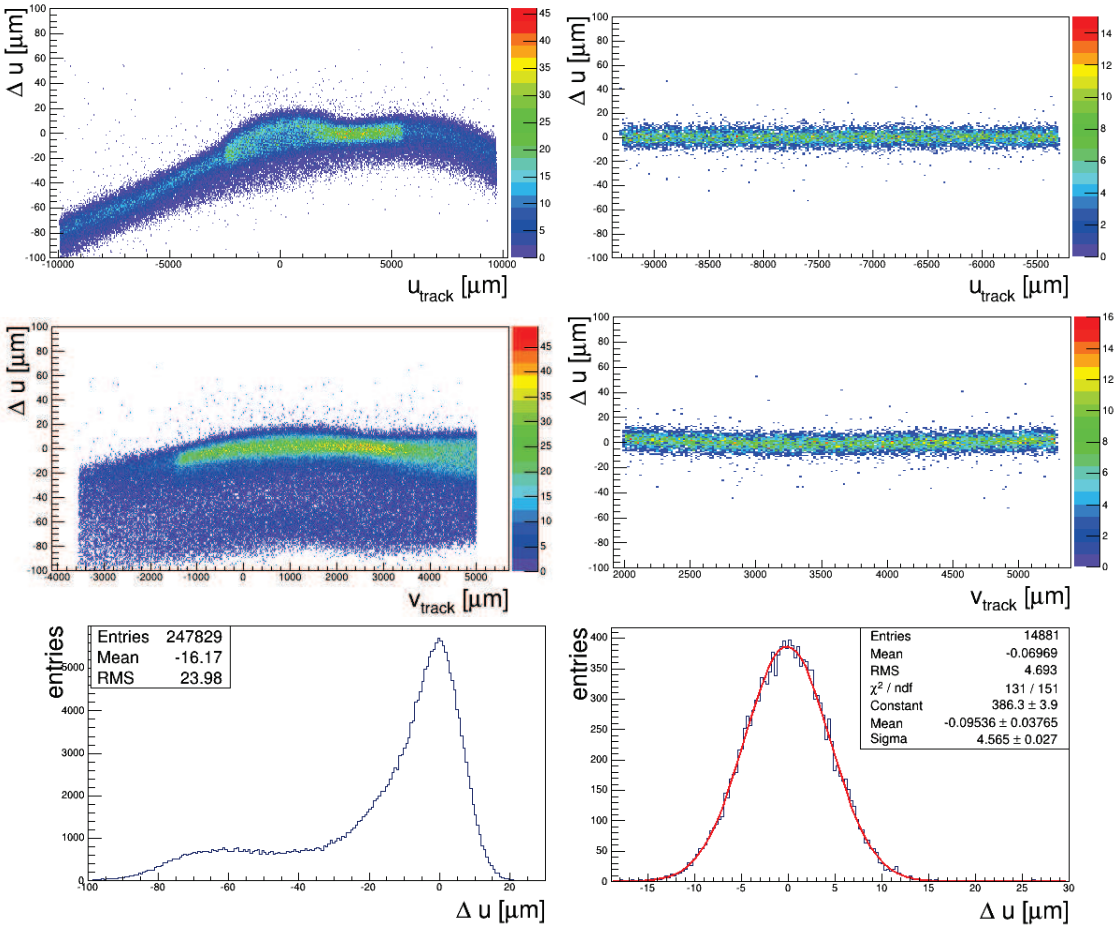


**Figure 5.10:** Les distributions du résidu $\Delta u$ observé pour traces inclinées de $\theta$=36° par rapport au DUT. La partie gauche correspond à un alignement globale de tout le capteur et la droite, à un alignement d'une sous-partie du capteur considéré comme plan au niveau micromètrique.

# V. Conclusion et perspectives

Le travail présenté dans cette thèse a été mené dans le cadre de l'expérience Belle II, dont l'objectif est d'enregistrer les collisions délivrées par l'accélérateur $e^+e^-$ SuperKEKB. Cette expérience est actuellement dans sa dernière étape de préparation avant le démarrage de la prise de données. Notre travail a porté sur trois points, tous liés aux performances du trajectomètre interne de Belle II.

Durant les trois années de la thèse, les algorithmes développés par la collaboration et utiles à nos études (notamment celle de la trajectométrie et de la reconstruction de vertex) n'ont cessé d'évoluer. C'est pourquoi cette thèse présente des études préliminaires pour les analyses de Belle II à venir.

Tout d'abord, nous avons étudié la sensibilité de Belle II à l'angle $\beta_c$ du triangle d'unitarité $c-u$. Cet angle a une valeur prédite très précise, de 0.035°, mais il n'a pas encore été mesuré de façon expérimentale. Si une valeur de $\beta_c$ plus élevée que prévu était trouvée, cela indiquerait la présence d'une physique au-delà du Modéle Standard. Cette mesure repose sur la reconstruction de la distance de vol de $D^0$, et par conséquent de la résolution du trajectomètre interne. Nous estimons qu'une précision de l'ordre de 3° pour cet angle peut être atteinte de Belle II. L'incertitude statistique restera néanmoins le facteur limitant cette mesure. Les contributions des longues distances impactant les prédictions théoriques dans le systéme $D^0$ -$\bar{D}^0$ devraient être mieux évaluées dans le futur grâce aux progrès des calculs de chromodynamique quantique sur réseau.

Notre deuxième étude a resulté en la proposition d'un nouvel estimateur améliorant la reconstruction des faibles impulsions dans Belle II. Les particules à faible impulsion jouent un rôle important dans le programme physique de Belle II, et en particulier dans la mesure de $\beta_c$. Actuellement, leur estimation est basée sur un ajustement de la trace par une hélice. L'estimateur de faibles impulsions développé dans cette thèse prend en compte les dépôts d'énergie de particules chargées dans les couches en silicium du trajectomètre interne. Ses performances sont aussi bonnes voire meilleures pour les faibles impulsions que celles observées pour l'estimateur utilisé jusqu'à présent. La collaboration de Belle II envisage d'utiliser ces résultats pour améliorer la mesure des faibles impulsions. Ces travaux sont aussi une piste pour améliorer les rejets des impacts dus aux particules de bruit de fond générées

par les nano-faisceaux de SuperKEKB.

Enfin, nous avons analysé les données récoltées lors d'un test en faisceau pour un détecteur double-couche PLUME, équipé de capteurs CMOS. Nous avions pour but de vérifier des caractéristiques particulières de l'échelle afin d'améliorer la conception et la procédure de construction d'une deuxième génération. Ce nouveau prototype de PLUME sera utilisé pendant la mise en route de l'expérience Belle II, afin de caractériser le bruit de fond produit par le collisionneur SuperKEKB dans la région d'interaction. Pour ce faire, la distance effective entre deux capteurs adjacents a été évaluée, de l'ordre de 500 $\mu$m, et la planéité de la surface des capteurs a été étudie, afin d'élaborer une nouvelle méthode de collage automatique des capteurs sur l'échelle.

# Bibliography


[1] A.D. Sakharov, Violation of CP Invariance, C Asymmetry, and Baryon Asymmetry of the Universe, Pisma Zh. Eksp. Teor. Fiz.: 5:32-35, 196

[2] N. Cabibbo, Unitary Symmetry and Leptonic Decays, Phys. Rev. Lett. 10, 531, (1963)

[3] M. Kobayashi and T. Maskawa, CP Violation in the Renormalizable Theory of Weak Interaction, Prog. Theor. Phys. 49 (1973) 652

[4] J.H. Christenson *et al.*, First Evidence for Direct CP Violation, Phys. Rev. Lett. 13, 138 (1964)

[5] BABAR Collab: B. Aubert *et al.*, Observation of direct CP violation in $B^0 \to K^+\pi^-$ decays, Phys. Rev. Lett. 93, 131801 (2004).

[6] Belle Collab: K. Abe *et al.*, Improved Measurements of Direct CP Violation in $B \to K^+\pi^-, K^+\pi^0$ and $\pi^+\pi^0$ Decays, arXiv:hep-ex/0507045

[7] BABAR Collab: B. Aubert *et al.*, Dalitz-plot analysis of the decays $B^\pm \to K^\pm\pi^{mp}\pi^\pm$, Phys. Rev. D72, 072003 (2005)

[8] Belle Collab: A. Garmash *et al.*, Evidence for large direct CP violation in $B^\pm \to \rho(770)^0 K^\pm$ from Analysis of the Three-Body Charmless $B^\pm \to K^\pm\pi^\pm\pi^\pm$ Decay, Phys. Rev. Lett. 96, 251803 (2006)

[9] LHCb collaboration: R. Aaij *et al.*, A search for time-integrated CP violation in $D^0 \to K^-K^+$ and $D^0 \to \pi^-\pi^+$ decays, LHCb-CONF-2013-003

[10] CDF collaboration: T. Aaltonen *et al.*, Measurement of the difference of CP-violating asymmetries in $D^0 \to K^+K^-$ and $D^0 \to \pi^+\pi^-$ decays at CDF, arXiv:1207.2158

[11] B. R. Ko for Belle collaboration, CP violation and mixing in the charm sector at Belle, and current HFAG averages, arXiv:1212.5320 [hep-ex], 2012

[12] M. Gell-Mann, A Schematic Model of Baryons and Mesons, Phys.Lett. 8 (1964) 214-215

[13] G. Zweig, An SU(3) Model for Strong Interaction Symmetry and its Breaking, CERN Report No.8182/TH.401

[14] Belle Collab: K. Abe *et al.*, Properties of X(3872) at Belle, ICHEP04, arXiv:hep-ex/0408116v2, 2004

[15] LHCb collaboration: R. Aaij *et al.*, Observation of $J/\Psi p$ resonances consistent with pentaquark states in $\Lambda_b^0 \to J/\Psi K^- p$ decays, Phys. Rev. Lett. 115, 072001 (2015)

[16] ATLAS Collaboration, Observation of a new particle in the search for the Standard Model Higgs boson with the ATLAS detector at the LHC, Phys. Lett. B 716 (2012) 1

[17] CMS Collaboration, Observation of a new boson at a mass of 125 GeV with the CMS experiment at the LHC, Phys. Lett. B 716 (2012) 30

[18] Y. Fukuda *et al.*, Evidence for oscillation of atmospheric neutrinos, Phys. Rev. Lett. 81, 1562, 1998

[19] I. I. Bigi, A. I. Sanda, CP violation, second edition, Cambridge monographs on particle physics, nuclear physics and cosmology, 2009

[20] G. D. Rochester and Dr. C. C. Butler, Evidence for the existence of new unstable elementary particles, Nature 160, 855-857 (1947)

[21] K. Nishijima, Charge Independence Theory of V Particles, Prog. Theor. Phys. Vol. 13, 285, (1955)

[22] M. Gell-Mann, The interpretation of the New Particles as Displaced Charge Multiplets, Nuovo Cimento 4, Suppl. 2, 848 (1956)

[23] S. L. Glashow, J. Iliopoulos, L. Maiani, Weak Interactions with Lepton-Hadron Symmetry, Phys. Rev. D2, 1285, (1970)

[24] J. J. Aubert *et al.*, Experimental Observation of a Heavy Particle J, Phys. Rev. Lett. 33, 1404 (1974)

[25] J. E. Augustin *et al.*, Discovery of a Narrow Resonance in $e^+e^-$ Annihilation,

Phys. Rev. Lett. 33, 1406 (1974)

[26] M. Veltman, Facts and Mysteries in Elementary Particle Physics, 2003

[27] L. Maiani, The GIM Mechanism: origin, predictions and recent uses, arXiv:1303.6154, 2013

[28] T Morii, C.S. Lim, S.N. Mukherjee, The Physics of the Standard Model and Beyond, World Scientific Publishing, 2003

[29] L. L. Chau and W. Y. Keung, Comments on the Parametrization of the Kobayashi-Maskawa Matrix, Phys. Rev. Lett. 53, 1802 (1984)

[30] Marco Battaglia *et al.*, The CKM Matrix and the Unitarity Triangle, in the Workshop on CKM Unitarity Triangle (CERN 2002-2003), hep-ph/0304132

[31] A. Ceccuci, Z. Ligeti, Y. Sakai, Review of Particle Physics, Particle Data Group, 2014

[32] L. Wolfenstein, Parametrization of the Kobayashi-Maskawa Matrix, Phys. Rev. Lett. 51, n. 21, 1983

[33] A. Buras, M. Lautenbacher, G. Ostermaier, Waiting for the top quark mass, $K^+ \to \pi^+ \nu\bar{\nu}$, $B_s^0 - \bar{B}_s^0$ mixing and CP asymmetries in B-decays, Phys. Rev. D50, 3433 (1994)

[34] A.J. Buras *et al.*, Universal unitarity triangle and physics beyond the standard model, Phys. Rev. D50, 3433 (1994) [hep-ph/9403384]

[35] J. Charles *et al.* [CKMfitter Group], CP Violation and the CKM Matrix: Assessing the Impact of the Asymmetric B Factories Eur. Phys. J. C41, 1 (2005) [hep-ph/0406184

[36] B.R.Martin and G. Shaw, Particle Physics, Third Edition, Wiley 2008, p 304

[37] C. Jarlskog, CP violation, Advance series on directions in high energy physics vol.3, 2001

[38] C. Jarlskog, Commutator of the Quark Mass Matrices in the Standard Electroweak Model and a Measure of Maximal CP Nonconservation, Phys. Rev. Lett. 55, 1039, 1985

[39] A. de Angelis, M. J. M. Pimenta, Introduction to Particle and Astroparticle

Physics, Questions to the Universe, Springer 2015

[40] I. I. Y. Bigi and A. I. Sanda, On the Other Five KM Triangles hep-ph/9909479

[41] http://ckmfitter.in2p3.fr/

[42] http://utfit.org/UTfit/

[43] A. J. Bevan, G. Inguglia, B. Meadows, Time-dependent CP asymmetries in D and B decays, arXiv:1106.5075 [hep-ph], 2013

[44] W. F. Fry *et al.*, Evidence for a Long-Lived Neutral Unstable Particle, Phys. Rev. 103, 1904 (1956)

[45] M. Gell-Mann and A. Pais, Behavior of Neutral Particles under Charge Conjugation, Phys. Rev. 97, (1954)

[46] C. Albajar *et al.*, Search for $B^0 - \bar{B}^0$ oscillations at the cern proton - anti-proton collider 2. Phys. Lett., B186:247, 1987

[47] A. Abulencia et al. [CDF Collaboration], Phys. Rev. Lett. 97(2006) 242003

[48] H. Albrecht et al., Phys. Lett., vol. B192, p. 245, 1987.

[49] Belle collaboration: M. Staric *et al.*, Evidence for $D^0$ - $\bar{D}^0$ Mixing, Phys.Rev.Lett.98:211803,2007

[50] BaBar collaboration: B. Aubert *et al.*, Evidence for $D^0$ - $\bar{D}^0$ Mixing, Phys.Rev.Lett. 98, (2007)

[51] CDF collaboration: T. Aaltonen *et al.*, Evidence for $D^0$ - $\bar{D}^0$ Mixing using the CDF II Detector, Phys.Rev.Lett. 100 (2008)

[52] Heavy Flavor Averaging Group (HFAG) Collaboration,Y. Amhis *et al.*, Averages of $b$-hadron, $c$-hadron, and $\tau$-lepton properties as of summer 2014, arXiv:1412.7515 [hep-ex]

[53] Alexey A Petrov, Charm mixing in the standard model and beyond. Int. J. Mod. Phys., A21:5686-5693, 2006

[54] Adam F. Falk, Yuval Grossman, Zoltan Ligeti, Yosef Nir, and Alexey A. Petrov. The D0-D0 mass difference from a dispersion relation. Phys. Rev., D69:114021, 2004

[55] Gustavo Burdman and Ian Shipsey. D0-D0 mixing and rare charm decays. Ann. Rev. Nucl. Part. Sci., 53:431-499, 2003

[56] Adam F. Falk, Yuval Grossman, Zoltan Ligeti, and Alexey A. Petrov, SU(3) breaking and D0-D0 mixing. Phys. Rev., D65:054034, 2002

[57] John F. Donoghue, Eugene Golowich, Barry R. Holstein, and Josip Trampetic. Dispersive effects in D0-D0 mixing. Phys. Rev., D33:179, 1986

[58] A. Petrov, On dipenguin contribution to $D^0 - \bar{D}^0$ mixing., Phys.Rev. D56, 1685-1687 (1997)

[59] K.Hosoyama *et al.*, Development of the KEK-B superconducting crab cavity, Proceedings of EPAC08, Genoa, Italy, 2008

[60] Alessandro Gaz, On the behalf of the Babar and Belle Collaborations, Indirect constraints on New Physics from the B-factories, arXiv:1411.1882 [hep-ex]

[61] K. Wille, The physics of particle accelerators: an introduction, Oxford University Press, 2000

[62] Belle II collaboration, Belle II Technical Design Report, Machine Parameters, 2010

[63] P. Raimondi, Status of the SuperB Effort, Presentation at the 2nd Workshop on SuperB Factory, LNF-INFN, Frascati, 2006

[64] M Zobov *et al.*, Test of ï£¡Crab-Waistï£¡ Collisions at the DAΦNE Φ Factory, Phys. Rev. Lett. 104, 174801 , 2010

[65] Y. Funakoshi, Some considerations on beam background after beam injection, Belle II internal note

[66] D. Zhou, Beam Dynamics Issues in SuperKEKB, The 20th KEKB Accelerator Review Committee, Feb. 23, 2015

[67] Y. Funakoshi for the KEKB Commissioning Group, Operational experience with crab cavities at KEKB, CERN Yellow Report CERN-2014-004, pp.27-36 arXiv:1410.4036

[68] M. E. Biagini, Status and perspectives of high luminosity Flavour Factories, POS EPS-HEP 2013, 548

[69] A. Kuzmin, Upgrade of the electromagnetic calorimeter for Belle II, Calorimetry for High Energy Frontier, 2013

[70] I Adachi, Belle II Construction and Schedule, The 20th KEKB Accelerator Review Committee, 2015 Feb. 23-25

[71] T. Abe, Calculations of the radiation dose from the synchrotron radiation for the Belle silicon vertex detector, KEK Proceedings 2002-18, p 33-36

[72] H. Nakayama, Beam background and MDI design for SuperKEKB / BELLE II, Proceedings of IPAC2011, San Sebastian, Spain

[73] C. Kiesling for the MPI Belle Group, B-Physics with Belle and Preparations for Belle II at SuperKEKB, Project Review 2011

[74] S. Tanaka, The interaction region and BEAST II, FJ-PPL meeting on Belle II, 24 Oct 2013

[75] S. Uno, H. Nakayama, Beam background at SuperKEKB / Belle-II, The Technology and Instrumentation in Particle Physics 2011, Chicago

[76] H. Nakayama on behalf of Belle2 Beam background group, Beam background at BEAST, 20th ARC, Febr 23-25

[77] Belle II collaboration, Belle II Technical Design Report, 2010.

[78] C. Lacasta, DEPFET pixel detectors for future electron-positron experiments, IC-HEP (2014) 505

[79] T. Bergauer, The Silicon Vertex Detector of the Belle II Experiment, EPS-HEP 2013, 487

[80] F. Mueller on behalf of the DEPFET Collaboration, DEPFET at Belle II, INSTR 2014

[81] M. Tobias Koch, Development of a test environment for the characterization of the current digitizer chip DCD2 and the DEPFET pixel system for the Belle I experiment at SuperKEKB, dissertation Bonn 2011

[82] D Levit *et al.*, FPGA Based Data Read-Out System of the Belle 2 Pixel Detector, arXiv:1406.3864v1, physics.ins-det, 2014

[83] J. Schieck for DEPFET collaboration, DEPFET Pixels as a Vertex Detector

for the Belle II Experiment, arXiv:1304.0870v1, 2013

[84] M. Friedl *et al.*, The Belle II Silicon Vertex Detector, TIPP 2011

[85] M. Friedl, Lorentz and Windmill Revisited, SVD Meeting, 2011

[86] H. Spieler, Introduction to Radiation Detectors and Electronics, 1999

[87] M. Friedl *et al.*, The Belle II Silicon Vertex Detector readout chain, Topical Workhop on Electronics for Particle Physics, Oxford 2012

[88] T. Iwashita, Tracking Detectors for Belle II, BEAUTY 2014 - 15th International Conference on B-Physics at Frontier Machines

[89] M. Barett on behalf of iTOP group, Particle identification with the iTOP detector at Belle-II, DPF 2013

[90] Y. Horii, TOP Detector for Particle Identification at the Belle II Experiment, EPS-HEP 2013

[91] I. Adachi *et al.*, 144-channel HAPD for Aerogel RICH at Belle II, RICH Proceedings of the Eighth International Workshop on Ring Imaging Cherenkov Detectors Shonan, Kanagawa, Japan, December 2-6, 2013

[92] Belle-ECL, V. V Aulchenko *et al.*, Electromagnetic calorimeter for Belle II, Journal of Physics: Conference Series 587 (2015) 012045

[93] C. Y. E. Ho, Noise Studies on Silicon Avalanche Photodiodes and Caesium Iodide Crystals for the Belle II Experiment, The Third Annual Undergraduate Physics Research Symposium (2013)

[94] A. Beaulieu for the Canadian Belle II group, Belle-II calorimeter endcap upgrade, CAP Congress, June 2014

[95] A. Kuzmin for Belle II ECL, Upgrade of the electromagnetic calorimeter for Belle II, CHEF 2013

[96] T. Aushev *et al.*, A scintillator based muon and $K_L$ detector for the Belle II experiment, Nucl.Instrum.Meth. A789 (2015)

[97] T. Uglov, Neutral long-living kaon and muon system of the Belle II detector, arXiv:1310.2162, 2013

[98] A. Moll, The Software Framework of the Belle II Experiment, CHEP 2010

[99] ROOT website, https://root.cern.ch/drupal/

[100] F. Bianchi *et al.*, Belle 2 Analysis Software Design Documentation 2013

[101] T. Sjöstrand *et al.*, An Introduction to PYTHIA 8.2

[102] A. Ryd *et al.*, EvtGen A Monte Carlo Generator for B-Physics, EVTGEN-V00-11-06

[103] C. Pulvermacher, The Belle II Software Framework and ROOT, ROOT Users Workshop 2013

[104] R. Aaij *et al.*, Measurement of CP asymmetry in $D^0 \to K^+K^-$and $D^0 \to \pi^+\pi^-$decays, JHEP07-2014-041, arXiv: 1405.2797

[105] G. Inguglia, Time-dependent CP violation in charm mesons, PhD dissertation, 2014

[106] M. Gersabeck *et al.*, On the interplay of direct and indirect CP violation in charm sector, J. Phys. G: Nucl. Part. Phys. 39 045005, 2012

[107] A. L. Kagan *et al.*, On indirect CP violation and its implications for $D^0$ -$\bar{D}^0$ and $B_{(s)} - \overline{B}_{(s)}$ mixing, Phys. Rev. D80: 076008, 2009

[108] R. Aaij *et al.*, A search for time-integrated CP violation in $D^0 \to h^+h^-$ decays, LHCb-CONF-2011-061

[109] S. Bianco *et al.*, A Cicerone for the Physics of Charm,Riv.Nuovo Cim.26N7:1-200, 2003

[110] Y. Grossman, A. Kagan, Y. Nir, New Physics and CP Violation in Singly Cabibbo Suppressed D Decays, Phys. Rev. D 75, arXiv:hep-ph/0609178, 2006

[111] M. Bobrowski, A. Lenz, J. Riedl and J. Rohrwild, How large can the SM contribution to CP violation in $D^0$ -$\bar{D}^0$ mixing can be?, JHEP 1003 (2010) 009 arXiv:1002.4794 [hep-ph] DO-TH-10-04, TTK-10-2

[112] T. Aaltonen *et al.*, Measurement of the difference in CP-violating asymmetries in $D^0 \to K^+K^-$and $D^0 \to \pi^+\pi^-$decays at CDF, Phys Rev Lett. 2012 Sep 14;109(11):111801. Epub 2012 Sep 11

[113] B. R. Ko for Belle collaboration, CP violation and mixing in the charm sector at Belle, and current HFAG averages, arXiv:1212.5320 [hep-ex], 2012

[114] B. R. Ko for Belle collaboration, Direct CP violation in charm at Belle, 36th International Conference on High Energy Physics, July 4-11, 2012 Melbourne, Australia

[115] A. Contu, Measurements of CPV and mixing in charm decays, Rencontres de Physique de la Valée d'Aoste

[116] R. Aaij *et al.*, Measurement of indirect CP asymmetries in $D^0 \to K^+K^-$and $D^0 \to \pi^+\pi^-$decays using semileptonic B decays, JHEP 04 (2015) 043

[117] J. P. Lees *et al.*, Measurement of $D^0$ -$\bar{D}^0$ Mixing and CP Violation in Two-Body $D^0$ Decays, Phys. Rev. D 87 (2012) 012004

[118] M. Staric, New Belle results on $D^0$ -$\bar{D}^0$ mixing, 5th International Workshop on Charm Physics, Hawaii, 2012

[119] M. Staric, $D^0$ mixing at Belle, The 2007 Europhysics Conference on High Energy Physics

[120] A. J. Bevan, B. Meadows, Bounding hadronic uncertainties in $c \to u$ decays, Phys. Rev. D 90, 094028, 2014

[121] E. Nakano, Belle PID, Nucl. Instr. Meth. A494, 402 (2002)

[122] W. Verkerke, D. Kirkby, RooFit Users Manual v2.91

[123] B. Aubert *et al.*, Measurement of the CP Asymmetry Amplitude $sin2\beta$, Phys.Rev.Lett. 89 (2002)

[124] K.A. Olive *et al.* (Particle Data Group), The Review of Particle Physics, Chin. Phys. C, 38, 090001(2014) [http://pdg.lbl.gov].

[125] The BaBar collaboration, Measurement of CP-Violating Asymmetries in $B^0$ Decays to CP Eigenstates, arXiv:hep-ex/0102030, 2001

[126] Passage of particles through matter, PDG, 2012 review.

[127] J. F. Ziegler, The Stopping of Energetic Light Ions in Elemental Matter, J. Appl. Phys / Rev. Appl. Phys., 85, 1249-1272 (1999)

[128] S.P. Moller *et al.*, Antiproton Stopping at Low Energies: Confirmation of Velocity-Proportional Stopping Power, Phys. Rev. Lett. 88 (2002)

[129] H. Bichsel, Straggling in thin silicon detectors, Rev. Mod. Phys. 60 (1988) 663

[130] M Friedl, The CMS Silicon Strip Tracker and its Electronic Readout, PhD dissertation, 2001

[131] H. Bichsel, A method to improve tracking and particle identification in TPCs and silicon detectors, Nuclear Instruments and Methods in Physics Research A 562 (2006) 154-197

[132] S.D. Paganis, J.L. Tang, Momentum Resolution Improvement Technique for Silicon Tracking Detectors using dE/dx, arXiv:hep-ex/0104006v1

[133] E. R. Fossum, CMOS Image Sensors: Electronic Camera On A Chip, IEEE Trans. on Electron Devices, vol. 44, no. 10 (1997), pp. 1689-1698

[134] R. Turchetta, Talk presented at the Second SOCLE Workshop, LAL-Orsay, France, 23 February, 1999

[135] R. Turchetta *et al.*, A monolithic active pixel sensor for charged particle tracking and imaging using standard VLSI CMOS technology, Nuclear Instruments and Methods in Physics Research A 458 (2001) 677-689

[136] M. Winter, Introduction to CMOS pixel sensors, EDIT school, CERN 2011

[137] The ILD Concept Group, The International Large Detector: Letter of Intent, arXiv:1006.3396 [hep-ex], 2010

[138] M. Caccia *et al.*, High resolution pixel detectors for $e^+e^-$ linear colliders, arXiv:hep-ex/9910019

[139] J. Baudot *et al.*, Fully depleted CMOS Pixel Sensors (CPS) development and potential applications, ANIMMA, 20-24 April, Lisboa, 2015

[140] M. Koziel, Development of radiation hardened pixel sensors for charged particle detection, PhD dissertation, IPHC 2011

[141] M. Szelezniak, Development of pixel detectors with integrated microcircuits for the Vertex Detector in the STAR experiment at the RHIC collider, PhD dissertation 2008

[142] http://www.eudet.org/

[143] W. Dulinski *et al.*, Beam Telescope for Medium Energy Particles based on Thin, Submicron Precision MAPS, IEEE Nuclear Scince Sypmposium, Conference Record: 995- 1002, 2007

[144] W. Dulinski, TAPI: High Precision Beam Telescope based on MIMOSA-18 Monolithic Pixel Sensor and TNT2 Data Acquisition Boards, EUDET-Memo-2008-22, 2008

[145] C. Hu-Guo *et al.*, First reticule size MAPS with digital output and integrated zero suppression for the EUDET-JRA1 beam telescope, Nucl. Instrum. Meth. 623 (2010) 480

[146] J. Behr, Test Beam Measurements with the EUDET Pixel Telescope, EUDET-Report-2010-01

[147] J. Aguilar *et al.*, Infrastructure for Detector Research and Development towards the International Linear Collider, arXiv:1201.4657 [physics.ins-det]

[148] I. Valin, A reticle size CMOS pixel sensor dedicated to the STAR HFT, JINST 7 C01102, 2012

[149] S. Senyukov *et al.*, Development of CMOS pixel sensors for tracking and vertexing in high energy physics experiments, IPRD13, 7-10 October 2013, Siena, Italy

[150] F. Morel *et al.*, MISTRAL & ASTRAL: two CMOS Pixel Sensor architectures suited to the Inner Tracking System of the ALICE experiment, JINST 9 C01026, 2014

[151] I. Ripp-Baudot, L'expérience Belle II et le démarrage de SuperKEKB, IPHC seminar 13.02.2015

[152] M. Winter for PICSEL team, Upcoming Perspectives offered by CMOS Pixel Sensors for Vertexing & Tracking at the ILC, ALCW 2015, KEK, 21st April 2015

[153] N. Chon-Sen *et al.*, Development of ultra-light pixelated ladders for an ILC vertex detector, LCWS/ILC 2010

[154] M. Winter *et al.*, 2001-2004 R&D Programme on Monolithic Active Pixel Sen-

sors for Charged Particle Tracking at a Future Linear Collider Vertex Detector, PRC R&D, 2001

[155] http://www.iphc.cnrs.fr/List-of-MIMOSA-chips.html

[156] Y. Voutsinas, Optimisation of the ILC vertex detector and study of the Higgs couplings, thesis dissertation, 2012

[157] Y. Zhou, Development of a CMOS pixel sensor for embedded space dosimeter with low weight and minimal power dissipation, PhD dissertation, IPHC 2014

[158] A. Himmi *et al.*, JRA-1 Milestone SDC Prototype 2 ready, EUDET-Memo-2007-55

[159] J. Baudot. Future of Low Mass Pixel Systems with MAPS, 19th International Workshop on Vertex Detectors. Loch Lomond, Scotland, UK, June 6-11 2010

[160] L. Cousin, Trajectométrie dans le cadre du project européen AIDA, PhD dissertation, IPHC 2015

[161] A. Nomerotski *et al.*, Ultra-light ladders for linear collider vertex detector, Nucl.Instrum.Meth. A650 (2011) 208-212

[162] J. Baudot emphet al., Development of Single- and Double-sided Ladders for the ILD Vertex Detectors, LCWS 2011, Granada, Spain, 2011

[163] J. Baudot, TAF short manual

[164] C. A. Dritsa, Design of the Micro Vertex Detector of the CBM experiment: Development of a detector response model and feasibility studies of open charm measurement, PhD dissertation

[165] D. Cantarato, Silicon Detectors for Particle Tracking at Future High-Energy Physics Experiments, PhD dissertation, Hamburg 2005

[166] J. Baudot *et al.*, P.L.U.M.E. test beam results, internal note IPHC, 2012

[167] B. Boitrelle, Intelligent detection layers for advanced trackingin high-energie physics, ongoing thesis ,IPHC

[168] J. Goldstein, Mechanical update, PLUME meeting 2011, Bristol University

[169] M. Goffe, PLUME 2010, PICSEL group internal document